Experimental Study and Test Preparation for New Generation MEMS Vaporising Liquid Microthrusters

Manufacturing, Characterisation, Interfacing, and Preliminary Testing

Andrei Pârvulescu

Delft University of Technology

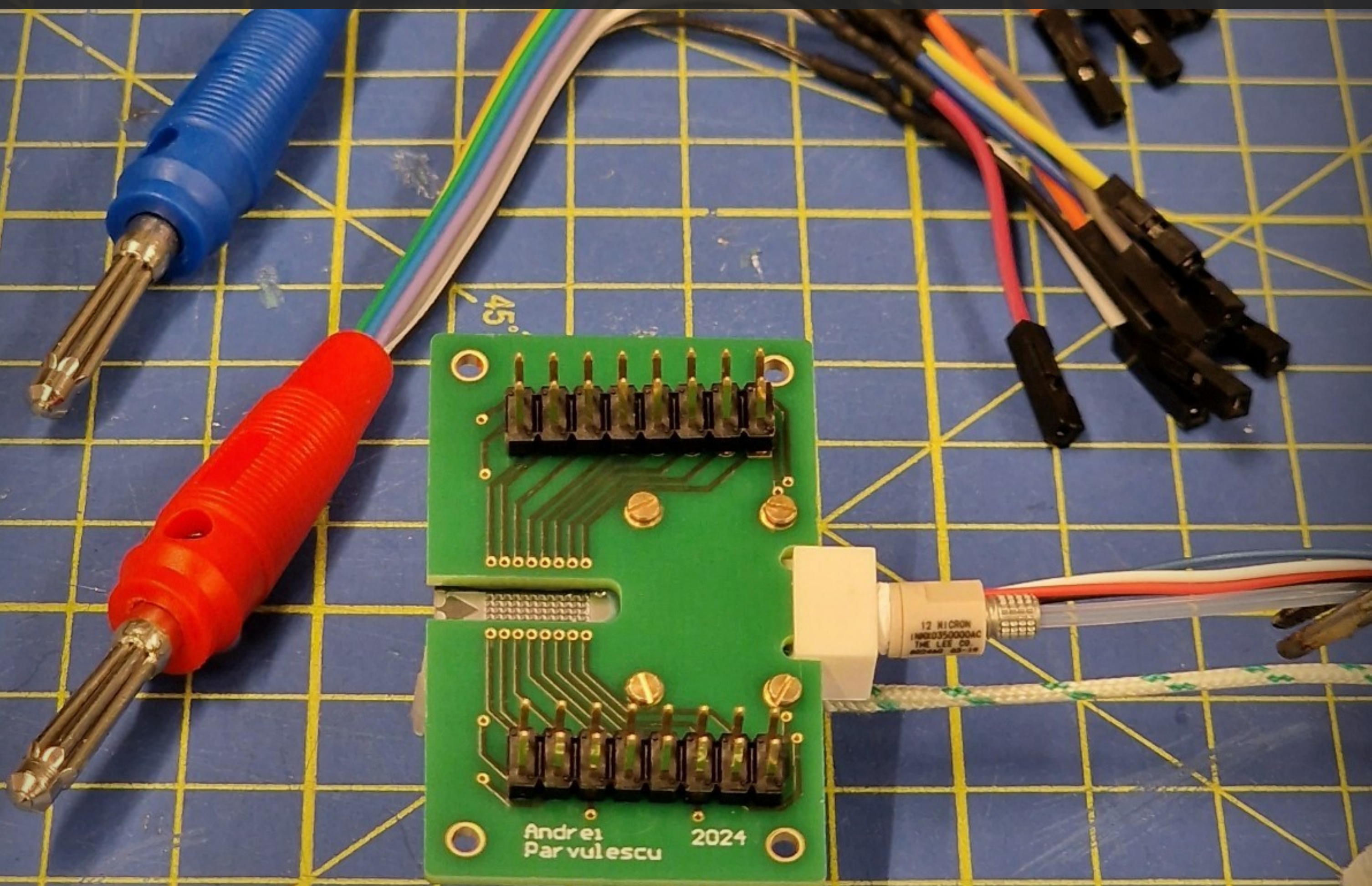

TU Delft

Experimental Study and Test Preparation for New Generation MEMS Vaporising Liquid Microthrusters

Manufacturing, Characterisation, Interfacing, and Preliminary Testing

by

Andrei Pârvulescu

to obtain the degree of Master of Science
at the Delft University of Technology – Faculty of Aerospace Engineering,
to be defended publicly on Tuesday, 26th of November 2024 at 14:30.

Student number:	5118344	
Project duration:	February 2024 – November 2024	
Thesis committee:	Dr. Angelo Cervone,	TU Delft, supervisor
	Dr. Alessandra Menicucci,	TU Delft, chairperson
	Ir. Marc C. Naeije,	TU Delft, external examiner
	Dr. Ing. Henk W. van Zeijl,	TU Delft, additional member

Cover: Assembled microthruster and interfaces, together with power supply cables placed above
Disclaimer: The LaTeX code for most of the tables used in this work was generated using OpenAI's ChatGPT. This tool was not used to generate or modify any content or data, just for reformatting the layout of tables.

An electronic version of this thesis is available at http://repository.tudelft.nl/.

TU Delft

Preface

This thesis work marks the end of my study period of five years at TU Delft. The decision that I took during the last year of high school to study here had a profound impact on where and who I am today. Even though it was a hard decision, it was a decision I do not regret at all, and I am thankful for everything that I have learned, all the projects and programmes I have been part of, and all the people I have met. I am proud to be part of the aerospace community, and really excited for what the future holds.

I would like to give thanks to the people that have made this work possible, without the help of whom I would have never made it this far. My thesis supervisor Angelo Cervone answered every question I have ever asked, and guided me throughout the whole thesis when I had uncertainties. Henk van Zeijl proved to be a very enthusiastic and attentive mentor for the fabrication steps at EKL, sharing from his extensive knowledge and aiding me along the way. Şevket Uludağ provided me with information and advice regarding the Space Engineering cleanroom, while Stefano Speretta verified and proposed changes to my PCB designs. I would like to also thank the staff from EKL, from DASML, and from DEMO, who have provided me with training, advice on using equipment, and manufacturing services.

Special thanks also go to my family: my father who provided me with invaluable input during intense brainstorming sessions and the thirst to pursue a practical thesis, my mother that was always a pillar of support whenever I doubted my abilities, my grandfather that instilled the love of physics in me from a very young age, my grandparents for their support throughout my life, and all other members of my family – present and past. I would also like to thank the friends I have made along the way and from before, wherever you may be: Ploiești, Bucharest, Delft, Eindhoven, London, Zurich, or Bremen. Each of you contributed to who I am today. And of course, I could not forget the other students along whom I have spent hours in the Space Engineering workshop and cleanroom. To each and every one of you I say a warm "Mulțumesc".

Andrei Pârvulescu
Delft, November 2024

Abstract

With the price of launching satellites remaining high, many companies and universities are turning towards smaller satellites as more affordable options. This requires the miniaturisation of their different components, including the propulsion subsystem. At TU Delft, Vaporising Liquid Microthrusters (VLM) are being developed, with the latest iteration being a new generation Micro-Electromechanical System (MEMS) design. In this work, the updated design of this microthruster is remanufactured and prepared for future operational validation, heat transfer and instabilities studies. This is done by simplifying the manufacturing process, creating a testing interface, and performing measurements and extensive experimental characterisation of the thruster and test set-up. The newly-created interface allows for the study of heat transfer efficiency and convection heat transfer coefficient (HTC) from the silicon wall to the propellant, as well as multiple ways to study the instabilities in the system. One interface + thruster assembly was shown to survive to at least 180 °C temperature and 6-7 bar relative pressure. On the manufacturing side, the fabrication process was streamlined by reducing the number of steps by 13%, most significantly by the use of a soft photolithography mask instead of a hard silicon dioxide one. The deviations in horizontal dimensions are in the same order of magnitude as the ones obtained by the previous student working on this project, and lower than other previous attempts at the Faculty of Aerospace Engineering. The etching process encountered some difficulties, leading to inconsistencies in the feature depth between wafers. Across wafers, etching rate deviations as large as 8% were observed. Within the final production wafer, the range of deviation from the design values on throat depth was from +3.5% to −16.5%, showing a measurable higher etching rate at the edges of the wafer than in the centre. Recommendations were given on which features' depths are most important to be measured, in order to increase the confidence in the predicted values. With these results, future researchers are ready to use the produced thrusters and testing interfaces. It is recommended to continue with the experimental studies, especially by measuring the heat transfer efficiency, thrust levels, HTC, and by studying any instabilities that could appear.

Contents

Preface i

Abstract ii

Nomenclature xiv

1 Introduction 1

2 Literature Review 2
2.1 State-of-the-Art VLMs . . . 2
2.1.1 Silva's 2018 TU Delft VLM thruster . . . 3
2.1.2 Fontanarosa et al.'s 2022 VLM Thruster . . . 4
2.1.3 Wang et al.'s 3D Printed VLM Thruster . . . 7
2.1.4 Cen & Xu's VLM Thruster . . . 8
2.1.5 Singh's 2023 TU Delft VLM Thruster Design . . . 8
2.2 Flow Instabilities in Microchannels . . . 9
2.2.1 Types of Instabilities in Microchannels . . . 9
2.2.2 Experimental Microchannel Instability Studies in Literature . . . 14
2.3 Heat Transfer in VLMs . . . 16
2.3.1 Effect of Shape on Heat Transfer . . . 17
2.3.2 Effect of Type of Flow on Heat Transfer . . . 18
2.4 Numerical Modelling . . . 20
2.4.1 Non-Dimensional Numbers . . . 21
2.4.2 Heat Transfer Coefficient (HTC) and Flow Region Predictions . . . 22
2.4.3 Quasi-1D . . . 22
2.4.4 Lattice-Boltzmann Modelling . . . 23
2.4.5 CFD Modelling . . . 24
2.5 Research Gap . . . 25
2.6 Research Objective & Research Questions . . . 26
2.6.1 Updated Research Objective & Research Questions . . . 26

3 Analytical Performance Model 29
3.1 Introduction of the Model . . . 29
3.2 Explanation of the Model . . . 30
3.3 Verification of the Model . . . 33
3.4 Derivation of Estimated Efficiencies . . . 34
3.5 Estimated Values for Operating Conditions . . . 37

4 Manufacturing and Characterisation of the Thrusters 39
4.1 Manufacturing and Measurement Equipment . . . 39
4.1.1 Manufacturing Equipment at EKL . . . 39
4.1.2 Measurement Equipment at EKL & AE and Uncertainty Estimation . . . 40
4.2 Design of the Thruster . . . 42
4.2.1 Thruster Nomenclature . . . 48
4.3 Manufacturing Steps and Modifications . . . 48
4.3.1 Complete Manufacturing Steps . . . 48
4.3.2 Tuning of the Exposure Energy . . . 50
4.3.3 Tuning of the DRIE Number of Loops . . . 50
4.3.4 Changes in Dicing . . . 52
4.4 Issues Encountered During Manufacturing . . . 53
4.4.1 Contamination on Titanium Heater Photoresist . . . 53

4.4.2 Incomplete Titanium Etching . . . 53
4.4.3 Residue in Nozzle Image Exposure . . . 54
4.4.4 Needle-like Contamination . . . 55
4.4.5 Etching Artefacts in Wafers 3 & 6 . . . 55
4.4.6 Handling Issues . . . 57
4.5 Fluidic Side Measurements . . . 57
4.5.1 Wafer 15 Measurements . . . 57
4.5.2 Wafer 3 Depth Measurements . . . 59
4.5.3 Comparison Between Wafers 15, 3, and 6 Etch Depth . . . 62
4.5.4 Wafer 6 Measurements . . . 63
4.5.5 Surface Roughness Properties . . . 66
4.6 Heater Side Measurements . . . 69
4.6.1 Heaters Dimensional Measurements . . . 69
4.6.2 Estimation of the Resistance Values . . . 70
4.6.3 Measurement of the Resistance Values . . . 70
4.6.4 Comparison between Design, Estimated and Measured Resistances . . . 71
4.7 Summary and Conclusions . . . 71

5 Design, Manufacturing & Assembly of the Interfaces **73**
5.1 Interface Requirements . . . 73
5.2 Thruster & Assembly Nomenclature . . . 76
5.3 Overall Design Decisions . . . 77
5.3.1 Glass Wafer Layer . . . 77
5.3.2 Sealing Connections . . . 77
5.3.3 Electrical Connections of the Heaters . . . 78
5.3.4 Material and Manufacturer . . . 78
5.4 Fluidic Interface . . . 79
5.4.1 Thruster Interface . . . 80
5.4.2 P/T Sensor Interface . . . 80
5.4.3 MINSTAC 062 Interface . . . 82
5.4.4 Clearance for Wire Bonding . . . 82
5.4.5 Previous Design Iterations . . . 83
5.5 Electrical Interface . . . 85
5.5.1 Wire Bonding Pads . . . 87
5.5.2 2.54 mm Pitch Header Pins . . . 87
5.5.3 Mounting Holes . . . 87
5.6 Assembly of the System . . . 87
5.6.1 Glueing the Interface, Thruster and PCB . . . 88
5.6.2 Wire Bonding . . . 89
5.6.3 P/T Sensor & Thermocouple Holder . . . 90
5.7 Verification of the Design Requirements . . . 91
5.8 Current Assembly & Fabrication Status . . . 92

6 Preliminary Tests **95**
6.1 Measurement Uncertainties . . . 95
6.2 Exploratory Thermal Camera Tests . . . 97
6.2.1 Temperature Comparison Aluminium Bar . . . 97
6.2.2 Temperature Comparison VLM Thruster . . . 99
6.3 Flow Rate Sensor and Syringe Pump Calibrations . . . 101
6.4 Syringe Pump Oscillations . . . 106
6.5 Maximum Pressure Tests . . . 110
6.5.1 Coarse Estimation of Pressure Loss From Flow-Back . . . 113
6.6 Powering Up and Maximum Temperature Tests . . . 114
6.7 Temperature Coefficient of Resistivity . . . 121

7 Conclusion **125**
7.1 Testing Interface Conclusions . . . 126
7.1.1 Updated Research Question 1.1 . . . 126

7.1.2 Updated Research Question 1.2 . . . 126
7.1.3 Updated Research Question 1.3 . . . 126
7.1.4 Updated Research Question 1.4 . . . 127
7.2 Microthruster Manufacturing Conclusions . . . 127
7.2.1 Updated Research Question 2.1 . . . 127
7.2.2 Updated Research Question 2.2 . . . 127
7.2.3 Updated Research Question 2.3 . . . 128
7.3 Overall Conclusions . . . 129

8 Recommendations 130

References 132

A Chemical Species Properties 139

B New Wafer Layouts 141

C EKL Manufacturing Flowchart 147

D Thruster Dimensional Measurements 161

E Technical Drawings of the Fluidic Interfaces 166

List of Figures

2.1 Diagram of a VLM propulsion system [2]. 2
2.2 Masks with the designs of the different components of the microthruster: heaters, channels, and nozzles [2]. 3
2.3 Schematic of the VLM developed by Fontanarosa et al., including its embedded sensors [12]. 5
2.4 Electro-thermal instability experienced during experimental testing of a VLM. Taken from [12] 6
2.5 CAD model of the 3D printed VLM, together with a detail of the simulated and tested micropin designs [14] 7
2.6 Pressure drop vs mass flow rate for constant heat flux in a channel [19] 11
2.7 Simplified system for the explanation of density wave oscillations. Image taken from [25]. 13
2.8 Diagram showing the parallel channel instability. A darker colour of the liquid corresponds to a larger pressure. Image taken from [27]. 14
2.9 Variation of heat transfer coefficient (left) and amplitude of pressure drop fluctuations (right) with heat flux in a straight microchannel [32] 15
2.10 Parallel microchannels with three different inlet and outlet configurations [33] 16
2.11 The description and dimensions of the microfin geometries inside the vaporisation chamber [35] 18
2.12 Aspects of the heat sink: (a) schematic of the microchannels, (b) and (d) photos of the straight and wavy microchannels, (d) photo of the cross-section of the microchannels [36] 18
2.13 Types of two-phase flows in microchannel. From the top: bubbly, slug and annular [38]. 19
2.14 Schematics of the flow regimes and heat transfer coefficient variation in microchannels for nucleate boiling dominant (top) and convective boiling dominant (bottom) flows [39] 20
2.15 Diagram of the calculation steps for the quasi-1D VLM model. Taken from [43] 23
2.16 Comparison of HTC between CFD results, experimental data and an analytical correlation for the low Ca case using artificial wettability [37] 24
2.17 Comparison of HTC between CFD results and experimental data for the low Ca case using true wettability [37] 25

4.1 The design of the heater used in the current generation of VLM thruster. Image from [18]. 43
4.2 Diagram of the mask layout used for the microthruster fabrication. Image from [15]. The different sections used for the VLM are labelled using letters. 43
4.3 Dimensions of the serpentine microchannels used in the current generation VLM. Image from [15] 44
4.4 The design of the CD nozzles used in the current VLM generation. Image from [15]. The image represents a conical nozzle, but the same nomenclature is used for the bell nozzles. 45
4.5 The design of the aerospike nozzles used in the current VLM generation. Image from [15]. 45
4.6 W01A wafer layout, with configurations rearranged for this thesis. Rearranged from the original design in [15]. 46
4.7 Cell arrangements for a thruster on the fluidic side. Cells marked with (a) represent `channel_element_3200x1280` (making up the entrance), with (b) `Serpentine_Rob_Poyck_design` (making up the vaporisation chamber), and with (c) `ShortNozzle_X` (which corresponds to a nozzle, and can have varying number of and different types of cells). 47
4.8 Cell arrangements for a thruster on the heater side. Heater cells (shown in red, with name `top_heater_George_Spernovasilis`) are 6 mm wide and 1 mm high, compared to the 7×1.28 mm cells of the fluidic side of the thruster (which are also shown as comparison, with the same colouring scheme as explained in Figure 4.7). 47

4.9 The main steps of the VLM fabrication process, shown as evolutions of the cross-sectional profile of the wafers. These steps are explained in more detail in the text. In this diagram, the front (heater) side is on top, while the back (fluidic) side is on the bottom. 48
4.10 DRIE steps. Image adapted from [73], which was generated using Synopsys. 51
4.11 Microchannel depth on wafer 15 as measured on the thrusters from row 2. 51
4.12 Comparison between intact heater photoresist, and photoresist with residue from coating. 53
4.13 Ti layer incompletely etched on wafer 7. 54
4.14 Mark seen on the converging side of ShortNozzle_1 in the photoresist layer. 54
4.15 Etching leftover from mask debris of ShortNozzle_1. 54
4.16 Needle debris present on wafer 3. Images captured with optical option of Keyence VK-X250. 55
4.17 Top down views of laser scans (including lighting) of thruster R2C09 from wafers 15, 3 and 6. The height features were scaled to 9× for better visualisation of the bottom surface. The scan was made using Keyence VK-X1000 for W15 and VK-X250 for W3 and W6. . . 55
4.18 Nozzle overviews of thruster R2C09 from wafers 15 (without glass) and wafer 3 (with glass and diced). Optical images taken with Keyence VK-X1000 at 2.5× magnification. . 56
4.19 Horizontal height profiles of the nozzles of thruster R2C09 from the wafers W15, W3 and W6. One profile is taken exactly at throat level, while the other is taken 120 µm above the throat profile. 56
4.19 Horizontal height profiles of the nozzles of thruster R2C09 from the wafers W15, W3 and W6. One profile is taken exactly at throat level, while the other is taken 120 µm above the throat profile (cont.). 57
4.20 SEM images of the profiles of the entrance to the serpentine microchannels and of the nozzle throat of thruster W15R2C06. The tapering effect of increasing width with depths is visible in both profiles. The samples are viewed at a 45° tilt. 58
4.21 CAD model of the inclined holder for measuring the profile of the thruster. 58
4.22 The inclined holder being used with the VK-X1000 microscope. 58
4.23 Optical focus variation image of the W15R2C06 microchannels entrance, using HDR mode. The thruster is tilted 45 degrees. 59
4.24 Laser confocal image of the W15R2C06 nozzle throat. The thruster is tilted 45 degrees. . 59
4.25 Polynomial fits of the microchannel depths on wafer 3. 61
4.26 Polynomial fits of the depths of different nozzle throat types and width on wafer 3, alongside the best-fit from the microchannels. The dots represent measured values, while the lines are the least-squares fits. CD means convergent-divergent nozzles, while AS mean aerospike nozzles. The 25, 50, and 75 numbers represent the design throat width in µm. 61
4.27 Polynomial fits of the microchannel depths on wafer 6 from measured and estimated values. 64
4.28 Polynomial fits of the depths of different nozzle throat types on wafer 6, alongside the best-fit from the microchannels. The dots represent measured or estimated values, while the lines are the least-squares fits. CD means convergent-divergent nozzles, while AS mean aerospike nozzles. The 25, 50, and 75 numbers represent the design throat width in µm. 64
4.29 Box plots of the relative difference between the measured (or calculated for the average CD throat width) and design values of the in-plane dimensions. See `matplotlib.pyplot.boxplot` [76] for the meaning of the elements making up the box plot. 65
4.30 The masks used on the laser measurements of the nozzle of thruster W15R2C09, for calculating the surface roughness properties. 66
4.31 Variation of skewness (Ssk) with height distribution. Image from [78]. 67
4.32 Variation of kurtosis (Sku) with height distribution profile shape. Image taken from [80]. 67
4.33 Variation of root-mean-square gradient (Sdq) with coarseness of the surface features. Image taken from [78]. 67

5.1 Previous design of the VLM fluidic interface. The top left image shows a CAD version of the assembled system, the bottom left an exploded view of the system, and the right image shows the interface in reality. Image taken from Silva [2]. 73
5.2 Example CAD model of a VLM thruster chip with nozzle. The glass layer was removed for clarity. 75

5.3 Example CAD model of a VLM thruster chip without nozzle. The glass layer was removed for clarity. 75
5.4 Exploded view of the assembly for a thruster with nozzle. The flow of propellant is from the top left towards bottom right. 76
5.5 Damaged heater connection pads on a previous-generation VLM thruster. Image from [54]. 78
5.6 Final design of the fluidic interfaces. The left column shows the inlet for the thruster with nozzle, the middle column the inlet for the thruster without nozzle, and the right column the outlet for the thruster without nozzle. The top row shows perspective views from the heater side of the thruster, and the bottom row from the microchannel side. The red "x" arrow shows the direction of the fluid flow, except for the outlet, in which case it flows opposite to the red arrow "x". The material is shown as semi-transparent, to see internal structures 79
5.7 The 3D printed final fluidic interfaces. From left to right: with-nozzle inlet, no-nozzle inlet, no-nozzle outlet. The numbers on the background pad represent dimensions in mm. 80
5.8 Detail of the connection between the fluidic interface and the VLM. 80
5.9 O-ring on P/T sensor. 81
5.10 P/T sensor holder for batch 2. 81
5.11 P/T sensor holder for batch 2 assembled on top of the fluidic interface. 81
5.12 MINSTAC 062 tubing connected to a batch 1 fluidic interface, using a 062 MINSTAC 12 micron safety screen. 82
5.13 First iteration of the fluidic interface. 83
5.14 Detail of the thruster interface of the first iteration inlet. The golden area represent the surface on which the silicon layer of the thruster would rest, and the blue area the surface on which the glass layer of the thruster would rest. All dimensions are in mm. 83
5.15 Second iteration of the fluidic interface inlet design. 84
5.16 Outlet design corresponding to the second iteration of the fluidic interface. 84
5.17 CAD assembly of the VLM and 2nd iteration fluidic interface with a single PCB design, used as holder for the whole assembly. The PCB is shown as semi-transparent, even though in reality it is opaque. 85
5.18 CAD assembly of the VLM and 2nd iteration fluidic interface with a twin PCB design. The PCBs would be glued to the fluidic interface, and a piece of glass would be used to seal the fluidic interface. The PCBs are shown as semi-transparent, even though in reality they are opaque. 85
5.19 Layout of the PCB for the thruster configuration with nozzle. The placement of the thruster is indicated by the thin yellow lines. The fluidic interface would be placed at the bottom cut-out. The external dimension of the board is 46×29 mm. 86
5.20 Layout of the PCB for the thruster configuration without nozzle. The placement of the thruster is indicated by the thin yellow lines. The fluidic interfaces (inlet and outlet) would be placed at the bottom and top. The external dimension of the board is 46×37.5 mm. 86
5.21 CAD assembly of the VLM thruster with nozzle configuration. Flow direction is from the bottom-left towards top-right 88
5.22 CAD assembly of the VLM thruster without nozzle configuration. Flow direction is from the bottom-left towards top-right. 88
5.23 The inlet version for thrusters with nozzles. The adhesive application area is shown with blue. 89
5.24 The PCB version for thrusters with nozzles, viewed from the fluidic side. The adhesive application area is shown with blue. Note that the header pins are shown on the wrong side in this view. 89
5.25 Thruster assemblies after glueing. 89
5.26 Diagram of the wire bonding connections from the thruster heaters to the PCB bonding pads. The nomenclature is L/R for left/right, I/O for inner/outer, and the heaters are numbered 1 through 8 from the inlet side to the outlet or nozzle side. 90
5.27 W6R3C06 thruster assembly in the wire bonder. 90
5.28 W6R3C06 thruster assembly after wire bonding. 90
5.29 Fully assembled thruster W6R3C02, including the thermocouple, P/T sensor, and MINSTAC tubing. The power supply cables are not connected to the header pins. 91

6.1 Aluminium bar temperature test comparison between thermocouple and thermal camera. The thermocouple is between the blue vacuum tape and the aluminium bar. 97
6.2 Data collection locations from the thermal camera measurement during the aluminium bar temperature comparison test. 98
6.3 Aluminium bar temperature comparison test results after heating up with heat gun. The uncertainties mentioned in Section 6.1 apply. 98
6.4 VLM thruster assembly temperature test comparison between thermocouple and thermal camera. The thermocouple is between the blue vacuum tape and the heater side of the thruster. 99
6.5 Data collection locations from the thermal camera measurement during the VLM thruster assembly temperature comparison test. 100
6.6 VLM assembly temperature comparison test results after heating up with heat gun. The uncertainties mentioned in Section 6.1 apply. 100
6.7 Test setup of the flow meter and pump calibration. 102
6.8 Detailed view of the exit tube in the beaker. The tube does not touch the sides or the bottom of the beaker, and its exit is fully submerged underwater. 102
6.9 Relative error of SLI-1000 measurements compared to uncorrected and corrected flow rate, as measured using the analytical balance. 104
6.10 Measured SLI-1000 flow rates $\dot{V}_{SLI}$ plotted against evaporation-corrected weigh scale-calculated flow rates $\dot{V}_{corr}$. 105
6.11 Evaporation-corrected weigh scale-calculated flow rates $\dot{V}_{corr}$ plotted against syringe pump-set flow rate values $\dot{V}_{set}$. 105
6.12 Flow rate sensor reading through time for 22 mL calibration test number 7. 106
6.13 Fast Fourier Transform (FFT) plot for the quasi-steady-state component of the flow rate for 22 mL syringe calibration tests at 150 µL/min. The average of the signal was subtracted from the data before performing the FFT. The relative amplitude is calculated as the ratio between the true amplitude of the oscillations and the average of the quasi-steady-state flow rate value. Please note that the x-axis is logarithmic, ... 107
6.14 Comparison between the measured and predicted main oscillation frequencies at different flow rates. The graph on the bottom shows the ratio between the measured frequency f and the predicted f_p at the same average flow rate. Note that the frequency f in the top graph, as well as the average flow rate in both graphs, are plotted logarithmically. 109
6.15 Blocked nozzle of the W6R3C07 thruster. 110
6.16 Pattex Power Epoxy bought from Praxis in Delft. 111
6.17 Maximum pressure test setup. 111
6.18 Maximum pressure test results. 112
6.19 Water leak observed during the maximum pressure test. This appeared at the interface between the syringe needle and the MINSTAC tubing. 112
6.20 Electrical diagram of a possible powering of the VLM heaters in parallel. LO, LI, RI, and RO represent the connections on the PCB, as explained in Subsection 5.6.2. The R_S are the resistances that would be in series with each heater. AI represent the analogue inputs on the PCI-9226. V_{PSU} is the positive voltage connection of the power supply, while the icon on the bottom-right represents its ground connection. 115
6.21 Heater connector cable. 116
6.22 Initial test setup for the maximum temperature tests. The parts not relevant to this test were blurred, to focus the attention to the relevant components. 116
6.23 Initial thermocouple placement on the thruster assembly. the thermocouple is taped down using vacuum tape. 117
6.24 Detail of the results of maximum temperature test 4. The PSU voltage and current values were corrected by their 0-value readings of 0.8 V and −14.9 mA. The resistance was calculated as the ratio between PSU voltage and current. The value of the resistance was set to zero when the current reached close-to-zero values, to prevent unrealistically extreme measurements. 117
6.25 New designed MS5837-30BA and thermocouple holder. The first part would be screwed into the inlet fluidic interface of the thruster assembly, and the second part would be screwed on the first part. 118

6.26 Thermocouple holder assembled on top of the W6R3C02 thruster assembly. 118
6.27 W6R3C02 thruster showing cracks on the heater side after temperature test. The cracks are encircled in red. 119
6.28 Thermocouple holder assembled on top of the W6R3C01 thruster assembly. The thermocouple was placed at an angle, and fewer screws were used. 119
6.29 Results of maximum temperature test 11. The PSU voltage and current values were corrected by their 0-value readings of 0.8 V and −14.9 mA. The resistance was calculated as the ratio between PSU voltage and current. The value of the resistance was set to zero when the current reached close-to-zero values, to prevent unrealistically extreme measurements. The PSU voltage and current values were also filtered using a low-pass filter. 120
6.30 Diagram of the resistance sources for powering the VLM. The resistances with index H are those of the heaters on the chip themselves. Those with I are the combination of header pins, PCB, and bonding wires. The ones with C correspond to the new heater connector cables, with R for red and B for black. R_{BR} and R_{BB} are for the banana cable connections to the PSU on the positive and negative side, respectively. 121
6.31 Resistance measured during the maximum temperature test 11, plotted versus measured temperature from the thermocouple. The fits of the three mentioned models are included. 123
6.32 Prediction of the heaters' temperature from the measured resistance, alongside the measured temperature. 124

B.1 W01A wafer layout, with configurations rearranged for this thesis. Rearranged from the original design in [15]. 142
B.2 W02A wafer layout, with configurations rearranged for this thesis. Rearranged from the original design in [15]. 143
B.3 W03A wafer layout, with configurations rearranged for this thesis. Rearranged from the original design in [15]. 144
B.4 W04A wafer layout, with configurations rearranged for this thesis. Rearranged from the original design in [15]. 145
B.5 W05A wafer layout, with configurations rearranged for this thesis. Rearranged from the original design in [15]. 146

List of Tables

2.1 Types of instabilities in (micro)channels . . . 10

3.1 Inputs for the nitrogen verification datasets . . . 33
3.2 Outputs for the nitrogen verification datasets . . . 33
3.3 Inputs for the water verification datasets . . . 34
3.4 Outputs for the water verification datasets . . . 34
3.5 Measured VLM performance by Silva [2] and ideal conditions calculated with the analytical model. . . . 35
3.6 Measured VLM performance by Melaika [54] and ideal conditions calculated with the analytical model. Datasets with the note NCD were not used for calculating C_d; idem for the note NPE for calculating η_h . . . 36
3.7 Measured VLM heater performance by Spernovasilis [54] and ideal conditions calculated with the analytical model. . . . 37
3.8 Ideal values of the expected performance of the VLM thrusters of this thesis. For the thrust values, the reported values are the maximum and minimum for a certain throat width, varying through the corresponding expansion ratios. . . . 38
3.9 Estimated real values of the expected performance of the VLM thrusters of this thesis. For the thrust force, no nozzle corrections were applied. These values thus can be treated as maximums. Also for the thrust values, the reported values are the maximum and minimum for a certain throat width, varying through the corresponding expansion ratios. 38

4.1 Tools used for performing physical and dimensional measurements on the VLM thrusters. 40
4.2 Measurement uncertainty for the optical measurements of the Keyence microscopes, for different magnifications. . . . 41
4.3 Measurement uncertainty for the measurements of the SEM, for different magnifications. 41
4.4 Dimensions of the conical nozzles on the fabrication mask. AR is area ratio. The notation corresponds to the one in Figure 4.4. Image no. is the numbering as presented in Figure 4.2. For all nozzles W_{in} = 3 mm. *For the throat, the ideal value is specified, while the value between parentheses is the actual value on the mask. . . . 45
4.5 Dimensions of the bell nozzles on the fabrication mask. AR is area ratio. The notation corresponds to the one in Figure 4.4. r_{exit} is the radius at the exit of the nozzle, aimed to mimic a true bell nozzle shape. Image no. is the numbering as presented in Figure 4.2. For all nozzles W_{in} = 3 mm. *For the throat, the ideal value is specified, while the value between parentheses is the actual value on the mask. . . . 45
4.6 Dimensions of the aerospike nozzles on the fabrication mask. AR is area ratio. The notation corresponds to the one in Figure 4.5. Image no. is the numbering as presented in Figure 4.2. . . . 46
4.7 Measurements and results of the profile measurements from three thrusters of wafer 15. 59
4.8 Inlet height measurements using Dektak 8 for W3 (62 + 10 DRIE cycles) . . . 60
4.9 Comparison of depth measurements between Dektak and Keyence at different locations on W3. . . . 60
4.10 Comparison between W3 and W6 microchannel depths. . . . 62
4.11 Comparison between W3 and W6 nozzle throat depths. . . . 63
4.12 Surface roughness properties measured for the same thruster from three different wafers. 68
4.13 Design and measured dimensions for different features of the VLM heaters. All dimensions are in µm. . . . 69
4.14 Thickness of Ti and Al layers as measured on wafer W3. . . . 70

4.15 4-wire resistance measurements of the heaters of the assembled thrusters. All values are in Ω. There are missing values for W6R3C07 because wire bonding was unsuccessful for some pads, leaving some heaters partially or completely unconnected. For all measurements, the uncertainty is ±0.05 Ω. 70
4.16 Comparison between the design, estimated, and measured resistance values for heater 1 of thrusters W6R2C06 and W6R2C11. All values are in Ω. 71

5.1 Requirements for the test interface of the new generation VLM. 74
5.2 Wire bonding parameters used on the Accelonix TPT HB10 wire bonder 90
5.3 Assembled thrusters (with or without soldered header pins) that can be found in the SpE cleanroom workshop. Some additional details are included in the table. 93

6.1 Measurement uncertainties of values used in the preliminary tests. 97
6.2 Flow rate calibration measurements, part 1. Where N/A is mentioned, the author forgot to turn on the data acquisition and storage of the SLI software. 103
6.3 Flow rate calibration measurements, part 2. 103
6.4 Main oscillation frequencies observed in the flow rate calibration tests. *The value of f_1 at 50 µm/min is at the limit of what the FFT can calculate, and might thus be inaccurate. 107
6.5 Main oscillation frequency factors k_f observed in the flow rate calibration tests. *The value of the f_1 factor at 50 µm/min is at the limit of what the FFT can calculate, and might thus be inaccurate. 108
6.6 Resistance values (in Ω) of cables and internal connections. The thruster-dependant measurements were done on thruster W6R3C01's assembly. 122
6.7 Descriptions and derived quantities of the three resistance models and their fits. 123

A.1 NASA Polynomial coefficients and temperature validity ranges for gaseous water [52] . 139
A.2 NIST coefficients and temperature validity ranges for liquid water [51] 139
A.3 NIST coefficients and temperature validity ranges for gaseous nitrogen [51] 140
A.4 Other properties of the species used as propellant in the analytical model (water and nitrogen). (g) represents gaseous state for water, while (l) is liquid state. Source for molar mass and enthalpy of formation: [51] and for viscosity properties: [58] 140

D.1 Microchannel depth measurements on wafer 3 using VK-X250. Values are in µm. N/A means that the thruster location is outside the wafer, while dashes signify that no measurements were done for that thruster. 162
D.2 Nozzle throat depth measurements on wafer 3 using VK-X250. Values are in µm. N/A means that the thruster location is outside the wafer, while NN signifies a thruster with no nozzle. 162
D.3 Microchannel depths on wafer 6. Values are in µm. N/A means that the thruster location is outside the wafer, while dashes signify that no measurements were done for that thruster. BD means that the thruster was broken during dicing. For thrusters R2C07 to R2C12, the values are measured, whereas for the rest they are estimated based on the W6/W3 ratio. 162
D.4 Nozzle throat depth measurements on wafer 6. Values are in µm. N/A means that the thruster location is outside the wafer, while NN signifies a thruster with no nozzle. Dashes signify no estimations for that thruster, while BD means that the thruster was broken during dicing. For thrusters R2C07 to R2C12, the values are measured, whereas for the rest they are estimated based on the W6/W3 ratio. 163
D.5 Microchannel widths measured on wafer 6, using VK-X1000. Values are in µm. N/A means that the thruster location is outside the wafer, while dashes signify that no measurements were done for that thruster. BD means that the thruster was broken during dicing. For all measurements, the uncertainty is ±1.8 µm. 163
D.6 Surface throat widths measured on wafer 6, using VK-X1000. Values are in µm. N/A means that the thruster location is outside the wafer. BD means that the thruster was broken during dicing, while NN signifies that the thruster does not have a nozzle. For all measurements, the uncertainty is ±1.8 µm. 163

D.7 Nozzle convergent (full) angles measured on wafer 6, using VK-X1000. Values are in degrees. N/A means that the thruster location is outside the wafer, while AS signifies that the nozzle is of the aerospike type. BD means that the thruster was broken during dicing, while NN signifies that the thruster does not have a nozzle. 164
D.8 Nozzle divergent (full) angles measured on wafer 6, using VK-X1000. Values are in degrees. N/A means that the thruster location is outside the wafer, while AS signifies that the nozzle is of the aerospike type. BD means that the thruster was broken during dicing, while NN signifies that the thruster does not have a nozzle. 164
D.9 Nozzle exit widths measured on wafer 6, using VK-X1000. Values are in µm. N/A means that the thruster location is outside the wafer, while AS signifies that the nozzle is of the aerospike type. BD means that the thruster was broken during dicing, while NN signifies that the thruster does not have a nozzle. 164
D.10 Average throat widths calculated for the CD nozzles on wafer 6. Values are in µm. N/A means that the thruster location is outside the wafer, while AS signifies that the nozzle is of the aerospike type. BD means that the thruster was broken during dicing, while NN signifies that the thruster does not have a nozzle. 165

Nomenclature

Abbreviations

AE	(Faculty of) Aerospace Engineering
AI	Analog Input
AR	Aspect Ratio
AS	Aerospike
ASML	Advanced Semiconductor Materials Lithography
ASTM	American Society for Testing and Materials
CAD	Computer-Aided Design
CD	Convergent-Divergent
CFD	Computational Fluid Dynamics
CHF	Critical Heat Flux
CNC	Computer Numerical Control
CTF	Continuous Two-phase Flow
DAQ	Data Acquisition
DEMO	Dienst Elektronische en Mechanische Ontwikkeling (Electronic and Mechanical Support Division)
DLP	Digital Light Processing
DRIE	Deep Reactive Ion Etching
DSMC	Direct Simulation Monte Carlo
EKL	Else Kooi Laboratory
ENIG	Electroless Nickel Immersion Gold
FDM	Fused Deposition Modelling
FR-4	Flame Retardant 4
HDR	High Dynamic Range
HTC	Heat Transfer Coefficient
HTCC	High-Temperature Co-fired Ceramic
IRT	Ideal Rocket Theory
LBM	Lattice-Boltzmann Method
LO, LI, RI, RO	Combination of Left (L), Right (R), Outer (O) and Inner (I)
LPM	Low Pressure Microthruster
LTAF	Liquid / Two-phase Alternating Flow
LTCC	Low-Temperature Co-fired Ceramic
LTVAF	Liquid / Two-phase / Vapour Alternating Flow
MEMS	Micro-Electromechanical System
MINSTAC	Miniature Inert System of Tubing And Components
NASA	National Aeronautics and Space Administration
NBR	Nitrile Butadiene Rubber
NIST	National Institute of Standards and Technology
OFI	Onset of Flow Instabilities
ONB	Onset of Nucleate Boiling
P/T	Pressure & Temperature
PC	Polycarbonate
PCB	Printed Circuit Board
PECVD	Plasma-Enhanced Chemical Vapour Deposition
PI-D	Proportional Integral-Differential
PLA	Polylactic Acid
PR	Photoresist
PSU	Power Supply Unit
PWM	Pulse Width Modulation
RTD	Resistance Temperature Detector
SEM	Scanning Electron Microscope

SLA Stereolithography

SpE Space Engineering

TCR Temperature Coefficient of Resistivity

TEOS Tetraethyl Orthosilicate

TNM Transient Numerical Method

TU Delft or TUD Delft University of Technology

UNF Unified National Fine thread

VFS Volume Fraction Sensors

VLM Vaporising Liquid Microthruster

Chemical Symbols

Al Aluminium

C_4F_8 Octafluorocyclobutane

SF_8 Sulphur Hexafluoride

SiO_2 Silicon Dioxide

Si Silicon

Ti Titanium

Greek Symbols

α Temperature coefficient of resistivity [K^{-1}]

χ_{th} Thermodynamic vapour quality [-]

η_F Thrust quality factor [-]

η_s Specific impulse quality factor [-]

η_h Heating efficienty [-]

Γ Vandenkerckhove function [-]

γ Ratio of specific heats for the gaseous propellant [-]

γ_a Ratio of specific heats of air [-]

λ_{lv} Latent heat of vaporisation of water [J/kg]

μ Dynamic viscosity of fluid [$Pa \cdot s$]

μ_0 Reference dynamic viscosity at reference temperature $T_{0,\mu}$ [$Pa \cdot s$]

μ_c Dynamic viscosity of fluid at the end of the heating chamber [$Pa \cdot s$]

Ω Collision term for LBM equation

ρ_l Density of liquid water [kg/m^3]

ρ_t Density of the propellant gas at the throat [kg/m^3]

ρ_v Density of water vapour [kg/m^3]

ρ_{Ti} Resistivity of pure titanium at room temperature [$\Omega \cdot m$]

σ Standard deviation. Unit is depentent on the value being studied

σ_d Uncertainty in microscope dimensional measurements [m]

σ_{st} Surface tension coefficient [N/m]

θ_1, θ_2, θ_3 Geometrical angles for the aerospike nozzles [rad]. See Figure 4.5

θ_{in} Convergent half-angle of a convergent-divergent nozzle [rad]

θ_{out} Divergent half-angle of a convergent-divergent nozzle [rad]

ε Expansion ratio of the nozzle [-]

ξ_β Particle velocity component in β dimension [m/s]

Latin Symbols

A Empirical constant for $\dot{V}$ formula [-]

a Constant used during pressure loss rate estimation calculations, during the maximum pressure test [$Pa \cdot m^{3 \cdot 1.4}$]

A_e Cross-sectional area of the nozzle exit [m^2]

A_t Cross-sectional area of the throat [m^2]

a_T, a_p, b Fitting parameters for average vapour volume equation [m^3/K, m^3/Pa, m^3]

A_w Wetted microchannel silicon area in the VLM [m^2]

Bo Boiling number [-]

Ca Capillary number [-]

C_b Confidence level of test to bogey results [-]

C_d Coefficient of discharge [-]

$C_{d,KH}$ Coefficient of discharge based on Kuluva and Hosack model [-]

Co Confinement number [-]

$\overline{C}_p$ Molar specific heat of the gas at constant pressure [J/(mol · K)]

c_p Specific heat capacity of the fluid. In the case of a gas, in constant-pressure conditions [J/(kg · K)]

c_v Specific heat capcity of the gas at constant volume conditions [J/(kg · K)]

D Syringe inner diameter [m]

d_{cal} Distance measured using callipers [m]

D_h Hydraulic diameter of the microchannel [m]

d_h Thickness of the heater (or thickness of the titanium layer) [m]

$D_{h,t}$ Hydraulic diameter of the throat [m]

d_m Microchannel depth [m]

$d(r)$ Etching depth as a function of radial position on wafer [m]

d_{res} Length of a pixel in a certain image [m/px]. Inverse of pixel density

d_t Depth of the throat [m]

Eo Eötvös number, also called Bond number [-]

f Frequency of oscillations [Hz]

f_1, f_2, f_3 Observed base frequencies of pump-induced oscillations [Hz]

F_β External body force component in β dimension [N]

f_p Predicted pump-induced frequency [Hz]

f_{par} Probability density function of finding a particle in a certain location and with a certain momentum, in the LBM

F_T Thrust force [N]

G Mass flux through the thruster [kg/(m^2·s)]

g Gravitational acceleration [m/s^2]

$\overline{H}$ Molar enthalpy [J/mol]

h (Local) specifc enthalpy of the fluid [J/kg]

h Converctive heat transfer coefficient [W/(m^2·K)]

$\overline{H}_f^0$ or $\overline{H}_{298.15\,\mathrm{K}}$ Molar enthalpy of formation at standard conditions [J/mol]

$h_{sat,l}$ Specifc enthalpy of saturated liquid [J/kg]

$h_{sat,v}$ Specifc enthalpy of saturated vapour [J/kg]

I_{PSU} Current reading from the power supply unit [A]

I_{sp} Specific impulse [s]

K_1 Non-dimensional number to characterise the movement of the gas-liquid boundary [-]

k_d Frequency factor used for correlating frequency, syringe diamter and average volume flow rate [m^{-1}]

k_l Thermal conductivity of the liquid [W/(m · K)]

$L_1, L_2, L_{2'}, W_{out}$ Geometrical dimensions for the aerospike nozzles [m]. See Figure 4.5

l_i Length of heater section i [m]

l_t Distance between upper and lower extremities of the heater serpentine loops [m]

$\dot{m}$ Mass flow rate through the thruster (assumed uniform over its whole length) [kg/s]

$\dot{m}_1$ Inlet mass flow rate [kg/s]

$\dot{m}_2$ Vaporisation rate [kg/s]

$\dot{m}_{bal}$ Mass flow rate as measured with the Mettler Toledo analytical balance [kg/s]

$m_{\mathrm{H_2O}}$ Mass of water during calibration [kg]

M_W Molar mass of the propellant [kg/mol]

n_{samp} The required number of samples according to the test to bogey method [-]

Nu Nusselt number [-]

Δp or ΔP Pressure drop / loss [Pa]

p Pressure [Pa]

p_a Ambient pressure [Pa]

$\overline{p}$ Average pressure during the 2-second interval invertigated for the pressure loss rate during the maximum pressure test [Pa]

p_c Pressure in the chamber of the thruster (just before the nozzle) [Pa]

p_e Theoretical nozzle exhaust pressure [Pa]

P_{heater} Electrical power applied to the heater [W]

p_i Initial pressure of air trapped in the thruster system during the maximum pressure test [Pa]

p_{in} Inlet pressure [Pa]

$P_{loss,dry}$ Heat losses during dry operation [W]

P_{req} Required heater power [W]

Pr Prandtl number [-]

P_t Perimeter of the throat cross-sectional surface [m]

p_t Pressure at the nozzle throat [Pa]

q Heat flux from microchannel to the propellant [W/m^2]

$\dot{Q}_{ideal}$ Heat flow required for heating the propellant, assuming ideal mass flow rate [W]

$\dot{Q}_{real}$ Heat flow required for heating the propellant, assuming real mass flow rate [W]

R Instantaneous heater resistance [Ω]

r Radial distance of a certain feature on the wafer, from the wafer centre [m]

R_0 Heater resistance at reference temperature T_0 [Ω]

R_1, R_2, R_3 Radii of tapers applied on the aerospike nozzles [m]. See Figure 4.5

R_A Universal gas constant = $8.3145\,\mathrm{J/(mol \cdot K)}$

R_b Minimum required reliability for test to bogey [-]

R_{BR}, R_{BB} Resistance of positive and negative banana conection cables to the PSU [Ω]

r_c Radius of the longitudinal curvature of the throat [m]

$R_{Cn,R}$, $R_{Cn,B}$ Resistance of individual parallel wire n in the red and blue new cable connections, respectively [Ω]

Re_t Reynolds number at the nozzle throat [-]

r_{exit} Radius of rounding effect applied at the end of bell nozzles

R_{heater} Total resistance of a single heater [Ω]

R_{Hn} Heater resistance of thruster heater n [Ω]

R_{In} Sum of resistances of header pins, PCB traces, and bonding wires, for thruster heater n [Ω]

R_n Sum of $R_{Cn,R}$, $R_{Cn,B}$, and R_{In} [Ω]

R_{Sn} Resistance of shunt resistor n used to measure current [Ω]

r_t Radius of the cross-sectional curvature of the throat [m]

s Pitch of the syringe pump screw [m]

Sa Arithmetic mean height of the surface [m]

Sdq Root-mean-square gradient of the surface [m]

S_i Surface area of heater section i [m^2]

s_i Width of heater section i [m]

Sku	Kurtosis of the surface [-]
S_μ	Sutherland constant [K]
Sp	Maximum peak of the surface [m]
Sq	Square mean height of the surface [m]
Ssk	Skewness of the surface [-]
s_u	Uncertainty in placement of measurement point [pixels, px]
Sv	Maximum valley of the surface [m]
Sz	Maximum height of the surface [m]
T	Temperature [K]
t	Time [s]
T_0	Reference temperature for resistance-temperature relation [K]
$T_{0,\mu}$	Reference temperature for Sutherland's law [K]
T_1	Vaporisation temperature of water at 1 atm. Equals 373.12 K
T_{amb}	Ambient temperature [K]
T_c	Heating chamber final propellant temperature [K]
T_{cam}	Thermal camera temperature reading [K]
T_f	Fluid propellant temperature [K]
T_H	Heater temperature [K]
T_{in}	Initial / inlet propellant temperature [K]
T_{noz}	Temperature of the thruster around the nozzle [K]
T_{tc}	Thermocouple temperature [K]
T_{vap}	Vaporisation temperature of water at a certain pressure [K]
T_w	Microchannel wall temperature [K]
u_{bubble}	Velocity of a bubble in a microchannel [m/s]
$\dot{V}$	Time derivative of instantaneous vapour volume, or volume flow rate [m^3/s]
$\langle \dot{V} \rangle$	Average value of multiple $\dot{V}$ readings [m^3/s]
V	Volume [m^3]
V_{av}	Average volume of vapour in microchannels [m^3]
$\dot{V}_{bal}$	Volume flow rate as calculated using measured data from Mettler Toledo analytical balance [m^3/s]
$\dot{V}_{corr}$	Volume flow rate derived from $\dot{V}_{bal}$, corrected for evaporation during calibration [m^3/s]
v_e	Nozzle exhaust veolcity [m/s]
V_i	Initial volume of air trapped in the thruster system during the maximum pressure test [m^3]
V_{PSU}	Voltage reading from the power supply unit [A]
$\dot{V}_{set}$	Volume flow rate set in the syringe pump [m^3/s]
$\dot{V}_{SLI}$	Volume flow rate read using the SLI-1000 sensor [m^3/s]
v_t	Axial velocity at the throat [m/s]
w_0 to w_8	Widths of the heater loop segments [m]. See Figure 4.1
W_{in}	Width of the entrance of the nozzle [m]
w_m	Microchannel width [m]
W_t	Throat width in the nomenclature of Singh [m]
w_t	Width of the throat [m]

1 Introduction

As the price of launching satellites into space is still large (in the range of thousands or tens of thousands of USD/kg[1]), academia and companies alike are turning towards smaller, lighter and cheaper alternatives of getting their required technologies to orbit. The market for nanosatellites kept increasing until 2017, after which it had a slow decrease until 2020 [1]. However, since then, it has steadily grown and overtook the 2017 peak in the 2021 – 2022 period, with expectations to keep increasing further.

With the unique size and mass constraints that these small satellites have, novel micropropulsion technologies are being developed and tested. One of these technologies, that has received interest in recent years, is Micro-Electromechanical Systems (MEMS) -based resistojet using liquid propellant, also known as Vaporising Liquid Microthruster (VLM). These thrusters work by heating up a liquid to its boiling point, transforming it into gas, and then being expanded and exhausted through a convergent-divergent nozzle. At TU Delft, a new generation MEMS VLM was designed and partially manufactured, requiring further testing. Numerical studies were also done on the heat transfer properties of microchannels, but the validation data is very limited.

In this context, the research objective of this thesis is to remanufacture and prepare the new generation TU Delft MEMS VLM thruster for future operational validation, heat transfer and instability studies. This will be done by simplifying the manufacturing process, creating a testing interface, and performing measurements and extensive experimental characterisation of the thruster and test set-up.

The structure of this thesis report is as follows. In Chapter 2, a review of existing literature is presented, at the end of which the research gap is identified, and the research objective defined. In Chapter 3, a simple analytical model of the performance of the microthruster is included, that will aid in test set-up decisions and future thruster efficiency calculations. Chapter 4 presents the manufacturing process for refabricating the MEMS VLM, as well as an extensive measurement characterisation of the resulting thrusters. In Chapter 5, the design of the testing interfaces is shown, including the decision process and the resulting assembly steps. Chapter 6 details the preliminary tests that were done to validate the design of the interfaces, as well as prepare the test set-up for future experimental studies. Lastly, Chapter 7 includes the conclusions of this report, while Chapter 8 proposes some recommendations for improvement and future work. Appendix C presents the MEMS manufacturing steps employed at the Else Kooi Laboratory (EKL) at TU Delft for the fabrication of the microthrusters.

[1] https://aerospace.csis.org/data/space-launch-to-low-earth-orbit-how-much-does-it-cost/

2

Literature Review

In this chapter, a review of the existing literature is made. This focuses on determining the state of the art and the current limitations regarding heat transfer and flow instabilities in serpentine microchannels for VLMs. This is done by assessing the work done so far at TU Delft and externally in the field, using both experimental and numerical methods. Additionally, the types and characteristics of flow instabilities in microchannels, as well as the heat transfer phenomena in VLMs, are investigated.

First, the state-of-the-art in VLMs is given in Section 2.1. Then, studies into flow instabilities and heat transfer in VLMs and microchannels are presented in Section 2.2 and Section 2.3, respectively. Section 2.4 considers the numerical modelling techniques attempted in the past. Afterwards, the knowledge gap is emphasised in Section 2.5, and a research objective and research questions are defined for the rest of the thesis in Section 2.6.

2.1. State-of-the-Art VLMs

This section begins with a definition of a vaporising liquid microthruster (VLM) and a short history of the development of VLMs. Afterwards, some of the state-of-the-art research into these thrusters is presented.

A VLM is a thruster that operates using a liquid (usually water) as propellant, which is vaporised via heating and then exhausted via a nozzle. The device is usually produced using micro-electromechanical systems (MEMS) manufacturing methods due to its small size and requirement of fine features. A diagram of such a thruster can be seen in Figure 2.1.

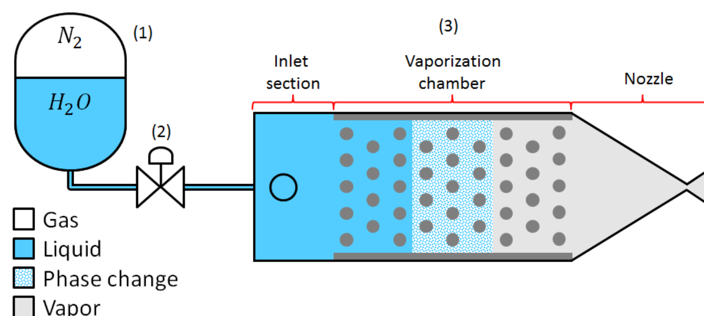

Figure 2.1: Diagram of a VLM propulsion system [2].

Besides the tank and the valve, the VLM itself is made from an inlet (also called entrance), a vaporisation chamber (also called heating, boiling, or acceleration chamber), and a nozzle. The inlet directs the incoming liquid flow to the specific geometry of the vaporisation chamber. In the vaporisation chamber,

the phase of the propellant changes gradually from liquid to gas, passing through a two-phase regime. This is done using one heater (or multiple) placed in the vicinity of the chamber. The now gaseous flow is then redirected through a usually convergent-divergent nozzle, in order to produce thrust at higher levels of specific impulse (I_{sp}).

A comprehensive review of the history of VLM development is presented in [3]. This includes VLMs manufactured with MEMS technology, starting from the 1990s [4] up to present day. These developments included different designs of the heating chamber, from an open chamber [5], to single-channel [6] and parallel channel [7] configurations. However, VLMs were also manufactured using different technologies, such as low-temperature co-fired ceramic (LTCC) [8] and high-temperature co-fired ceramic (HTCC) [9]. While most designs used a resistive heater, some novel developments used inductive heating [10], or operation in the Leidenfrost boiling regime [11].

In the next subsections, the state-of-the-art designs from literature, that are most relevant to this thesis, are briefly described.

2.1.1. Silva's 2018 TU Delft VLM thruster

AT TU Delft, a MEMS VLM thruster has already been previously manufactured and tested, as described in the work of Silva [2]. A modular design was chosen, which included two types of heaters, three nozzle types, and four heating chamber configurations. Their designs are shown in Figure 2.2.

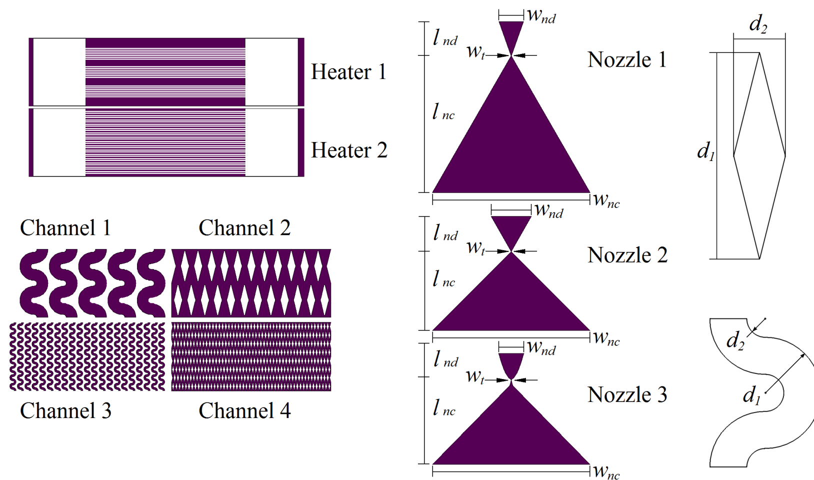

Figure 2.2: Masks with the designs of the different components of the microthruster: heaters, channels, and nozzles [2].

The two heaters consisted of (1) three sets of 7 lines each and (2) fifteen sets of 2 lines each. The nozzles included two linear nozzles (one long and one wide), and a bell nozzle. The heating chamber was either made of serpentine channels (large or small) or from diamond pillars / microfins (large or small).

Mechanical, electrical and operational tests were performed on some of the fabricated thrusters. For the operational tests, inlet pressure, mass flow rate and applied power were measured, alongside heater resistance (which was used to derive an approximate value of temperature). Heat transfer efficiencies of between 20% and 27% were found by Silva during experimental testing. The produced thrust and I_{sp} were calculated from the available data and models, but not directly measured.

The direct heater efficiency is very rarely reported in literature for VLMs, authors usually choosing to include data such as the total power consumption, produced thrust, and specific impulse. In order to calculate the heater efficiency, many conditions of the flow need to be known, such as initial and final temperature from the heating chamber, state of the fluid at the exit, mass flow rate, operational pressure etc. These are usually not completely reported. For this reason, [3] introduced an overall efficiency parameter η_O, with the following formula:

$$\eta_O = g_0 I_{sp} \frac{F_T}{P_{heater}} \tag{2.1}$$

Where $g_0 = 9.806\,65\,\mathrm{m/s^2}$ is the standard gravitational acceleration on Earth, I_{sp} is the specific impulse, F_T is the thrust force, and P_{heater} is the total electrical power supplied to the heater of the VLM. Values for η_O vary significantly in value, from 0.03% to 17.8% [3]. Ignoring the outliers with very low overall efficiencies, the range reduces to between 4.8% and 17.8%.

In order to compare with other thrusters found in literature, this overall efficiency factor is also calculated for the thruster of Silva. However, as no experimental data was collected for the thrust and specific impulse, the values as calculated or simulated by the original author were used. This lead to η_O values between 11.2% and 14.1%. These are in the upper range of the values reported earlier. As measured values only for P_{heater} and the mass flow rate were used, the true nozzle efficiency is not considered in this calculation.

Furthermore, in Silva's work also a numerical model for control was developed, partially based on the experimental data that was obtained prior. Most relevant for this thesis is the model used for determining the vaporisation rate of the propellant.

The expected average vapour volume in the heating chamber was correlated to the nozzle temperature and inlet pressure of the thruster, from experimental data. This led to an equation of the following form:

$$V_{av} = a_T \cdot T_{noz} + a_p \cdot p_{in} + b \tag{2.2}$$

where V_{av} is the average volume of vapour in the microchannels, T_{noz} is the temperature of the thruster around the nozzle, p_{in} is the inlet pressure, and a_T, a_p and b are fitting parameters. This is then used to find an expression of the time derivative of the instantaneous vapour volume $\dot{V}$:

$$\dot{V} = A \cdot (V_{av} - V) \tag{2.3}$$

where A is an empirical constant. Finally, the vaporisation rate $\dot{m}_2$ is calculated as:

$$\dot{m}_2 = \dot{m}_1 - \dot{V} \cdot \rho_l \tag{2.4}$$

where $\dot{m}_1$ is the inlet mass flow rate and ρ_l is the density of the liquid water.

In order to derive the temperature T_{noz}, another experimental correlation was made between the applied power to the heaters, and the measured temperature using the variable resistance of the heaters, as given by the following equation:

$$R = R_0 \left[1 + \alpha \left(T - T_0\right)\right] \tag{2.5}$$

where R is the instantaneous resistance, T is the instantaneous temperature, the index 0 signifies reference values, and α is the temperature coefficient of resistivity, found experimentally.

For reference with future works, the measured operational conditions of the thruster are:

- Inlet pressure: $p_{in} \approx 5\,\mathrm{bar}$
- Mass flow rate: $\dot{m} = 0.55 - 0.83\,\mathrm{mg/s}$
- Required power: $P_{req} = 7.3 - 8.8\,\mathrm{W}$

2.1.2. Fontanarosa et al.'s 2022 VLM Thruster

A VLM that contains embedded capacitive volume fraction sensors (VFS) and 4-wire resistance temperature detectors (RTD) to characterise the flow properties was created by Fontanarosa et al. [12]. In each of the channels, a secondary heater is placed on top, for applying local heat control. The main propellant heater can be found on the bottom of the thruster. In order to perform the tests, a programmable syringe pump is used, as well as a vacuum chamber. The VLM consists of 8 microchannels of 90 µm width and 230 µm depth. A schematic of the VLM is shown in Figure 2.3.

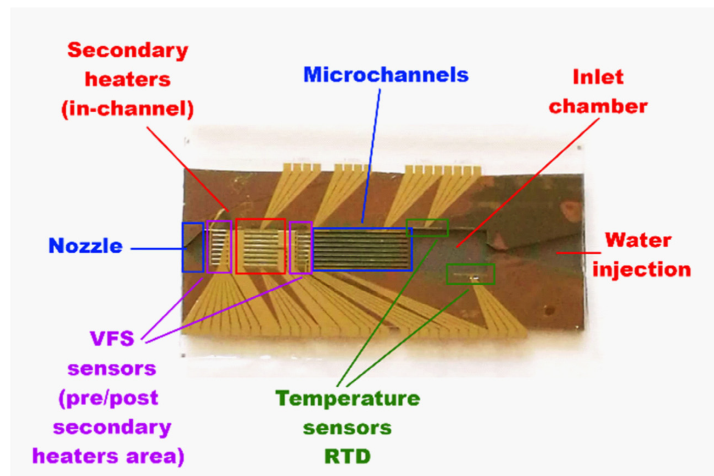

Figure 2.3: Schematic of the VLM developed by Fontanarosa et al., including its embedded sensors [12].

Other values measured during the experiments were the pressure and temperature along the inlet line before the microthruster, as well as the pressure of the vacuum chamber. One embedded RTD and two VFSes were used to characterise the embedded sensors. Furthermore, the exhaust plume was analysed through Schlieren images.

The article mentions that a heater efficiency of 55% was obtained, significantly higher than the values obtained by Silva. The difference is surprising, as both devices are MEMS-based. A partial explanation might be due to the test set-up, as Fontanarosa tested in a vacuum chamber, while Silva tested at atmospheric conditions. No thrust or specific impulse values are reported for calculating η_O.

The most important findings of this experiment are the establishment of the electro-thermal instability, and the study of the behaviour of injected droplets through the inlet needle. These are presented in the next two paragraphs.

The electro-thermal instability manifests as follows: a small rise in the electrical power delivered to the heater leads to an increase of the heat flux transferred to the VLM. This in turn raises the temperature. This is more pronounced when the flow turns fully vaporised, as the heat transfer coefficient between the VLM and the propellant is decreased. The increase in temperature of the VLM then leads to a larger resistance of the heater, which in turn leads to a lower current (at constant voltage) and lower electrical power. The opposite then happens, with lower heat flux, lower temperature and lower heater resistance. This in turn leads to an increase in electrical current (at constant voltage) and power, and so the cycle repeats. This process can also be visualised in Figure 2.4. Individual droplets are formed at the injection in the inlet, especially when the flow is mostly liquid. The droplets tend to coalesce at the entrance to the microchannels, and then get absorbed into the microchannels. In certain conditions, especially when the flow was still two-phase at the nozzle, a backflow would occur from the microchannels back into the inlet chamber. This is called a reverse flow boiling instability.

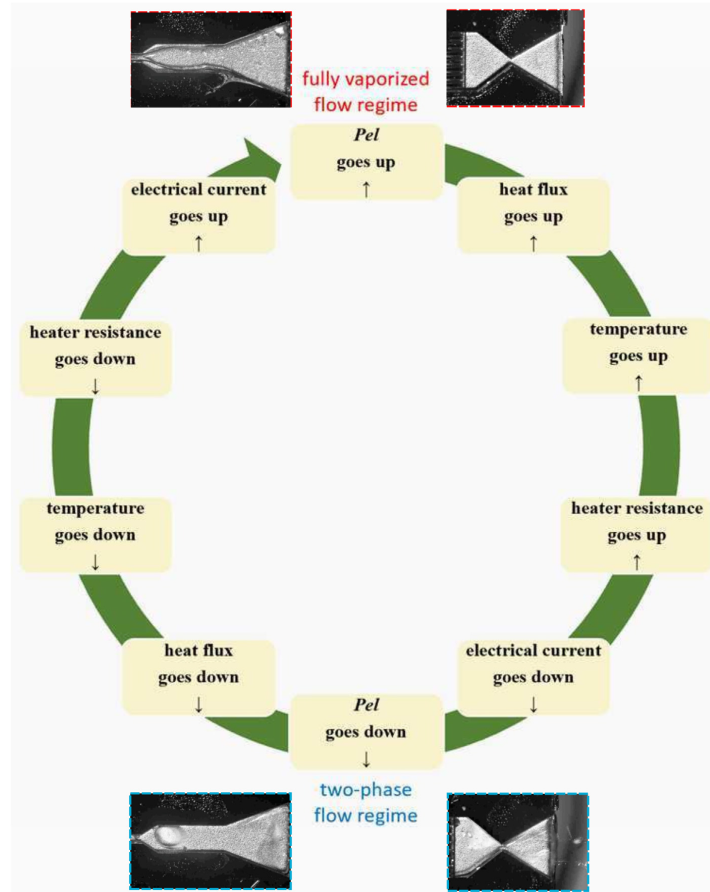

Figure 2.4: Electro-thermal instability experienced during experimental testing of a VLM. Taken from [12]

.

In a subsequent article [13], the active control of the temperature of the VLM was attempted. This was performed by applying a pulse width modulation (PWM) control signal to the main heater. The choice to control the heating of the VLM through its temperature was directly linked to the previously-mentioned electro-thermal instabilities experienced during power-controlled testing.

A problem that was encountered was the inherent non-linear characteristic of the system, as well as the impossibility of accurately modelling the two-phase behaviour of the flow. As such, a data-driven calculation of the parameters for the PI-D (Proportional Integral-Differential) controller was used, based on historical results.

The paper claims that a 90% heating efficiency has been reached, much higher than without using the active control (55.3% [12]). However, a different definition of the heating efficiency was used. Usually, the heating efficiency is defined as:

$$\eta_h = \frac{\dot{Q}_{real}}{P_{heater}} \tag{2.6}$$

where $\dot{Q}_{real}$ is the heat flow required for heating the liquid water to the saturation temperature, evaporating it, and heating the vapour to the set temperature (using the real mass flow rate value). P_{heater} is the electrical power applied to the heater. In contrast, the definition in [13] removes the heat losses that also appear during dry operation ($P_{loss,dry}$), obtaining the following equation:

$$\eta_{h,alt} = \frac{\dot{Q}_{real}}{P_{heater} - P_{loss,dry}} \tag{2.7}$$

As a result, mostly the losses due to heat transfer from the heaters to the fluid are taken into account, and no longer also the ones to the environment. The original author mentions that using this definition, the efficiency "provides a measure of the energy transfer losses due to the thermodynamic irreversibilities occurring during the overall heating process". This is of special interest to the temperature-control model attempted in the article, as the losses to the environment cannot be prevented by it. They do not however mention why they changed the efficiency definition compared to the traditional one.

A direct comparison between this efficiency and the one from their previous work, which uses a different definition, is not fully correct, as different phenomena are included in these definitions. In spite of this, the temperature-control does seem to increase the efficiency of heat transfer compared to a simply power-controlled system. A direct calculation using the same efficiency definition is though required for a proper comparison.

The study mentions that low mass flow rate flow is inherently less stable, due to lower efficiency of heat transfer, and the possibility of flow reversal in the microchannels and of explosive boiling in the inlet chamber.

2.1.3. Wang et al.'s 3D Printed VLM Thruster

A 3D-printed design for VLMs was implemented for the first time by Wang et al. [14]. This increased the design freedom of the heating channels and the heater elements. They used micro pin fins in the vaporising chamber to increase the heat transfer surface. Three different models were investigated: circular, square, and diamond. These were either inline, or staggered, as shown in Figure 2.5.

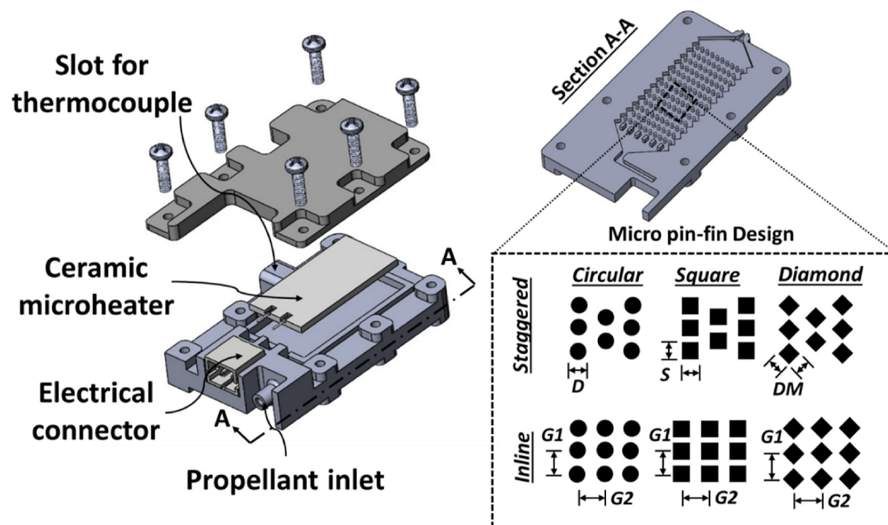

Figure 2.5: CAD model of the 3D printed VLM, together with a detail of the simulated and tested micropin designs [14]

It is to be noted that the design values for the fluidic path are almost an order of magnitude larger than what is usually the case for MEMS VLMs. For example, a 500 µm diameter throat was used for the nozzle, versus a 150 µm × 50 µm as used by Singh [15]. This might affect the regimes that appear in the two-phase flow. Furthermore, in the computational fluid dynamics (CFD) investigations of the vaporising chamber, only single phase simulations were performed.

A clear result of their investigation is that square pins have the largest effect in increasing the heat transfer, as the flow is being disturbed (and slowed down) the most, hence increasing the residence time and the amount of received heat. The same can be said for favouring the inline configuration versus the staggered one. However, it once again needs to be mentioned that these results are for single-phase flow, and as such the inherent two-phase heat transfer phenomena are not considered.

Using the reported thrust, power consumption, and specific impulse values, an overall efficiency of $\eta_O = 2.2\%$ is calculated. This in the middle to lower range of the efficiencies in literature, indicating that significant improvements could be made to the device.

2.1.4. Cen & Xu's VLM Thruster

Experimental studies on the design of a VLM, including mass flow rate, chip temperature and thrust measurements were performed by Cen & Xu [7]. The most interesting are the flow visualisations that are described by the authors, which reveal the instability modes encountered during operations at different mass flow rate regimes.

Explosive boiling takes place at the interface between the inlet and the microchannels, pushing the flow both backward into the inlet, and forward into the channels. The water droplets conglomerate in the channels due to surface tension, clogging the channels until partial vaporisation was achieved. Similar phenomena were observed when a taint was present, indicating that in general, complex geometries lead to the early onset of nucleate boiling (ONB).

In a microchannel, the superheat temperature (temperature of liquid above its saturation temperature) required for ONB is inversely proportional to its hydraulic diameter [16]. As such, narrower microchannels require a higher degree of superheat before boiling starts. On a flat plate (such as is the inlet), Cen & Xu [7] observed that also large superheat is needed. These are both in contrast to what is observed at sharp corners, when there is a taint present, or when an insoluble gas bubble exists in the flow.

The observed oscillations for the thrust and inlet pressure were found to be mostly in phase, with the small size of the thruster given as reason. The authors report that they found a dependency between the frequency of the oscillations and the boiling number Bo:

$$f \propto \frac{T_w - T_f}{\dot{m}} \propto \mathrm{Bo} \tag{2.8}$$

where f is the frequency of the oscillation, T_w is the wall temperature and T_f is the temperature of the fluid. This is in accordance to the findings of Kandlikar [17], which defined a dimensionless number K_1 to characterise the movement of the gas-liquid boundary. This number is defined as the ratio between the evaporation momentum force and the inertia force, including the effect of the boiling number in its definition. It has the following form:

$$K_1 = \left(\frac{q}{G \cdot \lambda_{lv}}\right)^2 \cdot \frac{\rho_l}{\rho_v} = \mathrm{Bo}^2 \cdot \frac{\rho_l}{\rho_v} \tag{2.9}$$

where q is the heat flux from the channel to the propellant, G is the mass flux, λ_{lv} is the latent heat of vaporisation, ρ_l is the density of liquid water, and ρ_v is the density of water vapour.

2.1.5. Singh's 2023 TU Delft VLM Thruster Design

The thruster that is going to be experimentally tested during this thesis is based on the design from Singh [15]. In this work, both the design decisions and some manufacturing results (mechanical and electrical) are presented.

The design improved on the work of Silva [2] by redesigning the nozzle and the inlet designs. The heating chamber utilises the 5 large serpentine microchannel design. Furthermore, it implemented the heater design found in the thesis work of Spernovasilis [18].

Redesigning the nozzle, Singh predicts an 18% increase in simulated thrust compared to previous iterations using the same input conditions. This value was simulated using CFD software, and still has to be validated experimentally. The new inlet design lead to a much more uniform simulated distribution of the flow velocity profile in the inlet, mainly because the fluidic interface is in-axis with the flow of the propellant in the thruster, compared to perpendicular to it. The improved heater design was selected after a series of simulations performed by Spernovasilis, in order to improve the uniformity of the heat distribution among the microchannels.

One of the big advantages of Singh's design is the reduction in fabrication complexity, lowering the number of processing steps required during manufacturing. This is in contrast with Spernovasilis' design. The latter included a multitude of sensors incorporated in the thruster itself, such as pressure

and vapour fraction sensors. However, these greatly increased the complexity of the thruster, leading to 94+18 fabrication steps, versus only 45 required for Singh's design.

Some order of magnitudes for comparing with other articles / experiments are given below. These were either taken from the thesis of Singh, or calculated by the author of the current thesis afterwards.

- Target temperature $T_{target} = 700\,\mathrm{K}$
- Input pressure $p_{in} = 6\,\mathrm{bar} = 0.6\,\mathrm{MPa}$
- Expected ideal mass flow $\dot{m} = 3.5\,\mathrm{mg/s}$
- Power requirement (at 100% efficiency): $\dot{Q}_{real} = 2.798\,\mathrm{W}$. If assuming 25% efficiency: $P_{heater} \approx 11.2\,\mathrm{W}$.
- Microchannel dimensions (ideal): depth of $d_m = 150\,\mathrm{\mu m}$ and width of $w_m = 212\,\mathrm{\mu m}$
- Resulting mass flux : $G = \frac{\dot{m}}{5 \cdot d_m \cdot w_m} = 22\,\mathrm{kg/(m^2 \cdot s)}$
- Resulting heat flux: $q = \frac{\dot{Q}_{real}}{A_w} = 90.6\,\mathrm{kW/m^2}$. A_w is the wetted microchannel silicon area.
- Resulting mass flux to heat flux ratio: $q/G = 4.12\,\mathrm{kJ/kg}$

2.2. Flow Instabilities in Microchannels

In this section, the flow instabilities present in microchannels (and thus also in VLMs) are presented. First, the types of instabilities and their causes are given, after which a short review of the findings in the literature of experimental studies is given.

2.2.1. Types of Instabilities in Microchannels

The main types of instabilities in boiling channels are presented shortly in Table 2.1. These are split in two categories: static and dynamic instabilities. Static instabilities appear when the system is in a state of unstable equilibrium, and has the tendency to convert to a state of stable equilibrium. On the other hand, dynamic instabilities are periodic oscillations of certain values (such as pressure, mass flow rate, temperature etc.) that take place around an equilibrium point.

The different types of instabilities are shortly presented in the following subsubsections. However, it is to be noted that some instabilities are not relevant for the microchannel flow in the context of the VLM.

Table 2.1: Types of instabilities in (micro)channels

Instability type	Cause	Description	Source(s)
Static instabilities			
Ledinegg instability	Slope of internal pressure drop curve is smaller than the external one	The flow changes mass flow rate from an unstable equilibrium condition to a stable one Can be overcome by installing an inlet restrictor, or a throttling valve.	[19]
Boiling crisis	High heat flux at the wall evaporates the liquid very fast, leading to dry out	Cyclic fluctuations in the flow appear, as phase changes happen from one state to the other and vice versa. High wall temperature and low heat transfer coefficient also appear during dry-outs	[20] [21]
Flow transition instability	Transition from one flow regime to another. Usually when close between transition from bubbly to annular flow.	Small reduction in flow rate in bubbly flow → small increase in vapour fraction (same heat flux) → annular flow → lower pressure drop → increase in flow rate → decrease in vapour fraction (insufficient heat flux) → bubbly flow	[21]
Geysering	Usually in vertical channels in gravitational field with little to no movement, caused by the "liquid superheat"	A rapid ejection of liquid is caused by the violent boiling, and the fallback of the liquid. May lead to hammerhead effect.	[22]
Dynamic instabilities			
Density wave oscillation	A small flow rate drop increases enthalpy rate, which increases density. This in turn affects the pressure drop and heat transfer, which can lead to "resonance"	Usually low frequency (around 1 Hz) related to the travel time of a "continuity wave"	[21]
Pressure drop oscillations	Upstream compressibility induced, or compressibility in the heated section. Operation on the negative slope of the pressure drop - flow rate curve.	"CHF (critical heat flux) always occurs during the excursion that initiated the first cycle"[21] When L/D (channel length / diameter) >150, there is enough internal compressibility such that pressure drop oscillations will occur. Inlet throttling will not help	[20] [21]
Acoustic oscillations	Film thickness variation and bubble collapse → change in pressure	"Propagation of pressure waves with speed of sound in two-phase mixture" Usually high frequency (10–100 Hz, up to 10 kHz), the period related to the time a pressure wave needs to travel through the system. Usually small amplitude, but can become significant	[20] [21]
Thermal oscillations	Instability of thin film near heated tube wall. Requires density wave oscillations. Can be caused by dryout at high pressures, constant heat flux.	Large amplitude. Movement of dryout location.	[20] [21]
Parallel channel oscillations	Result of density wave oscillations within each channel + feedback	Moderate flow oscillations. Inconsistently in- and out-of phase	[20] [21]

Ledinegg Instability

The Ledinegg (or flow excursion) instability is a type of static boiling instability, in which the system is found at an unstable equilibrium combination of mass flow rate, pressure drop and heat flux. As such, when a small turbulence appears in one of these quantities, the system tends towards a new and stable equilibrium configuration, which might not be desirable for the operation of the thruster.

The instability appears when, in the pressure drop versus mass flow rate plot, the slope of the demand pressure drop (from the microchannel) is less (in an algebraic sense) than the slope of the supply pressure drop (from the pump). This can be written as [19]:

$$\left.\frac{\partial(\Delta P)}{\partial G}\right|_{channel\,demmand} \leq \left.\frac{\partial(\Delta P)}{\partial G}\right|_{pump\,supply} \tag{2.10}$$

where ΔP is the pressure drop and G is the mass flux (in the paper of Zhang et al. [19] given in kg/s instead of kg/(m^2·s)).

In Figure 2.6, a typical pressure drop demand curve for a constant heat flux flow though a microchannel is given. ONB signifies the onset of nucleate boiling, while OFI the onset of flow instabilities. The OFI is the point after which, when decreasing G, the flow has a high chance of becoming unstable (but is not guaranteed to, as the supply curve is also needed for this). As an example in this figure, at point a, if the slope of the demand curve is less negative (higher algebraically) than the demand one (as is for slope A), the flow is unstable, and will tend to jump to stable regions, such as b and c.

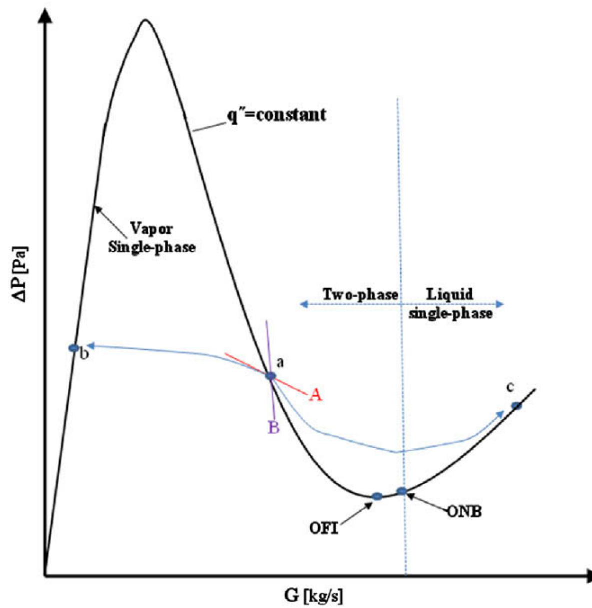

Figure 2.6: Pressure drop vs mass flow rate for constant heat flux in a channel [19]

In the same figure, the following regions can be observed, in order of decreasing mass flux G (for a constant heat flux):

- The liquid single-phase region, corresponding approximatively to the positive slope region in the right third of the graph
- The two-phase region, corresponding approximatively to the negative slope region in the middle third of the graph
- The vapour single-phase region, corresponding approximatively to the positive slope region in the left third of the graph

These states represent the state of the flow at the exit from the microchannels. The Ledinegg instability only appears in the two-phase region of the pressure drop, as it requires the slope of the channel demand

curve to be negative. However, the usual operational regime of the microchannels in a VLM is in the single-phase vapour region, as the flow needs to be fully vaporised before entering the nozzle. This limits the possible appearance of this instability only to when the flow is about to be fully vaporised. This is important for studying the heat transfer coefficient at not fully vaporised conditions (the prime region for this type of instability), but not for the operational conditions of the thruster.

Additionally, a syringe pump was used in the tests done in the past at TU Delft with a water-fed MEMS VLM, and is also proposed for the tests in this thesis. This syringe pump acts as a positive-displacement pump, which has a very steep negative slope at the set flow rate. As such, the possibility of the channel demand curve to be steeper than that of the pump supply is very low, diminishing the importance of such type of instability.

The discussion above applies to a single microchannel. However, when multiple microchannels are operated in parallel (which is also the case for the VLM), complex phenomena can appear, leading to Ledinegg instability only in one of the microchannels. This is described in the work of Kingston et al. [23], where the flow through two parallel thermally-isolated microchannels was studied. It was observed that the Ledinegg instability appears at the onset of nucleate boiling in only one of the channels, leading to uneven flow. However, once ONB appears in the other channel as well, the flow becomes uniform once again. As this instability appears in the conditions near the local minimum in Figure 2.6, it is not considered relevant for the operation of the VLM microchannels.

Boiling Crisis

The boiling crisis instability appears when the heat transfer does not take place uniformly in the flow [20]. In a particular region, excessive heat transfer leads to local vaporisation of the flow (dry-out), creating an insulating layer. This in turn increases significantly the wall temperature. This instability is related to the explosive boiling observed and explained in Subsection 2.1.4, and can be considered as a prerequisite for it. Therefore, such phenomenon is expected to appear in VLMs.

Flow Transition Instability

The flow transition instability appears when the flow is at the boundary between two different types of flow, usually between bubbly and annular flows. This was observed by Huh [24] in two-phase flow, leading to large mass flux and pressure drop fluctuations. The amplitude of the oscillations increased with the q/G ratio, which varied between 1.25 and 1.57 kJ/kg. The expected q/G ratio of 4.12 kJ/kg for the TUD MEMS VLM (with the theoretical ideal values from Singh's design) is even larger than this range of tested ratios. As such, it is not fully clear what effect this instability will have on the operation of the VLM, especially at full vaporisation operation.

Geysering

Geysering is a flow instability that usually appears in vertical channels, heated only on one end [21], involving boiling delay, condensation, and return of liquid [20]. However, these conditions are not representative of the operating conditions of the VLM. As such, this instability is not discussed further.

Density Wave Oscillations

In order to explain this type of instability, a schematic of an example system is given in Figure 2.7, taken from the work of Kakac & Bon [25]. The system is composed of a supply tank with assumed constant pressure P_I, and a heater with flow restrictions at the entrance and exit. P_0 is the inlet pressure, while P_e is the assumed constant exit pressure. The following explanation is also based on the explanation from their work.

Assume that a small decrease in the pressure drop takes place. The flow at the exit is fully vaporised, as shown by the location of the pressure drop vs mass flux graph in the left positive-slope region. Almost immediately, P_0 will also decrease, as P_e is constant. The pressure in the supply tank P_I is converted to the inlet pressure P_0 and flow dynamic pressure $\frac{1}{2}\rho_i u_i^2$, where ρ_i is the inlet density of the fluid, and u_i is the inlet velocity of the fluid. As such, $P_I = P_0 + \frac{1}{2}\rho_i u_i^2$. It is clear that with a decrease in P_0, u_i will increase. This also leads to an increase in mass flux. As the slope of the pressure drop vs mass flux is positive, this in turn results in an increased pressure drop. As P_e is constant, this means that P_0 increases. This in turn decreases u_i (from the previous pressure equation), which decreases the mass flux. This results in a decrease in the pressure drop, which then repeats the cycle. The variation of mass

flow rate also induces a variation of the time spent in the heater section, which in turn creates a periodic variation in the density of the fluid at the exit.

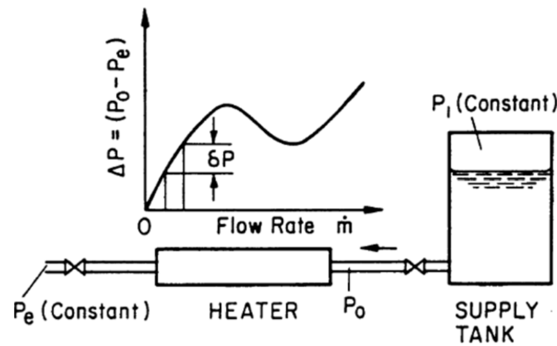

Figure 2.7: Simplified system for the explanation of density wave oscillations. Image taken from [25].

This instability thus appears in the single-phase vapour region of the ΔP vs G plot, which represents also the operational conditions for the VLM. As such, it is highly expected for this type of instability to appear during operation.

Pressure Drop Oscillations

Pressure drop oscillations are caused by the compressibility in the system, either upstream or internal to the heating channels. An explanation of the establishment of these instabilities is given in the work of Kakac & Bon [25].

As prerequisites for this type of instability, the following conditions need to be met [26]:

- Operation on the negative slope of the internal ΔP vs G curve
- The slope of the external ΔP vs G is steeper than that of the internal curve (opposite of the Ledinegg instability condition)
- Existence of a compressible volume in the system (internal or external)

As for the Ledinegg instability, operation is mostly in the positive slope part of the pressure drop curve. As such, the first condition is reached only when the flow is not fully vaporised.

When using a syringe pump, the slope of the external pressure drop curve is indeed steeper than that of the internal curve. However, there is no compressible volume in the system. The syringe and the inlet are filled with liquid water (considered incompressible). Internal compressibility appears when the ratio between the channel length and diameter (L/D) is 150 or more [21]. However, this is not the case for the TUD MEMS VLM, which has a L/D ratio of around 70. In this case, pressure drop oscillations are not expected.

If, however, the thruster were to be operated with a blow-down system, which is pressurised using an external gas, an upstream compressible volume appears. This can lead to the appearance of pressure drop oscillations in the regime of incomplete vaporisation. However, this is outside the scope of this thesis.

Acoustic Oscillations

According to Saha & Celeta [20], acoustic oscillations usually appear under conditions of "film boiling, subcooled boiling, and cryogenic systems". Oscillations have a frequency of 10 to 100 Hz. In the context of microchannels, Saha & Celeta [20] and Wang et al. [27] state that these oscillations have a weak effect on the performance of the system. As such, they are not further considered.

Thermal Oscillations

Thermal oscillations appear after the initiation of dry-out, leading to film boiling. In these conditions, the fluid near the heating walls is in vapour form, severely decreasing the heat transfer coefficient. The

oscillation appears from the drift of the dry-out location, leading to large temperature fluctuations. According to [21], density wave oscillations are required for the establishment of thermal oscillations.

As the VLM operates in complete vaporisation mode, thermal oscillations are expected to appear in the system, especially near locations where vapour quality is around 1 or slightly below. While this does not significantly affect the pressure and mass flow rate [20], this oscillation might be visible in the wall temperature readings, or when calculating the convective heat transfer coefficient. The thrust values are not expected to be affected.

Parallel Channel Oscillations

There are two types of parallel channel oscillations: static and dynamic [27]. The static parallel channel oscillations are caused by the Ledinegg instability, and were explained in the last paragraph of the Ledinegg Instability subsubsection. In the following paragraphs, the dynamic parallel channel oscillations are explained.

(Dynamic) parallel channel oscillations are caused by the density wave oscillations in each individual channel, superimposed with the feedback from the inter-channel interactions. When a vapour bubble forms and grows at a high rate, its boundary moves upstream, which influences the flow distribution in the other microchannels [27]. If the bubble growth is out-of-phase between different microchannels, this leads to non-uniform flow. A graphical example of this phenomenon is shown in Figure 2.8.

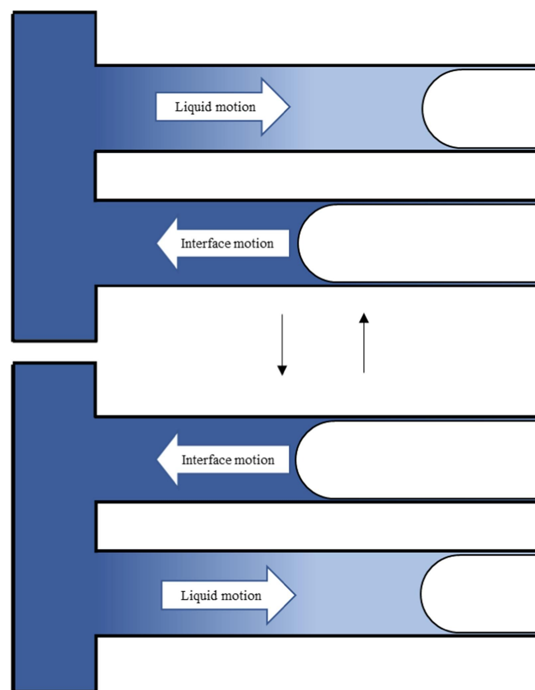

Figure 2.8: Diagram showing the parallel channel instability. A darker colour of the liquid corresponds to a larger pressure. Image taken from [27].

As density wave oscillations are expected to be seen in the VLM, and as the VLM has multiple parallel channels, this phenomenon is also expected to appear. This can accentuate the establishment of explosive boiling, which was reported in previous VLMs with parallel channels [7].

2.2.2. Experimental Microchannel Instability Studies in Literature

While an extensive review of experimental studies on instabilities in microchannel flows can be found in the work of Saha & Celeta [20], only the most important findings are summarised here.

The hydrodynamic instability of two-phase flow in a heat sink with 21 parallel microchannels was investigated by Qu & Mudawar [28]. The dimensions of the microchannels were of 231×713 µm. Two main instabilities were encountered: severe pressure drop oscillations, and mild instability due to the

parallel channels. The large pressure drop oscillations were encountered when the inlet valve was fully open, and were attributed to the compressible volume in the upstream flow loop. This was mitigated by throttling the inlet valve, which let only the parallel channels instabilities through.

Three boiling instability types were determined by Wu & Cheng [29], depending on the applied heat flux. In order of increasing heat flux, there are:

- Liquid / two-phase alternating flow (LTAF)
- Continuous two-phase flow (CTF)
- Liquid / two-phase / vapour alternating flow (LTVAF)

These instabilities gave rise to temperature, pressure and mass flow rate oscillations. While for LTAF the inlet pressure and temperature oscillations were in phase, the inlet pressure and mass flow oscillations were out of phase. For CTF, the mass flow and pressure oscillations were in phase.

For other studies, flow reversal was observed, as well as a general trend of increasing the amplitude and period of pressure and mass flux oscillations with increasing heat flux [20]. Multiple times, the ratio of heat flux to mass flux (q/G) was used to divide the different stability regions. These were usually a stable regime (q/G less than a certain value), a low-frequency high-amplitude regime (q/G within two boundaries), or a high-frequency low-amplitude regime (q/G larger than a certain value). These were also found to vary between configurations: the limits for a single channel were smaller than for multiple parallel channels [30], and were also lower for higher water inlet temperatures [31]. Using the q/G ratio derived from the ideal values from Singh's thesis, the TUD MEMS VLM is expected to operate in a low-amplitude, high-frequency unstable flow boiling regime.

The trend of instabilities increasing with q/G, however, seems to not hold for annular flow regime in microchannels. Balasubramanian et al. [32] reported that while in bubbly and slug flows, there is indeed a positive correlation, once nucleate boiling is no longer dominant and the annular flow regimes takes hold, there is a negative correlation between instabilities and q/G. This can be clearly seen in Figure 2.9.

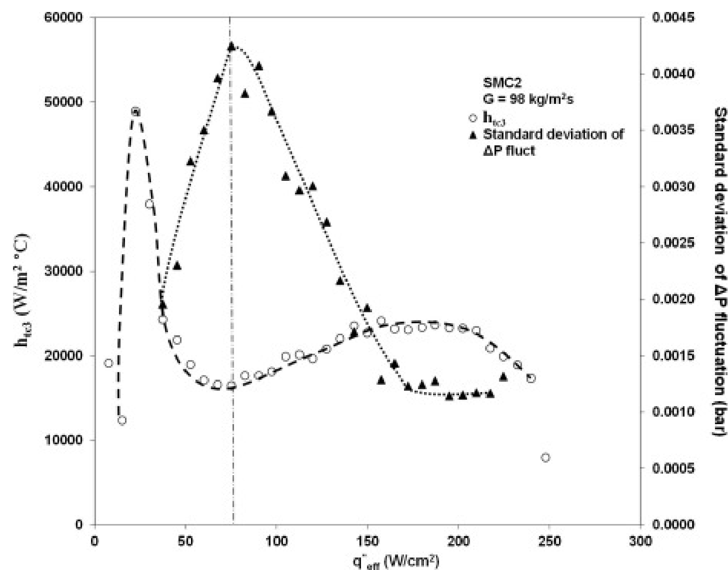

Figure 2.9: Variation of heat transfer coefficient (left) and amplitude of pressure drop fluctuations (right) with heat flux in a straight microchannel [32]

Another trend seen in the plot is that the heat transfer coefficient (HTC) has an inverse correlation with instabilities: the higher the pressure fluctuation is (especially in the transitional region between bubbly/slug and annular flows), the lower the HTC is. The HTC has two peaks: the first in the nucleate boiling dominated region, and the second in the annular flow region.

Three types of inlet/outlet configurations were studied by Wang et al. [33], presented in Figure 2.10. Type A had the inlet and outlet perpendicular to the microchannels, type B had them in parallel, and

type C differed from B by the addition of a restriction at the inlet.

It was found that type B presented lower oscillations in temperature and pressure, as well as less reversed flow, versus type A. Type C presented steady boiling without any oscillations or flow reversal. The configuration of the new generation TUD MEMS VLM corresponds to type B.

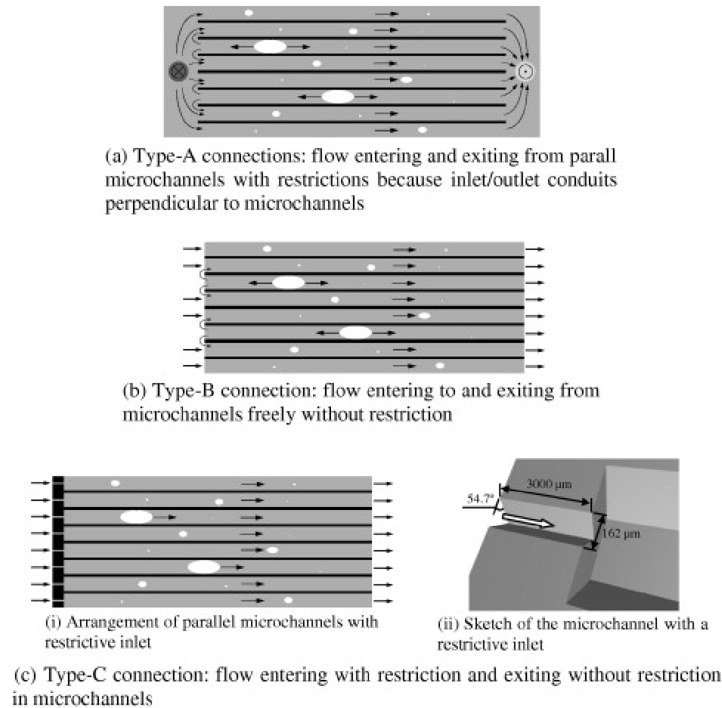

(a) Type-A connections: flow entering and exiting from parall microchannels with restrictions because inlet/outlet conduits perpendicular to microchannels

(b) Type-B connection: flow entering to and exiting from microchannels freely without restriction

(i) Arrangement of parallel microchannels with restrictive inlet

(ii) Sketch of the microchannel with a restrictive inlet

(c) Type-C connection: flow entering with restriction and exiting without restriction in microchannels

Figure 2.10: Parallel microchannels with three different inlet and outlet configurations [33]

Compressibility
The effect of upstream compressibility on both the heat transfer coefficient and the flow instabilities was reported by Liu et al. [34]. A buffer reservoir which could contain a varying amount of gas was used to simulate hard inlet (no compressibility - i.e., the volume of gas in the reservoir was 0) and soft inlet conditions for a single microchannel.

A great difference was observed in the oscillations of the mass flow rate and inlet pressure for the different compressibilities. The hard inlet produced no mass flow rate fluctuations, but only irregular pressure fluctuations. On the contrary, the soft inlet conditions produced in-phase fluctuations of both mass flow rate and pressure, with a well-defined frequency.

It was also observed that the pressure drop through the channel decreases with an increase in buffer volume, which in turn affects the saturation temperature of the fluid in the microchannel.

Another very important finding is that the heat transfer coefficient (HTC) increases mostly by increasing the mass flow rate and not by heat flux in the hard inlet condition. On the contrary, for a soft inlet, the HTC increases with increasing heat flux, and not by mass flow rate. The paper also claims that the fluctuations that appear are not a result of the boiling mechanism, but of the system itself. As such, these fluctuations influence the boiling, which in turn produce the changes in HTC.

It is also claimed that flow reversal is to be expected due to the mass flow rate oscillations, especially in the two-phase region.

2.3. Heat Transfer in VLMs

In the VLM, the heat transfer from the heaters to the propellant flow happens mostly in the microchannels, and to a lesser extent in the inlet. As such, the focus of the literature research on heat transfer was on heat transfer through the boiling two-phase microchannel flows. Most literature on this subject

is available from the domain of heat and thermal management, which has the scope of achieving an as-high-as-possible heat transfer and heat transfer efficiencies, while diminishing instabilities. The goal of increasing heat transfer efficiency also applies to the VLM, as it would reduce the power requirements of the thruster. Similarly, a stable VLM decreases the chance of appearance of phenomena that diminish the performance of the thruster. However, for the heat transfer itself, the situation is more complex.

A higher heat transfer (and especially a higher heat transfer coefficient) has the benefit of reducing the temperature difference between the wall and the propellant flow, required to transfer the same amount of heat. This reduces the required heater temperature of the device. As such, heat losses to the environment are reduced, or allows the operation of the thruster at higher final propellant temperatures and pressures (for the same heater temperature).

On the other hand, a high heat transfer has the risk of increasing the probability of and the strength of flow instabilities. From the instabilities explored earlier in this chapter, particularly sensitive would be the boiling crisis, explosive boiling, and thermal oscillations. This risk could be decreased by increasing the length of the microchannels to allow the same heat flow spread over a larger area, and thus reduce the heat flux. However, this would increase heat losses (as there is a larger area to transfer heat to the environment) and pressure losses.

An additional requirement for the VLM is that the propellant has to be fully vaporised by the time it exits the microchannels. This is not a requirement for microchannels used for heat and thermal management. On the contrary, full vaporisation is usually avoided in those cases, as it severely decreases the heat transfer coefficient, and can lead to unnecessary high temperatures of the structure.

In the first subsection, the effect of shape on heat transfer in microchannels is presented. Then, the effect of the type of flow on heat transfer is shortly presented.

2.3.1. Effect of Shape on Heat Transfer

The most prominent shape of microchannel in VLMs (and in other applications) is the straight channel, due to its simplicity in manufacturing. However, other designs used in literature include serpentine (sometimes also called wavy) microchannels, or have the heating area containing differently-shaped fins. Examples of both cases were presented in Subsection 2.1.1 and Subsection 2.1.3.

In the work of Silva [2], the performance tests were performed for different combinations of heater, heating chamber, and nozzle shapes. As not one parameter was varied at a time, it is hard to get to a conclusion as to which shape of the heating chamber proved to be most efficient, especially with different levels of mass flow rates. However, it seems that the configuration with the small diamond pin fins heating chamber achieved the highest heat transfer efficiency.

As previously mentioned in Subsection 2.1.3, the one-phase simulated flow showed that the square pins have the largest effect, increasing the heat transfer. However, as these represent only simulation results, and not of two-phase flow, the literature available on experimental studies on heat sink two-phase microchannel flows is addressed.

Experimental tests of boiling water two-phase flows in microfin structures in heat sinks were performed by Wan et al. [35], with four primary shapes: square, circular, diamond and streamline. These shapes can be seen in Figure 2.11. These designs were not compared with a similar straight microchannel configuration, and thus can only be compared with each other.

It was observed that the square fins provided the best HTC values, followed by circular and streamline, with diamonds performing the worst. However, the diamond microfins experienced the lowest pressure drop, followed by square, circular, and streamline. The worst instabilities were seen for the diamond configuration, whereas square and circular designs were the most stable.

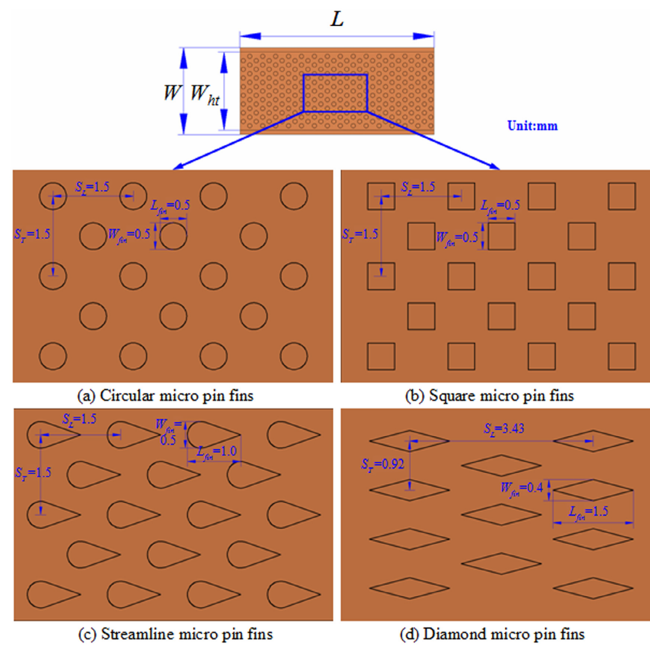

Figure 2.11: The description and dimensions of the microfin geometries inside the vaporisation chamber [35]

Another study [36] investigated the difference in HTC between straight and sinusoidal wavy microchannels using HFE-7100 as working fluid. Even though the wavy microchannels do not have the exact same shape as the serpentine ones used in the works of Silva [2] and Singh [15], the effect of these shapes is considered comparable. It should be noted that Cui & Liu [36] used triangular profile channels instead of rectangular. The geometry can be observed in Figure 2.12.

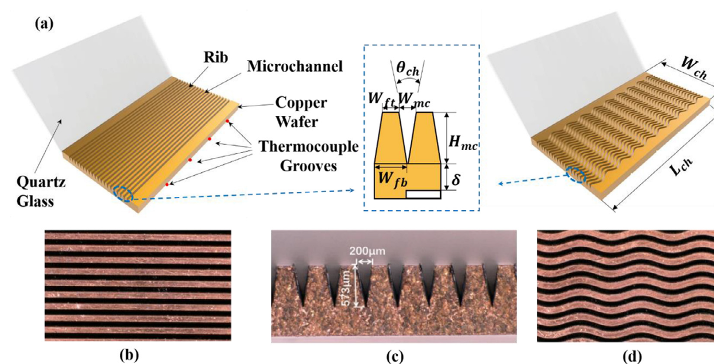

Figure 2.12: Aspects of the heat sink: (a) schematic of the microchannels, (b) and (d) photos of the straight and wavy microchannels, (d) photo of the cross-section of the microchannels [36]

Increases in HTC of around 55–60% were observed in the nucleate boiling regions, and of around 22–52% in the convection boiling regions. The increase in the nucleate region is explained by an increase in the heat transfer area which creates more nucleation sites, and the fact that the centrifugal acceleration of the main flow enhances the ability of the bubbles to detach. In the convective boiling regime, the increase can be explained by the lower thickness of the thin liquid film on the inside of the curves, which increases heat transmission.

2.3.2. Effect of Type of Flow on Heat Transfer

In this subsection, the effect of the type of flow on heat transfer is summarised. A more in-depth analysis can be found in the literature study of Bianchi [37], on which this subsection is based.

There are multiple classifications of two-phase flow types available in literature, which makes a direct

comparison between them more difficult. However, a common division is the following [38]:

- Bubbly flow: the flow is mostly liquid, with bubbles of vapour present throughout. The bubbles' diameter is smaller than the channel dimension, and the flow is not confined.
- Slug flow: the vapour pockets have an elongated shape, looking similar to a bullet. The radius of the slug is close to the channel dimension, with a thin film of liquid between the gas and the wall. Between two consecutive vapour slugs, there are liquid slugs.
- Annular flow: the vapour slugs have coalesced and become one continuous cylindrical core of gas, surrounded by a layer of liquid between itself and the channel wall.
- Mist flow: the flow consists of mainly a continuous vapour phase, with entrained liquid droplets.

The bubbly, slug and annular flows are depicted in Figure 2.13.

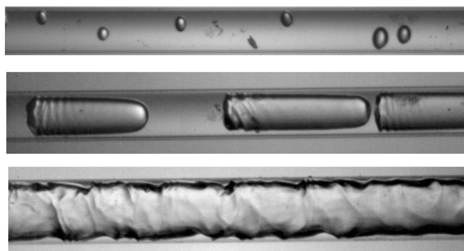

Figure 2.13: Types of two-phase flows in microchannel. From the top: bubbly, slug and annular [38].

The main phase change mechanisms encountered in boiling microchannel flows are nucleate boiling and convection boiling. Nucleate boiling appears when bubbles start forming at the channel wall, reducing the superheat and increasing heat transfer. On the other hand, convective boiling consists of the growth of a pre-existing vapour bubble/slug or increase in vapour core in annular flow, by phase change at the liquid-vapour interface; the heat is transferred through convection from the wall to the liquid [37].

These mechanisms lead to different tendencies of variation for the heat transfer coefficient (HTC). It was observed that during nucleate boiling, the HTC varies with heat flux, whereas during convective boiling it varies mostly with mass flux [37]. In Figure 2.14, the variation of HTC with the different types of flow presented earlier is shown.

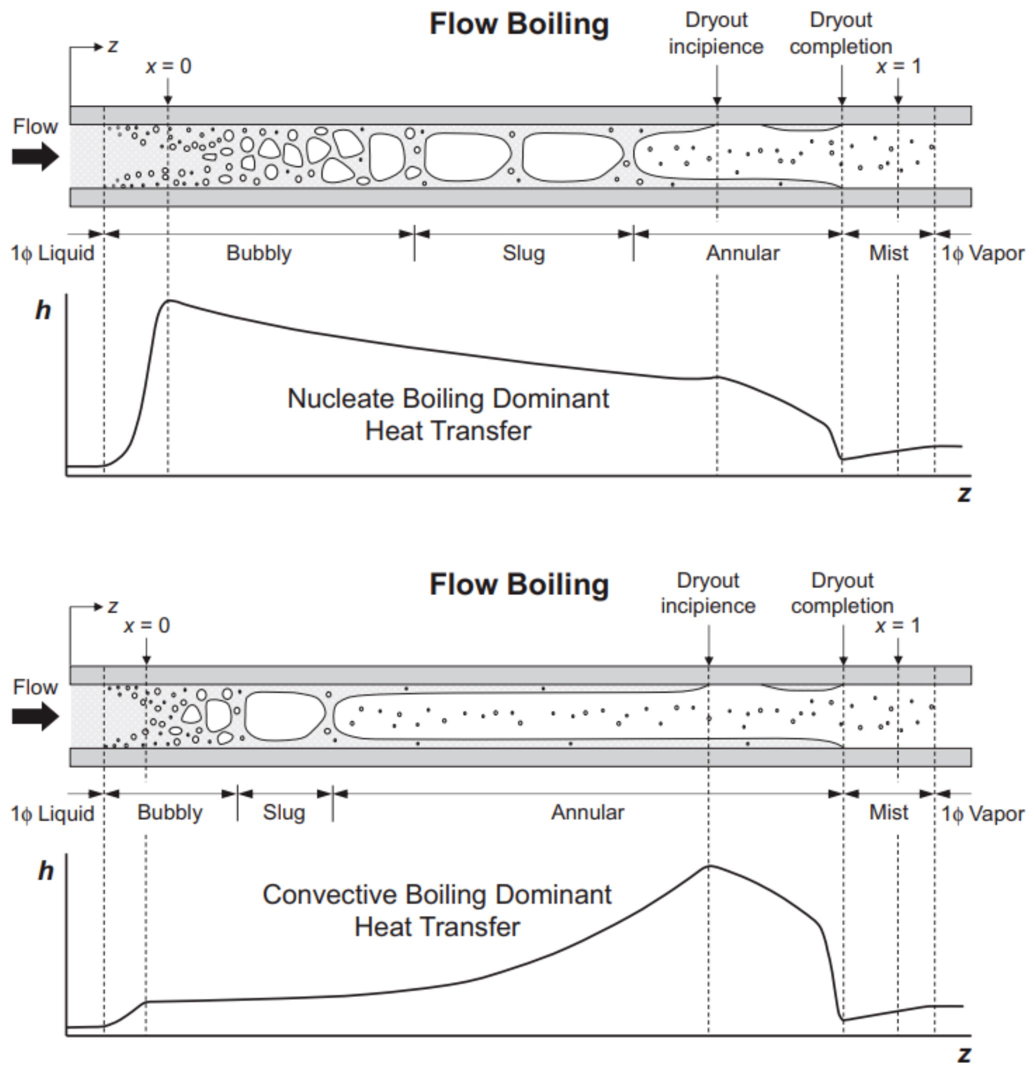

Figure 2.14: Schematics of the flow regimes and heat transfer coefficient variation in microchannels for nucleate boiling dominant (top) and convective boiling dominant (bottom) flows [39]

As can be seen from the figure and is also expected, nucleate boiling takes place mostly in the bubbly flow regime, whereas in the slug and annular regimes convective heat transfer is dominant. However, many experimental studies in the literature have observed that a trend similar to the one for nucleate boiling appears for microchannel flows, even during the slug and annular regimes [37]. Bianchi gives as possible explanations for this phenomenon the evaporation of the microlayer between the gaseous slug and the channel wall, but also on oscillations from upstream compressibility. The latter are also mentioned in Subsection 2.2.2.

2.4. Numerical Modelling

In this section, some aspects related to numerical and/or analytical modelling of the flow in VLMs are presented, with an emphasis on methods used for modelling the vaporising / heating chamber. The first subsection presents typical non-dimensional numbers that can be encountered in the study of boiling in microchannels (and which are used in the following models). The second section presents the most used methods for predicting the HTC and flow regions in a semi-empirical way. The rest of the subsections summarise some attempts at numerical and/or analytical modelling of VLMs.

2.4.1. Non-Dimensional Numbers

In this subsection, some non-dimensional numbers, relevant for the characterisation of the type of flow in the microchannels, are shortly presented.

The boiling number is usually defined as [40]:

$$\mathrm{Bo} = \frac{q}{G \cdot \lambda_{lv}} \tag{2.11}$$

where q is the heat flux [W/m^2], G is the mass flux [kg/(m^2·s)] and λ_{lv} is the specific heat of vaporisation [J/kg]. This number represents the ratio between the heat flux provided externally and the heat flux required for the full instantaneous vaporisation of the fluid flow.

The capillary number can be defined as [40]:

$$\mathrm{Ca} = G \cdot \frac{\mu}{\rho} \cdot \sigma_{st} \text{ or } G \cdot \frac{\mu}{\rho_l - \rho_v} \cdot \sigma_{st} \tag{2.12}$$

where μ is the dynamic viscosity of the fluid (most often of the liquid phase), ρ is the density of the fluid (with the indices l and v denoting the liquid and vapour phases, respectively), and σ_{st} is the surface tension coefficient. The first definition is the one used by Bianchi [37], but considering the ratio of the mass flux to density ratio as being the velocity of the bubble (G/ρ becomes u_{bubble}).

The confinement number is defined as [40]:

$$\mathrm{Co} = \sqrt{\frac{\sigma_{st}}{g \cdot (\rho_l - \rho_v) \cdot D_h^2}} \tag{2.13}$$

where g is the gravitational acceleration and D_h is the hydraulic diameter of the channel. It relates surface tension forces to buoyancy forces, but loses significance in microgravity situations. A related number is the Bond or Eötvös number, which is related as $\mathrm{Eo} = 1/\mathrm{Co}^2$. Its expression is given as:

$$\mathrm{Eo} = \frac{g \cdot (\rho_l - \rho_v) \cdot D_h^2}{\sigma_{st}} \tag{2.14}$$

Another important non-dimenisonal number is the Nusselt number, which relates the convective heat transfer to conductive heat transfer [41, 40]:

$$\mathrm{Nu} = \frac{h \cdot D_h}{k_l} \tag{2.15}$$

where h is the convective heat transfer coefficient [W/(m^2·K)] and k_l is the thermal conductivity of the liquid [W/(m · K)].

The Prandtl number is defined as the ratio between momentum diffusivity and thermal diffusivity [42]. Its formula is:

$$\mathrm{Pr} = \frac{c_p \cdot \mu}{k} \tag{2.16}$$

where c_p is the specific heat capacity of the fluid (in the case of gas, at constant pressure).

Lastly, the Reynolds number is the ratio between inertial and viscous forces, defined as [40]:

$$\mathrm{Re} = \frac{\rho \cdot u \cdot D_h}{\mu} = \frac{G \cdot D_h}{\mu} \tag{2.17}$$

where u is the average flow velocity.

2.4.2. Heat Transfer Coefficient (HTC) and Flow Region Predictions

The limit between different flow regions, as well as an estimate of the HTC are very hard to predict analytically, due to the complex two-phase constricted flow in microchannels. For this reason, several authors have attempted to create semi-empirical relations between these limits / values and certain non-dimensional numbers, some of which were presented in the previous subsection.

For estimating the HTC, Tibiriçá et al. [40] differentiates the two-phase flow in pre-dryout and post-dryout regions. In the pre-dryout region, an equation relating the Nusselt number to the Prandtl, Laplace, Reynolds and Boiling numbers, as well as to the local vapour quality, is given. Then, the HTC can be calculated as $h = \mathrm{Nu} \cdot k_l / D_h$.

For the post-dryout phase, this equation is no longer valid, and a linear interpolation is made between the value at the dryout location (as predicted by the previous equation), and the vapour-only value estimated by the Dittus-Boelter equation. For the dryout location, the minimum of either the incipient dryout vapour quality, the critical vapour quality, or 0.95, is used. Tibiriçá et al. [40] claims a mean absolute error of 19%, and that 81.1% of the data used is predicted with less than 30% error. This is the method that De Giorgi & Fontanarosa [43] also used for their quasi-1D model for estimating the performance of a VLM.

Tibiriçá et al. [40] also derived formulae for the critical heat flux (CHF), the critical vapour quality, flow pattern transition vapour qualities (bubble-slug, slug-churn and churn-annular), frictional pressure drop, void fraction, and liquid entrainment.

Tang et al. [44] also developed a model for the flow regimes and HTC based on semi-empirical equations. They divide the HTC calculation in more regions than done by Tibiriçá et al., namely liquid single-phase, subcooled boiling, saturated boiling, and partially dried-out flow. Similar non-dimensional numbers are used for determining their values. For the boundaries of these regimes, estimates for the temperature of the onset of nucleate boiling (ONB), as well as flow type transitions from the work of Tibiriçá et al. are used. Another model based on similar principles was also developed by Ma et al. [45], which was also verified experimentally using a parallel microchannels aluminium heat sink.

2.4.3. Quasi-1D

A quasi-1D analytical model was created by De Giorgi & Fontanarosa [43] for VLMs, in order to predict their overall performance. The two-phase boiling region consisted of the inlet and the microchannels of the thrusters. Here, equations for the 1D conservation of mass, momentum and energy were applied for averaged liquid-vapour values, based on the local vapour quality. For the heat transfer values, the model described by Tibiriçá et al. [40] for steady-state boiling flow in microchannels was used, which is explained in the previous subsection.

For the micronozzle, the ideal rocket theory (IRT) equations were used, to which some semi-empirical corrections for the mass flow rate (namely, the discharge coefficient) and for the exit velocity (namely, the I_{sp} efficiency) were applied to take into account losses due to viscous effects, such as the establishment of a boundary layer.

These two calculations were iterated on each other's results until a convergence of the mass flow rate and the transferred heat flux was obtained. A diagram of the working principle of this model is given in Figure 2.15. The authors claim good predictions, of at most 7.3% deviation from the experimental values for thrust and I_{sp} values.

Similar steady-state models for the design of VLM microthrusters were also created in the past at TU Delft [46, 47].

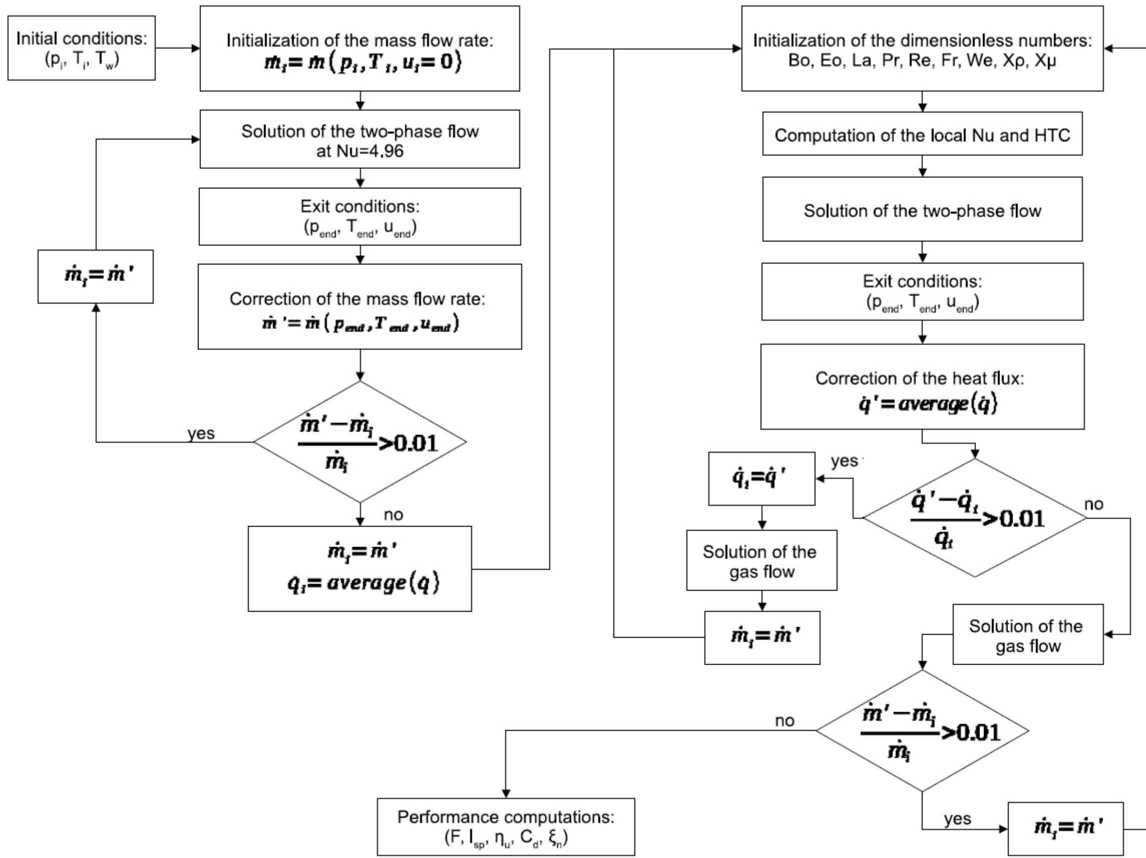

Figure 2.15: Diagram of the calculation steps for the quasi-1D VLM model. Taken from [43]

2.4.4. Lattice-Boltzmann Modelling

Weinmiller [48] considered using the Lattice-Boltzmann Method (LBM) for simulating the multiphase flow, including phase change, in VLM microchannels. The Lattice-Boltzmann Method starts from the probabilistic description of kinetic theory, in the form of the Boltzmann equation:

$$\frac{\partial f_{par}}{\partial t} + \xi_\beta \frac{\partial f_{par}}{\partial x_\beta} + \frac{F_\beta}{\rho} \frac{\partial f_{par}}{\partial \xi_\beta} = \Omega(f_{par}) \tag{2.18}$$

Where f_{par} represents a probability density function of finding a particle in a certain location and with a certain momentum, t is time, ξ is the particle velocity, F represents the external body forces, ρ is the macroscopic density, β is the index for dimension, and Ω represents the term for collisions. The equation uses the Einstein notation.

The LBM attempts to solve this equation by discretising the domain into a lattice, in which each node has a series of density components. These components represent both the actual density in the node, and the density of the fluid that is convecting to a neighbouring node (in multiple directions). The collision term also requires special handling, and multiple models are available to simplify its description.

While usually solving the Boltzmann equation is regarded mostly useful for rarefied gas dynamics, such as using the Direct Simulation Monte Carlo (DSMC) method, it has been shown that other fields can be described well by solving the equation [49]. The LBM can be successfully used for non-ideal fluids, slip-flows, microfluidics, multiphase flows, aerodynamics and more. For these reasons, Weinmiller [48] attempted to use such a method to study the multiphase and phase-changing flow in VLM microchannels. He started from the OpenLB framework, and extended it to include phase-change capabilities.

One of the biggest difficulties observed was the presence of spurious currents due to the large density ratio between the liquid and gas phases. This was partially solved by increasing the diffusion interface

between the phases. However, this leads to the impossibility of detecting nucleation inside the microchannels. This led Weinmiller to not be able to complete the VLM microchannel simulations, and as such the software was not validated on this specific use case. A recommendation for fixing the issues is given, but the implementation time would be in the order of several months.

2.4.5. CFD Modelling

Another attempt at accurately numerically modelling the flow in the microchannels is made in the thesis of Bianchi [37]. A conventional CFD method of solving the Navier-Stokes equations is used, namely Volume-of-Fluid method for multiphase flows. Due to the dimensions of microchannel flow, surface tension was included in the simulations via the Continuum Surface Force method. It was also coupled with the PLIC algorithm to increase the sharpness of the interface. Phase change was implemented according to the Lee model, which changes the fraction of fluid proportionally to the deviation from the saturation temperature.

Due to a lack of high-resolution experimental data for VLMs, the simulation results were compared with data from thermal management system microchannels. At dimensions and regimes similar to those found in VLMs (lower Capillary number Ca), the simulation failed to predict the heat transfer that was expected in this type of flow, as can be seen in Figure 2.16. In this figure, the thermodynamic vapour quality is defined as [37]:

$$\chi_{th} = \frac{h - h_{sat,l}}{h_{sat,v} - h_{sat,l}} \tag{2.19}$$

where h is the local specific enthalpy of the fluid, $h_{sat,l}$ is the specific enthalpy of saturated liquid, and $h_{sat,v}$ is the specific enthalpy of saturated vapour.

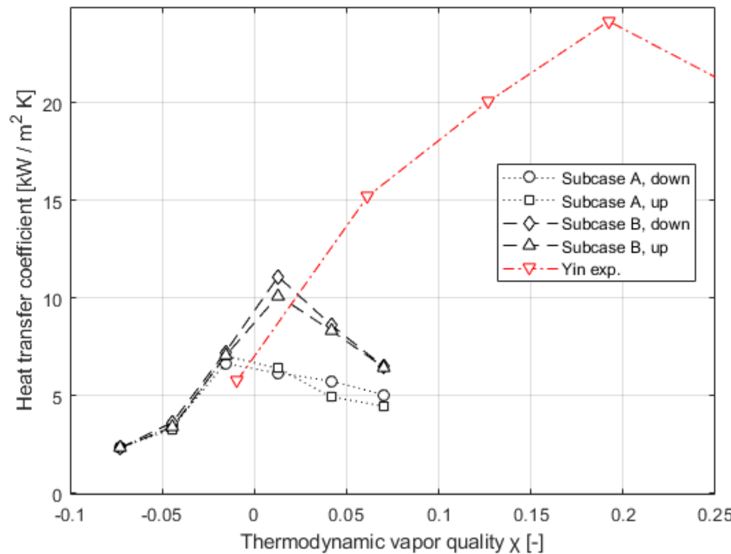

Figure 2.16: Comparison of HTC between CFD results, experimental data and an analytical correlation for the low Ca case using artificial wettability [37]

This figure represents the second attempt of simulating the low Ca flow, with an artificially low wettability of the liquid. The previous attempt using the true/ experimental wettability provided even worse results, due to not predicting the formation of a liquid thin film near the wall. The results can be seen in Figure 2.17.

However, Bianchi [37] mentions that because VLMs have a higher heat flux to mass flux ratio (q/G), the heat transfer mechanism would be convection boiling-dominated. As such, the Lee model simulation might provide better results.

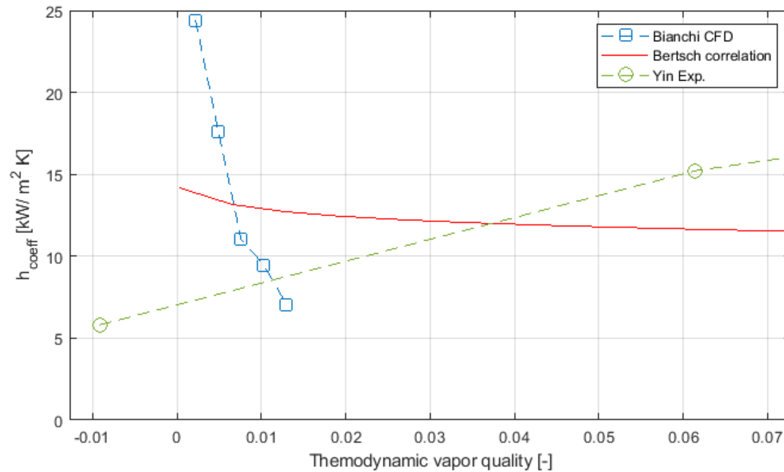

Figure 2.17: Comparison of HTC between CFD results and experimental data for the low Ca case using true wettability [37]

One of the largest impediments to utilising the CFD method is the large simulation time. While using the DelftBlue supercomputer provided enough computational power to run 2D single-channel simulations during the duration of a master thesis, running 3D and/or multichannel simulations would prove to be too time-consuming for a master thesis, and would require maybe the length of a PhD thesis. The author recommends the prioritisation of obtaining high-resolution VLM-specific experimental data over attempting to fix the issues seen in the simulations, or attempting more complex / different models.

2.5. Research Gap

In this section, the observed research gap in literature and at TU Delft is summarised.

At TU Delft, during the development of the CFD analysis for microchannels, Bianchi [37] mentions the need of higher-resolution experimental tests on the VLM thruster. This is required to characterise the thruster's performance, such that a proper validation of the CFD technique can be made on data with relevant dimensions. Bianchi recommends single- and multichannel configuration tests.

Singh [15] mentions that the next step after the VLM thrusters have been fabricated is to test them at operational conditions, in order to validate the design parameters. He also recommends some design improvements for the thrusters themselves. However, most design changes would prove to be very time-consuming for the current thesis. New (and more advanced) simulations would be needed, as well as the fabrication of a new exposure mask for the photolithography of the features on the thruster. Extensive reprogramming of the photolithography tool would also be required.

Besides design improvements, a closed-loop feedback control mechanism is mentioned for control of the thrust level. This idea could be applied also for the control of temperature to decrease instabilities, similarly to the work of Fontanarosa et al. [13]. Furthermore, a redesign of the inlet is recommended, in order to perform the required tests. On top of this, a fluidic, mechanical and electrical interface also needs to be designed for experimental tests.

Silva [2] also mentions the need of controlling the temperature of the thruster in order to obtain a smooth operation of the VLM system. This could be done through the integration of electronics for the power control of the heaters. An improvement of the interface of the thrusters is also required, to reduce size and improve the thermal insulation. Furthermore, the requirement of tests in the following conditions is also raised: in vacuum to reduce heat losses, with a thrust bench to measure the actual thrust and specific impulse, and testing the heaters in a hot plate in vacuum to reduce noise for determining temperature.

Parameswaran [46] mentions that the available correlations for the heat transfer coefficient in microchannels found in literature have ranges of validity that do not fully encompass the operating conditions of TU Delft VLM thrusters. This also emphasises the need for an experimental study on the heat transfer

properties of the TU Delft MEMS VLM thruster, especially on the performance of the microchannels.

Previous models were developed at TU Delft to aid in the design of the thruster [46, 47]. However, these were only investigating steady-state conditions, and could not cover the transient behaviour of the thruster (variation with time). This would be required when a controller needs to be developed, or when instabilities are to be studied (especially during start-up). The model developed by Silva [2] for control was focusing on the control of thrust for orbital and attitude manoeuvres. For operational stability, the control of the thruster's temperature would be most useful.

2.6. Research Objective & Research Questions

Given the research gaps previously identified, the need for experimental testing of the VLM is clear. As such, the following research objective was proposed:

Research Objective

The research objective is to extensively characterise the TU Delft VLM thruster's operational conditions and heat transfer properties through experimental testing and a temperature control method, in order to validate the design parameters, provide data for future model validations, and be able to reliably operate the thruster.

In order to achieve this research objective, the following research questions should be answered:

Research Question 1

How can the inlet and interface of the VLM thruster be modified / designed to decrease losses, be easy to operate and obtain more data?

- RQ1.1: How can the inlet and interface of the thruster be modified to provide more data about heat transfer in the microchannels?
- RQ1.2: How can the mechanical, electrical and fluidic interfaces be designed for ease of operations and control?
- RQ1.3: How can the heat losses be minimised by the design of a VLM interface?
- RQ1.4: How can instabilities be studied through the implementation of multiple inlet designs?

Research Question 2

How does the remanufactured TU Delft VLM thruster perform during its experimental characterisation?

- RQ2.1: Which instabilities can be observed during experimental testing?
- RQ2.2: How close to the parameters of the original design does the thruster operate in practice?
- RQ2.3: How does the heat transfer coefficient vary with time and position in the microchannels of the VLM?

Research Question 3

How can a method for the control of the thruster temperature be designed and used to increase the operational stability of the thruster?

- RQ3.1: How accurately does the controller perform in order to maintain the set operational temperature?
- RQ3.2: How does utilising the temperature control model affect the operational parameters (such as thrust and specific impulse)?

2.6.1. Updated Research Objective & Research Questions

As the thesis progressed, significant delays were encountered. The most important was regarding the production of the microthrusters. Initially, it was believed that the thrusters are only a few steps away

from being fully fabricated, and that the author would only need to help in the very last steps. Upon reaching the Else Kooi Laboratory, it became clear that there were some issues with the previous batch of thrusters, and that a new batch would need to be made from the beginning. This created significant delays to the schedule, as the author had to be in the cleanroom manufacturing the thrusters. However, this also introduced the opportunity of tweaking the manufacturing process, making it more efficient, and to also partially alter the design of the thrusters. These became core objectives of the work in the first half of the thesis. Other sources of delay included some tools requiring maintenance in the EKL cleanroom, and the author underestimating the amount of time required to learn and get familiar with new tools (software and hardware) required for the work in this thesis.

In order to take into account the reality of the situation, and to obtain results relevant to the new timeline of the thesis, the extent of the research gaps that should be (partially) addressed by the research objective and questions was redefined. As such, the following (summarised) researched gap is considered relevant:

- The need of higher resolution tests for the heat transfer properties of the VLM, to get better validation data for future simulation models [37].
- Slight design changes of the VLM, and the need of finishing the fabrication [15].
- Redesign of the inlet for the tests, and the creation of a fluidic, mechanical, and electrical interface.
- The requirement of tests in vacuum to reduce heat losses, and with a thrust bench to measure the actual thrust and specific impulse [2].

From this, the updated research objective is formulated:

Updated Research Objective

The research objective is to remanufacture and prepare the new generation TU Delft MEMS VLM thruster for future operational validation, heat transfer and instability studies, through experimental testing, by simplifying the manufacturing process, creating a testing interface, and performing measurements and extensive experimental characterisation of the thruster and test set-up.

The following updated research questions should be answered to achieve this research objective:

Updated Research Question 1

How can the testing interface of the VLM thruster be designed to survive harsh operational conditions, be easy to operate, and obtain more data?

- URQ1.1: How can the interface of the thruster be designed to provide data about heat transfer in the microchannels?
- URQ1.2: How can the mechanical, electrical and fluidic interfaces be designed for ease of operations and control?
- URQ1.3: What are the operational conditions at which the interface survives?
- URQ1.4: How can instabilities be studied using the new testing interface?

Updated Research Question 2

How does the remanufactured TU Delft VLM thruster compare to its original design?

- URQ2.1: How can the fabrication process be made more efficient?
- URQ2.2: Which problems can be expected during the fabrication process?
- URQ2.3: What are the differences between the measured and design properties of the thruster?

In order to answer these research questions, the rest of the thesis is structured as follows.

In Chapter 3, an analytical model for the performance of the VLM is created, verified, and expected operational conditions are derived. This is required to determine under what conditions is the thruster

expected to operate, and also what are the requirements of the interfaces. As such, it aids in answering URQ1.3.

Chapter 4 begins by explaining the design of the thruster itself, as well as the manufacturing process - including any problems that have arisen. It continues by performing measurements on the dimensions, surface properties, and heater resistance values of the fabricated thrusters. This chapter is used to answer any subquestions of URQ2.

The design, manufacturing, and assembly of the interfaces are explained in Chapter 5. Based on a set of requirements, fluidic and electrical interfaces are created, and the assembly method exemplified. This chapter aids in answering all subquestions of URQ1.

Finally, the test preparation is described in Chapter 6. Here, preliminary tests were performed to decide which test configuration would be best for future performance tests, as well as to test the capabilities of the newly-created testing interface. This chapter mainly focuses on answering URQ1.2 and URQ1.3. It also significantly aids in reaching the objective of performing the extensive experimental characterisation of the test set-up.

3
Analytical Performance Model

In this chapter, a simple analytical model for calculating performance characteristics of the VLM is derived. This is required in order to estimate the values of different parameters used in testing, such as pressure, mass flow rate, and required power.

In the preliminary calculations, the theoretical design values will be used to predict the performance parameters. As measurements of the manufactured components are performed, these calculations can be updated using the new values as inputs.

Section 3.1 presents an introduction to the performance model, while Section 3.2 explains how the model functions. A verification of the model with previous works is provided in Section 3.3, while the estimated expected efficiencies of the VLM performance parameters are derived in Section 3.4. Lastly, the estimated values for the operating conditions of the thrusters are included in Section 3.5.

3.1. Introduction of the Model

The VLM Performance Model, implemented in the Python programming language, has the purpose of predicting parameters such as power usage, mass flow rate and thrust. These can be used to calculate efficiency factors such as heater efficiency η_h, coefficient of discharge C_d, thrust quality factor η_F, and I_{sp} quality factor η_s. These are defined as follows:

$$\eta_h = \frac{\dot{Q}_{real}}{P_{heater}} \tag{3.1}$$

$$C_d = \frac{\dot{m}_{real}}{\dot{m}_{ideal}} \tag{3.2}$$

$$\eta_F = \frac{F_{T,real}}{F_{T,ideal}} \tag{3.3}$$

$$\eta_s = \frac{I_{sp,real}}{I_{sp,ideal}} \tag{3.4}$$

In Equation 3.1, $\dot{Q}_{real}$ is the heating power transmitted from the VLM heaters to the water flowing through the channels (assuming the real value of the mass flow rate), while P_{heater} is the electrical power supplied to the heater.

In Equation 3.2, $\dot{m}_{real}$ is the true mass flow rate through the VLM, while $\dot{m}_{ideal}$ is the ideal value calculated using ideal rocket theory (IRT). The same definition is used for thrust F_T and specific impulse I_{sp} in Equation 3.3 and Equation 3.4, respectively.

To calculate these efficiency parameters, both ideal values (from theory) and real values (from experiments) are needed. The next section deals with the calculation of the former using IRT.

3.2. Explanation of the Model

The equations that form the basis of this model are from the ideal rocket theory (IRT) model, as explained in [41]. These, among others, are reproduced below. However, some of the assumptions of this theory need to be discussed, as they differ from the reality of the VLM thruster.

An important assumption is that the flow is inviscid. This is an assumption that can be safely made when the Reynolds number at the throat is large, as the boundary layer is small compared to the throat dimension. However, this is not the case for very small throat dimensions that lead to small throat Reynolds numbers Re_t. As mentioned in the work of Cervone [50], at Reynolds numbers between 500 and 1000, significant drops in C_d occur. This will be expected also in the VLM that will be tested in this thesis, and as such a method to estimate it from previous experiments is recommended.

Other assumptions made in this model include (based on [50] and [41]):

- The fluid flowing in the thruster is ideal (follows the ideal gas law). However, it is only calorically perfect in the nozzle. The latter is a requirement of IRT.
- The flow is considered to have reached steady-state.
- The water is already vaporised by the time it reaches the nozzle, having a homogenous composition.
- The flow through the nozzle is adiabatic, but not in the heating chamber.
- A sufficient pressure ratio between the chamber pressure p_c and ambient pressure p_a is required, in order to assure the sonic throat condition (Mach number at the throat is 1).
- The flow is inviscid. Along the heating chamber, there is no pressure loss.

For the last one to occur, the following relation needs to be satisfied:

$$\frac{p_c}{p_a} \geq \left(\frac{\gamma+1}{2}\right)^{\left(\frac{\gamma}{\gamma-1}\right)} = \left(\frac{p_c}{p_t}\right)_{crit} \tag{3.5}$$

Where γ is the ratio of specific heats of the gas, also known as isentropic coefficient, p_t is the pressure at the throat, and the index $crit$ represents the critical conditions required for sonic flow at the throat.

To calculate γ, the following formula is used:

$$\gamma = \frac{c_p}{c_v} = \frac{c_p}{c_p - R_A/M_W} = \frac{\overline{C}_p}{\overline{C}_p - R_A} \tag{3.6}$$

Where c_p and c_v are the specific heats of the gas at constant pressure and volume respectively (in $\mathrm{J/(kg \cdot K)}$), $R_A = 8.3145\,\mathrm{J/(mol \cdot K)}$ is the universal gas constant, M_W is the molar mass of the gas, and $\overline{C}_p$ is the molar specific heat of the gas at constant pressure (in $\mathrm{J/(mol \cdot K)}$).

When the pressure ratio condition in Equation 3.5 is met, the mass flow rate $\dot{m}$ through the thruster can be estimated as:

$$\dot{m} = \frac{p_c \cdot A_t \cdot \Gamma}{\sqrt{\frac{R_A}{M_W} \cdot T_c}} \tag{3.7}$$

Where A_t is the cross-section area of the throat, T_c is the heating chamber final temperature, and Γ is the Vandenkerckhove function, defined as:

$$\Gamma = \sqrt{\gamma \cdot \left(\frac{1+\gamma}{2}\right)^{\left(\frac{1+\gamma}{1-\gamma}\right)}} \tag{3.8}$$

To estimate the power $\dot{Q}$ needed to heat the water from initial liquid state to saturation temperature, to vaporise, and then heat up to the final temperature as a vapour, the difference between specific enthalpy (in J/kg) at the exit h_{fin} and entrance to the heating chamber, multiplied by $\dot{m}$, is used:

$$\dot{Q} = \dot{m} \cdot \left(h_{fin} - h_{init}\right) = \frac{\dot{m}}{M_W} \cdot \left(\overline{H}_{fin} - \overline{H}_{init}\right) \tag{3.9}$$

Here, $\overline{H}$ represents the molar enthalpy (in J/mol). This is required, as most chemistry databases use molar values. To calculate $\dot{Q}_{ideal}$, $\dot{m}_{ideal}$ is used. For $\dot{Q}_{real}$, $\dot{m}_{real}$ is used.

The enthalpies need to be evaluated for the correct phase and temperature (initial and final). The model was implemented for water and nitrogen as propellants. As such, the properties of three values were required: nitrogen gas, liquid water, and water vapour. The nitrogen gas and liquid water properties were taken from the NIST Chemistry Webbook [51]. For water vapour, it only provided values for the enthalpy and specific heat from 500 K, excluding some lower values that were needed. As such, for this species, data using the NASA polynomials [52] was used.

The NASA Polynomials database provides coefficients for two temperature intervals, which can be used to calculate enthalpy, entropy and specific heat. The molar enthalpy $\overline{H}$ and molar specific heat at constant pressure $\overline{C}_p$ from the NASA polynomials can be calculated as follows as a function of temperature T (in K):

$$\frac{\overline{H}_{NASA}}{R_A \cdot T} = a_1 + a_2\frac{T}{2} + a_3\frac{T^2}{3} + a_4\frac{T^3}{4} + a_5\frac{T^4}{5} + \frac{a_6}{T} \tag{3.10}$$

$$\frac{\overline{C}_{p,NASA}}{R_A} = a_1 + a_2 T + a_3 \cdot T^2 + a4 \cdot T^3 + a5 \cdot T^4 \tag{3.11}$$

The used NASA Polynomials coefficients for the water in gaseous state are provided in Table A.1 in Appendix A.

The NIST Webbook provides similar coefficients, but the relations used for deriving $\overline{H}$ and $\overline{C}_p$ are different. These are:

$$\left(\overline{H} - \overline{H}_{298.15\,K}\right)_{NIST} = a_1 \cdot t_T + a_2 \cdot \frac{t_T^2}{2} + a_3 \cdot t_T^3 3 + a_4 \cdot \frac{t_T^4}{4} - \frac{a_5}{t_T} + a_6 - a_8, \quad \text{where } t_T = \frac{T\,[\mathrm{K}]}{1000} \tag{3.12}$$

$$\overline{C}_{p,NIST} = a_1 + a_2 \cdot t_T + a_3 \cdot t_T^2 + a_4 \cdot t_T^3 + \frac{a_5}{t_T^2}, \quad \text{where } t_T = \frac{T\,[\mathrm{K}]}{1000} \tag{3.13}$$

It is to be noted that the molar enthalpy difference with regard to the standard temperature of 298.15 K is given. As such, this value (also called enthalpy of formation at standard conditions $\overline{H}_f^0$) is also needed to calculate the absolute value of $\overline{H}$, which is also taken from the NIST Webbook. This is included in Table A.4 in Appendix A. The NIST coefficients for liquid water and for nitrogen are included in Table A.2 and Table A.3, respectively.

The final temperature when exiting the heating chamber can either be set at a certain value, or set to be the saturation / vaporisation temperature T_{vap} (while assuming full vaporisation at the exit). In order to

calculate the vaporisation temperature from the set chamber pressure, the Clausius-Clapeyron relation [53] is used (reproduced from [54]):

$$T_{vap} = \frac{T_1 \cdot h_{vap} \cdot M_W}{T_1 \cdot R_A \cdot \ln\left(\frac{p_1}{p_c}\right) + \lambda_{lv} \cdot M_W} \tag{3.14}$$

Where $T_1 = 373.12\,\mathrm{K}$ is the vaporisation temperature of water at a pressure of $p_1 = 101\,325\,\mathrm{Pa}$ [55], and λ_{lv} is the latent heat of vaporisation of water at p_1 [55].

In order to calculate the ideal thrust force F_T, the following equation is used:

$$F_T = \dot{m} \cdot v_e + A_e \cdot (p_e - p_a) \tag{3.15}$$

Where v_e is the true exhaust velocity, A_e is the nozzle exhaust cross-sectional area, and p_e is the nozzle exhaust theoretical pressure. As such, p_e and v_e are required. p_e can be calculated using the implicit Equation 3.16, while v_e follows from Equation 3.17.

$$\varepsilon = \frac{A_e}{A_t} = \frac{\Gamma}{\sqrt{\frac{2\gamma}{\gamma-1} \cdot \left(\frac{p_e}{p_c}\right)^{2/\gamma} \cdot \left[1 - \left(\frac{p_e}{p_c}\right)^{\left(\frac{\gamma-1}{\gamma}\right)}\right]}} \tag{3.16}$$

$$v_e = \sqrt{\frac{2\gamma}{\gamma - 1} \cdot \frac{R_A}{M_W} \cdot T_c \cdot \left[1 - \left(\frac{p_e}{p_c}\right)^{\left(\frac{\gamma-1}{\gamma}\right)}\right]} \tag{3.17}$$

In order to estimate the mass flow rate losses due to friction, a comparison to the non-dimensional Reynolds number Re_t (at the throat) is to be used. The following definition is used:

$$\mathrm{Re}_t = \frac{\rho_t \cdot v_t \cdot D_{h,t}}{\mu_c} = \frac{\dot{m} \cdot D_{h,t}}{A_t \cdot \mu_c} \tag{3.18}$$

Where ρ_t is the density of the gas at the throat, v_t is its axial velocity at the throat, μ_c is the dynamic viscosity of the gas at the exit of the heating chamber, and $D_{h,t}$ is the hydraulic diameter of the throat. The same definition as used by [56] is employed here, which follows the ISO 9300 standard [57]. The hydraulic diameter is calculated as follows:

$$D_{h,t} = \frac{4A_t}{P_t} = \frac{2 \cdot w_t \cdot d_t}{w_t + d_t} \tag{3.19}$$

Where P_t is the perimeter of the throat cross-sectional surface, w_t is the width of the nozzle throat, and d_t is the depth of the nozzle throat. A rectangular cross-section is assumed.

The dynamic viscosity as a function of temperature is calculated using Sutherland's law [58]:

$$\mu = \mu_0 \cdot \left(\frac{T}{T_{0,\mu}}\right)^{3/2} \cdot \frac{T_{0,\mu} + S_\mu}{T + S_\mu} \tag{3.20}$$

Where μ_0 is the reference dynamic viscosity at reference temperature $T_{0,\mu}$, and S_μ is the Sutherland constant. Values for these are given in Table A.4.

3.3. Verification of the Model

Verification of the model is required to avoid any implementation mistakes. While this will not prove that the model can predict real values (which it inherently cannot, as it is based on ideal theory), it will prove that the formulae above are adapted correctly for future calculations and predictions.

Two verifications were performed: of the IRT part using two nitrogen datasets from Hutten's [56] and Versteeg's [59] master theses, and of the whole model using water datasets from Silva's PhD thesis [2]. For all calculations made in this section, it is assumed that the initial propellant temperature is T_{in} = 298.15 K (25 °C).

For the nitrogen datasets, the inputs are presented in Table 3.1, and the outputs in Table 3.2. Both datasets were used in the works of both Hutten and Versteeg, with the same inputs as presented in Table 3.1. These were chosen as they were among the few works that employed a straightforward and very similar model to that of the current author, while also providing enough data for verification.

These datasets were used by Versteeg to compare the experimental results of tests TTH-1.1 and TTH-4.1 to the model he had derived. Hutten then used these same inputs to verify his analytical model, comparing it to the ideal results of Versteeg. This work also uses these datasets for verification of the ideal outputs and Reynolds number calculation. As such, all three models should produce results as close as possible to each other.

Table 3.1: Inputs for the nitrogen verification datasets

Input	Dataset 1	Dataset 2
Propellant	N_2	N_2
T_c [K]	305.5	670.7
p_c [bar]	1.356	1.66
p_a [Pa]	184	209
d_t [µm]	496	496
w_t [µm]	142.34	142.34
ε [-]	7.53	7.53

Table 3.2: Outputs for the nitrogen verification datasets

Output	Dataset 1			Dataset 2		
	This work	Hutten	Versteeg	This work	Hutten	Versteeg
Ideal						
$F_{T,ideal}$ [mN]	15.46	15.45	15.4	19.03	19.02	19
$\dot{m}_{ideal}$ [mg/s]	21.77	21.78	21.8	17.87	17.87	17.8
$I_{sp,ideal}$ [s]	72.40	72.34	72.34	108.60	108.6	108.58
$\dot{Q}_{ideal}$ [W]	0.17	-	-	7.04	-	-
Expected						
Re_t [-]	3761	3641	4120	1789	1677	1820

As it can be seen, for the ideal parameters, the values are very close to each other, within rounding error. $\dot{Q}$ was not included in Hutten's or Versteeg's models. A more significant difference can be observed in the values for the Reynolds number between Versteeg's model on one side, and the models from this work and Hutten's, which arise from the fact that Versteeg calculated the Reynolds number using the throat viscosity. However, there is still a slight difference between the Reynolds numbers calculated by this work and Hutten, of 3–7%. This difference is expected to be from the way the viscosity is calculated, as it is the only parameter that does not appear in any other relation used to calculate the parameters that are close to each other. As Hutten did not explicitly explain how the viscosity is calculated, this reasoning cannot be fully verified. Nevertheless, the deviation is considered small.

For the water datasets, the inputs are presented in Table 3.3 and the outputs in Table 3.4. Silva [2]

used the measured values of some of the fabricated MEMS VLM thrusters, in order to predict their performance. The final temperature was set to the boiling temperature, with the assumption that full vaporisation takes place. The depth of the throat was assumed to be 100 µm, which is the average that Silva measured using a Dektak Surface Profiler. This was the only channel depth data present in his thesis.

Table 3.3: Inputs for the water verification datasets

Input	**Nozzle L**	**Nozzle W**	**Nozzle B**
Propellant	H_2O	H_2O	H_2O
T_c [K]	boiling	boiling	boiling
p_c [bar]	5	5	5
p_a [Pa]	0	0	0
d_t [µm]	100	100	100
w_t [µm]	25.1	26	20.1
ε [-]	19.49	29.91	24.51

Table 3.4: Outputs for the water verification datasets

Output	**Nozzle L**		**Nozzle W**		**Nozzle B**	
	This work	Silva	This work	Silva	This work	Silva
$F_{T,ideal}$ [mN]	2.18	2.16	2.29	2.27	1.76	1.75
$\dot{m}_{ideal}$ [mg/s]	1.90	1.91	1.97	1.97	1.52	1.53
$I_{sp,ideal}$ [s]	116.81	115.6	118.65	117.22	117.83	116.51
$\dot{Q}_{ideal}$ [W]	5.10	5.03	5.28	5.20	4.08	4.03

As it can be seen, the results are all close, with all values within 1.5%. These results, together with the results from the nitrogen datasets, verify the created analytical model.

3.4. Derivation of Estimated Efficiencies

Significant deviations are observed in literature between measured and ideal values. For this reason, in order to prepare for the test campaign, some estimates for the discharge coefficient C_d and heater efficiency η_h are derived from the experimental data of similar MEMS VLM microthrusters developed at TU Delft.

The experimental values will be taken from the works of Silva [2], Melaika [54] and Spernovasilis [18]. Using their conditions as inputs, the analytical model will calculate the ideal values of the performance parameters. From these and the measured data, the efficiencies can be calculated. The variations that are reported in this section represent one standard deviation (1 σ).

When calculating the heater efficiency, it has to be made sure that the decrease in mass flow rate shown by the discharge coefficient is taken into account. In this way, the ideal amount of heat flow required to heat up the propellant decreases by C_d. The heating efficiency can then be calculated as:

$$\eta_h = \frac{\dot{Q}_{real}}{P_{heater}} = \frac{\dot{Q}_{ideal} \cdot C_d}{P_{heater}} \tag{3.21}$$

Where $\dot{Q}_{real}$ is the heating power after applying the C_d correction, and $\dot{Q}_{ideal}$ is the ideal heating power as calculated using the inputs for the analytical model.

The data from Silva [2] is used to calculate both values for C_d and for η_h. The inputs, outputs and calculated values are included in Table 3.5. $\dot{Q}_{real,Silva}$ is the transfer heat flow as calculated by Silva, and is included for verification purposes only. The inlet propellant temperature T_{in} is assumed to be 25 °C.

Table 3.5: Measured VLM performance by Silva [2] and ideal conditions calculated with the analytical model.

Input				
Nozzle type	Nozzle L	Nozzle B	Nozzle L	Nozzle W
Thruster code	01-LS1-01	01-BS2-01	01-Ld1-01	01-WD2-01
Thruster no.	5	7	9	10
Propellant	H_2O	H_2O	H_2O	H_2O
T_c [K]	boiling	boiling	boiling	boiling
p_c [bar]	4.8	5.15	5.15	5
p_a [Pa]	101325	101325	101325	101325
d_t [µm]	100	100	100	100
w_t [µm]	23.1	16.5	20.9	23.6
Ideal output				
$\dot{m}_{ideal}$ [mg/s]	1.68	1.28	1.63	1.79
$\dot{Q}_{ideal}$ [W]	4.51	3.45	4.37	4.79
Re_t [-]	1927	1545	1886	2031
Measured by Silva				
$\dot{m}_{real}$ [mg/s]	0.55	0.75	0.83	0.61
P_{heater} [W]	7.29	8.76	8.19	7.72
Calculated by Silva				
$\dot{Q}_{real,Silva}$ [W]	1.47	1.99	2.21	1.62
Calculated				
C_d [-]	0.327	0.584	0.510	0.342
$\dot{Q}_{real}$ [W]	1.47	2.01	2.23	1.64
η_h [-]	0.202	0.230	0.272	0.212

Following these results, $C_d = 0.441 \pm 0.110$ and $\eta_h = 0.229 \pm 0.027$ are obtained. These are in the same range as what is observed in literature.

Melaika [54] does not provide dimensions for the thrusters that he has tested. As such, these are either taken from Silva [2], or from an Excel file found in the micropropulsion server at the faculty. Tests for thrusters without throat dimensions or with insufficient data are not included in the analysis. The inputs, outputs and calculated values are included in Table 3.6. All of these tests were done in ambient atmosphere ($p_a \approx 1\,\text{atm}$).

Table 3.6: Measured VLM performance by Melaika [54] and ideal conditions calculated with the analytical model. Datasets with the note NCD were not used for calculating C_d; idem for the note NPE for calculating η_h

Input								
Thruster code	01-BS2-01	01-BS2-01	01-Ld1-01	01-Ld1-01	01-Ld1-01	01-Ld1-01	01-Ws1-01	01-Ws1-01
Propellant	H_2O	H_2O	H_2O	H_2O	H_2O	H_2O	H_2O	H_2O
T_{in} [K]	321	321	321	322	305	328	319	319
T_c [K]	boiling	boiling	boiling	boiling	boiling	boiling	boiling	boiling
p_c [bar]	3.79	3.23	1.92	2.61	1.97	4.4	1.12	1.74
d_t [µm]	100	100	100	100	100	100	100	100
w_t [µm]	16.5	16.5	20.9	20.9	20.9	20.9	21.4	21.4
Ideal output								
$\dot{m}_{ideal}$ [mg/s]	0.96	0.82	0.63	0.85	0.65	1.40	0.39	0.59
$\dot{Q}_{ideal}$ [W]	2.46	2.10	1.60	2.16	1.68	3.57	0.97	1.49
Re_t [-]	1191	1039	812	1057	830	1650	520	761
Measured by Melaika								
$\dot{m}_{real}$ [mg/s]	0.14	0.28	0.14	0.28	0.42	0.55	0.14	0.42
P_{heater} [W]	2.20	2.80	2.60	3.20	4.35	4.30	2.30	3.40
Calculated by Melaika								
$Q_{real,Melaika}$ [W]	0.30	0.70	0.30	0.70	1.00	1.30	0.30	1.00
Calculated								
C_d [-]	0.144	0.337	0.219	0.326	0.640	0.396	0.358	0.704
Q_{real} [W]	0.355	0.708	0.349	0.703	1.077	1.411	0.346	1.049
η_h [-]	0.162	0.253	0.134	0.220	0.248	0.328	0.151	0.309
Note	NCD	-	-	-	NCD, NPE	-	NCD	NCD

Some of the datasets were not used for calculating the average C_d and η_h. The tests with thruster 01-Ws1-01 did not have a high enough p_c to respect Equation 3.5. As such, these were not used for calculating C_d. The test with thruster 01-Ld1-01 at $\dot{m}_{real}$ = 0.42 mg/s was stopped prematurely, and the true pressure was not reached. Additionally, the heater power does not follow the trend set by the other 3 tests with the same thruster, a fact mentioned also by the original author. As such, this dataset is used for neither C_d nor η_h. Lastly, the test with thruster 01-BS2-01 and $\dot{m}_{real}$ = 0.42 mg/s has a reported chamber pressure larger than the one reported for the same thruster at double the mass flow rate. This is contradicting the expected behaviour of the mass flow rate being proportional to the pressure, in accordance with Equation 3.7. For this reason, this test is not used for calculating the average C_d.

With the remaining datasets, the calculated averages for Melaika's tests are C_d = 0.319 ± 0.064 and η_h = 0.222 ± 0.072.

Spenovasilis [18] does not provide enough information on his thruster to calculate C_d. However, enough data is provided for calculating the heater efficiency. This, along with the outputs of the analytical model and the efficiency values, are provided in Table 3.7.

Table 3.7: Measured VLM heater performance by Spernovasilis [54] and ideal conditions calculated with the analytical model.

Input					
Propellant	H_2O	H_2O	H_2O	H_2O	H_2O
T_{in} [K]	298.15	298.15	298.15	298.15	298.15
T_c [K]	453.15	453.15	453.15	453.15	453.15
$\dot{m}_{real}$ [mg/s]	0.2	0.4	0.6	0.8	1
Ideal output					
$\dot{Q}_{real}$ [W]	0.55	1.09	1.64	2.19	2.74
Measured by Spernovasilis					
P_{heater} [W]	1.9	3	5	6	8.2
Calculated					
η_h	0.288	0.365	0.328	0.365	0.334

For all of these test, it is assumed that the initial propellant temperature T_{in} is 25 °C, and that the final chamber temperature T_c is 180 °C. Using these results, a heater efficiency of 0.336 ± 0.028 is calculated. This efficiency is about 1.5 times higher than the ones observed by both Silva and Melaika, showing the improvement of the heater design created by Spernovasilis.

For the final value of the expected C_d, both result sets of Silva and Melaika are used to calculate an average value. This is because they theoretically are from the same production batch, and should have similar properties. A value of 0.380 ± 0.108 is calculated, and will be used for the performance estimations of the new VLMs.

Regarding the heater efficiency, it was decided to go with the value as predicted from Spernovasilis' data. This is because the same heater design is used in the VLM design of this thesis. Furthermore, as far as the author can understand from the thesis report, the thrusters of Spernovasilis did not have microchannels, the heating chamber being one continuous parallelepiped. As such, a slightly better efficiency is expected from the current thruster.

3.5. Estimated Values for Operating Conditions

Using the analytical model verified in this chapter, together with the efficiency factors estimated in the previous section, the ideal and expected performance values can be calculated. Specifically, the mass flow rate $\dot{m}$, the heater power P_{heater}, and the thrust force F_T are reported. The conditions under which these values are calculated are:

- Propellant is water
- The initial temperature is $T_{in} = 25\,°C$
- The final temperature is the boiling temperature at the corresponding supply pressure. This will result in the minimum power required to operate the thruster with fully-vaporised flow
- The thruster is assumed to operate in imperfect vacuum, such that $p_a \approx 5.5$ mbar. In the thesis of Hutten [56], the value of p_a during water tests varied between 5.1 and 6.3 mbar, with an average value of 5.5 mbar. As the same vacuum oven and vacuum pump are to be used in future tests, this average value is considered representative.
- The supply absolute pressure p_c is varied from 1 to 6 bar (the maximum operational pressure mentioned by Singh [15])
- For the throat geometry, an ideal depth of 150 µm is assumed. The width is assumed ideal as well. As will be shown in the next chapter, there are multiple nozzle designs. For the purpose of these calculations, only the convergent-divergent (CD) nozzles are considered, which have the widths of 25 µm, 50 µm, and 75 µm.

- There are multiple CD nozzle designs, with in total 9 different expansion ratios, varying from 5 to 40. Specifically, there are 3 for the 25 µm throat width, 5 for the 50 µm, and 5 for the 75 µm. For each throat width, the thrust values for all relevant expansion ratios are calculated, and only the minimum and maximum are reported.

The results of the ideal calculations are shown in Table 3.8, and the estimated true values in Table 3.9.

Table 3.8: Ideal values of the expected performance of the VLM thrusters of this thesis. For the thrust values, the reported values are the maximum and minimum for a certain throat width, varying through the corresponding expansion ratios.

p_c [bar]	$\dot{m}_{ideal}$ [mg/s]			$\dot{Q}_{ideal}$ [W]			$F_{T,ideal}$ [mN]			T_{vap} [°C]
	25 µm throat	50 µm throat	75 µm throat	25 µm throat	50 µm throat	75 µm throat	25 µm throat	50 µm throat	75 µm throat	
1	0.61	1.21	1.82	1.57	3.14	4.70	0.58 – 0.61	1.18 – 1.22	1.78 – 1.83	99.6
2	1.18	2.36	3.54	3.10	6.19	9.29	1.25 – 1.26	2.39 – 2.52	3.58 – 3.78	120.4
3	1.74	3.48	5.23	4.61	9.22	13.83	1.91 – 1.92	3.59 – 3.82	5.39 – 5.73	133.7
4	2.29	4.59	6.88	6.12	12.23	18.35	2.56 – 2.58	4.80 – 5.12	7.20 – 7.68	143.6
5	2.84	5.68	8.51	7.61	15.22	22.84	3.21 – 3.25	6.01 – 6.43	9.01 – 9.64	151.7
6	3.38	6.76	10.13	9.10	18.21	27.31	3.87 – 3.92	7.21 – 7.73	10.82 – 11.60	158.6

Table 3.9: Estimated real values of the expected performance of the VLM thrusters of this thesis. For the thrust force, no nozzle corrections were applied. These values thus can be treated as maximums. Also for the thrust values, the reported values are the maximum and minimum for a certain throat width, varying through the corresponding expansion ratios.

p_c [bar]	$\dot{m}_{real}$ [mg/s]			P_{heater} [W]			$F_{T,est}$ [mN]			T_{vap} [°C]
	25 µm throat	50 µm throat	75 µm throat	25 µm throat	50 µm throat	75 µm throat	25 µm throat	50 µm throat	75 µm throat	
1	0.23	0.46	0.69	1.77	3.55	5.32	0.18 – 0.22	0.44 – 0.49	0.66 – 0.74	99.6
2	0.45	0.90	1.35	3.50	7.00	10.51	0.45 – 0.48	0.97 – 1.01	1.45 – 1.51	120.4
3	0.66	1.32	1.99	5.21	10.43	15.64	0.71 – 0.75	1.50 – 1.53	2.24 – 2.29	133.7
4	0.87	1.74	2.61	6.92	13.83	20.75	0.98 – 1.01	2.02 – 2.04	3.03 – 3.07	143.6
5	1.08	2.16	3.24	8.61	17.22	25.83	1.25 – 1.28	2.55 – 2.57	3.83 – 3.85	151.7
6	1.28	2.57	3.85	10.30	20.59	30.89	1.51 – 1.54	3.08 – 3.09	4.61 – 4.63	158.6

These values will be used for planning the future tests. Initial thrusting tests shall be done only up to 4 bar supply pressure, in order to not stress the system to its limits. If these are successful, the pressure could be further increased to 6 bar. However, for the thrusters with 75 µm wide throat, 4 bar is still the recommended maximum, in order to maintain the maximum power at around 20 W or less. The reason for choosing the 4 bar limit is explained in the following paragraphs.

Many of the adhesives that were considered at some point in the thesis have a maximum operational temperature of 150 °C, which means that operating the chip at higher temperatures risks the chance of the adhesives failing. However, estimating the corresponding maximum propellant temperature (and thus also maximum pressure level) is not straightforward.

For heat to transfer from the silicon wall to the propellant flow through convection, a temperature difference is required between the two. The required difference is very hard to estimate, as no reliable convection heat transfer coefficient data is available for the specific conditions of the TUD MEMS VLM for two-phase flow. Attempting to calculate this difference would be very time-consuming, outside the scope of this thesis, and would probably lead to inaccurate results (as the HTC is not known reliably).

The pressure at which the 150 °C limit would be reached, as if the propellant reached the same temperature as the silicon chip (corresponding to infinite HTC) is 4.8 bar. It was rather arbitrarily chosen to initially limit the operation to 4 bar, resulting in an allowable 6.6 °C difference between the propellant and the silicon wall temperatures. A better estimate should be made once further tests are performed, and the real behaviour of the thruster during operational conditions is known.

4 Manufacturing and Characterisation of the Thrusters

This chapter focuses on the updated fabrication process of the microthrusters, including an evaluation of the resulting thrusters. It begins with Section 4.1, by presenting the manufacturing and measurement equipment required for the fabrication and characterisation of the thrusters, as well as the measurement uncertainties relevant for this chapter. Then, the design of the thruster is detailed in Section 4.2. Next, in Section 4.3, the MEMS manufacturing steps and their modifications are included. Section 4.4 shows the issues that were encountered during manufacturing. In Section 4.5, the measured dimensions of the thrusters on the fluidic side are presented, as well as the surface properties. In Section 4.6, the dimensions of the heaters and their resistances are provided. The chapter ends with Section 4.7, where a summary of the chapter is made, and additional conclusions are presented.

4.1. Manufacturing and Measurement Equipment

In this section, the equipment used for manufacturing and measurement of the VLM is presented. The manufacturing equipment used at EKL is first shortly given as a list in Subsection 4.1.1, followed by the measurement equipment and the measurement uncertainties estimation in Subsection 4.1.2.

4.1.1. Manufacturing Equipment at EKL

The following equipment was used for the manufacturing of the vaporising liquid microthrusters at EKL in Cleanroom 100:

- Wet benches: These are benches with baths of different substances used for cleaning or etching wafers.
- EVG120: This is a system that has two functions: coating the wafers with photoresist before exposure, and developing the photoresist after exposure.
- ASML PAS5500/80 wafer stepper: This tool is used to expose the preferred features on the coated photoresist on the surface of a wafer. These features are exposed according to a layout programmed in the machine.
- Trikon Ωmega 201 plasma etcher: This is a device that etches (eliminates substrate material up to a certain depth) relatively shallow features on the surface of a wafer.
- PVA TePla GIGAbatch 360: This is a system that removes a photoresist layer that is no longer needed, using oxygen plasma.
- Novellus Concept One PECVD: This is a machine that deposits a thin layer of material on top of the surface of a wafer, using a process called plasma-enhanced chemical vapour deposition (PECVD).

- Trikon Sigma 204 sputter coater: This device is used to coat the surface of a wafer with a metal layer via sputtering.
- Rapier Omega i2L DRIE etcher: This machine is used to etch relatively deep features on the surface of a wafer, using a process called deep reactive ion etching (DRIE).
- AML wafer bonder: This is a device that sticks together two wafers made of silicon and alkali glass, respectively, through a process called anodic bonding.
- Wafer dicer: This is a machine used to dice the wafers using a water jet under pressure. As the process was not performed with the presence of the author, details on its operation are not known.

4.1.2. Measurement Equipment at EKL & AE and Uncertainty Estimation

Dimensional Measurements

The equipment that was used for dimensional measurements is given in Table 4.1.

Table 4.1: Tools used for performing physical and dimensional measurements on the VLM thrusters.

Tool	Description	Location	Usage
Keyence VK-X1000	Confocal scanning microscope	AE DASML	Optical imaging and laser surface imaging
Keyence VK-X250	Confocal scanning microscope	EKL Cleanroom 100	Optical imaging and laser surface imaging
JEOL JSM-7500F	Scanning electron microscope	AE DASML	Electron surface imaging
Veeco Dektak 8	Stylus surface profilometer	EKL Cleanroom 100	Contact surface measurement on one line
FR-Scanner Reflectometer	Spectral intensity reflectometer	EKL Cleanroom 100	Thickness measurement of SiO_2 and PR layers, among other uses

The Keyence microscopes are used for both 2D (in-plane) and 3D (out-of-plane) measurements. For in-plane measurements, the normal microscopic function of the devices is used. For 3D measurements, two modes are available: laser confocal measurements and focus variation measurements. Laser confocal microscopy works by emitting a laser focused on a small area of the sample. It detects the reflected laser from the sample, using "a pinhole to eliminate out-of-focus light coming from the sample" [60]. Focus variation microscopy uses low depth of field optics, which, through movement of the sample or optical system, find the best in-focus image for a certain height [61]. A 3D image is then created by stitching up these 2D images. These two methods can be used to complement each other, to obtain better imagery.

The JEOL JSM-7500F is a scanning electron microscope. It works by using an electron gun to produce an electron beam. This is then focused using a system of magnetic lenses, and also directed on the specimen using a scanning coil. Secondary electrons are emitted from the specimen upon the impact of the electron beam, which are then collected by the secondary electron detector and used to display an image [62]. This method has the advantages of achieving higher levels of magnification than optical microscopes, as well as a larger depth of field for the same magnification level.

The Dektak 8 is a stylus surface profilometer, which uses a stylus to measure the surface topography of the sample. The stylus is placed in contact with the sample, and is dragged across it to measure the local height. It uses a feedback mechanism based on the force required to keep the probe under a certain torque. The deflection of the tip is measured and transformed in a computer-readable signal [63].

The FR-Scanner Reflectometer is a spectral intensity reflectometer, used for measuring film thicknesses. It works by pointing a light source perpendicularly to the wafer surface, and measuring the intensity spectrum of reflected light [64]. Based on this measurement, and a pre-existing model for the spectral response of the material as a function of thickness, the layer thickness can be calculated by fitting the measurements to the model.

For proper reporting of the measured values, the measurement uncertainties need to be estimated for each of the tools used in performing the measurements.

There are multiple types of data that were obtained from this equipment. For the measurements that resulted in measuring distances based on an image (optical images from the Keyence microscopes, and SEM images), the uncertainty is estimated based on the number of pixels that the true dimension can vary from the real one. Assuming that s_u is the number of pixels that an edge of a linear dimension can vary by on either side of the true location, that d_{res} is the length that a pixel represents, and that σ_d is the final uncertainty in length units, this can be calculated using:

$$\sigma_d = s_u \cdot d_{res} \cdot \sqrt{2} \tag{4.1}$$

This equation makes use of the fact that a length measurement requires the correct placement of two points or edges, and thus the final measurement is the equivalent of the uncertainty of the addition or subtraction of the uncertainty of these points or edges. The uncertainty of the addition / subtraction of two values is $\sigma_c = \sqrt{\sigma_a^2 + \sigma_b^2}$ (according to Bell [65]), where σ_a and σ_b are the uncertainties of the other two values. As such, for a distance measurement, the uncertainty is that of a single point / edge times $\sqrt{2}$.

For each magnification at which measurements were made, the length (in µm) and resolution (in pixels or px) of the scale shown in the images is used to calculate d_{res}. For the Keyence microscopes, s_u was first assumed to be half of the width of a measurement line on the screen; this resulted in $s_u = 1$ px. However, during measurements it was observed that for some images, the inaccuracy could increase to 2 pixels; thus, this was used as the value for s_u. For the SEM images, s_u is assumed to be 2 px, due to the noise in the image which makes the edges of structures fuzzy. Exception is the 1000× magnification, for which, due to even more noise, $s_u = 4$ px. The results of the uncertainty calculations are summarised in Table 4.2 for the Keyence microscopes, and in Table 4.3 for the SEM.

Table 4.2: Measurement uncertainty for the optical measurements of the Keyence microscopes, for different magnifications.

Magnification	Scale resolution [px]	Scale length [µm]	$d_{\mathbf{res}}$ [µm/px]	s_u [px]	σ_d [µm]
2.5×	60	300	5.000	2	14.1
5×	126	300	2.381	2	6.7
10×	248	300	1.210	2	3.4
20×	480	300	0.625	2	1.8

Table 4.3: Measurement uncertainty for the measurements of the SEM, for different magnifications.

Magnification	Scale resolution [px]	Scale length [µm]	$d_{\mathbf{res}}$ [µm/px]	s_u [px]	σ_d [µm]
×130	138	100	0.725	2	2.1
×300	32	10	0.313	2	0.9
×400	42	10	0.238	2	0.7
×500	53	10	0.189	2	0.5
×550	58	10	0.172	2	0.5
×1000	106	10	0.094	4	0.5

For the Dektak 8 profiler, it was found from its manual [66] that the resolution of the measurements are 4 nm at a measurement range of 262 µm, 1 nm at a range of 65.5 µm, and 0.1 nm at a range of 6.5 µm. Furthermore, in [67] it is mentioned a step height repeatability of 0.75 nm (1 σ). The larger of these errors is considered to be the greatest source of uncertainty in the measurements. As such, for microchannel depths, this results in 4 nm uncertainty, while for thickness of the heaters, it gives 2.25 nm uncertainty (3σ). For the purpose of measuring the etching depths, it is considered that these errors are very low compared to the values being measured. As such, the values from the Dektak will be considered to be the true values for etching depths, and errors for these will not be reported further. However, for the thicknesses of the metal layers, an uncertainty of 2.25 nm will still be used.

For both of the Keyence microscopes, for the laser step height measurements, it was found in their datasheets [68, 69] that they have an accuracy of $0.2 + L/100$ µm, where L is the vertical measurement length in µm. This will be used for the estimation of the uncertainty measurements.

For the reflectometer, the most important measurement was of the thickness of the PR layer before DRI etching. As the RF-Reflectometer has a much better accuracy [70] than the parameters used for fitting the reflectance spectrum to the PR thickness, the uncertainty of its measurement is assumed to be half of the reading resolution, namely 0.05 µm.

Electrical Measurements
Besides the equipment used for the dimensional measurements, a multimeter was also required for testing the true resistances of the thrusters. For this purpose, the HP 34401A Multimeter (equivalent to the Keysight 34401A Multimeter) was used, present in the Space Engineering (SpE) workshop at the Faculty of Aerospace Engineering (AE).

According to its datasheet [71], measurements done in the 1000 Ω range have an accuracy of 0.01% of the full range, plus 0.001% of the measured value. These values correspond to a 1-hour warm-up time, with measurements done at 23 ± 5 °C and within 1 year after the last calibration. Using the above values, and knowing that no resistance larger than 150 Ω was measured, an accuracy of ±0.025 Ω is calculated. However, the 1-hour warm-up time was not always respected, and it is not known when was the multimeter last calibrated. As such, twice this value is taken as the measurement uncertainty, at ±0.05 Ω.

4.2. Design of the Thruster

The design of the thruster is almost identical to the one from the MSc thesis of Singh [15]. At the beginning of the thesis, it was believed that the fabrication of the thrusters is almost done, and that only adding the glass layer and dicing remained. As such, no significant effort was put into the design of the thrusters, as this was already done. However, when actually resuming the fabrication process, it was observed that the thrusters had some manufacturing defects, and that the whole process would need to be redone from the beginning. This meant that the design of the thruster could have been changed - however, there were some limitations regarding this.

When fabricated, the thruster is made up of component blocks called cells. When the desired layout is exposed by the wafer stepper on the wafer, these cells are stacked horizontally on a 2D pattern, realising the final design. The cells are custom-made on a mask, that is used for the manufacturing of all wafers in the same batch. As the ordering and manufacturing of another mask would prove to be both expensive and time-consuming, this option was eliminated early on in the manufacturing timeline.

As such, the only design changes that could be made would be the rearrangement of the cells in the overall layout. However, this also comes with a significant disadvantage: reprogramming the layout in the wafer stepper is very time-consuming, due to its old and unoptimised user interface. Additionally, it requires specialised staff. A significant point to consider is also that the more the layout changes compared to the original, the more time is required to recalculate all positions and reprogram the tool.

For the layout of the VLM wafers, the most time-consuming changes would have been to change the position of the thrusters, total thruster length, microchannel length, or heater number / position, as a change in one of them would require the recalculation and change of the others. Due to time constraints, this was considered off-limits. Because of this, one of the few acceptable changes that could be made was regarding the type of nozzles used, and their configuration among the thrusters. Additionally, the nozzles of some thrusters could also be replaced completely by empty fluidic sections. Lastly, the thrusters could also be redistributed on the wafer, but maintaining the overall layout. These were the only changes that were applied, as detailed near the end of this section.

As such, while few changes were made to the design, the fabrication process was further simplified, which will be explained further in the next section. This section continues by describing the design of the thruster, and the changes that were made compared to Singh's design.

The thruster has two sides – the front side (also called the heater side) and the back side (also called the fluidic side). The front side contains the titanium heaters that are used to heat up the propellant

in the vaporisation chamber. The heaters' design is directly adopted from the work of Spernovasilis [18]. He performed FEM studies to optimise the shape of the heater, such that an optimal temperature distribution is obtained. The result is shown in Figure 4.1. 8 heaters are included for each thruster, with a pitch of 1 mm.

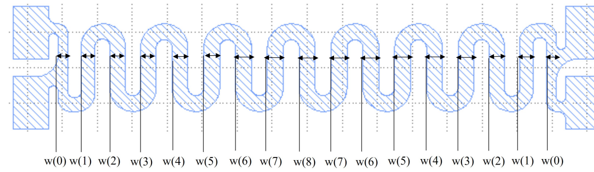

Figure 4.1: The design of the heater used in the current generation of VLM thruster. Image from [18].

Titanium was chosen due to its ability to resist high operating temperatures, and the fact that it is a semi-clean metal. The latter signifies that the wafers with the thrusters can be used in most of the cleanroom machines without special contamination control measured that contaminated / red metals (such as copper, platinum, etc.) would require. The connection pads are made out of aluminium, a common metal to be used for external connections on MEMS devices, and also a semi-clean metal.

On the back side, the following elements can be found: the entrance (also called the inlet of the thruster chip), the vaporisation chamber (which comprises 5 parallel serpentine microchannels), and the nozzle. The design of this side is modular in the sense that it consists of multiple 7 mm wide by 1.28 mm high cells placed on top of each other, to build up the thruster. The width of the thruster is thus also fixed at 7 mm, although this is not the width of the fluid region. Using these cells, different designs for the nozzles can be implemented, as well as for the entrance and for the microchannels.

The design for these elements and for the heater are imprinted on a mask, that is used by the ASML Wafer Stepper at EKL to expose the photoresist layer with the desired pattern. This is used for further etching or deposition steps. The VLM elements can be 1, 2, or 3 cells high. A diagram of these cells is shown in Figure 4.2 (obtained from [15]).

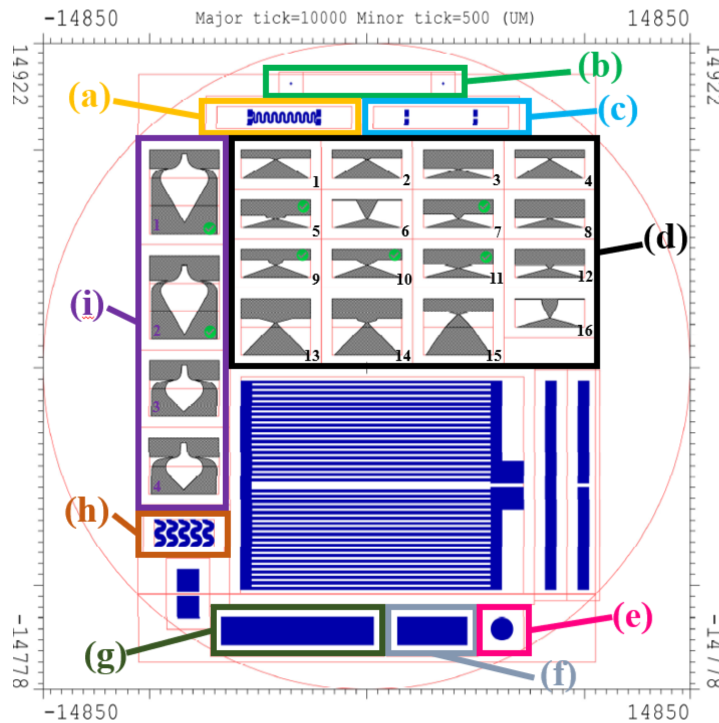

Figure 4.2: Diagram of the mask layout used for the microthruster fabrication. Image from [15]. The different sections used for the VLM are labelled using letters.

The different labelled areas on the diagrams are presented in the following list. The unmarked areas contain elements for the fabrication of a Low Pressure Microthruster (LPM), which is not the subject of this thesis.

(a) Titanium heater, in a 6 × 1 mm cell
(b) Dicing markers. Not used in the design of this thesis
(c) Aluminium bonding pads used for connecting the heater, in a 6 × 1 mm cell
(d) Convergent-divergent (CD) conical and bell nozzles
(e) Inlet hole used in a previous VLM design. Not used in the design of this thesis
(f) 3.2 mm wide by 1.28 mm high rectangle used for the entrance of the thruster Additionally, also used for thrusters without nozzle for the exit
(g) 7 mm wide by 1.28 mm high rectangle, the size of a full cell. Not used in the design of this thesis
(h) Serpentine microchannels, in a 5-parallel configuration. The cell contains two repeating sections per channel.
(i) Aerospike nozzles

The dimensions of a serpentine channel section are presented in Figure 4.3. The pitch of the parallel channels is 0.552 mm.

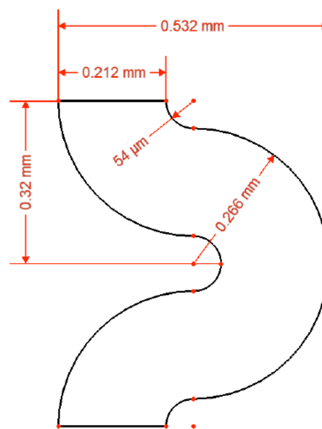

Figure 4.3: Dimensions of the serpentine microchannels used in the current generation VLM. Image from [15]

There are two main types of nozzles used: convergent-divergent (CD) nozzles, and aerospike nozzles. The CD nozzles are further split into conical and bell nozzles. The bell nozzles are just the conical nozzles, with a radius fillet applied at the exit, to mimic the profile of a true bell nozzle. All of these nozzles however are not true axisymmetric nozzles, but 2D planar reproductions of them with the same profile.

Compared to an axisymmetric nozzle, a 2D planar nozzle has sharp corners in its cross-section. These are locations where vortices can appear, disturbing the flow. Furthermore, a rectangular cross-section has a larger perimeter than a circular one, which increases the area affected by the boundary layer. Thus, it is expected that their performance is lower compared to their axisymmetric counterparts.

The designs for these nozzles were created by Singh [15]. However, as their dimensions were not fully reported in his thesis report, these were reproduced in Table 4.4, Table 4.5 and Table 4.6 for conical, bell and aerospike nozzles, respectively. The nomenclature for the dimensions is the one from Figure 4.4 for the CD nozzles, and from Figure 4.5 for the aerospike nozzles. It is to be noted that Singh defines the area ratio for the bell nozzles using the exit width of the conical version of the nozzle (without considering the exit radius fillet). This is corrected in the data reported in this thesis.

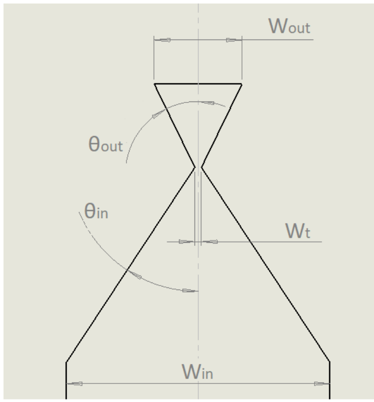

Figure 4.4: The design of the CD nozzles used in the current VLM generation. Image from [15]. The image represents a conical nozzle, but the same nomenclature is used for the bell nozzles.

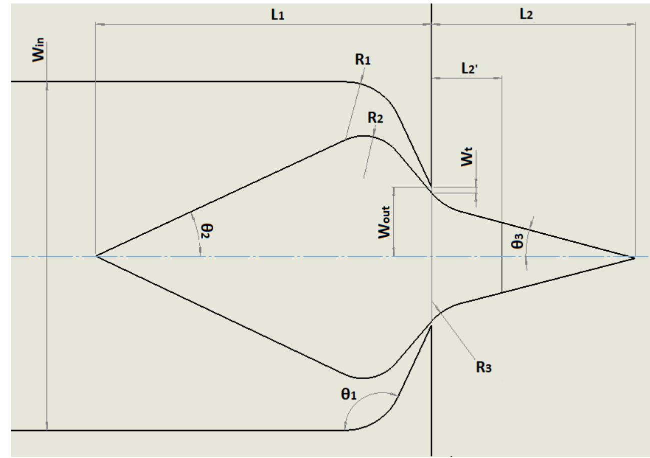

Figure 4.5: The design of the aerospike nozzles used in the current VLM generation. Image from [15].

Table 4.4: Dimensions of the conical nozzles on the fabrication mask. AR is area ratio. The notation corresponds to the one in Figure 4.4. Image no. is the numbering as presented in Figure 4.2. For all nozzles W_{in} = 3 mm. *For the throat, the ideal value is specified, while the value between parentheses is the actual value on the mask.

Mask name	**Image no.**	W_t* [µm]	θ_{in} [°]	θ_{out} [°]	**AR [-]**
ShortNozzle_1	(d) 1	50 (44)	60	75	10
ShortNozzle_3	(d) 3	50 (44)	75	75	10
ShortNozzle_4	(d) 4	50 (44)	60	55	5
ShortNozzle_6	(d) 6	25 (19)	75	30	40
ShortNozzle_7	(d) 7	25 (19)	75	45	20
ShortNozzle_10	(d) 10	50 (44)	70	60	20
ShortNozzle_11	(d) 11	75 (69)	75	75	20
ShortNozzle_12	(d) 12	75 (69)	75	45	5
LongNozzle_1	(d) 13	75 (69)	45	75	20
LongNozzle_3	(d) 15	75 (69)	35, then 45	75	15

Table 4.5: Dimensions of the bell nozzles on the fabrication mask. AR is area ratio. The notation corresponds to the one in Figure 4.4. r_{exit} is the radius at the exit of the nozzle, aimed to mimic a true bell nozzle shape. Image no. is the numbering as presented in Figure 4.2. For all nozzles W_{in} = 3 mm. *For the throat, the ideal value is specified, while the value between parentheses is the actual value on the mask.

Mask name	**Image no.**	W_t* [µm]	θ_{in} [°]	θ_{out} [°]	**AR [-]**	r_{exit} [µm]
ShortNozzle_2	(d) 2	50 (44)	60	75	6.4	32
ShortNozzle_5	(d) 5	75 (69)	75	75	12.4	99
ShortNozzle_8	(d) 8	75 (69)	75	75	6.4	47
ShortNozzle_9	(d) 9	50 (44)	70	60	13.6	159
LongNozzle_2	(d) 14	75 (69)	45	75	12.4	99
ShortNozzle_13	(d) 16	25 (19)	75	30	29.5	850

Table 4.6: Dimensions of the aerospike nozzles on the fabrication mask. AR is area ratio. The notation corresponds to the one in Figure 4.5. Image no. is the numbering as presented in Figure 4.2.

Mask name	Image no.	W_t [µm]	L_1 [mm]	θ_1 [°]	θ_2 [°]	θ_3 [°]
AeroSpike_1	(i) 1	25	2.5	100	30	5
AeroSpike_2	(i) 2	50	2.5	100	30	5
AeroSpike_3	(i) 3	25	1.5	100	45	5
AeroSpike_4	(i) 4	50	1.5	100	45	5

Mask name	W_{in} [mm]	$L_{2'}$ [mm]	W_{out} [mm]	R_1 [mm]	R_2 [mm]	R_3 [mm]
AeroSpike_1	3	0.66	1.5	0.5	0.45	0.6
AeroSpike_2	3	0.66	1.5	0.5	0.45	0.6
AeroSpike_3	3	0.66	1	0.5	0.425	0.35
AeroSpike_4	3	0.66	1	0.5	0.425	0.35

In order to create the final arrangement of the elements for the entrance, vaporisation chamber and nozzle, the cell arrangements need to be programmed in the wafer stepper. An example of such arrangement is shown in Figure 4.6 for the back / fluidic side. Figure 4.7 shows how the cells in the layout of the fluidic side correspond to the final design on the thruster. The example thruster is taken from the second row of the layout. Figure 4.8 shows the same, but for the cells on the heater side. As the design of the heater was taken from the work of Spernovasilis, they use a different cell size of 6×1 mm, instead of the fluidic side cell size of 7×1.28 mm.

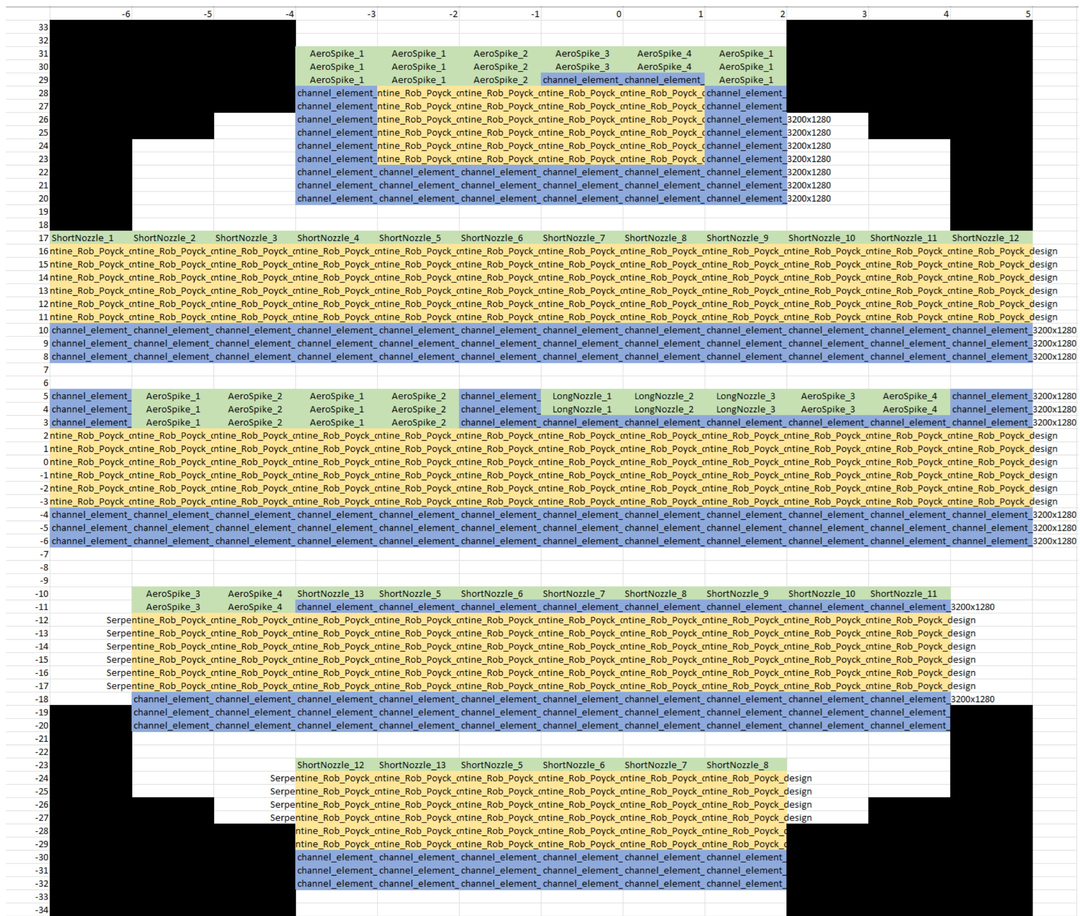

Figure 4.6: W01A wafer layout, with configurations rearranged for this thesis. Rearranged from the original design in [15].

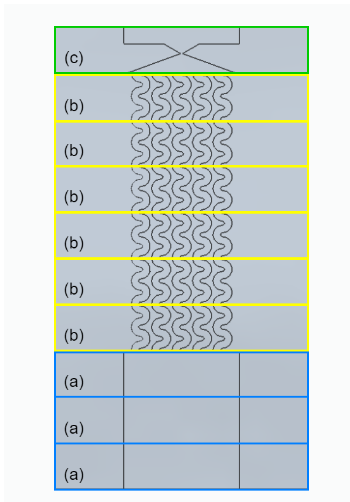

Figure 4.7: Cell arrangements for a thruster on the fluidic side. Cells marked with (a) represent `channel_element_3200x1280` (making up the entrance), with (b) `Serpentine_Rob_Poyck_design` (making up the vaporisation chamber), and with (c) `ShortNozzle_X` (which corresponds to a nozzle, and can have varying number of and different types of cells).

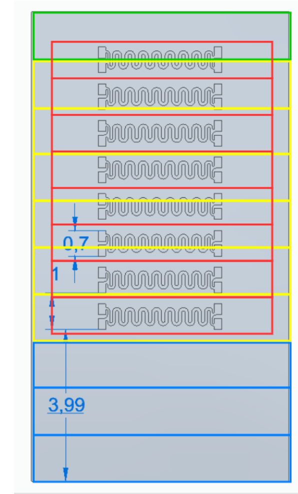

Figure 4.8: Cell arrangements for a thruster on the heater side. Heater cells (shown in red, with name `top_heater_George_Spernovasilis`) are 6 mm wide and 1 mm high, compared to the 7×1.28 mm cells of the fluidic side of the thruster (which are also shown as comparison, with the same colouring scheme as explained in Figure 4.7).

This is where a change compared to the design of Singh was made, in the arrangement and choice of configurations. Singh only used the nozzles ShortNozzle_7, ShortNozzle_10, ShortNozzle_11, ShortNozzle_5, ShortNozzle_9, AeroSpike_1, and AeroSpike_2 for the fabrication of the wafers. For this thesis, it was decided to fabricate all nozzle types. This allows future studies into the influence of the nozzle type and shape on thrust generation, instabilities, etc. Some nozzles appear more often in the layouts of the wafers, these being considered more scientifically interesting. The nozzles are distributed across all new created layouts relatively uniformly. This is to decrease the negative effect in case one wafer breaks during fabrication; in this case, one single design is not fully lost, and can be found also on the other wafers.

Another change to the layout is regarding thruster configurations without microchannels or without nozzles. For the former, Singh reserved one whole wafer, in order to study in the future the influence of having microchannels or not on the heat transfer capabilities. This configuration was retained, but the total number of thrusters using it was decreased.

The no nozzle configuration is new for this thesis, and is supposed to be used to connect both ends of the microchannels to an inlet/outlet. This is useful in determining the pressure drop over the channels, which is not possible when the nozzle is present. This is because a CD nozzle significantly decreases the pressure through its convergent-divergent design, making reading the pressure at the exit from the nozzle meaningless for the pressure drop over the microchannels. If the drop in pressure can be predicted reliably from this data, a more accurate description of ideal conditions in the nozzle flow can be given, based on the true pressure at the end of the microchannels. This in turn can lead to more accurate C_d and thrust efficiency estimations.

Another use is to study the possibility of the appearance of instabilities in the microchannels. As explained in Subsection 2.2.1, the steady-state pressure drop - mass flux relation is used in determining the operational conditions for the appearance of instabilities such as Ledinegg instability, density wave instabilities, and pressure drop instabilities. The most important are the density wave oscillations, which can lead to parallel channel instabilities. Therefore, if by studying the pressure drop - mass flux - heat flux relations, the findings in literature are also confirmed for VLM's microchannels, the phenomena can be thoroughly explained and perhaps contained. If this is not the case, other explanations could be searched for. The difference in assembly of this configuration without nozzle is explained in Chapter 5.

The new wafer layouts can be found in Appendix B.

4.2.1. Thruster Nomenclature

In order to avoid confusion, a standardised naming convention will be used for the thrusters in this thesis. There are three elements that make up the name of a thruster: the wafer number, the row, and the column.

There were 15 wafers initially prepared, from W01 to W15. On each wafer there are 5 rows. These are numbered from the top as C1 to C5. On each row, there is a variable number of thrusters / columns. As such, the numbering is done as if all columns were used, which is the case for rows R2 and R3. The columns are numbered from the left, from C01 to C12. For rows R1 and R5, the columns are from C04 to C09. For row R4, they are from C02 to C11. For rows R2 and R3, the full column set is used.

As an example, looking at Figure 4.6, the left-most thruster from the fourth row would be R4C02, as it is in the second column wafer-wide. Assuming that it is on wafer W01, its full code is W01R4C02. The leading zeroes in the code can sometimes be omitted; this however does not change the meaning of the numbers.

4.3. Manufacturing Steps and Modifications

In this section, the manufacturing steps in the Cleanroom 100 of EKL are presented. The latest fabrication flowchart (corrected and updated with the modifications in this thesis) can be found in Appendix C. These will be summarised here, with further emphasis being put on the changes to Singh's version - especially on the tuning of exposure energy and etching number of loops.

4.3.1. Complete Manufacturing Steps

The manufacturing steps are based on the ones followed by Singh and documented in his thesis [15]. In spite of this, as the process had to be restarted from the beginning, some modifications were made, aimed at trying to simplify the backside fabrication. While this attempt was a success, it required some slight recipe tuning. This however makes the process more straightforward for future manufacturing.

The steps are summarised graphically in Figure 4.9. They are presented shortly below, after the image. The base silicon wafer has a thickness of 300 ± 10 µm and a diameter of 100 mm.

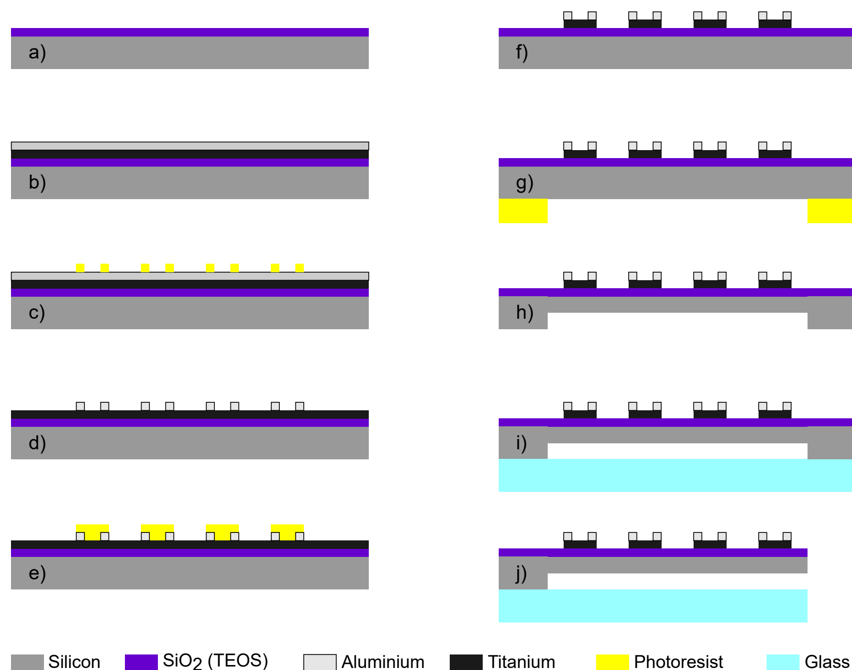

Figure 4.9: The main steps of the VLM fabrication process, shown as evolutions of the cross-sectional profile of the wafers. These steps are explained in more detail in the text. In this diagram, the front (heater) side is on top, while the back (fluidic) side is on the bottom.

The very first steps are required for most wafer fabrication workflows, and are not unique to the VLM. These are the steps for creating the alignment markers on the front side (also called the zero layer), which will be used to ensure a correct alignment of the wafer during further photoresist exposures. The first steps are the coating with positive photoresist, its exposure with the correct alignment marker layout, and the development of the photoresist. After inspection, the wafers are numbered using a glass pen. Then, the resulting pattern is etched using a plasma etcher, and the photoresist stripped.

The next steps are specific for the VLM, and are (using the nomenclature from Figure 4.9):

(a) Silicon oxide layer deposition on the front side. This has the role of electrical insulator between the titanium heaters and the silicon substrate. Plasma-enhanced chemical vapour deposition (PECVD) is used to deposit 500 nm of SiO_2 using TEOS (tetraethylorthosilicate), having the advantage of good uniformity [72]. The oxide thickness was then measured using an FR-Scanner Reflectometer. During the process of Singh, this was 456 nm. During the process described in this report, a layer thickness of 471 nm was obtained.

(b) Deposition of the titanium and aluminium metal stack for the heaters. 500 nm of Ti is deposited using a sputter coater, followed by 200 nm of Al (containing 1% Si)

(c) Coating, exposure, and development of negative photoresist with the correct shape and layout for the aluminium bonding pads.

(d) Wet etching of the Al layer in the surrounding area of the pads, followed by photoresist stripping.

(e) Coating, exposure, and development of negative photoresist with the correct shape and layout for the titanium heaters.

(f) Dry plasma etching of the Ti layer in the surrounding area of the heaters, followed by photoresist stripping.

(g) Coating, exposure and development of a thick layer of positive photoresist with the correct shape and layout for the entrance, microchannels, and nozzles, on the backside of the wafer. This layer acts as the mask for the silicon etching process.

(h) Deep reactive ion etching (DRIE) of the backside silicon to around 150 µm depth, followed by photoresist stripping. Optional depth measurements can be done at this step.

(i) Anodic wafer bonding of 525 µm thick borosilicate glass. This has the role of closing the fluidic path, as well as allowing optical observation of the flow through the channels and nozzle.

(j) Dicing of the individual thrusters from the wafer.

In total, 15 wafers were completely or partially processed. Of these, wafer 15 was a sacrificial wafer for testing and tuning the thick photoresist (PR) exposure and backside etching processed; it did not have the heaters fabricated on the front side. Wafers 1–7 were selected for full fabrication. Wafers 8–14 were held as a back-up batch in stand-by, in case the new design had issues, and an old design of the VLM might need to be fabricated. Wafers 8–14 were fabricated up to and including step 16 on the new flowchart.

One of the main changes compared to the process of Singh was the removal of using a SiO_2 layer deposited on the backside as mask for the DRIE of silicon channels. Instead, a thicker layer of PR acts as mask. While it has lower selectivity than using a SiO_2 mask, the 4 µm layer of PR was more than enough for etching 150 µm deep channels, as will be show in Subsection 4.5.2.

Another change was the removal of the application of protective photoresist on the heater side, to protect it and the SiO_2 electrical insulator from the DRIE of the channel side. As the removal of the hard SiO_2 mask on the channel side no longer took place (as it was not used in the first place), this PR layer was not needed any more.

These changes reduced the overall number of process steps from 45 to 39. Another more significant advantage is the elimination of certain fabrication issues reported by Singh [15], such as the unanticipated oxide deposition on the heater side from the channel side and the adhesion issues with protective photoresist.

However, as a new and thicker photoresist was used, this required tuning of the exposure energy and development recipe that were used.

4.3.2. Tuning of the Exposure Energy

Wafer 15 was used for the tuning of the exposure energy. Initially, one of Singh's layouts was used. The exposure energy was varied horizontally from 420 J/cm^2 to 585 J/cm^2 over the cells (which correspond to one thruster per horizontal cell), in steps of 15 J/cm^2. The focus offset was kept at −1 µm. The focus offset is important when a PR layer of significant thickness is applied and exposed.

After development using a single-puddle recipe, it was observed that the following thrusters had issues on the PR layer:

- Row 1: all thrusters
- Row 2: C1–C7 and C12
- Row 3: C1–C4 and C11–C12; C5 presented only slight issues
- Row 4: all thrusters
- Row 5: all thrusters

While a horizontal trend was seen, related to the variation of exposure energy, the main effect was on the area closer to the wafer edges, regardless of the exposure energy. After a discussion with the person responsible with the lithography room (Daniel van der Plaats), it was determined that the development process was the reason for these issues. As such, the development was changed from single-puddle to double-puddle.

Regarding the exposure energy, the row least affected by the edge effect was considered as reference (row 3). According to the cleanroom supervisor (Dr. Henk van Zeijl), the ideal exposure energy is around 50% higher than the one at which the defects no longer appear in the PR layer. Furthermore, he mentioned that for a double-puddle development, 2/3 of the exposure energy as for a single-puddle development is needed. On row 3, the thruster on column 5 seemed to be almost fully issue-free. As this thruster was exposed with 480 J/cm^2, it was calculated that the new ideal exposure energy is $480 \cdot 1.5 \cdot 2/3 = 480\,\text{J/cm}^2$.

To check this new exposure energy, the PR layer on wafer 15 was stripped and reapplied. The new W01A layout was exposed, again with a variable exposure energy, this time from 400 J/cm^2 to 620 J/cm^2, in steps of 20 J/cm^2. A double-puddle development was then used. After inspection, it was observed that the issues seen in the previous trial no longer appeared, even for the lower-than-ideal exposure levels. As such, a slightly lower than initially calculated exposure level was decided to be the standard for the exposure of the other wafers, namely of 450 J/cm^2.

4.3.3. Tuning of the DRIE Number of Loops

The same DRI etching recipe as used by Singh was also used for this thesis. However, as a new masking layer was employed, and possible other variations in manufacturing, it was decided that the required number of etching loops needs to be requantified.

DRIE (also known as the Bosch process) works by successive steps of passivation and etching. An illustration of these steps is shown in Figure 4.10 [73]. Once the shape has been slightly etched, passivation takes place, where octafluorocyclobutane (C_4F_8) is used to deposit a protection layer on the exposed surfaces of the wafer. Then, an anisotropic etch (called breakthrough) is performed using sulphur hexafluoride (SF_6), which etches the passivation layer on the bottom of the trench. Afterwards, the main isotropic etching takes place also using SF_6, which etches the main silicon layer. Anisotropy / isotropy of the etching is obtained by increasing / decreasing the platen power, which accelerates more/less the ions formed in the plasma. Once the main etching is finished, the cycle continues with a new loop of passivation–breakthrough–etching [74].

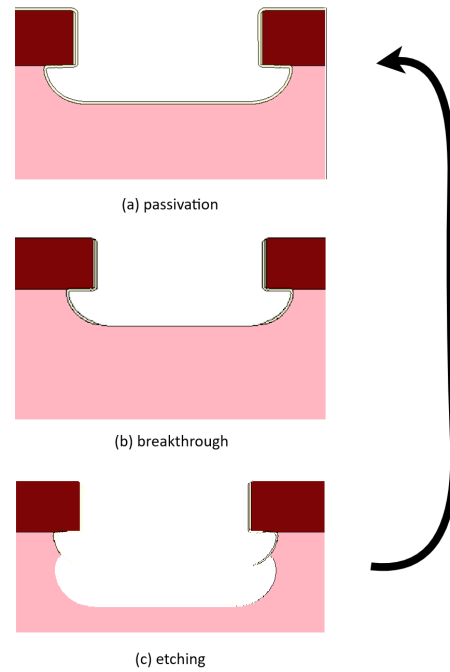

Figure 4.10: DRIE steps. Image adapted from [73], which was generated using Synopsys.

In the previous flowchart, an etching rate of 2.41 µm/cycle was mentioned, and was used to estimate an initial number of 62 cycles required to achieve 150 µm deep channels. This was used to etch wafer W15 (the tuning wafer), as well as the main batch wafers W1–W7.

After etching wafer 15, it was measured using a Keyence VK-X1000 confocal scanning microscope for the horizontal dimensions and depths of the thruster microchannels and nozzle throats in row two. This led to the observation of an almost-parabolic distribution of channel etching depth versus horizontal position of the thruster on the wafer, as can be seen in Figure 4.11. The average depth was 132.2 µm, below the required 150 µm.

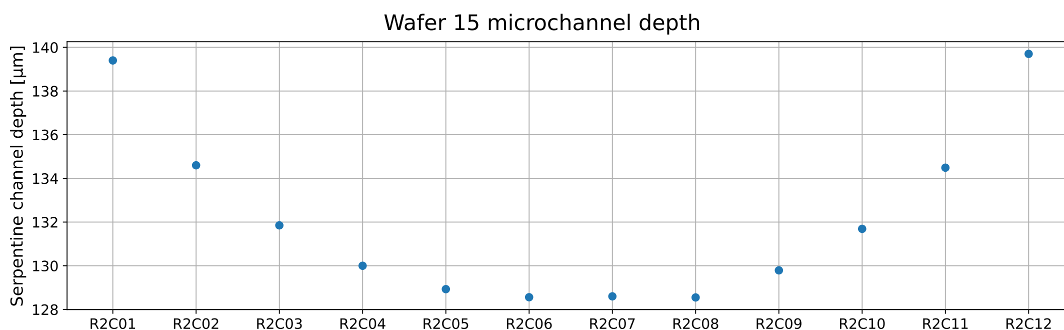

Figure 4.11: Microchannel depth on wafer 15 as measured on the thrusters from row 2.

Wafer 3, which had a constant exposure energy, was used for attempting to tune the etching process. This included both step height measurements using the Dektak 8 Surface Profiler, and the Keyence VK-X1000 confocal scanning microscope for etch depth. The estimation of the required number of loops encountered some issues, namely:

- The first Dektak 8 profiler measurements showed that the etching profile was much more uniform after 62 cycles (maximum deviation of ±0.6% compared to the mean) compared to the results found using the Keyence VK-X1000 (maximum deviation of ±5.2% compared to the mean). As the

Dektak is more accurate, it was considered that its results were the correct ones and were used for an initial estimation of loop number. However, in all later measurements, the Dektak also showed a parabolic profile with a maximum deviation of around ±5% compared to the mean for the depth of the microchannels. Therefore, this initial set of measurements is considered wrong.

- When measuring with the Dektak profiler, 3-point or 5-point measurements were usually done. This means that measurements were done in the middle, left, and right of the wafer, with the optional addition on the top and bottom. This is common practice in MEMS manufacturing. However, when calculating the average etch depth, this was overestimated, as the edge of the wafer had larger depths than the centre, which was also more uniform in its depth distribution.
- Some of the depth measurements were performed including the layer of photoresist, which was kept in case further etching was needed. As the selectivity between Si and PR was not known, it was assumed that around 2 µm were left after the first etch, and around 1 µm after the second. As it will be revealed, this is quite underestimated, and further contributed to estimation errors.

As a result, before comprehensive full-wafer measurements could be done, it was initially estimated that 10 more DRIE loops are required for reaching 150 µm depth, which were applied to wafer 3. After PR stripping this was partially remeasured, and after an overestimation of the etching rate in the last 10 loops, it was recalculated that only 7 more loops were needed versus the initial 62. As such, these extra 7 loops were applied to wafers 1, 2, and 4–7.

As wafer 3 was considered the send-ahead wafer to be bonded first, the measurements that could not be done after the glass wafer was bonded were performed. These were the depth measurements for the nozzle throat for all thrusters, and for the serpentine channel for one row and one column. Then, the wafer was partially bonded with a glass wafer, which had issues in sticking. It was then observed that the wrong type and thickness of glass was used, due to a mislabelling in the storage location. Due to these reasons, it was decided that a new wafer should be bonded and used for further processing, namely wafer 6. An attempt was made on unsticking the glass from wafer 3, but the latter partially broke in the process.

Due to time constraints, it was decided that remeasuring the depths of all thrusters nozzles and microchannels for wafer 6 was not practical. Adding to the fact that after the complete depth measurement of wafer 3, an average depth of 151.0 µm was calculated, it was decided that wafers 1, 2, and 4–7 be also etched 3 more loops to reach the same 72 loops as wafer 3. In theory, this should lead to the same depths on all wafers as on wafer 3. However, when checking this, it was observed that even though the total number of loops was the same, the depths on wafer 6 were around 6 µm to 11 µm smaller than on wafer 3.

This difference in etching depth between the two wafers could not be explained at the time. In spite of this, again due to time constraints, it was decided that some correction factors would be calculated for the depth, from some limited-in-scope measurements for the microchannels and nozzle throats. These would then be applied to the full set of depth measurements of wafer 3, to obtain the estimated true depths of wafer 6 (and the other remaining wafers, as they went through the exact same process was wafer 6). After wafer bonding and dicing, the horizontal dimensions of wafer 6 were also measured using the Keyence VK-X1000, through the glass layer.

4.3.4. Changes in Dicing

Another change was in the dicing process. As nozzles with different lengths were placed in the same row, dicing exactly where the exhaust of the nozzle is placed was no longer possible. As such, the dicing markers are no longer used, and the dicing is done at the edge of the nozzle images. These coincide with the edges of the thrusters. A visual guide on this step is provided on the last page of the fabrication flowchart, included in Appendix C.

A side effect of this change is that the exhaust of the nozzle will be partially constrained to a quasi-2D flow for a short distance. The effect of this on the performance is hard to quantify without CFD studies; however, it is believed to only slightly improve the performance, limiting divergence losses. Furthermore, the previous generation of VLMs had the same constraint at the exhaust, and no significant issues were reported because of it.

A further change in dicing is that the glass and silicon layers will be both cut at once in the same locations. This is contrary to the choice previously made by Singh to cut the layers differently at the inlet, by leaving the glass layer longer. This change was made due to a change in how the fluidic interface was designed, which is further detailed in Chapter 5.

4.4. Issues Encountered During Manufacturing

In this section, the issues that were encountered during manufacturing, and that were not already mentioned beforehand, are documented.

4.4.1. Contamination on Titanium Heater Photoresist

After the exposure and development of the titanium heater photoresist, it was observed that some of the wafers presented contamination on them, which looked like scratches to the naked eye. A comparison between an intact heater pattern in the photoresist and one where there was contamination is presented in Figure 4.12.

(a) Intact PR **(b)** PR with residue

Figure 4.12: Comparison between intact heater photoresist, and photoresist with residue from coating.

These residues were observed after coating and exposing the PR, and could be explained by some contaminants in the coater. However, this was not observed in other coatings before or after. Furthermore, it seems that the photoresist itself is the residue, and its application was faulty As such, the exact source is unknown.

The layer could have been stripped, reapplied, reexposed and redeveloped. However, due to time constraints, it was considered that while some heaters will not work, the loss is minimal. The following number of thrusters on each wafer were affected:

- Wafer 3: 6 thrusters
- Wafer 5: 1 thruster
- Wafer 6: 2 thrusters

As such, it was decided for wafer 3 to be the send-ahead wafer, followed by wafer 6.

4.4.2. Incomplete Titanium Etching

After the 500 nm titanium etch step, wafers 6 and 7 still had some titanium left near the edges. An example of wafer 7 with this effect can be seen in Figure 4.13. The whole surface of the wafer should have a uniform background colour of purple, which indicates that the top surface is a thin layer of SiO_2. However, in this image, there can be seen regions where the surface is silvery instead of purple, especially near the margins in the top, right, and bottom-right of the figure. This indicates that there are remains of unetched titanium.

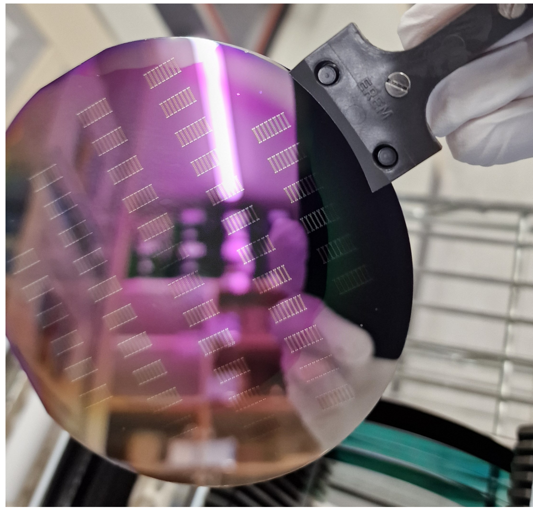

Figure 4.13: Ti layer incompletely etched on wafer 7.

This was corrected by re-etching the two wafers with a further 100 nm Ti etch recipe. This completely etched the remaining Ti near the edges.

4.4.3. Residue in Nozzle Image Exposure

After exposure and development of the thick backside photoresist, it was observed that there is a shape on the converging side of the nozzle ShortNozzle_1, as shown in Figure 4.14.

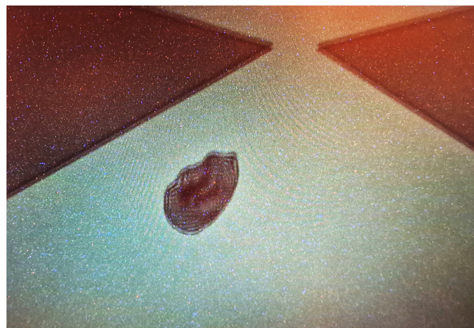

Figure 4.14: Mark seen on the converging side of ShortNozzle_1 in the photoresist layer.

This mark was observed also after etching, on both wafer 15 and wafer 3, as shown in Figure 4.15. The thruster from wafer 6 that had this nozzle was lost during the dicing process, and was not checked beforehand for this feature.

(a) W15R2C01 nozzle top-down view. Image captured with optical option of Keyence VK-X1000.

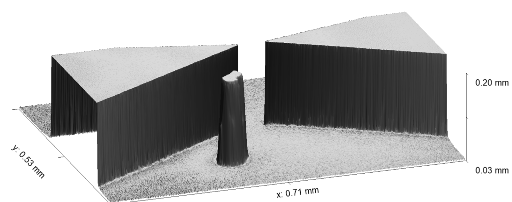

(b) W3R2C01 nozzle throat perspective view. Measurement done with laser option of Keyence VK-X250.

Figure 4.15: Etching leftover from mask debris of ShortNozzle_1.

It was deduced that there must be some residue on the photolithography mask, in the region of ShortNozzle_1, as this defect appeared consistently in the same spot. It is not considered crucial for the functioning of the thruster, especially being in the convergent part of the nozzle. However, its location close to the throat might affect the thruster performance.

As the thrusters were already exposed, and due to time constraints, it was decided not to investigate the issue further and clean the mask. As already mentioned, the thruster on wafer 6 that had this defect was broken during dicing. The mask could in the future be shortly cleaned with a nitrogen gun; however, this runs the risk of actually contaminating the mask more than it already is.

4.4.4. Needle-like Contamination

On wafer 3, after backside etching and PR stripping, needle-like debris was observed inside the etched regions. Some examples are included in Figure 4.16. The needles were observed at least in the W3R3C02 entrance, W3R4C02 nozzle exit, W3R2C02, W3R2C04, W3R2C11 serpentine channels entrance, and others. These contaminants were not observed in either wafer 15 or wafer 6. Their source is not known; however, as the other wafers do not seem to be affected, and as wafer 3 did not end up being used for the thrusters anyway, this issue was not investigated further.

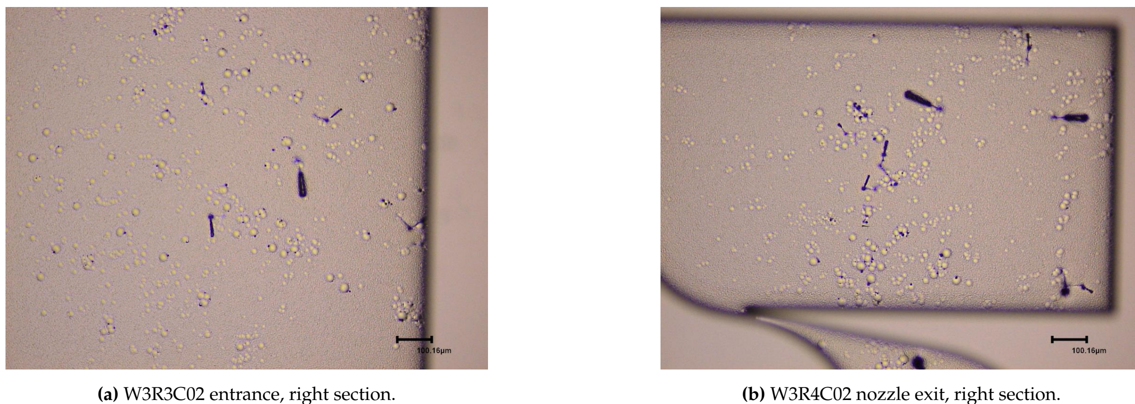

(a) W3R3C02 entrance, right section. **(b)** W3R4C02 nozzle exit, right section.

Figure 4.16: Needle debris present on wafer 3. Images captured with optical option of Keyence VK-X250.

4.4.5. Etching Artefacts in Wafers 3 & 6

When analysing the images captured for dimensional measurements of the thrusters, it was observed that the etched structures in wafers 3 and 6 contain some etching artefacts in the larger open-space regions, such as the inlet, nozzle (without throat), and entrances/exits to the microchannels. From top-down view, these appear as rounded inner contours of the original shape. Comparisons of the same thruster and nozzle on the different wafers can be seen in Figure 4.17 for laser imaging, and in Figure 4.18 for optical imaging. The lack of these artefacts (or the less severity of them) can be clearly observed in the thruster from wafer 15, compared to W3 and W6.

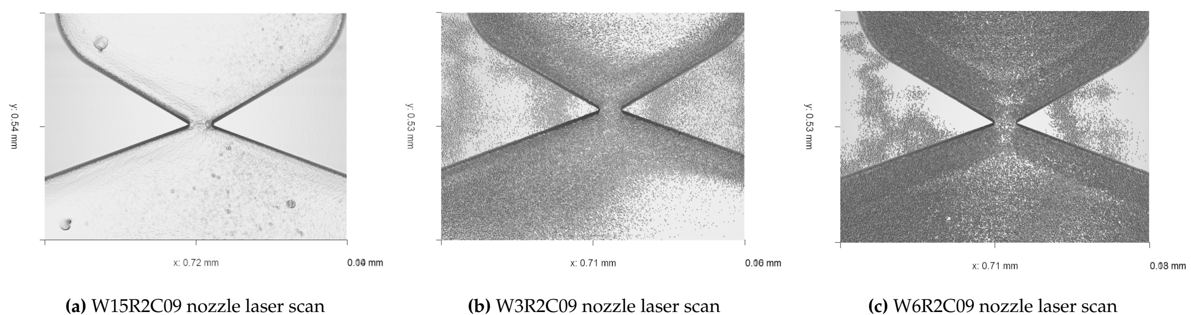

(a) W15R2C09 nozzle laser scan **(b)** W3R2C09 nozzle laser scan **(c)** W6R2C09 nozzle laser scan

Figure 4.17: Top down views of laser scans (including lighting) of thruster R2C09 from wafers 15, 3 and 6. The height features were scaled to 9× for better visualisation of the bottom surface. The scan was made using Keyence VK-X1000 for W15 and VK-X250 for W3 and W6.

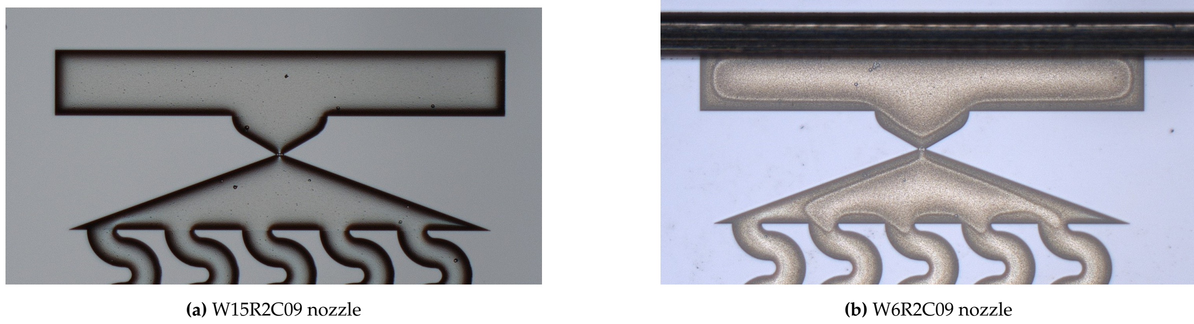

(a) W15R2C09 nozzle

(b) W6R2C09 nozzle

Figure 4.18: Nozzle overviews of thruster R2C09 from wafers 15 (without glass) and wafer 3 (with glass and diced). Optical images taken with Keyence VK-X1000 at 2.5× magnification.

For a better visualisation, the profiles from the laser measurements are given in Figure 4.19 for the same nozzle and wafers as above. Two horizontal profiles are given: one exactly through the throat, and one 120 µm above this line. The values that show a steep incline at the fluidic wall, raising from the bottom to the top, are artefacts of the measurement method using lasers operating in a top-down method. The actual profile has an undercut at those locations.

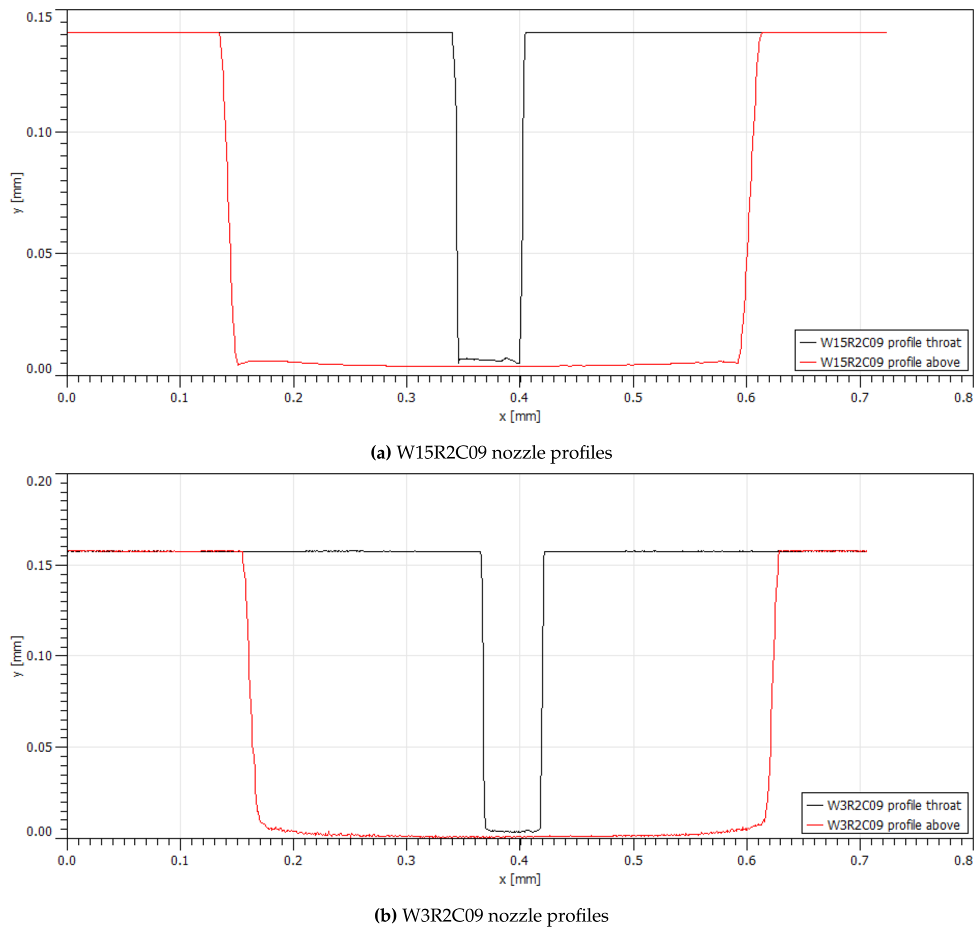

(a) W15R2C09 nozzle profiles

(b) W3R2C09 nozzle profiles

Figure 4.19: Horizontal height profiles of the nozzles of thruster R2C09 from the wafers W15, W3 and W6. One profile is taken exactly at throat level, while the other is taken 120 µm above the throat profile.

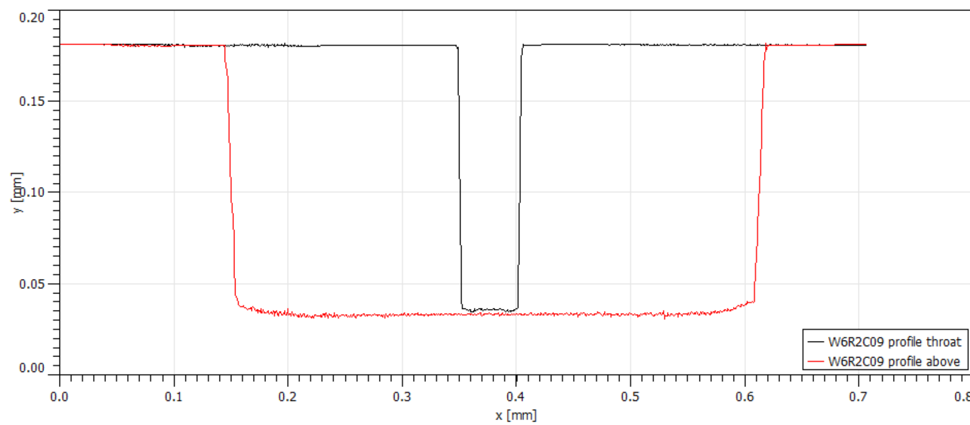

(c) W6R2C09 nozzle profiles

Figure 4.19: Horizontal height profiles of the nozzles of thruster R2C09 from the wafers W15, W3 and W6. One profile is taken exactly at throat level, while the other is taken 120 µm above the throat profile (cont.).

A clear difference on the profile of the bottom surface can be seen on the margins. On W15, a slightly convex shape can be observed near the margins, whereas on W3 and W6 at these locations a more rounded, concave shape is found. These are expected to continue also in the region affected by the measurement method (in the undercut region).

It is believed that this difference is caused by the stopping and restarting of the DRIE process. A thin layer of passivation material from the DRIE process can remain and affect some of the etching loops, resulting in a modified profile. This is visible with optical methods. Further study into this edge artefact was not prioritised, as the effects are expected to be minimal.

4.4.6. Handling Issues

Due to forgetting to align correctly the wafers W2, W4, W5 and W7 before developing the thick PR layer on the backside, an error occurred in the machine. Staff had to be asked to take the wafers out, and they were partially or totally re-developed. They were afterwards checked by Dr. van Zeijl and deemed to be correctly developed. However, this shows that it is important to always pay attention that all steps are followed correctly in operating any of the cleanroom machines. Furthermore, performing two tasks at the same time is discouraged, even if it seems that it might save time.

4.5. Fluidic Side Measurements

In this section, the dimensional measurements performed on the fluidic side of wafers 15, 3, and 6 are reported. Additionally, the surface properties are also studied.

4.5.1. Wafer 15 Measurements

For wafer 15, the most important measurements are related to the cross-sectional profile of the thrusters, specifically at the throat and at the microchannel entrance. These were done for wafer 15, as it was used as a sacrificial wafer to be cut before dicing, such that it fits in the SEM at the Aerospace Faculty. For both of the previously-mentioned profiles, a tapering effect was observed, where the wall of the etched profile is not perpendicular to the top and bottom surface, but at an angle, with the width increasing with depth. Pictures from the SEM showcase this effect in Figure 4.20.

Multiple attempts were made to measure this angle from the SEM images, using measurements of the different relevant dimensions. However, it was observed that the measurements are very inconsistent and outside the range of the expected uncertainty. For example, measuring the width of one microchannel at the entrance using the low magnification mode of the SEM, a value of 198.8 ± 0.7 µm was obtained. The same dimension, using the SEM mode of the same SEM microscope, showed a value of 238.8 ± 0.9 µm. Measuring this dimension with the optical VK-X1000 microscope, a value of 219.2 ± 1.8 µm was obtained. The design value was of 212.5 µm. It is considered that the SEM measurements are unreliable and diverge significantly from the expected values. For this reason, it was decided to not use them further.

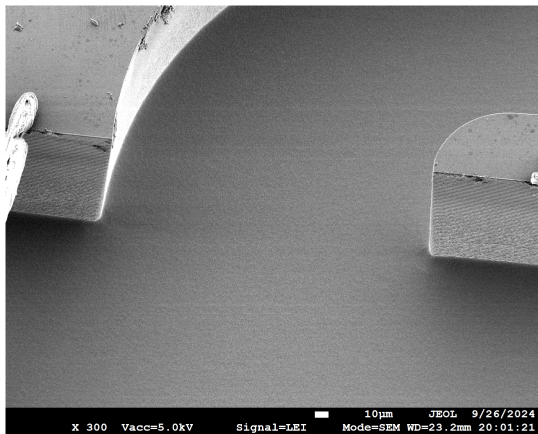

(a) W15R2C06 microchannel profile

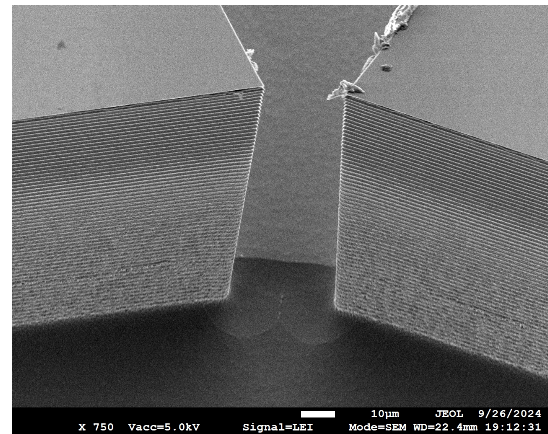

(b) W6R2C09 throat profile

Figure 4.20: SEM images of the profiles of the entrance to the serpentine microchannels and of the nozzle throat of thruster W15R2C06. The tapering effect of increasing width with depths is visible in both profiles. The samples are viewed at a 45° tilt.

Instead, it was attempted to use the Keyence VK-X1000 to visualise this profile. As the microscope had no inherent tilting mechanism, a holder for the thruster was 3D printed, to hold it at a 45° angle compared to the horizontal plane. A computer-aided design (CAD) model of it can be seen in Figure 4.21. Figure 4.22 shows how it was used on the microscope to observe the profile.

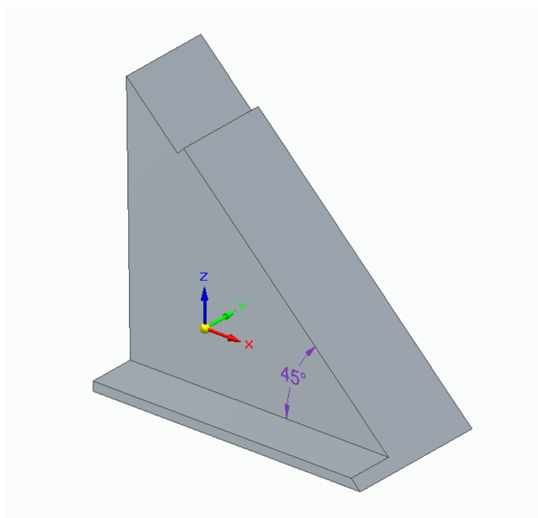

Figure 4.21: CAD model of the inclined holder for measuring the profile of the thruster.

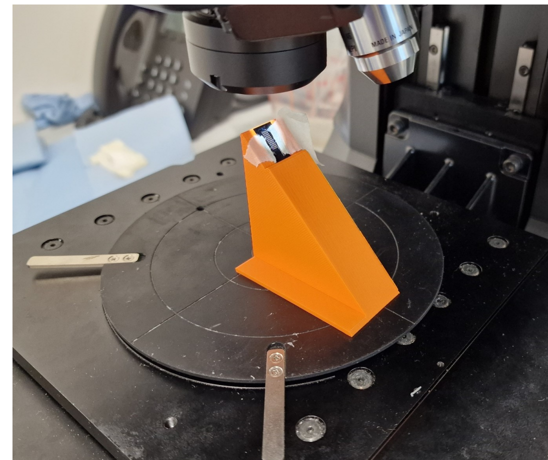

Figure 4.22: The inclined holder being used with the VK-X1000 microscope.

The holder is made from polylactic acid (PLA). After 3D printing, the inclination angle of the holder was checked with a protractor to be 45 ± 0.5°.

Some examples of the profile images generated using the VK-X1000 microscope for thruster W15R2C06 are presented in Figure 4.23 for the microchannels, and in Figure 4.24 for the nozzle throat. Acquiring a clear image was not straightforward, as the surface of the silicon is very specularly reflective. For the microchannels, it was found that using the purely optical mode with the HDR (High Dynamic Range) option enabled produced the clearest images, using focus variation. For the throat, a combination of the laser and optical measurements (using laser confocal scanning) produced the clearest images.

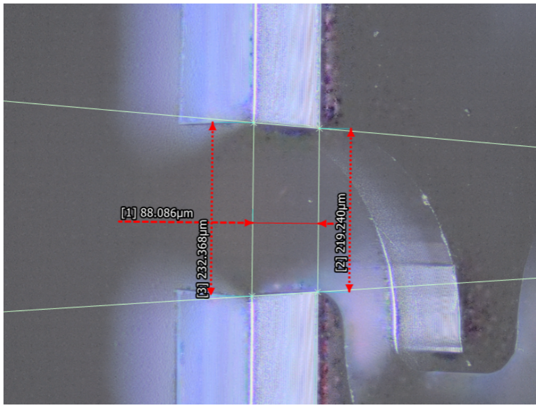

Figure 4.23: Optical focus variation image of the W15R2C06 microchannels entrance, using HDR mode. The thruster is tilted 45 degrees.

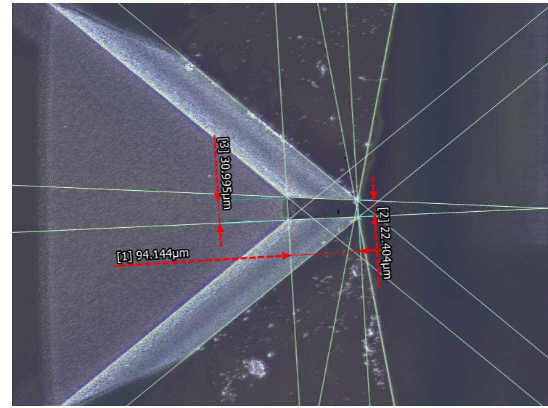

Figure 4.24: Laser confocal image of the W15R2C06 nozzle throat. The thruster is tilted 45 degrees.

Using similar images, the width at the top and bottom of the structures, as well as the height of the structures, were measured for three thrusters. From these, the slope angles of the taper (angle between the wall and the local vertical) were calculated. All of these results are presented in Table 4.7. The three thrusters were chosen to have different throat widths, to observe any difference in taper slope angle. For the measurements from these images, a pixel resolution of 0.707 µm/px was observed. As such, using Equation 4.1, and assuming a 2 pixel uncertainty in placing a point in the image, a distance measurement uncertainty of 2 µm is estimated.

Table 4.7: Measurements and results of the profile measurements from three thrusters of wafer 15.

Thruster Feature	W15R2C04 Microchannel	W15R2C05 Microchannel	W15R2C06 Microchannel	W15R2C04 Throat	W15R2C05 Throat	W15R2C06 Throat
Top width [µm]	219.5 ± 2.0	219.2 ± 2.0	219.2 ± 2.0	48.1 ± 2.0	77.6 ± 2.0	22.4 ± 2.0
Bottom width [µm]	232.8 ± 2.0	232.1 ± 2.0	232.3 ± 2.0	62.7 ± 2.0	100.1 ± 2.0	31.0 ± 2.0
Angled height [µm]	89.7 ± 2.0	88.4 ± 2.0	88.1 ± 2.0	95.4 ± 2.0	92.9 ± 2.0	94.1 ± 2.0
True height [µm]	126.9 ± 2.8	125.0 ± 2.8	124.6 ± 2.8	134.8 ± 2.8	131.4 ± 2.8	133.1 ± 2.8
Slope angle [°]	3.0 ± 0.6	3.0 ± 0.7	3.0 ± 0.7	3.1 ± 0.6	4.9 ± 0.6	1.8 ± 0.6

It can be observed that for the microchannel slope, the value is practically the same between the different thrusters, with an average of 3.0 ± 0.4°. For the throat, however, the slope angle varies, increasing from less wide throats (W15R2C06 has a nominal width of 25 µm) to wider throats (W15R2C04 has a nominal width of 75 µm). This shows that it is important to measure the slope angles for the different thrusters, and that specific values need to be used for each width.

Due to time constraints, more measurements were not performed to decrease the uncertainty in the slope, or to check if throats with the same widths have the same slope. As such, for the calculation of the average throat width of CD thrusters, the values corresponding to their widths will be used as derived in this subsection.

4.5.2. Wafer 3 Depth Measurements

Multiple measurements were taken for wafer 3 for the microchannels and nozzles, some of them erroneous. Only the measurements relevant for the final dimensions are recorded here.

Height measurements were done at the entrance of some thrusters on wafer 3, before and after stripping away the photoresists. These were done after 62 + 10 loops of DRIE. The results, including the calculated selectivity, are reported in Table 4.8. The initial PR layer thickness is assumed to be 3.8 µm, which was measured for wafer 15 using an RF-Reflectometer. As the RF-Reflectometer used for this purpose has a much better accuracy [70] than the parameters used for fitting the reflectance spectrum to the PR

thickness, the uncertainty in the initial layer is assumed to be half of the reading resolution, namely 0.05 µm.

Table 4.8: Inlet height measurements using Dektak 8 for W3 (62 + 10 DRIE cycles)

Location	Thruster	Depth with PR [µm]	Depth without PR [µm]	PR height [µm]	Etched PR [µm]	Selectivity
Left	R3C01	163.6	160.8	2.8	1.0 ± 0.05	161 ± 8
Centre	R3C07	150.9	147.9	3.0	0.8 ± 0.05	185 ± 12
Right	R3C12	162.6	159.8	2.8	1.0 ± 0.05	160 ± 8
Top	R1C07	-	150.5	-	-	-
Bottom	R5C07	-	158.9	-	-	-

A selectivity for Si/PR etching of 168 ± 14 (1σ) is calculated.

Some of the above-mentioned measurements done with the Dektak were repeated with the Keyence VK-X250 laser microscope, to observe if there are any differences between the two tools. The results are presented in Table 4.9.

Table 4.9: Comparison of depth measurements between Dektak and Keyence at different locations on W3.

Location	Thruster	Depth Dektak [µm]	Depth Keyence [µm]	Difference [µm]
Left	R3C01	160.8	162.4 ± 1.8	1.6
Centre	R3C07	147.9	149.4 ± 1.7	1.5
Right	R3C12	159.8	162.4 ± 1.8	2.6

For the above table, it is estimated that the Keyence measurements overestimate the height with 1.9 µm compared to the Dektak measurements, which are considered to be very close to reality. The first two measurements fall within the estimated uncertainty of the Keyence laser measurements. However, the last one overshoots this uncertainty by 0.8 µm. As such, the uncertainty of the laser step height measurements might be higher than reported by the datasheet. However, not enough measurements were taken to make a better estimation. For this thesis, the $0.2 + L/100$ µm formula for accuracy will be kept.

The depths of the microchannels were also measured with the Keyence VK-X250 and are reported in Table D.1. Similarly, the depths of the nozzle throats are reported in Table D.2.

As a quasi-parabolic depth profile was observed in wafer 15, it was attempted to predict the distribution of the depth based on the radial positioning from the centre of the wafer. As such, from the depth-versus-radial position data, the best fit of an even fourth-order polynomial was attempted, of the form:

$$d(r) = a_0 + a_1 \cdot r^2 + a_2 \cdot r^4 \tag{4.2}$$

Where $d(r)$ is the etch depth as a function of radial positioning r, and a_0, a_1, and a_2 are the fitting parameters.

This function was chosen based on previous profiles reported in literature [75], where a symmetric distribution was also observed. This requires only even-powered terms in the polynomial. Furthermore, adding a fourth order term to the initial parabolic function is required to better emulate the uniformity of the etching depth observed near the centre of the wafer, both during this thesis and in the literature [75].

Using this function and the measured depths of the microchannels in the horizontal and vertical data sets, the fits as shown in Figure 4.25 were obtained.

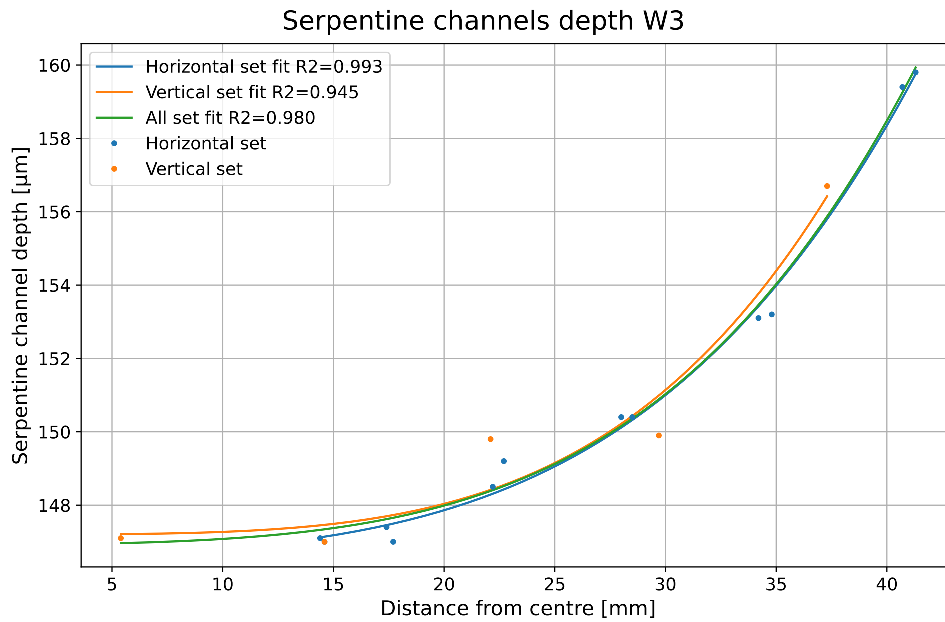

Figure 4.25: Polynomial fits of the microchannel depths on wafer 3.

Very good fits are obtained, with an R^2 value of 0.98 when using all the available data. This confirms the expected depth distribution, and shows that it can be predicted relatively well from a few measurements on the wafer.

The same procedure is repeated also for the measured depths of the throats, but dividing the fits by nozzle type (CD versus AS) and throat widths. The results are plotted in Figure 4.26, alongside the microchannel best-fit. For some of the least-squares fits, some of the fitting parameters had to be forced to be positive to maintain a physical expectation of the etching depth increasing with radial distance from the wafer centre. These were a_1 for CD 25 and AS 25, and a_2 for CD 50 and CD 75.

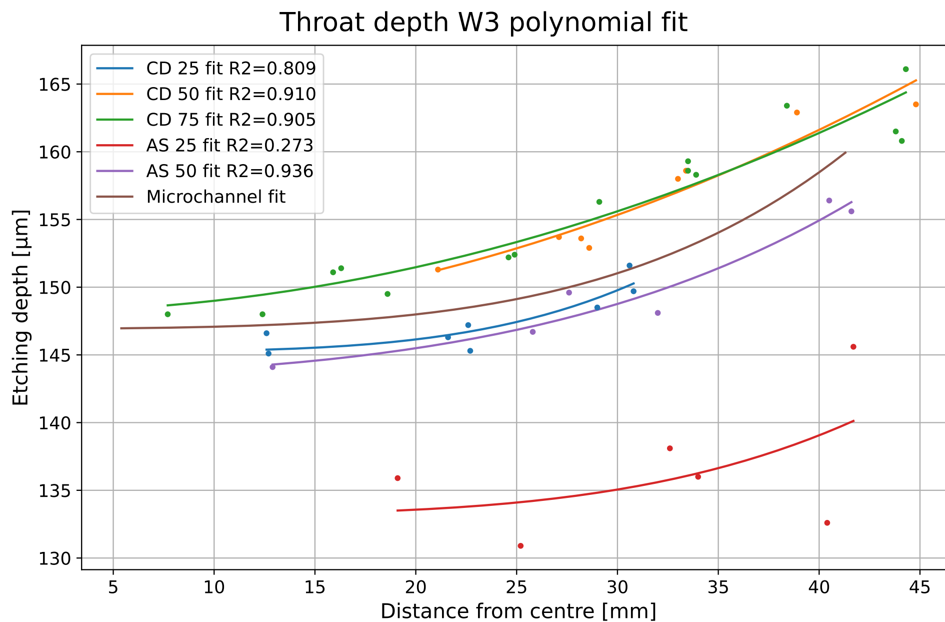

Figure 4.26: Polynomial fits of the depths of different nozzle throat types and width on wafer 3, alongside the best-fit from the microchannels. The dots represent measured values, while the lines are the least-squares fits. CD means convergent-divergent nozzles, while AS mean aerospike nozzles. The 25, 50, and 75 numbers represent the design throat width in µm.

As it can be seen, relatively good fits are obtained for the throats with widths of 50 µm or more, with R^2 exceeding 0.9. An acceptable fit of R^2 = 0.809 is obtained for CD 25, showing that it follows the general trend, but that it cannot be accurately predicted with this formula. AS 25 has a very low R^2 value, indicating that while a general trend of increasing depth with radial distance can be seen, the variation in depth makes it impossible to catch with a polynomial.

Another important finding is that, on average, the etching depth increases with throat width, this effect plateauing between 50 µm and 75 µm. This variation is very apparent for the aerospike nozzle, with a large difference in depths between the two widths. This might be explained by the fact that the flow of the etching gases in the aerospike throat is more constrained, being fully open on one side, but in an almost-constant width section on the other. This is not the case for the CD nozzles, which have almost-fully open regions on both sides of the throat, which can concentrate the flow of gases in the throat.

It is also interesting to note that the depths of the larger CD nozzles are bigger than for the microchannels, even if the latter have the larger widths by a factor of 3 or 4. This might also be explained by the concentration of etching gases in the throat region due to the CD nozzle shape.

The previously-described effects of structure geometry on etched depth is mentioned in literature as aspect ratio-dependent etching effects. These are very hard to quantify and predict for complex geometries, and are usually observed experimentally.

4.5.3. Comparison Between Wafers 15, 3, and 6 Etch Depth

Measuring all the depths of the thruster microchannels and nozzle throats is very time-consuming. It is also expensive, as it requires performing the measurements inside the EKL Cleanroom 100, as these need to be done before the glass wafer is bonded to the silicon base. The cleanroom hours per project are paid, and are limited. Furthermore, if one wafer becomes unusable during assembly (as was the case of W3), measurements would need to be redone for all thrusters on a new wafer (if etched differently) or for the thrusters that are different in the new etched configuration.

For these reasons, when W3 was bonded with the wrong glass and chipped when attempting to unstick it, it was decided to not redo all of the measurements on wafer 6, as this would require further time which was not available due to time constraints. Only measurements of the microchannel and throat depths for 6 thrusters were performed. These were then compared with their equivalent from wafer 3. Ideally, identical values would have been found, as both were etched 72 DRIE cycles in total. However, as slight but consistent differences were observed, some correction ratios were calculated for the microchannel depths and for the depths of the three different nozzle throat widths. As these measurements on W6 were done only on CD nozzles, the same factors are applied to the AS nozzles [with the same corresponding (single) throat width]. The results of these measurements and the correction factors are shown in Table 4.10 for the microchannels, and in Table 4.11 for the nozzle throats.

Table 4.10: Comparison between W3 and W6 microchannel depths.

Thruster	Depth W6 [µm]	Depth W3 [µm]	W6/W3 ratio [-]
R2C07	138.3	147.1	0.940
R2C08	138.4	147.4	0.939
R2C09	139.5	148.5	0.939
R2C10	141.0	150.4	0.938
R2C11	143.2	153.1	0.935
R2C12	148.2	159.4	0.930

Table 4.11: Comparison between W3 and W6 nozzle throat depths.

Thruster	Nozzle type and width [µm]	Depth W6 [µm]	Depth W3 [µm]	W6/W3 ratio [-]
R2C07	CD 25	140.9	147.2	0.957
R2C08	CD 75	143.6	152.2	0.943
R2C09	CD 50	145.3	153.6	0.946
R2C10	CD 50	149.5	158.0	0.946
R2C11	CD 75	152.7	163.4	0.935
R2C12	CD 75	155.3	166.1	0.935

The following correction factors are calculated (deviation is 1 σ):

- For microchannel depth: 0.937 ± 0.004
- For 25 µm width throat depth: 0.957 (only one measurement was done)
- For 50 µm width throat depth: 0.946 ± 0.0002
- For 75 µm width throat depth: 0.938 ± 0.005

These correction factors will be applied to the depth measurements of wafer 3 to obtain the expected depths of wafer 6, which will be documented in the next subsection.

The average etch rate of the microchannels was calculated from the directly-measured values of thrusters R2C07 to R2C12 for wafers W15, W3, and W6. For wafer 15, an average etch rate of 2.13 µm/loop was obtained, similar to W3's 2.10 µm/loop rate. However, W6 shows a significant decrease to 1.96 µm/loop, even though it has the same total number of loops as W3. All three wafers were first etched with 62 DRIE loops, although not at the same time. Then W3 was etched with another 10 loops. Lastly, W6 was etched 7 more loops after the initial 62, and then another 3.

After a discussion with Dr. van Zeijl, it was hypothesised that this decrease in etching performance can be caused by either the calibration of the etcher, or by the underperformance of initial loops in one etching step.

The DRI etching process was delayed during the fabrication of the wafers, as the etcher was out of service due to some malfunctions. This required recalibration by the tool owner, which could have modified some parameters since the tool was last used. Furthermore, as the etching steps were done a few days or weeks apart, further recalibrations of the tool might have occurred. More etched material could have also accumulated on the electrodes of the etcher through time, which would decrease its performance.

Regarding the underperformance of initial loops, the etcher requires a certain start-up time to reach the specified power. This can result in the initial etching loops either not etching at all (so-called dead loops), or to underperform. This could also partially explain the decrease in performance when restarting the process once (W3) or twice (W6), compared to no restart (W15).

As the exact source of this deviation is not fully known, it is highly recommended in the future to etch wafers in one go, with no restarts. As such, the etching rate of W15 of 2.13 µm/loop is to be used for calculations. To achieve an average depth close to the design value of 150 µm, 70 loops would be needed, which would result in an average depth of 149.1 µm.

4.5.4. Wafer 6 Measurements

In this subsection, the complete set of measurements done on wafer 6 is presented. This includes optical measurements (for horizontal dimensions), as well as calculated laser measurement depths, using the data from W3 and the previously-mentioned correction factors. All of the horizontal measurements on this subsection represent dimensions at the top surface of the silicon wafer, unless noted otherwise. As the etching profile is not straight, this value varies with depth, as demonstrated in Subsection 4.5.1.

Depth Measurements & Predictions

For the etching depth of the microchannels and nozzle throats, only the values for thrusters W6R2C07 to W6R2C12 were directly measured. The rest were calculated using the W6/W3 ratio, as computed in the previous subsection. As such, these are mostly estimates. However, they are still useful to determine the expected behaviour of the thrusters, as the true values can no longer be measured with the laser microscope. the measured and estimated depth values are reported in Table D.3 for the microchannels, and in Table D.4 for the nozzle throats.

From these values, similar fits to the ones for wafer 3 are done for the microchannel and throat depths. For microchannels, these are presented in Figure 4.27, while for the throats in Figure 4.28.

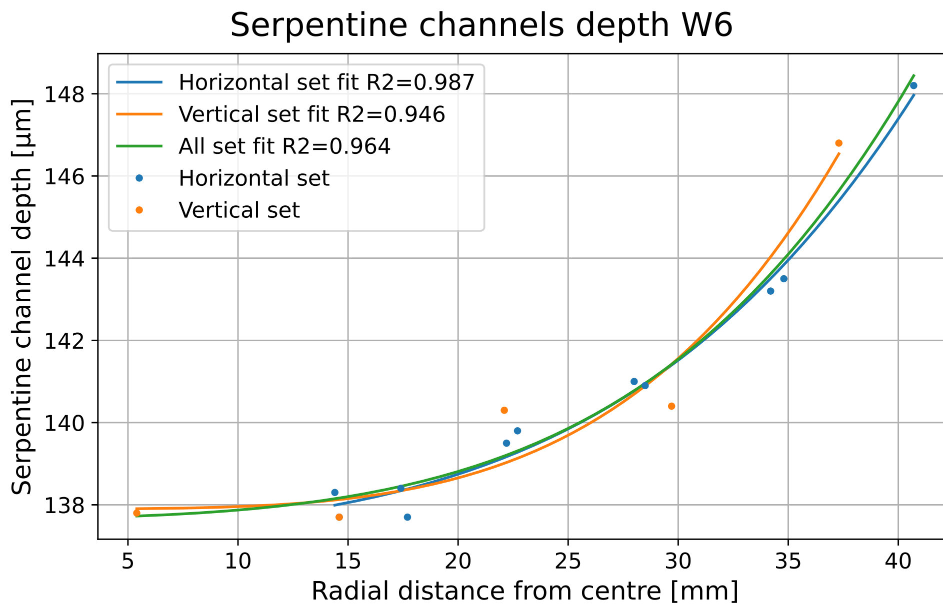

Figure 4.27: Polynomial fits of the microchannel depths on wafer 6 from measured and estimated values.

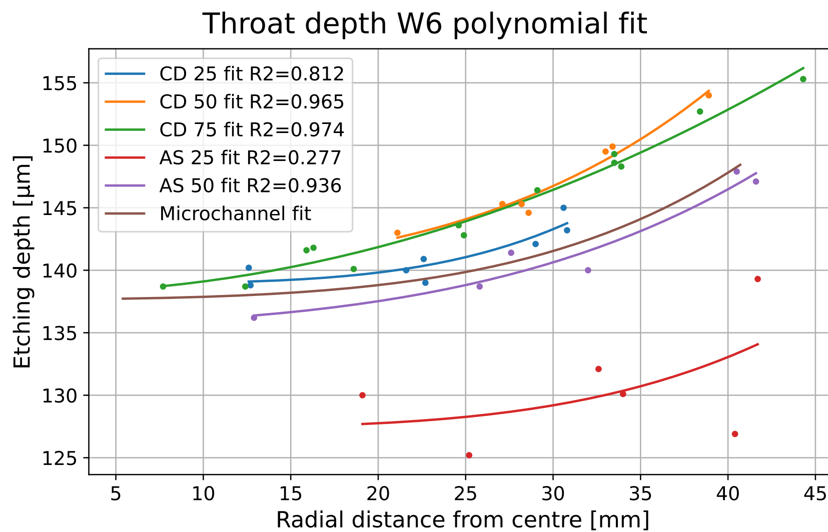

Figure 4.28: Polynomial fits of the depths of different nozzle throat types on wafer 6, alongside the best-fit from the microchannels. The dots represent measured or estimated values, while the lines are the least-squares fits. CD means convergent-divergent nozzles, while AS mean aerospike nozzles. The 25, 50, and 75 numbers represent the design throat width in µm.

The fits follow very similar trends, with good R^2 values of more than 0.9 for the microchannels, CD 50, CD 75, and AS 50 least-squares fits, an acceptable value of 0.8 for the CD 25 fit, and lack of correlation

for the AS 25 fit. This similarity is expected, as the W6/W3 correction factors were used to estimate most of the values reported in the plots, especially for the throats, thus only scaling their magnitude. A difference though is that the CD 25 depth is estimated now to be on average higher than that of the microchannels.

Horizontal Dimensional Measurements

The in-plane surface horizontal dimensions were measured directly using the VK-X1000 microscope, after the glass was bonded on top. This did not impede the measurements. The obtained values are reported in Appendix D, in Table D.5 to Table D.9. Furthermore, the average throat width is also estimated using the measured surface width, the estimated depth, and the estimated taper slope angle, as explained in the appendix. The obtained values are given in Table D.10.

For the horizontal dimensions, only the deviations compared to the design values are reported. No significant variation with radial location on the wafer was observed. Box plots of the relative difference for the different measured and estimated dimensions, are given in Figure 4.29.

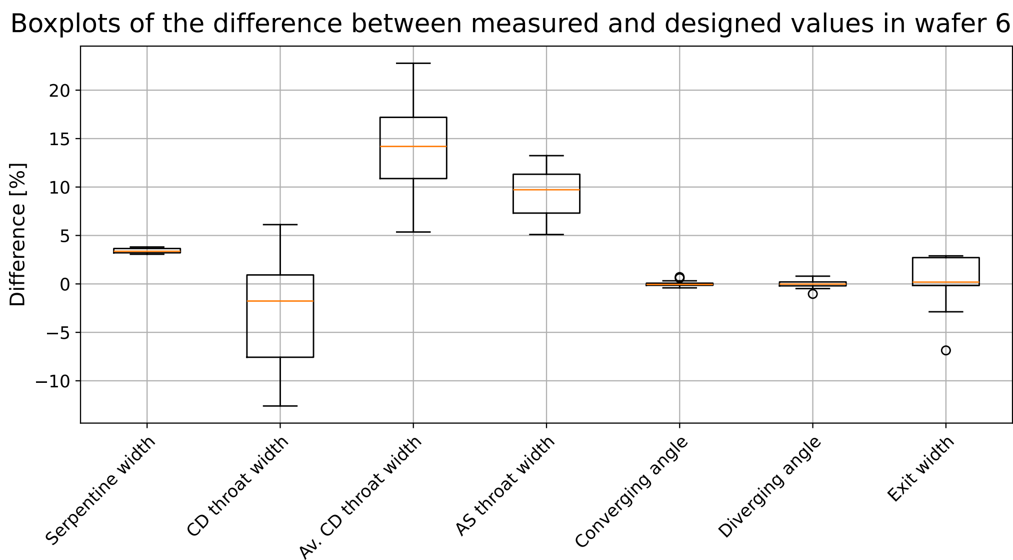

Figure 4.29: Box plots of the relative difference between the measured (or calculated for the average CD throat width) and design values of the in-plane dimensions. See `matplotlib.pyplot.boxplot` [76] for the meaning of the elements making up the box plot.

Similarly to the values reported by Singh [15] using the same DRIE recipe, the variation in the serpentine channel width, convergent and divergent angles is very small. However, in the current work, the median width is around 3.4% larger than the design value of 212 µm (overetched), compared to Singh's median difference of −8.5% (underetched). This difference could only be caused by the different masking layer used, the current work using a photoresist soft mask, while Singh used a SiO_2 hard mask. The median deviation is still lower than what was previously obtained by Silva [2], with a median deviation of above 20%.

Regarding the measured surface throat widths, the median deviation values are again larger arithmetically for the current work, but smaller in an absolute sense. For the in-place CD throat width, the current work has a median difference of −1.8%, while Singh has of −8.4%. Likewise for the AS, the current work has a difference of 9.7%, compared to Singh's −18.5%. This can again be attributed to the difference in the masking material. The interquartile range is slightly smaller in the current work for the in-plane CD measurements, and half for the in-plane AS measurements, indicating higher repeatability.

Comparing the estimated average CD throat width, the current work has an interquartile range 1.3 times larger than the one of Singh. The median difference is of 14.2%, while Singh's is smaller at around 9%. This shows lower repeatability and accuracy for this metric. However, it has to be considered that for the current work, the height and taper slope angle were estimated and not measured directly for the

majority of W6 thrusters. As such, better estimations by performing more measurements (especially for the taper slope angle) could be obtained, in which case the results might change.

4.5.5. Surface Roughness Properties

In this subsection, the surface roughness properties are presented as a comparison between the wafers that went through different etching steps. Namely, the compared wafers are W15, W3 and W6.

The roughness is calculated from the laser measurement data from the Keyence microscopes - namely VK-X1000 for W15, and VK-X250 for W3 and W6. The Gwyddion open-source software[1] is used for this purpose. Masks were created to isolate the top (unetched) and bottom (etched) surfaces of the thrusters. This is preferred to using a separation between waviness and texture to distinguish between the structures on the wafers and the surface properties, which can be quite arbitrary [77]. The two masks used for the top and bottom surfaces are exemplified in Figure 4.30 for the nozzle of the W15R2C09 thruster. For the mask of the bottom surface, the margin was removed to not be influenced by the effect of the etching artefacts described in Subsection 4.4.5.

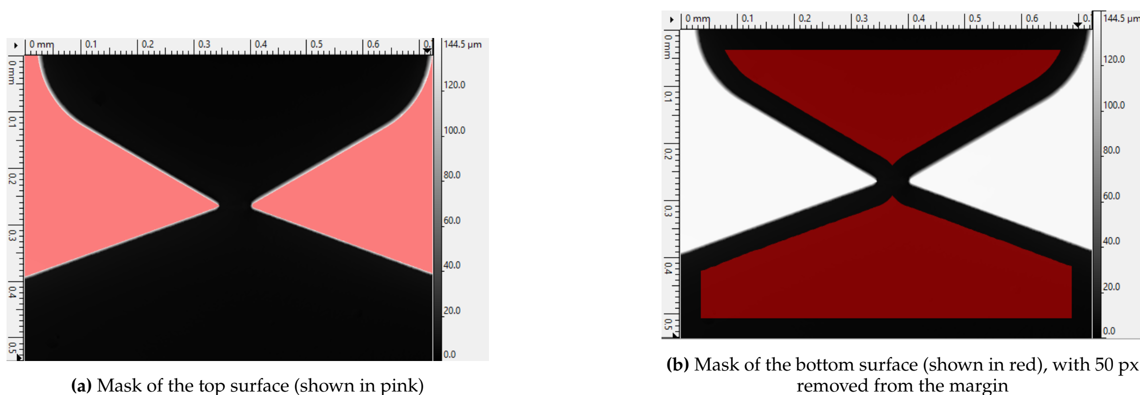

(a) Mask of the top surface (shown in pink)

(b) Mask of the bottom surface (shown in red), with 50 px removed from the margin

Figure 4.30: The masks used on the laser measurements of the nozzle of thruster W15R2C09, for calculating the surface roughness properties.

After the data was levelled based on the top surface, the surface properties were obtained from the Gwyddion software for the two masks. The following properties are reported in this thesis:

- Sq: The square mean height is "equivalent to the standard deviation of height distribution" and is used as a means to determine the unevenness of the surface [78]. It is the most used single number in the evaluation of roughness.
- Sa: The arithmetic mean height is "the mean difference in height from the mean plane" of the surface [78]. It is an alternative to Sa.
- Ssk: The skewness evaluates the degree of asymmetry that can be found in the height distribution [78]. An explanatory graphic is provided in Figure 4.31, taken from [78]. A positive value indicates mostly peaks in the surface, whereas a negative value indicates mostly valleys.
- Sku: The kurtosis is a measure of the sharpness of the height distribution profile [79]. A value of 3 indicates a Gaussian distribution, whereas a value less than 3 applies to a more rounded distribution, and larger than 3 for a sharper distribution. A sharper distribution also indicated sharper valleys or peaks. An explanatory graphic is provided in Figure 4.32, taken from [80].
- Sp, Sv, Sz: These represent the maximum peak, maximum valley, and maximum overall height (difference between a peak and a valley) [80]. These values are very prone to noise, as they represent maximum and not averaged values.
- Sdq: The root-mean-square gradient is used to represent the fineness of features, used to compare surfaces with similar roughness [78]. A graphic of how the surface affects this parameter is provided in Figure 4.33, taken from [78].

[1] `http://gwyddion.net`

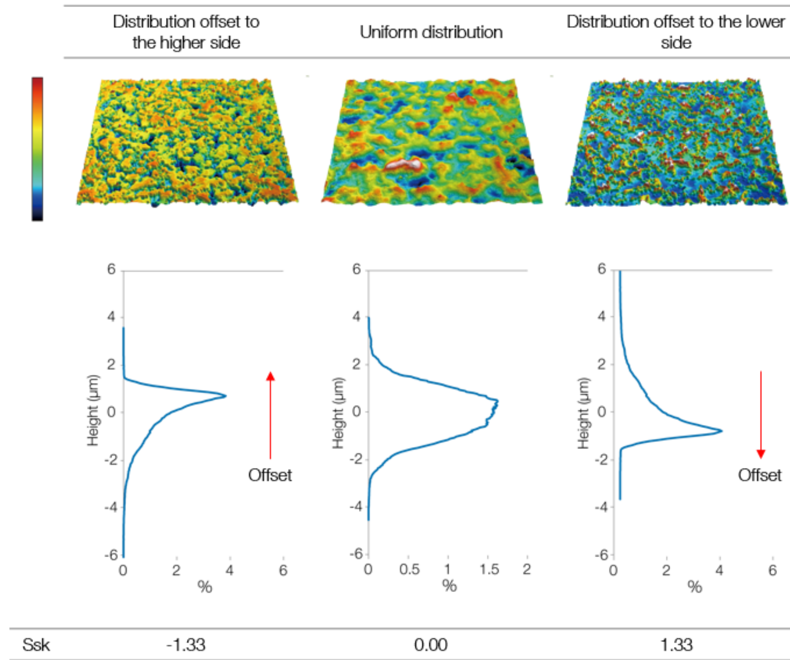

Figure 4.31: Variation of skewness (Ssk) with height distribution. Image from [78].

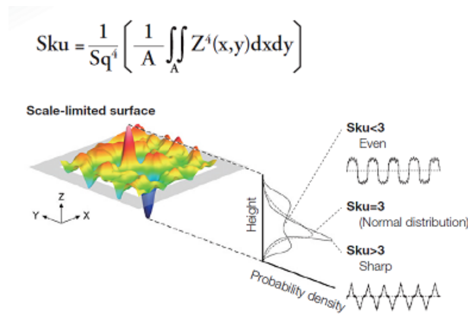

Figure 4.32: Variation of kurtosis (Sku) with height distribution profile shape. Image taken from [80].

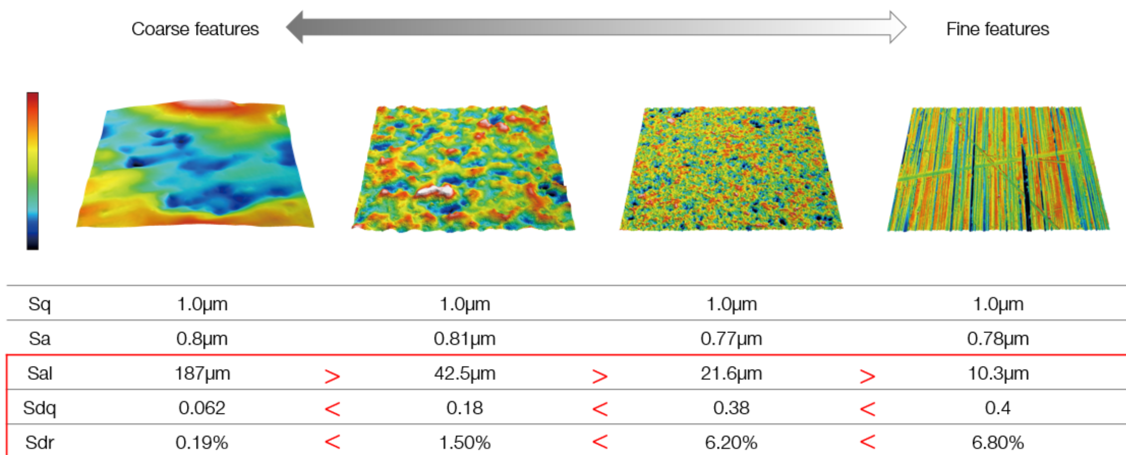

Sq	1.0µm		1.0µm		1.0µm		1.0µm
Sa	0.8µm		0.81µm		0.77µm		0.78µm
Sal	187µm	>	42.5µm	>	21.6µm	>	10.3µm
Sdq	0.062	<	0.18	<	0.38	<	0.4
Sdr	0.19%	<	1.50%	<	6.20%	<	6.80%

Figure 4.33: Variation of root-mean-square gradient (Sdq) with coarseness of the surface features. Image taken from [78].

These parameters are summarised in Table 4.12 for the top and bottom surfaces in the nozzle area of thrusters W15R2C09, W3R2C09, and W6R2C09. The same thruster on different wafer batches was chosen, in order to compare the effect of the etching process on the surfaces.

Table 4.12: Surface roughness properties measured for the same thruster from three different wafers.

Thruster	Surface	Sq [nm]	Sa [nm]	Ssk [-]	Sku [-]	Sp [µm]	Sv [µm]	Sz [µm]	Sdq [-]
W15R2C09	Top	65.9	49.6	1.39	119.67	3.73	0.60	4.33	0.041
	Bottom	737.5	594.6	0.73	3.05	2.42	2.45	4.86	0.062
W3R2C09	Top	170.9	130.1	-1.01	21.75	0.78	3.99	4.78	0.367
	Bottom	579.9	449.7	0.76	3.71	2.91	1.42	4.33	0.641
W6R2C09	Top	353.5	302.4	0.12	2.60	1.61	3.05	4.66	0.585
	Bottom	849.3	654.4	-0.50	3.76	3.37	4.29	7.66	1.602

The following were observed, regarding each of the measured parameters:

- Sq & Sa: The more etching steps (1 for W15, 2 for W3, 3 for W6), the larger the roughness becomes on the top layer. However, this is not the case for the bottom surface, which shows no clear correlation. This is unexpected, as the top surface is protected by the photoresist layer during etching. Another cause might be related to the photoresist stripping, even though the same programme was used on all wafers. Singh [15] mentions that a roughness of 100 nm or less is needed for wafer bonding, and of 500 nm or less for quality fluid flow in the microchannels. In this thesis, larger numbers on average for the surface roughness were obtained than in Singh; however, this might be due to the measurement method, as Singh used a linear instead of surface measurement. Regarding the roughness of the top surface for wafer bonding, a value 3.5 times the advised value is observed for wafer 6. However, the bonding of wafer 6 was performed without issues; as such, the 100 nm is proven to not be too strict. For the bottom surface, the roughness stays in the same order of magnitude as the recommended 500 nm. As such, the flow is not considered to be impacted significantly.
- Ssk: The Ssk of the top surface does not seem to follow a clear pattern, although it is smaller for W3 & W6 compared to W15. This indicates that the predominance of peaks in W15 mostly disappear in W3 & W6. For the bottom surface, however, the Ssk is negative for W6, compared to the other wafers which have approximately the same positive value. This might indicate that DRIE steps with fewer loops (the third step for W6 had only three loops) change the distribution on the bottom surface from mostly peaks to mostly valleys.
- Sku: For the top surface, the Sku is very large for W15 because the Sq is small, so the peaks appear as very sharp. This effect decreases the more Sq increases, which is to be expected. For the bottom surface, the Sku increases for W3 & W6, indicating a slight sharpening of the extreme peaks/valleys with subsequent restarts of the DRIE process.
- Sp, Sv, & Sz: The top surface shows smaller maximum peaks and larger maximum valleys in W3 & W6 compared to W15. This matches the average behaviour observed from the Ssk values. The bottom surface shows increases in both maximum peak and maximum height in W6 compared to W3, indicating a degradation of the surface quality.
- Sdq: For the top surface, the Sq roughness does not have similar values for the three wafers. As such, it might not be suitable for comparison of Sdq values. For the bottom surface, while the Sq roughness is not the same, it is fluctuating in the same order of magnitude, making a comparison more suitable. Regardless, for both surfaces Sdq increases from W15 to W3 and to W6, indicating that finer and finer features appear as the wafers are etched in more and more steps (having more and more process restarts).

As overall findings, multiple etching steps seem to increase roughness in the top surface, but not on the bottom. This can become an issue for wafer bonding, although it was not observed during bonding of wafer 6. The cause for this increase of roughness is not fully understood.

In contrast, the surfaces seem to be prone to the creation of valleys rather than peaks with multiple restarts of the DRIE process, especially on the W6 bottom surface. Additionally, sharper features were also observed on the bottom surfaces of W3 and W6. Furthermore, finer rather than coarser features are observed the more DRIE process restarts are performed.

4.6. Heater Side Measurements

In this section, the dimensional and resistance measurements performed on the heater side of wafer 6 (the final production wafer) are reported.

4.6.1. Heaters Dimensional Measurements

For the dimensions of the heaters, only heaters from two thrusters (one heater each) were measured to check the accuracy of the deposition and etching processes. This is due to multiple reasons. Firstly, for testing the final thruster, it is more important to know the true resistance of the heater, rather than how it compared to the theoretical value. This resistance value can be measured directly using a multimeter, as was done for the assembled thrusters. Secondly, even if these measurements are not done now, they can still be done at a later date, as the heaters remain exposed after the assembly process. However, it was still deemed important to check if the fabrication process proceeded as expended on this side of the thruster, even though this heater design was already used in two previous batches (of Spernovasilis [18], the original designer of these heaters, and of Singh [15])

The thrusters whose heater dimensions were measured are W6R2C06 and W6R2C11. They were chosen to be one close to the centre of the wafer (W6R2C06) and one near the edge (W6R2C11), to see if there are any significant differences between them. For both thrusters, the heater closest to the entrance (heater 1) was measured. The dimensions that were measured were the variable heater widths (using the same notation as shown in Figure 4.1, from w_0 to w_8), and the tallness of the heater (as the distance between the upper and lower outer extremities of the heater serpentine sections, denoted with l_t). The measured values, along with the design values, are included in Table 4.13.

Table 4.13: Design and measured dimensions for different features of the VLM heaters. All dimensions are in µm.

Dimension	Ideal	W6R2C06 heater 1	W6R2C11 heater 1
l_t	500	530.8 ± 14.1	527.0 ± 14.1
w_0	55	57.0 ± 1.8	54.9 ± 1.8
w_1	77.8	80.9 ± 1.8	79.8 ± 1.8
w_2	86.1	88.3 ± 1.8	88.7 ± 1.8
w_3	89.2	91.5 ± 1.8	91.9 ± 1.8
w_4	90.3	93.9 ± 1.8	92.7 ± 1.8
w_5	90.8	92.5 ± 1.8	93.2 ± 1.8
w_6	90.9	93.0 ± 1.8	93.1 ± 1.8
w_7	91.0	93.7 ± 1.8	93.4 ± 1.8
w_8	91.0	93.1 ± 1.8	93.4 ± 1.8

Comparing the dimensions between the two thrusters, all are within measurement accuracy of each other. While W6R2C06 heater dimensions are on average slightly larger compared to the ideal than the ones of W6R2C11, no confident conclusion can be taken, due to the measurement uncertainties.

Comparing to the ideal values, the widths are on average 2.7% larger than the design values, whereas l_t is 5.8% larger. Assuming the same thickness of the heaters, and using the model developed in the next chapter, it can be shown that the change in l_t alone can produce a deviation of as much as 5.5 Ω. However, assuming both the changes in widths and l_t at the same time, a maximum change of 2.8 Ω can be expected.

During the fabrication process at EKL, the thicknesses of the aluminium and titanium layers were also measured, using the Dektak 8. Measurements were done only on wafer W3; however, as all wafers went through the same processes for that side, it can be assumed that the values are very similar on the rest of the wafers. The thicknesses were measured on three thrusters, and are reported in Table 4.14.

Table 4.14: Thickness of Ti and Al layers as measured on wafer W3.

Location	Thruster	Ti+Al [nm]	Ti [nm]	Al [nm]
Left	R3C01	658 ± 2.3	454 ± 2.3	204 ± 3.2
Centre	R3C07	689 ± 2.3	473 ± 2.3	216 ± 3.2
Right	R3C12	659 ± 2.3	450 ± 2.3	209 ± 3.2

For both the titanium and aluminium layers, the thicknesses are within 10% of the design values, showing good compliance. However, this is a critical dimension, especially for the titanium layer, as 10% lower thickness would result in an 11.1% higher resistance for the reference design.

4.6.2. Estimation of the Resistance Values

In order to compare the ideal values of the heater resistances with the measured ones, a model for calculating the resistance from the known dimensions was derived. For this, the heater is divided in multiple sections, such as the semicircle discs at the top and bottom of the heaters, and the straight portions in-between. Their dimensions are estimated or measured, and then the resistivity of the section is assumed to be that of an ideal long and thin conductor (with uniform current density). These sections are then considered to be in series, such that their resistances are added up to obtain the total resistance. An equation describing this process is:

$$R_{heater} = \sum_i \rho_{\mathrm{Ti}} \frac{l_i}{S_i} = \frac{\rho_{\mathrm{Ti}}}{d_h} \sum_i \frac{l_i}{s_i} \tag{4.3}$$

Where R_{heater} is the total resistance of the heater, ρ_{Ti} is the resistivity of pure Titanium at room temperature (assumed to be $5.54 \cdot 10^{-7}\,\Omega \cdot \mathrm{m}$ [81]), l_i is the length of a section, S_i is the cross-sectional surface area of a section, d_h is the thickness of the heater, and s_i is the wideness of the section.

The design resistance was calculated to be 105.4 Ω. The resistances of W6R2C06 and W6R2C11 were also calculated, using the dimensional values from Table 4.13. For the thicknesses, the values from W3R3C07 and W3R3C12 were used, respectively. These were the closest measurements available, and were close to the geometrical placement of the thrusters on the wafer, even if on a different wafer. The expected resistance of heater 1 of W6R2C06 was 114.7 ± 5.4 Ω, whereas for heater 1 of W6R2C11 was 119.9 ± 5.7 Ω. This shows an increase of 23% and 20% respectively, compared to the design values.

4.6.3. Measurement of the Resistance Values

Four-wire resistance measurements were used for the heaters, in an attempt to eliminate reading errors from the connections. Only the thrusters that were glued and wire bonded to PCBs were measured. Other thrusters should be measured as they are assembled.

The measurements were done at room temperature, which can be assumed to be between 21 °C and 25 °C. The results of the measurements are included in Table 4.15.

Table 4.15: 4-wire resistance measurements of the heaters of the assembled thrusters. All values are in Ω. There are missing values for W6R3C07 because wire bonding was unsuccessful for some pads, leaving some heaters partially or completely unconnected. For all measurements, the uncertainty is ±0.05 Ω.

Batch	Thruster	Heater 1	Heater 2	Heater 3	Heater 4	Heater 5	Heater 6	Heater 7	Heater 8
1	W6R3C01	143.0	143.1	145.6	145.4	145.6	146.4	146.8	148.8
	W6R3C02	143.7	143	142.4	141.7	140.6	139.6	140.6	139.5
	W6R3C07	-	129.9	128.2	-	-	-	-	128.9
2	W6R2C06	130.1	130.1	130.3	131.0	131.6	132.2	132.7	133.0
	W6R4C07	130.7	130.3	130.2	129.6	127.9	129.7	128.4	128.0
	W6R2C10	134.5	134.8	135.0	135.3	135.7	136.3	136.8	136.8
	W6R2C11	138.1	138.0	138.1	138.5	138.9	139.5	140.0	140.4
	W6R2C12	144.8	145.3	145.8	145.9	146.2	146.2	146.4	147.3
	W6R3C06	130.6	130.4	130.3	129.8	129.5	129.4	129.4	130.1

4.6.4. Comparison between Design, Estimated and Measured Resistances

In Table 4.16, the design resistance, along with the estimated and measured resistances, are presented.

Table 4.16: Comparison between the design, estimated, and measured resistance values for heater 1 of thrusters W6R2C06 and W6R2C11. All values are in Ω.

Heater	Design	Estimated	Measured
W6R2C06 H1	105.4	114.7 ± 5.4	130.1 ± 0.05
W6R2C11 H1	105.4	119.9 ± 5.7	138.1 ± 0.05

The heaters have a resistance 13.5% and 15.1% higher than the estimated values, respectively. The difference cannot be explained by the uncertainties. Possible sources of this difference include:

- The value of the resistivity of the titanium layer is different from that used in the calculations. Titanium deposited using different technologies (such as sputtering versus evaporation [82]), at different sputtering power levels [83], or resulting in different grain sizes and film thicknesses [84], can significantly affect the value of the resistivity.
- The layer thicknesses that were used in these calculations did not correspond exactly to those of the thrusters.
- The geometry of the heater was only approximated using the above-mentioned sections. A more accurate calculation, especially for the regions near the contact locations of the heaters, would require time-expensive numerical simulations, which are outside the scope of this thesis.

These differences and many sources of uncertainty show that the calculation is not a suitable method of estimating the resistance of the heaters. This, together with the deviation of 23% to 31% of the measured values compared to the design resistance, shows the importance of performing direct resistance measurements using a multimeter. This way, the resistances can be accurately known, which is important in determining the required voltage and current levels during testing and operation.

4.7. Summary and Conclusions

In this section, a summary is made of the information presented in this chapter, including conclusions on some of the discussed items.

Thruster Design

The design of the thrusters remained very similar to Singh's version, with two main differences: the change of the nozzles' distribution, and rearrangement of the thrusters on the wafer layout. These were done to provide a greater diversity of configurations to be tested, and to also ensure that by breaking one wafer, most of the configurations would still be available. However, this made the comparison between the effects of different parameters on the fabrication results harder to quantify, as multiple parameters (such as thruster configuration and position on the wafer layout) were varied at once.

Fabrication Process & Issues

The fabrication process was simplified, reducing the total number of steps by 13%, which also eliminated some problems encountered in the work of Singh. Other issues were determined during the fabrication performed for this thesis; these were quantified and corrected where possible. As the DRIE process changed (most significantly by changing the masking layer on the wafer), this was recalibrated, both in the terms of exposure energy, but also on the number of etching loops.

Fluidic Side Measurements & Discussion

The etching process encountered observable variations, with differences in etching rates of up to 8% between wafers that had no or multiple DRIE process restarts. Differences were also seen in the surface quality of the wafers, showing a general degradation with increasing the number of restarts. This led to the recommendation of keeping the etching process to one single step, in order to avoid any stop-restart of the process.

A tendency of higher etch rates for thrusters near the edge of the wafer was observed, also called the bull's eye effect. For the final production wafer 6, this effect generated (estimated) relative variations between maximum and minimum depths of 7.6% for microchannel, 4.5 to 12.0% for CD nozzle throats, and 8.6 to 11.3% for AS nozzle throats. Furthermore, (estimated) relative deviations from the ideal 150 µm depth on wafer 6 were between −1.2% and −8.2% for the microchannels, and between +3.5% and −16.5% for the nozzle throats. These latter deviations are a result of both incorrect etch rate prediction, and aspect ratio-dependent etching effects, the latter of which can only be measured experimentally.

To quantify whether these variations and deviations are significant, their impact on thrust measurement is required. Using the analytical model from Chapter 3, it can be shown that a relative deviation in etching depth produces the same relative deviation in expected thrust – if, for example, there is a deviation of ±10% in etching depth, then a deviation of ±10% is also expected in the thrust values. Using the numbers from the previous paragraph, variations in thrust due to uneven etching of 4.5% to 12% can be expected. Deviations in thrust from incorrect etch rate due to DRIE stop-restart events and from aspect ratio-dependent etching effects are in the order of +3.5% to −16.5%. These values are in the same order of magnitude as the thrust measurement uncertainties of VLM tests with water reported by Hutten [56], which had an uncertainty of around ±12.6%. As such, these variations and deviations are considered significant for further experimental studies, and need to be predicted or suppressed.

Regarding the deviation from incorrect etch rate, this can be easily minimised by manufacturing thrusters in the future with a single DRIE step, which would also be beneficial for the surface quality. On the other side, the effect of aspect ratio-dependent etching is hard to quantify non-experimentally. As such, at least one measurement of the depth of each type of nozzle would be needed on a particular wafer. However, if multiple wafers go through identical process steps, the measurements from one wafer can be used on the others as well, for this specific effect.

In contrast to the incorrect etch rate, the variation from the bull's eye effect is harder to counteract. It would require either to discard the thrusters close to the edge of the wafer, or to perform the etching in two steps, using an intermediate protector layer at the edge of the wafer. These would either result in waste, or increased complexity of the process. For this reason, it was attempted to predict the bull's eye effect on the etch depth, by fitting the data to some polynomials.

Results show that microchannel depth and throat depths for throats at least 50 µm wide can be predicted well, and do not require measurements to obtain their values. The general trend of the increase in depth of 25 µm CD nozzle throats with distance from the centre of the wafer can also be predicted well, although individual values will vary more from the prediction than for wider throats. For 25 µm aerospike nozzles, the polynomial fit fails to predict the expected depth; as such, measurements will always be required for this type of nozzle for accurate values.

The horizontal dimensions of the thrusters on wafer 6 were also measured and analysed. Compared to Singh's work, surface-level dimensions are more accurate in the current work, while the average width of CD nozzle throats is less accurate. While a similar relation between horizontal dimensions variation and thrust variation appears as for between etch depth variation and thrust variation, this is not as critical. This is because the surface horizontal dimensions of new thrusters can always be measured after full fabrication, through the glass layer.

By analysing the profile of the throat, a taper slope angle was observed at the microchannels and at the throat of the thrusters, indicating that the width increases with depth. Initial measurements were made, and it was observed that the taper slope angle varies between microchannels and throats, and between throats of different widths. However, more measurements are required to increase the confidence in these findings, and to better predict the average throat widths of thrusters.

Heater Side Measurements

Regarding the heaters, it was attempted to predict their resistances using a model for the calculation of resistance from their geometry, using both ideal (design) values, as well as measured dimensions. Both measures were inaccurate, with deviations between 23% and 31% for the first method, and between 13.5% and 15.1% for the second method. Given the relative ease with which the resistances can be measured directly, especially after the assembly with the interfaces described in the next chapter, an analytical prediction of the resistances is not required.

5 Design, Manufacturing & Assembly of the Interfaces

In this chapter, the design of the fluidic and electrical interfaces is presented, as well as their manufacturing, and integration with the thruster and the rest of the assembly. Section 5.1 includes the design requirements for the testing interface. The nomenclature for the thruster and assembly used in the rest of the thesis is presented in Section 5.2. The top-level design decisions made for the interface are given in Section 5.3. The resulting fluidic and electrical interfaces are presented in Section 5.4 and Section 5.5, respectively. The assembly of the system is explained in Section 5.6, while the verification of the design requirements is performed in Section 5.7. The chapter ends by presenting the current status of the manufactured and assembled thrusters in Section 5.8.

5.1. Interface Requirements

A previous fluidic and electrical interface already existed for the VLM thruster, and was used by Silva [2] and Melaika [54], among others. Its design is shown in Figure 5.1.

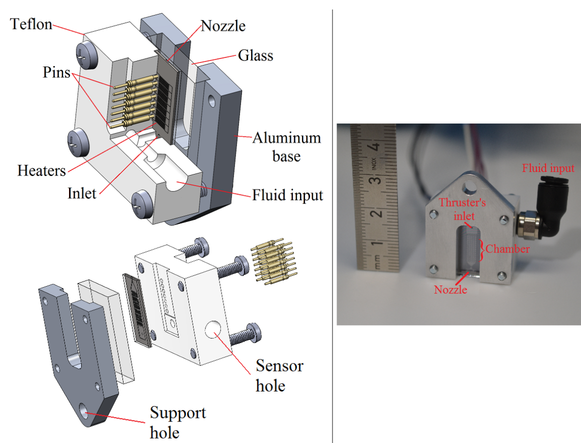

Figure 5.1: Previous design of the VLM fluidic interface. The top left image shows a CAD version of the assembled system, the bottom left an exploded view of the system, and the right image shows the interface in reality. Image taken from Silva [2].

This interface was designed to be reusable, and made for the layout of the previous generation VLM available at TU Delft. The water takes two 90° turns to enter the thruster, perpendicular to the flow in the chip. Electrical connection is insured through the spring-loaded pins, which touch the pads of the heaters on the chip. The glass on the other side ensures optical access to the fluid flow in the thruster. The aluminium base provides the support hole as interface for the thrust pendulum available at the

Faculty. Lastly, a sensor hole is present, where the pressure & temperature (P/T) sensor MS5837-30BA can be glued to.

Due to the design changes made by Singh in the last iteration of the VLM, this interface can no longer be used. The design of Singh assumes an in-line entrance of fluid flow in the thruster. This is chosen in order to enhance the uniformity of the flow velocity into the thruster, and to have a gradual pressure drop along the inlet [15].

Another reason why the previous interface can no longer be used is because another heater design was chosen for the thruster. The new heater has smaller contact pads, closer to each other, and in different locations than the previous heaters. As such, the need for a new interface was clear.

The main goal of the interface is to provide enhanced testing capabilities, and to adapt its design to what is available to the author in a timely manner for the completion of this thesis. Therefore, it is not intended to be used in a satellite, and its design was not optimised for minimisation of size and mass. However, it can serve as a basis for a future interface to be used in a satellite, once results of its performance from testing become available.

In order to provide guidance through the design process, a loose set of requirements was created. They are loose in the sense that they can be adapted to what is practically and immediately available. Furthermore, the design was supposed to be kept as simple as possible, to speed up the process. The requirements presented in Table 5.1.

Table 5.1: Requirements for the test interface of the new generation VLM.

Requirement ID	Description
REQ-VLM-INT-01	The interface shall provide an electrical connection to the VLM heaters.
REQ-VLM-INT-02	The electrical interface shall be independent for the 8 heaters present in the VLM.
REQ-VLM-INT-03	The interface shall maintain an unobstructed view to the glass side of the VLM.
REQ-VLM-INT-04	The interface shall have options for mounting to an external structure.
REQ-VLM-INT-05	The interface shall provide fluidic access to the inlet (on both sides when such configuration is used).
REQ-VLM-INT-06	The fluidic access to the inlet of the thruster shall be in-line with the propellant flow in the thruster.
REQ-VLM-INT-07	The interface shall support the MS5837-30BA pressure + temperature sensors required for testing.
REQ-VLM-INT-08	The interface shall maintain an unobstructed view to the heater side of the VLM.
REQ-VLM-INT-09	One design of the interface shall provide fluidic access to a thruster with only an inlet.
REQ-VLM-INT-10	One design of the interface shall provide fluidic access to a thruster with both an inlet and an outlet.
REQ-VLM-INT-11	The interface shall allow pressurised operation of the thruster up to 6 bar relative pressure to the ambient.
REQ-VLM-INT-12	The interface shall allow heated operation of the thruster with the heater temperature reaching at least 150 °C.
REQ-VLM-INT-13	The interface shall be compatible with vacuum environments according to the NASA low-outgassing standard ASTM E959.
REQ-VLM-INT-14	The fluid interfaces shall be compatible with MINSTAC 062 tubing connectors.

Rationale for the test requirements is presented in the following list:

- **REQ-VLM-INT-01**: Self-explanatory. Without an electrical connection, the heaters cannot produce heat for the propellant.
- **REQ-VLM-INT-02**: An independent electrical connection for the heaters allows for future iterations of heater control, based on temperature readings. It also allows the operation of only a portion of

the heaters, if the study of this effect is considered important.

- **REQ-VLM-INT-03**: This is required to observe the phase-change front of the water from liquid to gas. It also allows for the optical study of flow instabilities.
- **REQ-VLM-INT-04**: This is required for stability during testing, but also to provide a mechanical interface to the thrust pendulum for measuring thrust.
- **REQ-VLM-INT-05**: This is required such that propellant and flow into the thruster. Optionally, for a design with both inlet and outlet, the interface shall also allow propellant flowing out to be recaptured for measurement purposes, such as outlet pressure.
- **REQ-VLM-INT-06**: This is required to insure a flow with as little obstruction as possible high degree of uniformity, as numerically studied by Singh [15].
- **REQ-VLM-INT-07**: This is the sensor that was also used in previous iterations of the VLM interface, and has all the required data reading interfaces already available at the faculty.
- **REQ-VLM-INT-08**: This is to be able to read the temperature of the heaters. This can be done either with a thermal camera, or using thermocouple(s).
- **REQ-VLM-INT-09**: This is required for the operation of the normal thruster, composed of an inlet, vaporisation section (microchannels), and nozzle.
- **REQ-VLM-INT-10**: This is required for the operation of the thruster with no nozzle and symmetric inlet and outlet. This thruster is to be used to measure the pressure drop across the microchannels, as well as to study the possibility of the appearance of instabilities in the microchannels.
- **REQ-VLM-INT-11**: This pressure level is chosen as the design pressure according to Singh [15]. Lower pressure are still acceptable, though.
- **REQ-VLM-INT-12**: This temperature level is based on previous experience of previous VLM designs. Many materials fail around this temperature, and as such not going above this temperature allows for a wider choice in design. However, the higher temperature that can be sustained, the better.
- **REQ-VLM-INT-13**: This is required to insure correct and safe test operation in a vacuum chamber or vacuum oven.
- **REQ-VLM-INT-14**: The bulk of the microfluidic connections used in the past for VLMs in the Space Engineering department follow this standard from The Lee Company. Many components are already available and do not require extra ordering.

As mentioned in the above requirements, there are two main versions of the VLM thruster: one with nozzle, with an example shown in Figure 5.2, and one without, as shown in Figure 5.3. The version with nozzle is the standard, and will be used as a means of propulsion. The main purpose of the version without nozzle is for studying the behaviour of the microchannels. Namely, the pressure drop, as well as the possibility of the appearance of instabilities in the microchannels are the main points of interest. As this version of the thruster has both an inlet and outlet that need to be interfaced to, a modified interface is required.

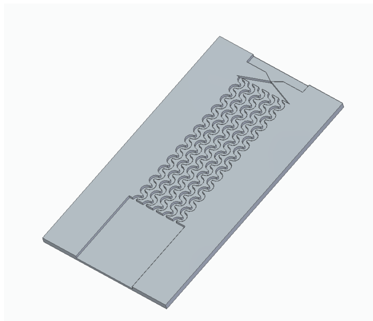

Figure 5.2: Example CAD model of a VLM thruster chip with nozzle. The glass layer was removed for clarity.

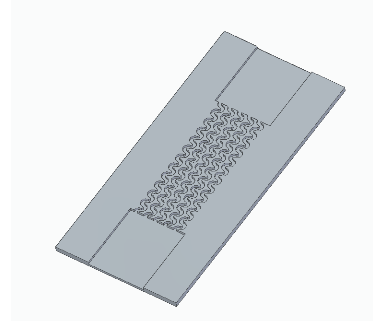

Figure 5.3: Example CAD model of a VLM thruster chip without nozzle. The glass layer was removed for clarity.

5.2. Thruster & Assembly Nomenclature

In this section, the nomenclature regarding the thruster and assembly is explained, in order to improve the understanding of the different terms throughout the rest of the thesis.

An exploded view of the thruster assembly is shown in Figure 5.4 for the configuration for a thruster with nozzle. A similar view applies also for a configuration without nozzle – the main difference is the additional presence of an outlet besides the inlet.

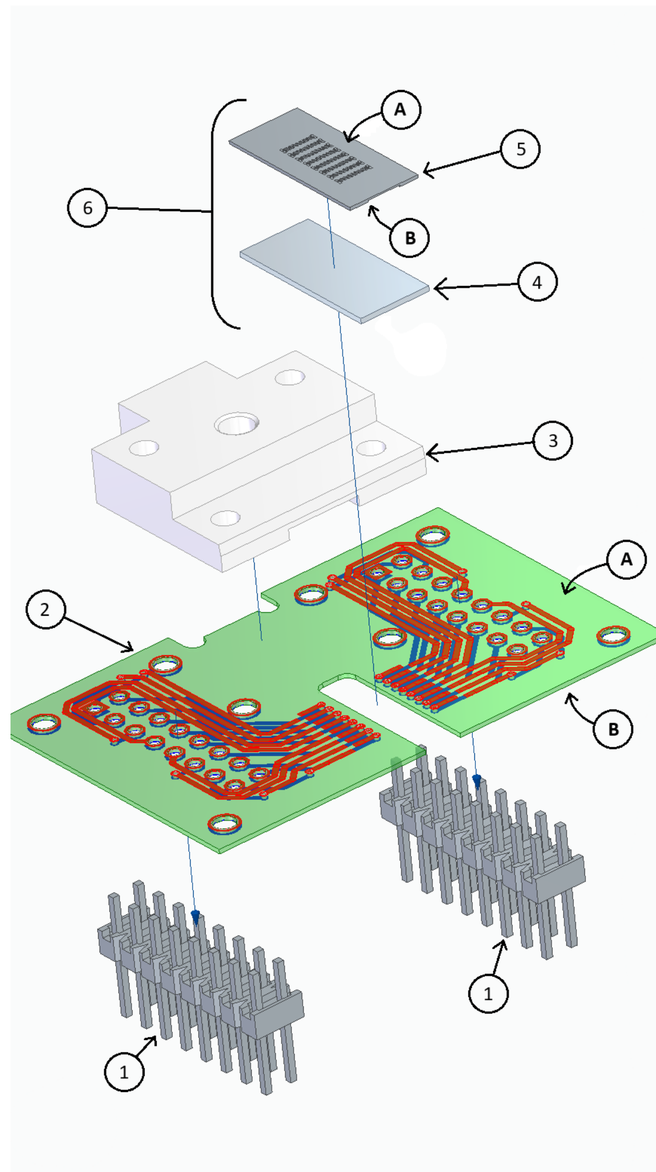

Figure 5.4: Exploded view of the assembly for a thruster with nozzle. The flow of propellant is from the top left towards bottom right.

The legend is provided below for the number labels:

1. 8×2 header pins for electrical connections
2. Printed circuit board, acting as mechanical support and sealing surface for the inlet
3. 3D printed fluidic inlet
4. Glass layer of the VLM
5. Silicon layer of the VLM

6. Complete VLM, composed of the silicon and glass layers. These are already anodically bonded following the thruster fabrication steps, as explained in Chapter 4

The letter labels represent the two sides of the thruster or of the PCB:

- Side A: the heater side. The heaters are deposited on this side of the thruster. The wire bonding pads can be found on this side of the PCB. Also on this side of the PCB is where the header pins are soldered.
- Side B: the fluidic side. The microchannels and nozzle of the thruster are etched on this side. The glass layer of the VLM is anodically bonded on this side of the silicon layer. The fluidic inlet and VLM thruster are glued on this side of the PCB.

5.3. Overall Design Decisions

In this section, the overall design decisions that affected all components of the thruster interface are presented. These can influence the electrical, fluidic, or mechanical properties and connections.

5.3.1. Glass Wafer Layer

Singh [15] proposes in his work that the thruster should have the wafer glass layer longer than the silicon layer, in order to provide mechanical support and alignment for the fluidic interface. Furthermore, a more stable propellant flow can be achieved this way.

The main disadvantage is the manufacturability of such an option. This would require the separate cutting of the glass and silicon layers. While possible, this procedure was not yet ever attempted at EKL. As such, a large amount of trial and error would be required until the technicians master the process, potentially losing a significant amount of thrusters. As such, it was decided to cut the glass and silicon at the same locations (both at once), simplifying the process. This also makes the thruster less fragile and easier to handle.

A preliminary CFD simulation of the water flow in the proposed interface showed good flow velocity uniformity at the exit, increasing confidence that this decision will not affect the stability of the flow.

5.3.2. Sealing Connections

Ideally, a reusable interface would be designed, which implies non-permanent sealing solutions. Multiple options were considered.

The first would be to provide liquid sealing through contact between adjacent pieces and tightening, which is what was done in the previous VLM interface. However, as reported by Melaika [54], this is not a perfect solution, as the materials used for the interface and thruster are relatively rigid. In turn, a leak-tight connection is almost impossible to ensure, and water leaked in-between the thruster and the glass piece used in the assembly.

The second option would be to use something similar to a rubber seal, to prevent the issues of option 1. However, this presents additional challenges.

Firstly, a custom seal would have to be manufactured, due to the specific dimensions of the thruster. Furthermore, there is no ideal placement of the seal in an in-line configuration. As the flow has to enter from a very thin edge of the thruster (overall thickness 825 µm, hole thickness 150 µm), placing a seal on this surface and tightening it would prove very hard geometrically, and very risky for the integrity of the thruster, as forces would have to be applied along it. Another option of placing the seal around the entrance of the thruster on the exterior would get into problems with the very sharp edges of the thruster, making a rounded seal hard to conform to that shape. Additionally, when tightening the connection from one direction (for example, top-bottom), the seal would expand on the perpendicular direction (in this example, left-right), leading to possible leakages.

Due to these problems, in order to maintain the in-line design, it was decided to go for a permanent sealing solution, using an adhesive. This has the advantage of filling any connection locations to the required geometry, ensuring no leaks happen during operation. However, this makes the interface single-use, with a new interface required for each thruster. As such, the cost of the interface becomes a very important factor. A high cost of a single use interface would become much more significant for

the total cost of the test campaign, as numerous thrusters were manufactured. This can easily lead to prohibitively large test phase costs.

5.3.3. Electrical Connections of the Heaters

The previous generation VLM interface used spring-loaded pins to contact the heater pads of the thruster. This has the advantage that it is a reversible solution, and the individual springs in the pins ensure contact even for uneven surfaces. However, after some use, Melaika notes that the friction between the pins and the pads have the effect of degrading the latter, and losing electrical contact [54]. An example of damaged heater pads from this effect is shown in Figure 5.5.

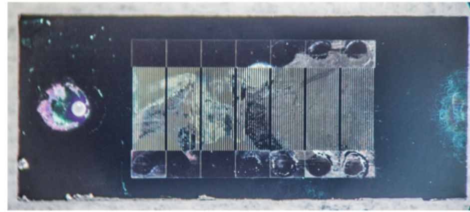

Figure 5.5: Damaged heater connection pads on a previous-generation VLM thruster. Image from [54].

Another issue with using such a solution for the current VLM is that the spacing of the pads is much closer than for the previous heater design. In the previous design, the pitch of the pads was of 1.29 mm, whereas now it varies between 0.4 and 0.6 mm. The author was not able to find any spring-loaded pins that would be small enough to satisfy the geometrical requirements. Non-spring-loaded pins would prove hard to ensure a reliable electrical connection. As such, this option was abandoned.

The current heater design, created by Spernovasilis [18], was made with wire-bonding in mind. This process involves connecting the heater to a conductive substrate, via a very thin wire (usually 25 – 33 µm in diameter, made out of aluminium, copper, or gold). The wire is bonded to the chip and to the substrate using ultrasonic power. A machine able to create this bonds is available at EKL. Furthermore, Dr. van Zeijl has significant experience operating this machine. Therefore, it was decided to go with this option. However, this required the creation of printed circuit boards (PCBs) to connect the heaters to.

5.3.4. Material and Manufacturer

Initially, it was considered to manufacture the interface at the DEMO workshop at TU Delft, as was done also with previous interfaces. Multiple processes are available at the workshop. However, due to the complex shape of the resulting interface, only methods like computer numerical control (CNC) milling and 3D printing could be used.

After talking with the technicians, the available 3D printing methods [fused deposition modelling (FDM) and stereolithography (SLA)] would not be able to produce the interfaces with the required precision. For CNC milling, only aluminium and Teflon were available as materials. A quote of between 100 and 400€ was given for producing one interface. This would mean that a single interface would consume almost the whole budget of the thesis. This was not acceptable if one interface is required per thruster. Furthermore, the material would ideally be non-conductive, to not give the possibility of creating any short-circuits in the case of touching the thruster. This would lead to Teflon being the only option. However, Teflon is notoriously difficult to glue to, going against the decision of using an adhesive as sealant. Furthermore, it was observed in previous tests performed at TUD that Teflon has the tendency of warping at high temperatures [85], which would lead to significant stress on the adhesive and surrounding structures. For these reasons, this option was discarded.

Through a personal connection of the author, a manufacturer in Ploiești, Romania was found that would be able to produce the interface at very high precision levels, while maintaining an affordable price. DiadVox[1] is a mainly dental component manufacturer, that utilises Asiga DLP (Digital Light Processing) 3D printing machines for production. These machines can be used for 3D printing of both dental and microfluidic components. It is not known which model of the Asiga printer the manufacturer used, but

[1] https://admdent.ro/en/

all machines have a precision of 62 µm or better [86]. This satisfies the requirements for the geometry of the current design.

The material used for 3D printing is Ultracur3D RG 3280 from BASF Forward AM. This is a 3D printing resin that contains 65% silica ceramic. It was chosen for the following capabilities [87]:

- Heat deflection temperature of more than 284 °C, satisfying REQ-VLM-INT-12
- Less than 0.3% water absorption after 24 h, making it suitable to work with water
- Passed the ASTM E959-15 outgassing test, satisfying REQ-VLM-INT-13

Furthermore, the manufacturer quoted a price of around 5€ per piece (without transport), making it an excellent choice for bulk ordering.

In the future, a manufacturer that uses a similar DLP technology and similar resin could be found in the Netherlands or nearby, in order to decrease transport costs. Theoretically, SLA printing should also be able to achieve these levels of resolution, although it is not fully clear why DEMO mentioned that SLA printing was not a suitable option.

5.4. Fluidic Interface

The fluidic interface of the design went through 3 design and manufacturing iterations (in three batches), in order to test the material, the accuracy of printing dimensions, and correct any design mistakes that appeared throughout the process. Mainly, the final design is presented in this section. The previous design iterations and the motivations for the changes between them are presented shortly at the end of this section.

Three versions of the fluidic interface were designed: an inlet each for the thrusters with and without nozzle, and an outlet for the thruster without nozzle. The CAD models of these can be seen in Figure 5.6, and a picture of the manufactured result in Figure 5.7. The technical drawings of the three designs are given in Appendix E.

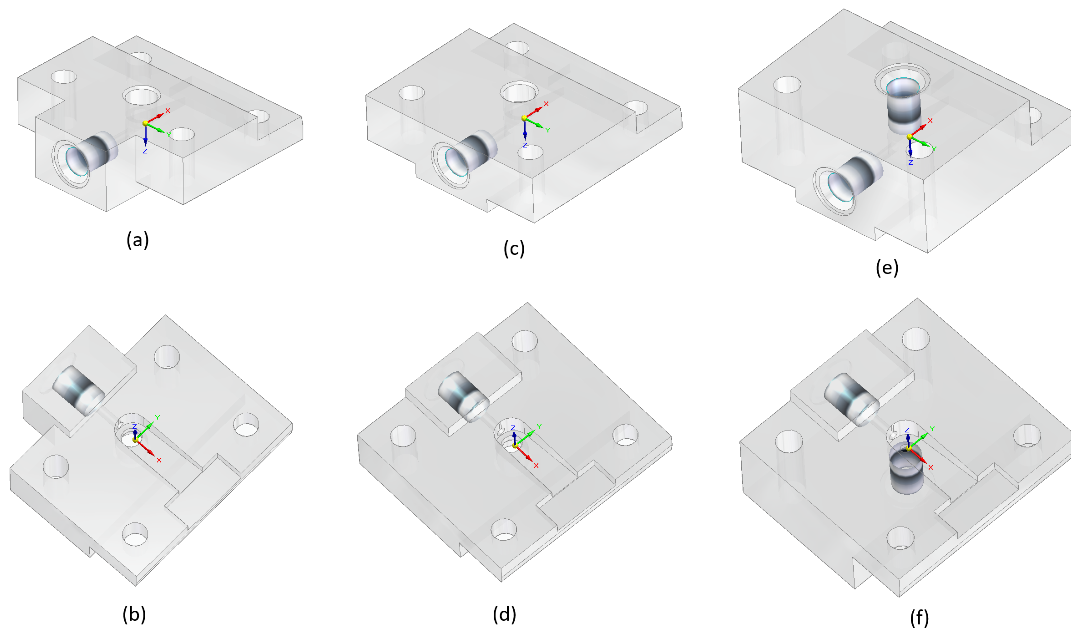

Figure 5.6: Final design of the fluidic interfaces. The left column shows the inlet for the thruster with nozzle, the middle column the inlet for the thruster without nozzle, and the right column the outlet for the thruster without nozzle. The top row shows perspective views from the heater side of the thruster, and the bottom row from the microchannel side. The red "x" arrow shows the direction of the fluid flow, except for the outlet, in which case it flows opposite to the red arrow "x". The material is shown as semi-transparent, to see internal structures

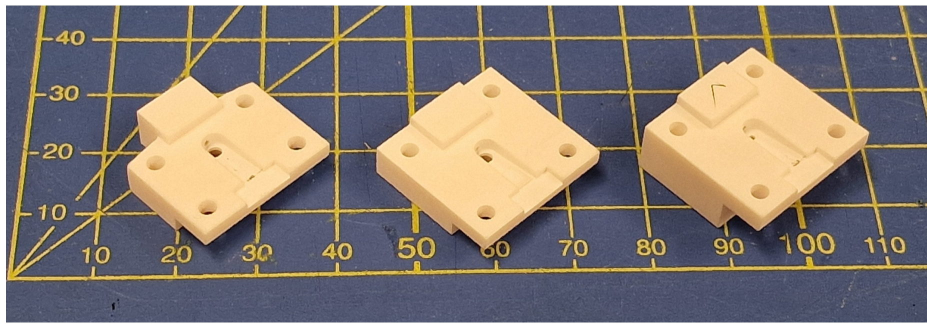

Figure 5.7: The 3D printed final fluidic interfaces. From left to right: with-nozzle inlet, no-nozzle inlet, no-nozzle outlet. The numbers on the background pad represent dimensions in mm.

In the following subsections, a more detailed look is taken at the different features of the fluidic interfaces.

5.4.1. Thruster Interface

This is the place where the thruster is supposed to connect to the fluidic interface. It is a feature for all three versions. A view of the connection is shown in Figure 5.8.

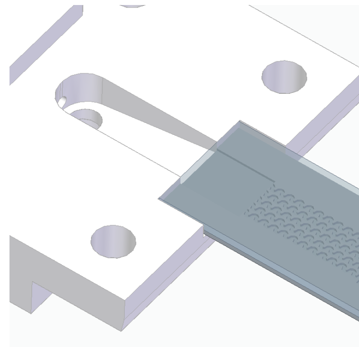

Figure 5.8: Detail of the connection between the fluidic interface and the VLM.

The nominal cross-sectional profile of the thruster is 7×0.825 mm. To provide a bit of clearance and leave space for the adhesive, the profile on the fluidic interface is 7.2×1 mm.

5.4.2. P/T Sensor Interface

For the MS5837-30BA pressure and temperature sensor, the interface was created according to the recommendations specified in its O-ring mount application note [88]. As the current fluidic interface is one per each thruster, glueing the P/T sensor to it would require one sensor for each thruster. Instead, a detachable interface was considered, such that the sensor can be transferred from one thruster to another.

A 1.78 mm by 1.76 mm NBR70 O-ring was ordered and used for the P/T sensor. This is close in value to the one recommended by the O-ring mount application note, and fit well around the sensor using some lubricant available in the SpE cleanroom workshop (Joker440 Synthetic Universal Spray). A picture of the O-ring on the sensor can be seen in Figure 5.9.

Figure 5.9: O-ring on P/T sensor.

For the sensor to not get out of its hole during the application of high pressures, a holder is required to keep it in place. A simple design that was 3D printed using PLA is shown in Figure 5.10. The holder is held in place by using metal screws and nuts, that go through it, the fluidic interface, and the electrical interface. This holder was used for a previous version of fluidic interface (batch 2), that did not have the full clearance for wire bonding. However, a design for the final version can be easily made and 3D-printed at the faculty. The mounted holder on the batch 2 interface is shown in Figure 5.11.

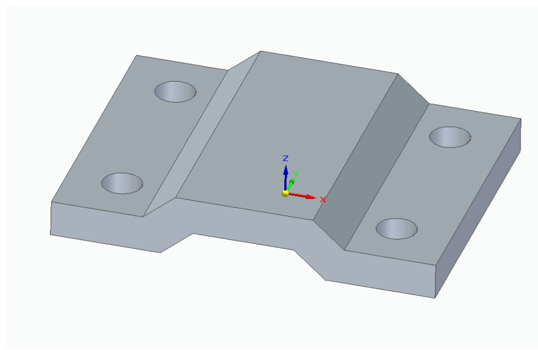

Figure 5.10: P/T sensor holder for batch 2.

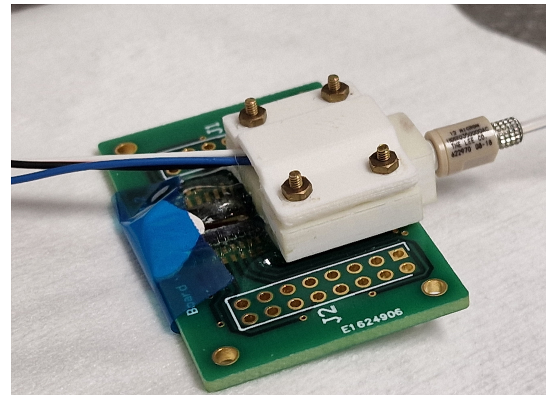

Figure 5.11: P/T sensor holder for batch 2 assembled on top of the fluidic interface.

For the assembly, M2 screws and nuts should be used. Believing that the holes in the fluidic interface for the P/T sensor holder can be threaded, these holes were made 1.6 mm in diameter for batch 2. However, when giving the interfaces to DEMO to thread, technicians informed the author that the material is too brittle to be threaded, and too brittle to be enlarged to 2.2 or 2.4 mm diameter to fit M2 screws. The reason for the former is not clear, as the threading for the UNF#6-40 was successfully done at DEMO. In any case, it was decided that it is better to not rely on the threading of the interface there, and to use nuts instead. For the interfaces of batch 2, M1.4 screws and nuts had to be used to fit the undersized holed, and the former had to be ordered. For batch 3 (final version), the holes are 2.4 mm in diameter, in standard for M2 screws.

The P/T sensor interface is included only in the designs of the two inlets, and not for the outlet. This is because at the outlet, the water vapours entering the fluidic interface will have more than 100 °C, depending on the operating pressure. Because the P/T sensor only works up to 85 °C, it was removed from the outlet. Instead, an additional MINSTAC 062 interface was put in its place. This way, a short MINSTAC tube can be connected to it, and then another interface with a P/T sensor already attached to it from a previous MSc thesis [54] can be used. With this intermediate tube filled with water, the pressure will still transmit to the sensor, but the temperature will not reach the vapour pressure in the system. This way, the sensor can still read the outlet pressure, without having to operate above 85 °C.

This method of reading the outlet pressure does come with a disadvantage. Due to the intermediate water column between the thruster exit and pressure sensor, high-frequency fluctuations in pressure at the outlet will be dampened and thus not reach the sensor. This could be considered undesirable in studying the flow instabilities. However, the main aim of the pressure-drop reading, excluding the better estimation of efficiency factors such as C_d, is to construct the pressure drop versus mass flux plot at different constant heat flux levels. This plot is useful for predicting and explaining the operational conditions at which instabilities can occur, as detailed in Section 2.2. In these plots, the flow is assumed to be in steady state; therefore, to construct these plots, only the average value of the pressure drop at a certain mass flux and heat flux is needed. To observe the actual flow instabilities, other methods can be employed, such as observing the pressure oscillations at the inlet, oscillations in flow rate, in heat transfer, in the two-phase front through the glass of the VLM, etc.

5.4.3. MINSTAC 062 Interface

In order to connect with the MINSTAC 062 tubing available at the department, a female MINSTAC 062 boss, as described in The Lee Company Handbook [89, p. L5], is included in the design for all interface versions. As explained in the previous subsection, the outlet has two such interfaces.

After the manufacturing of the first batch of interfaces, it was observed that the DLP printer cannot reproduce the required UNF#6-40 threading by itself. Therefore, a cylinder with the diameter of 2.89 mm [90] is printed, and then a tapping tool is used at DEMO AE to create the threading. While this works well for creating the threading and makes connection to the MINSTAC tubing possible, the material being removed by threading accumulates near the entrance into the 0.89 mm diameter inner flow path, often blocking it. This can easily be unblocked by using a syringe needle.

However, this accumulation of material damages the sealing surface as described in the Handbook. As a result, connecting the MINSTAC tubing directly to the inlet or outlet will result in leakages from the tubing itself, as it cannot seal itself properly without the correct sealing surface. For this reason, a 062 MINSTAC 12 micron safety screen (code INMX0350000A [89, p. L52]) is attached to the fluidic interface first, and then the tubing, as seen in Figure 5.12. This allows the same standard UNF threading to be used on the fluidic interface as the MINSTAC 062 standard, while also providing the required sealing surface for the tubing according to The Lee Company specification. In case leakage appears between the safety screen and the fluidic interface, it can be fixed by the simple application of some threading tape on the male end of the safety screen. Threading tape is available in the SpE cleanroom.

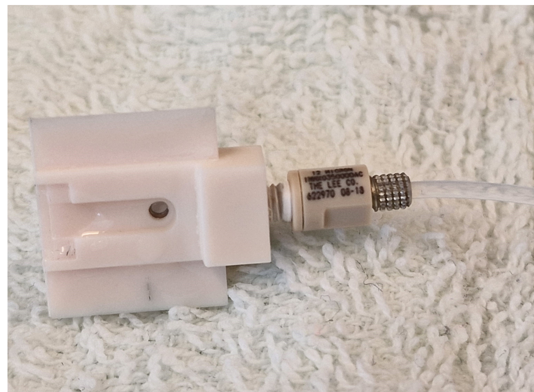

Figure 5.12: MINSTAC 062 tubing connected to a batch 1 fluidic interface, using a 062 MINSTAC 12 micron safety screen.

5.4.4. Clearance for Wire Bonding

One of the main changes made between batches 2 and 3 was the enlargement of the wire bonding clearance in the fluidic interface. In Figure 5.6, this can be seen as the step decrease towards the thruster location, on the heater side. A slight taper is applied on that edge for the same reason.

During wire bonding of thrusters using the batch 2 fluidic interfaces, it was observed that for some of the most-external bonding pads on the PCBs, a connection was barely possible, due to the wire bonder

dispensing needle hitting the fluidic interface. For this reason, the clearance was increased in the next iteration, eliminating this problem.

5.4.5. Previous Design Iterations

In this subsection, the previous design iterations of the fluidic interface are shortly presented, alongside the reasons for change between them.

Iteration 1

The first iteration of the fluidic interface was a very simplistic one. Its main goals were to test whether the manufacturing process produces acceptable results regarding dimensional and threading accuracy. Its design can be seen in Figure 5.13.

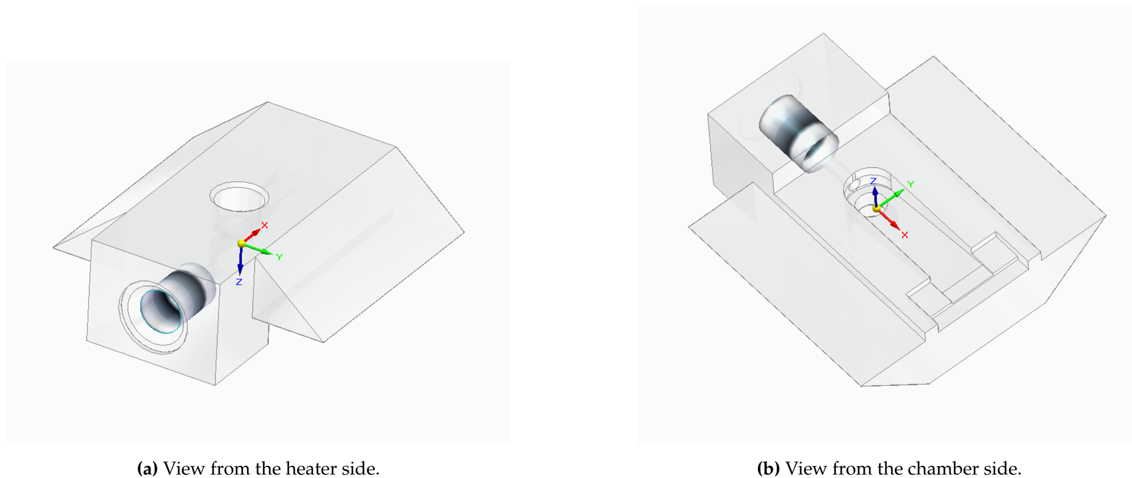

(a) View from the heater side.

(b) View from the chamber side.

Figure 5.13: First iteration of the fluidic interface.

In this design, it was still assumed that the glass layer of the VLM will be longer than the silicon layer, which can be seen by the height difference in the thruster interface part on the chamber side, detailed in Figure 5.14.

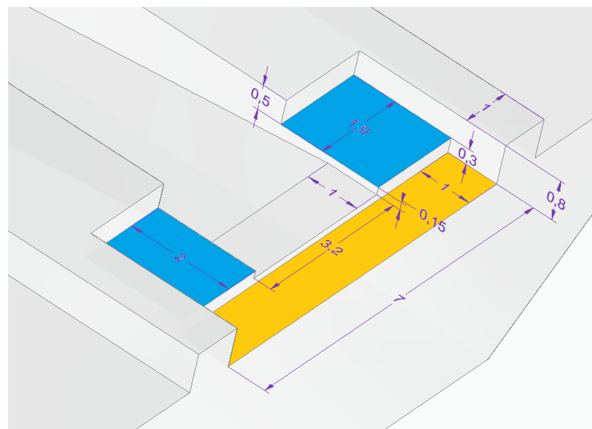

Figure 5.14: Detail of the thruster interface of the first iteration inlet. The golden area represent the surface on which the silicon layer of the thruster would rest, and the blue area the surface on which the glass layer of the thruster would rest. All dimensions are in mm.

Only two inlets were manufactured using this design. One included the thread of the MINSTAC connection in the part itself, while the other maintained the diameter required for tapping the thread after printing. As explained in Subsection 5.4.3, the 3D printing process could not capture correctly the threading; as such, only versions with the tapping diameter were manufactured from this moment on.

Another factor that was checked was the compliance of the printed dimensions to the design dimensions. Except for a non-critical dimension that deviated by 23.3% compared to its design value, the other dimensions deviated between -7.2% and 5.6%. As such, it was decided that no scaling shall be applied to the original design file, as no consistent bias could be observed.

Iteration 2

For iteration 2, the following changes were made:

- The thruster interface design was simplified, to allow easier connection to the thruster. This was also required as it was decided to no longer consider an extended glass layer of the VLM, and just dice the thruster's glass and silicon layers at the same locations. It was also enlarged, to allow around 0.2 mm tolerance in both thickness and width of the thruster.
- The triangle-profile overhang for the PCB was modified to a rectangular profile and has tapping holes (diameter 1.6 mm) for tapping M2 thread. This had a double role: to provide optional attachment methods for the PCB besides glueing, as well as to provide a fastening interface for an FDM-3D-printed part that would hold the pressure sensor in place when high pressures are used.
- The outlet was also now created as a modified version of the inlet. It is identical to the inlet, with the exception that instead of the interface for the pressure sensor, an interface for a secondary MINSTAC connector is placed. This will be connected to a tube filled with water, which is connected to a remote pressure sensor. This also required increasing the height of the piece.

The CAD model of the 2nd interface inlet is presented in Figure 5.15, while for the outlet it is included in Figure 5.16.

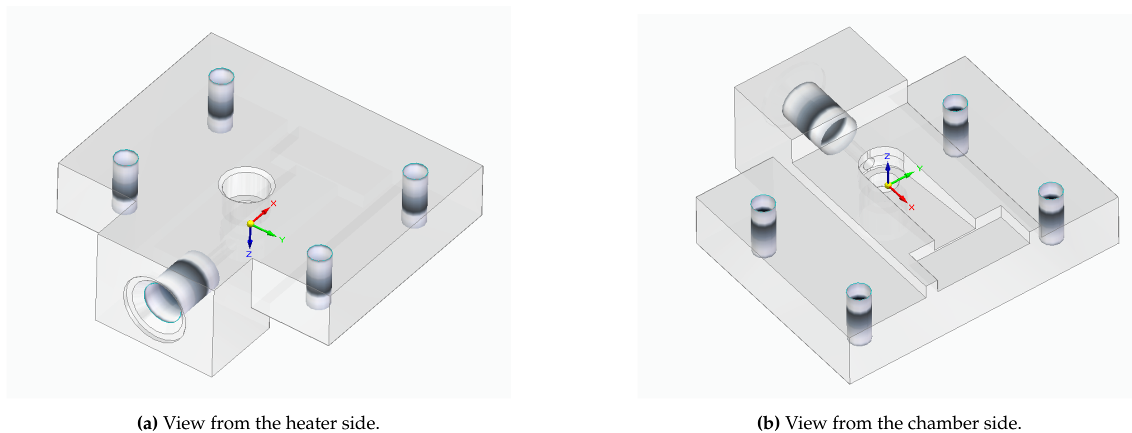

(a) View from the heater side. **(b)** View from the chamber side.

Figure 5.15: Second iteration of the fluidic interface inlet design.

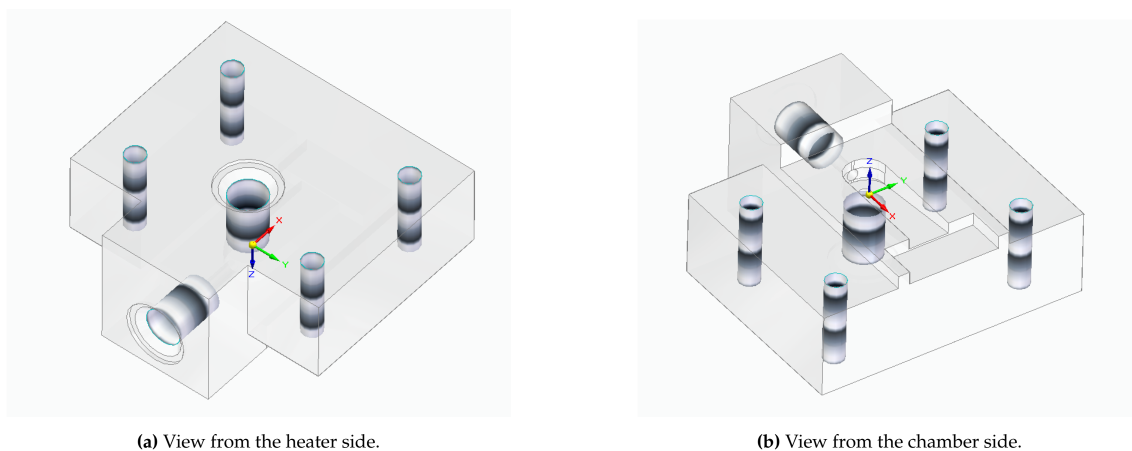

(a) View from the heater side. **(b)** View from the chamber side.

Figure 5.16: Outlet design corresponding to the second iteration of the fluidic interface.

In these images, the opaque gradient cylinders represent areas where a thread should be created via tapping.

For this design, it was not yet sure whether a single PCB would be used for support of the whole assembly (as shown in Figure 5.17), or two PCBs would be rested on each fluidic interface's overhangs (as shown in Figure 5.18. As such, the small height difference for the overhangs was maintained.

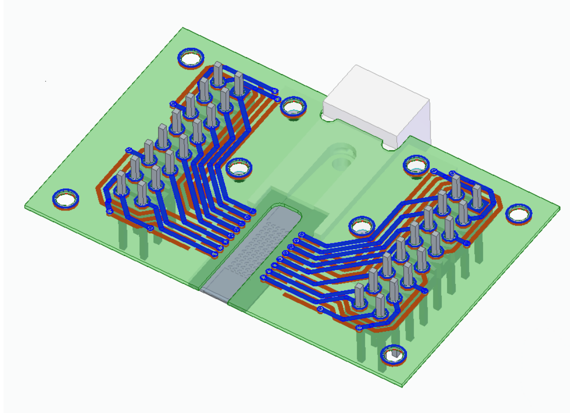

Figure 5.17: CAD assembly of the VLM and 2nd iteration fluidic interface with a single PCB design, used as holder for the whole assembly. The PCB is shown as semi-transparent, even though in reality it is opaque.

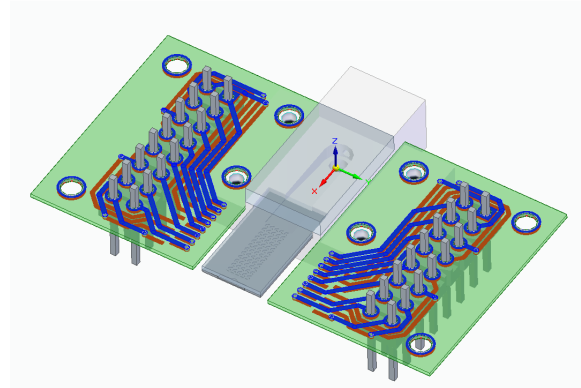

Figure 5.18: CAD assembly of the VLM and 2nd iteration fluidic interface with a twin PCB design. The PCBs would be glued to the fluidic interface, and a piece of glass would be used to seal the fluidic interface. The PCBs are shown as semi-transparent, even though in reality they are opaque.

Design Changes for Iteration 3

The design of the third (and final) iteration of the fluidic interface is not explained in this subsubsection, as it was already presented in the beginning of this section. However, the design changes compared to the second iteration are given below:

- By the time the design of the third fluidic interface was finalised, it was already decided that a single-PCB design would be used, for the reasons explained in Section 5.5. As such, the empty spacing between the overhangs and the single PCB were removed, ensuring a better mechanical design.
- The holes for the P/T sensor support were enlarged to 2.4 mm diameter, to fit M2 screws without tapping.
- The height of the interface at the MINSTAC connection was slightly decreased, to allow the PCB to sit perfectly horizontal during wire bonding. This also required moving the MINSTAC connection location slightly.
- A step difference was added on the heater side, to make wire bonding close to the inlet easier / possible
- Some of the mounting holes for the P/T sensor holder on the inlet and outlet for the no-nozzle configuration were moved, to be compatible with their PCB version. This resulted in slightly different designs for the inlet of the with-nozzle and no-nozzle thruster configurations.

5.5. Electrical Interface

For the electrical interface, simple PCBs were designed in Altium Designer to create the electrical connections between the VLM thrusters and the power source. Two versions were created: for the thrusters with nozzle, and without. The layouts of these PCBs are given in Figure 5.19 and Figure 5.20, respectively. The PCBs were manufactured by Eurocircuits[2].

[2] https://www.eurocircuits.com

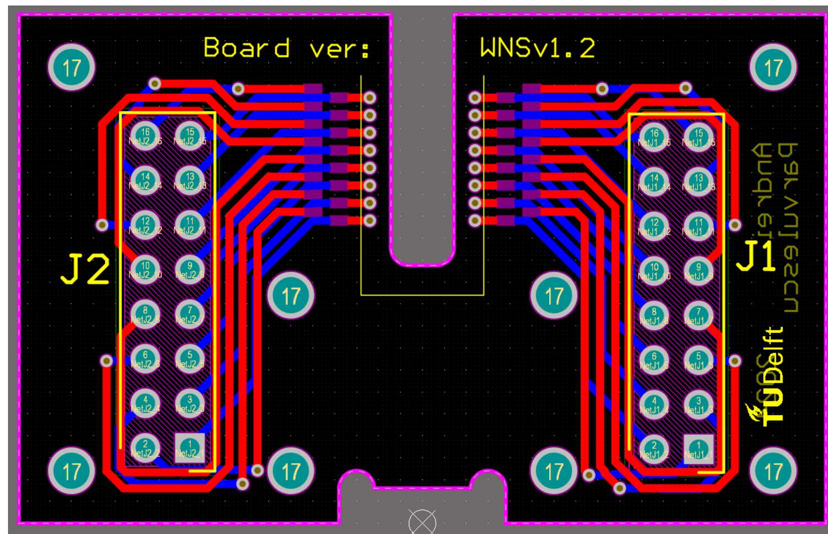

Figure 5.19: Layout of the PCB for the thruster configuration with nozzle. The placement of the thruster is indicated by the thin yellow lines. The fluidic interface would be placed at the bottom cut-out. The external dimension of the board is 46 × 29 mm.

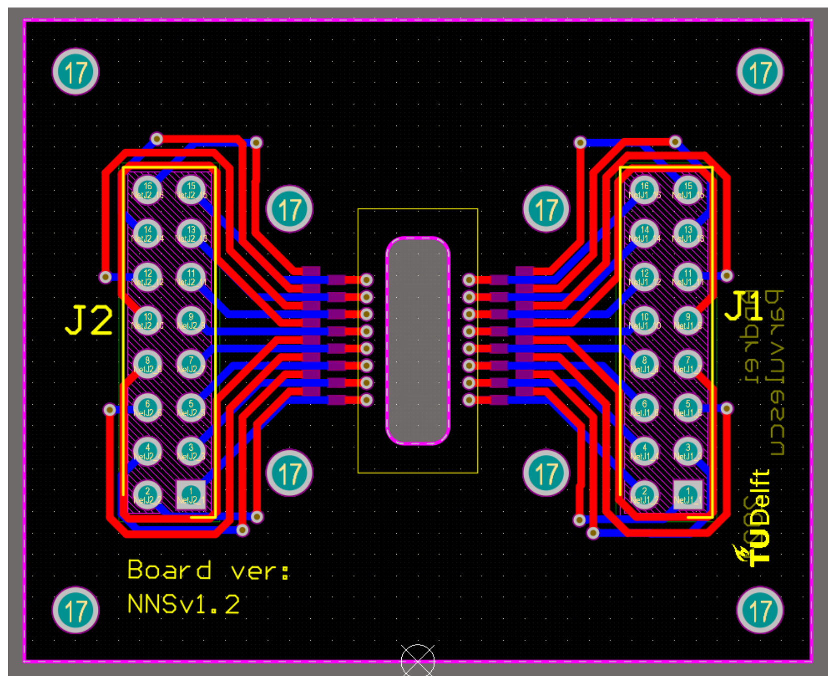

Figure 5.20: Layout of the PCB for the thruster configuration without nozzle. The placement of the thruster is indicated by the thin yellow lines. The fluidic interfaces (inlet and outlet) would be placed at the bottom and top. The external dimension of the board is 46 × 37.5 mm.

Initially, the design included two smaller PCBs per thruster, on each side, and using the fluidic interface as support, as shown in Figure 5.18. An additional piece of glass would have been needed to seal the fluidic interface. However, after a discussion with Mr. Stefano Speretta, it was decided to continue with a design that would require only one PCB per thruster, as it would be more resistant mechanically. In this case, part of the PCB would act as a fluidic barrier itself where the fluidic interface is, instead of the initially-proposed piece of glass. This is considered satisfactory, as the PCB has a layer of soldermask on the exterior, which is waterproof. This design is exemplified in Figure 5.17, in contrast to the previous twin-PCB design.

Regarding the heat resistance of the PCB, the FR-4 material of the board has a glass transition temperature

of 145–150 °C. This means that it should be suitable even for temperatures slightly higher than this. Furthermore, for the with-nozzle version of the board, it will never come into direct contact with the heated propellant, and is thermally isolated from the heaters (through the borosilicate glass layer of the thruster).

On the other hand, the no-nozzle version of the board will come in direct contact with the water vapour after heating up in the microchannels. If the operation pressure exceeds 4 bar, it is expected the vapour temperature to exceed 150 °C. As this scenario was not yet tested during the thesis, special attention has to be paid during no-nozzle tests at this temperature, checking if any leaks might appear, or if the board loses structural stability. Eurocircuits has an optional board material that has a glass transition temperature of 170–180 °C, but increases the price almost by a factor of 2. Due to the constraints of the thesis budget, this option was not pursued.

5.5.1. Wire Bonding Pads

The wire bonding pads follow an alternating pattern, in order to fit them more closely. This idea is borrowed from the design of Spernovasilis [18]. The pads themselves are 1×0.5 mm in size, allowing ample space for wire-bonding. The placement pitch on one row is 1 mm, leading to an overall pitch of 0.5 mm, which matches the average pitch of the heater pads. The thruster would be placed heater-side up, in between the bonding pads, on the location marked by the thin yellow outline in the layout (white outline in reality).

The bonding pads are plated with ENIG (Electroless Nickel Immersion Gold). This was chosen as gold is a good substrate for wire bonding, compared to other options. Furthermore, previous PCBs used at TU Delft for wire bonding were also manufactured at Eurocircuits using the same coating, proving that this method works.

5.5.2. 2.54 mm Pitch Header Pins

On the sides of the PCBs, through-hole header pins in a 8×2 configuration are added, to provide easier electrical connections with other equipment. The standard 2.54 mm (0.1 inch) pitch is used, for which connectors are widely available. For connection to individual pins, jumper cables can also be used, as they use the same pitch.

The traces on the PCB were laid such that the connection order on the bonding pads matches the connection order for the header pins. This is done in order to avoid confusion and make connections more straightforward.

5.5.3. Mounting Holes

There are two sets of mounting holes on the PCBs. The inner mounting holes are for the P/T sensor holder, and correspond to the mounting holes also present on the fluidic interfaces. As such, these have the double role of also being alignment markers for the fluidic interface. The outer mounting holes are used for mounting the board to external components, such as a possibly 3D-printed interface for the thrust pendulum. All mounting holes are 2.1 mm in diameter, to allow M2 screws to be used with them.

5.6. Assembly of the System

Once the fluidic interfaces and the PCBs are delivered, and the thrusters manufactured (up to and including the dicing step), these components need to be assembled. The expected assembly model is give in Figure 5.21 for the with-nozzle version, and in Figure 5.22 for the no-nozzle version. For both assemblies, it was eventually decided to solder the header pins on the fluidic side of the thruster / PCB. This is opposite to the placement shown in these CAD assemblies.

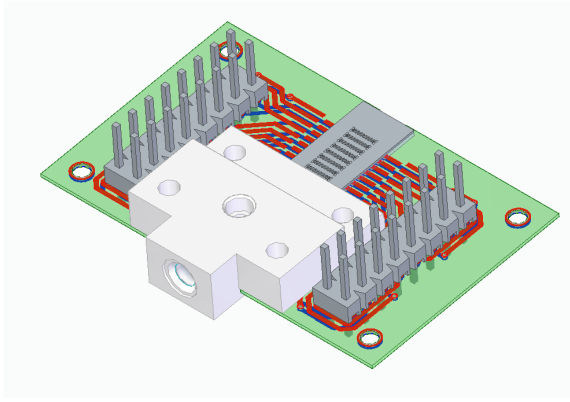

Figure 5.21: CAD assembly of the VLM thruster with nozzle configuration. Flow direction is from the bottom-left towards top-right

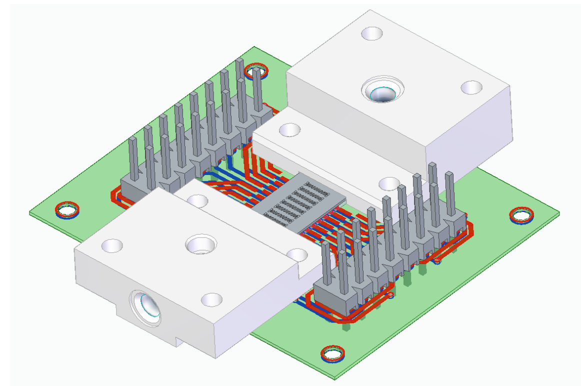

Figure 5.22: CAD assembly of the VLM thruster without nozzle configuration. Flow direction is from the bottom-left towards top-right.

The assembly of these components consists of two main steps: glueing the fluidic interface and the thruster to the PCB, and then wire bonding the thruster to the PCB golden pads. These steps are explained in the following subsections.

5.6.1. Glueing the Interface, Thruster and PCB

For glueing, a comprehensive list of available adhesives at the university was made, as well as looking online for different options. The main requirements that were looked for were:

- Non-conductive: as the glue will touch exposed areas on the PCB that should ideally not connect electrically to each other, the glue needs to be non-conductive
- Temperature resistance: the boiling point of water at 6 bar (the operating pressure mentioned in [15]) is around 159 °C [91]. Including a 10 °C margin due to possible temperature gradients in the silicon, a maximum operating temperature of at least 170 °C is looked for. At a minimum, a maximum operating temperature of 150 °C is looked for, corresponding to an operating pressure of 4 bar and margin.
- Vacuum compatibility: in order to be used in the vacuum chamber, the glue should have low outgassing, according to the NASA low-outgassing standard ASTM E959 [92].
- Relatively low viscosity: the glue should be able to be applied with a pressurised needle gun, due to the fine application required. Dr. van Zeijl mentioned that for this, a viscosity of around 50 000 cP (50 Pa · s) or lower is preferred.
- Working life: for ease of application, a work life of at least 30 min is preferred.
- Waterproofness: the glue has the main role of sealing the connections between the three assembly components. As such, it should be able to be waterproof for the short durations of the tests
- Material compatibility: the adhesive should bond with the materials of the three components, namely glass, silicon, PCB solder mask, and thermoset plastic.

The Ablestik Ablebond 84-3 non-conductive die-attach glue is chosen. This was in the possession of Dr. Henk van Zeijl at EKL, and was thus readily available and did not need to be ordered. It is electrically insulating, has a long work life, and is made specifically for bonding silicon chips to other substrates [93]. The glass transition temperature is of only 85 °C; however, as it will be shown in the next chapter, the assembly resisted up to temperatures of 180 °C (although not simultaneously tested under pressure). Furthermore, even though nothing about water compatibility is mentioned in its datasheet, it was also tested to sustain water pressures of up to 8 bar absolute (7 bar relative pressure), although at room temperature. The material was also found on the NASA Outgassing Database [94], passing the requirements of low-outgassing.

The adhesive is designed to be applied with a pressure needle gun. This is present at the MEMS Laboratory at EKL, and is also how the adhesive was applied in the context of this thesis. A pressure of

about 3.5 bar was used for the needle gun. The areas of application for the fluidic interface are shown in Figure 5.23, and for the PCBs in Figure 5.24. These are for a thruster with nozzle configuration, but similarly it can be done for one without nozzle. In that case, two fluid interfaces (an inlet and an outlet) would be glued, along the thruster and the PCB. Once the glue is applied and the components brought together, the assembly should look as in Figure 5.25.

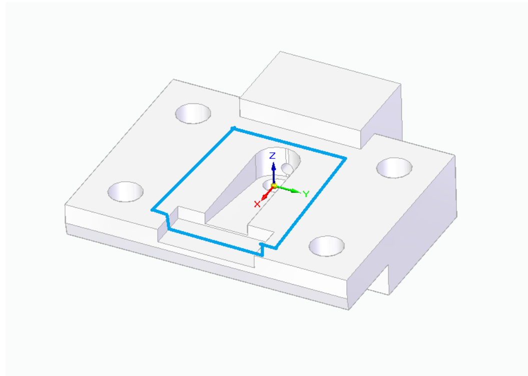

Figure 5.23: The inlet version for thrusters with nozzles. The adhesive application area is shown with blue.

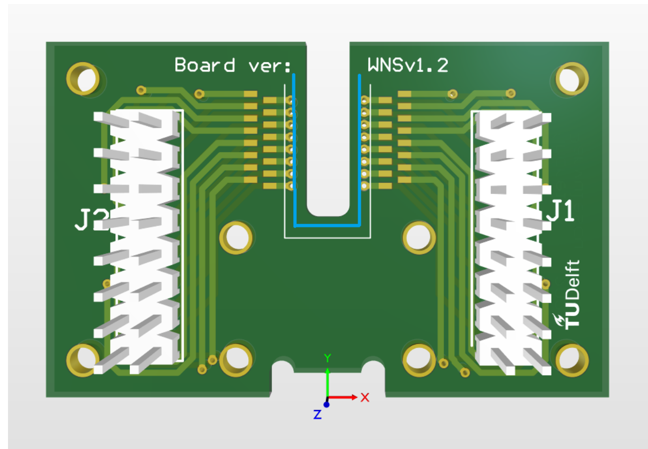

Figure 5.24: The PCB version for thrusters with nozzles, viewed from the fluidic side. The adhesive application area is shown with blue. Note that the header pins are shown on the wrong side in this view.

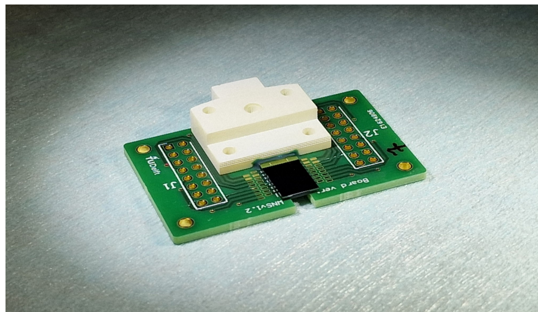

(a) W6R4C07 thruster assembly with nozzle.

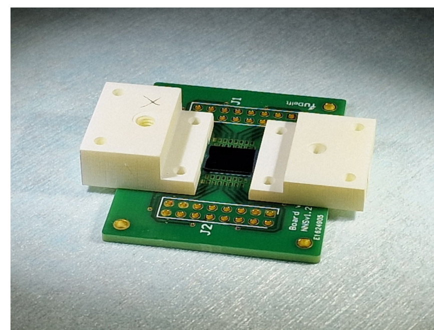

(b) W6R3C06 thruster assembly without nozzle

Figure 5.25: Thruster assemblies after glueing.

The next step is curing the adhesive at 150 °C for an hour, after which the glueing step is finished. This was done in a furnace, also in the MEMS Laboratory.

5.6.2. Wire Bonding

To connect the thruster heaters to outside interfaces, wire bonding is needed, where wires are bonded both to the aluminium pads on the thruster, and to the ENIG coated bonding pads on the PCB. Aluminium wires of 33 µm were used, two per connection. It was first attempted to bond using gold wires; however, this had issues with sticking to the ENIG pads. Furthermore, good clamping was required for obtaining consistent wire bonds.

The wire bonding diagram is presented in Figure 5.26, while in Table 5.2 the settings for the wire bonder can be found. The thruster assembly in the wire bonder can be visualised in Figure 5.27, while in Figure 5.28 an assembled configuration with no nozzle, post wire binding, can be seen.

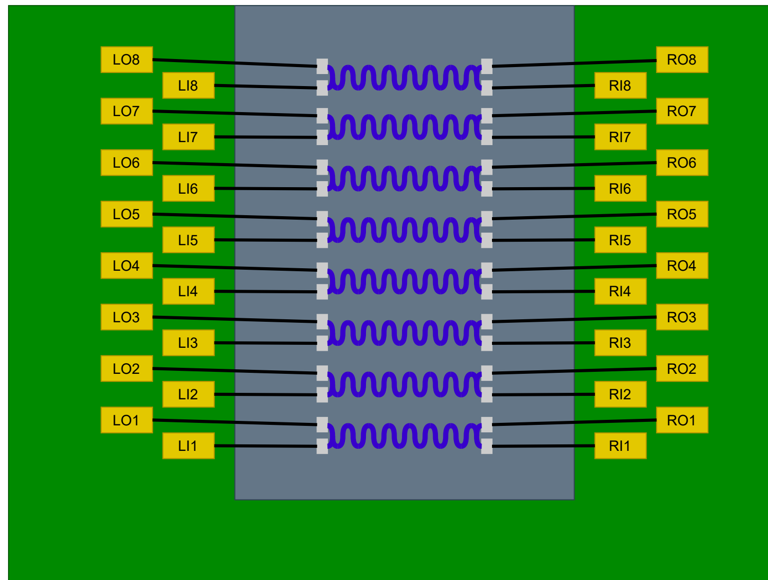

Figure 5.26: Diagram of the wire bonding connections from the thruster heaters to the PCB bonding pads. The nomenclature is L/R for left/right, I/O for inner/outer, and the heaters are numbered 1 through 8 from the inlet side to the outlet or nozzle side.

Table 5.2: Wire bonding parameters used on the Accelonix TPT HB10 wire bonder

	First bond	Second bond
Ultrasonic Power [mW]	700	800
Time [ms]	300	500
Force [mN]	450	800
Assumed wire length [µm]	3500	
Loop height [µm]	2000	
Tail feed [µm]	200	

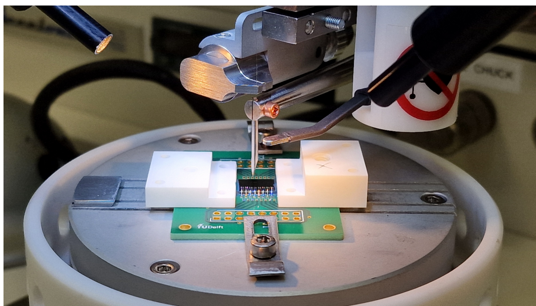

Figure 5.27: W6R3C06 thruster assembly in the wire bonder.

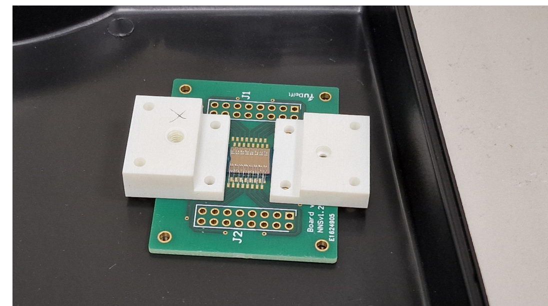

Figure 5.28: W6R3C06 thruster assembly after wire bonding.

The only remaining step is to solder the header pins on the PCB. Any 2 by 8 header pins configurations with 2.54 mm pitch can be used. For this thesis, header pins from TME[3] were ordered and soldered.

5.6.3. P/T Sensor & Thermocouple Holder

As discussed in Section 6.6, the wires on thruster W6R3C07 were encapsulated using a two-component epoxy adhesive. However, this proved to have a negative effect on the performance of the thruster, and

[3]https://www.tme.eu/nl/en/details/77313-818-16lf/pin-headers/amphenol-communications-solutions/

was abandoned for other thrusters.

In order to not accidentally touch the wires with a thermocouple used for reading the heater temperature, a holder was designed what was integrated into the P/T sensor holder. Its design can be seen in Figure 6.25. The design process is explained in more detail in Section 6.6.

A fully assembled thruster (using a batch 2 fluidic interface) can be seen in Figure 5.29. The assembled thrusters using a batch 3 interface would look similarly, with a new thermocouple & P/T sensor holder.

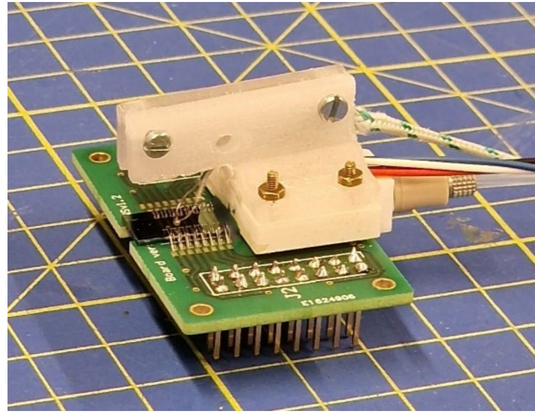

Figure 5.29: Fully assembled thruster W6R3C02, including the thermocouple, P/T sensor, and MINSTAC tubing. The power supply cables are not connected to the header pins.

5.7. Verification of the Design Requirements

In this section, the requirements are shortly verified to ensure compliance of the design.

- **REQ-VLM-INT-01**: The heaters of the thruster were successfully operated in the maximum temperature test described in Section 6.6. The interface successfully provided electricity to the VLM heaters, through the header pins, PCB, and bonded wires.
- **REQ-VLM-INT-02**: Each of the 8 heaters could be controlled independently, by making different connections through the 32 header pins. However, in this thesis, they are controlled together.
- **REQ-VLM-INT-03**: The cutouts in the PCBs offer optical access to the glass side of the VLM.
- **REQ-VLM-INT-04**: The outer mounting holes of the PCBs offer mounting options to external structures, through the use of M2 screws.
- **REQ-VLM-INT-05**: Fluidic access is provided through the fluidic interfaces, with the use of 062 MINSTAC 12 micron safety screens.
- **REQ-VLM-INT-06**: The fluidic access is in-line with the flow of propellant in the thruster, requiring no 90° turns.
- **REQ-VLM-INT-07**: The two inlet designs of the fluidic interfaces provide interfaces for the MS5837-30BA sensors, held in place with the use of a polycarbonate 3D-printed P/T sensor & thermocouple holder.
- **REQ-VLM-INT-08**: The heater side of the thruster remains exposed, allowing temperature reading via a thermocouple. If considered, a coating could be applied to the heaters to experiment with using a thermal camera for reading the temperature.
- **REQ-VLM-INT-09**: This is satisfied by the inlet of the with-nozzle configuration.
- **REQ-VLM-INT-10**: This is satisfied by the inlet and outlet of the no-nozzle configuration.
- **REQ-VLM-INT-11**: This was partially verified by the maximum pressure test described in Section 6.5, which showed no leaks in one thruster assembly up to 7 bar relative pressure under ambient atmospheric conditions. However, in order to increase the confidence in this result, multiple thrusters would need to be tested, as discussed at the end of Section 6.5. Furthermore, it still has to be coupled with a simultaneous test of maximum temperature.

- **REQ-VLM-INT-12**: This was partially verified by the maximum temperature test described in Section 6.6, which showed no electrical connection issues or structural issues up to around 180 °C heater temperature for one thruster assembly. However, in order to increase the confidence in this result, multiple thrusters would need to be tested, as discussed at the end of Section 6.5. Furthermore, it still has to be coupled with a simultaneous test of maximum pressure.
- **REQ-VLM-INT-13**: Most of the components were insured to use materials compatible with the ASTM E959. This was done by either direct information from the datasheet (as is the case for the Ultracur3D ceramic resin), or by checking the NASA Outgassing Database [94] for the same material (as is the case for the Ablestik Ablebond 84-3) or a similar material (for polycarbonate and PLA). However, the whole assembly still has to be tested under vacuum in the vacuum oven.
- **REQ-VLM-INT-14**: This is insured by threading the fluidic inputs according to the UNF#6-40 thread, and using the 12 micron safety screen.

5.8. Current Assembly & Fabrication Status

In this section, the current status of the available hardware that was manufactured and / or assembled for this thesis is presented.

Regarding the thrusters and wafers:

- All thrusters from wafer 6 were fully manufactured and diced, with the exception of W6R2C01, which broke during dicing. The thrusters from this wafer that were not yet assembled can be found in a wafer box in the SpE cleanroom workshop in the AE high-rise building, on the 8th floor. This wafer used the layout W01A, shown in Appendix B.
- Wafers 2 and 4 – 7 were manufactured up to and including the DRI etching step of the fluidic side (step 34 in Appendix C). These can be found in a transparent wafer box in the EKL Cleanroom 100. These are planned for further manufacturing (up to and including glass wafer bonding and dicing – steps 38 and 39) without further measurements.
- Wafers 8 – 14 were manufactured up to and including the coating of PR layer for the aluminium pads (step 16 in Appendix C). These wafers are back-ups, in case the new design of the thrusters or of the interfaces are inherently flawed, and the new batch cannot be used. It is recommended to fully manufacture them only after further experimental studies are performed with the already-produced thrusters & assemblies. These wafers can be found in a black box in the EKL Cleanroom 100.
- Wafer 3 was partially bonded with the wrong type of glass, and a part of the silicon layer broke when attempting to unstick the layers, as explained earlier in the chapter. This wafer can be found in one of the wafer boxes in the EKL Cleanroom 100 which were mentioned above.
- Wafer 15 (the test wafer) was only partially DRI etched, and has no glass layer bonded to the silicon layer. It was partially diced manually using a glass cutting pen. The resulting parts and thrusters can be found in a wafer box in the SpE cleanroom workshop in the AE high-rise building, on the 8th floor.

The fluidic side layout of each exposed wafer can be found in Appendix B. For up-to-date information on the wafers from the EKL Cleanroom 100, please contact Dr. Henk van Zeijl.

Regarding the PCBs, fluidic interfaces, and the assemblies:

- In total, 10 with-nozzle and 5 no-nozzle PCBs were ordered from Eurocircuits. However, 11 with-nozzle PCBs were delivered. There are 4 with-nozzle and 3 no-nozzle PCBs that remained unassembled so far. The unassembled PCB can be found in the thesis box of Andrei Pârvulescu in the SpE cleanroom workshop in the AE high-rise building, on the 8th floor.
- The following fluidic interfaces were produced (the unassembled fluidic interfaces can be found in the thesis box of Andrei Pârvulescu in the SpE cleanroom workshop in the AE high-rise building, on the 8th floor):
  - 8 second iteration inlet fluidic interfaces were 3D printed and threaded. Of these, 5 remain unassembled.

- 8 second iteration outlet fluidic interfaces were 3D printed and threaded. Of these, 7 remain unassembled.
- 7 third iteration with-nozzle inlet fluidic interfaces were 3D printed and threaded. Of these, 2 remain unassembled.
- 7 third iteration no-nozzle inlet fluidic interfaces were 3D printed and threaded. Of these, 6 remain unassembled.
- 7 third iteration no-nozzle outlet fluidic interfaces were 3D printed and threaded. Of these, 6 remain unassembled.

- 9 thrusters were assembled in total, with their fluidic interfaces and PCBs, in two batches: 3 in the first batch (using 2nd iteration fluidic interfaces) and 6 in the second batch (using 3rd iteration fluidic interfaces). These are presented in Table 5.3. Besides W6R3C07, they can be found in a black small box next to the thesis box of Andrei Pârvulescu in the SpE cleanroom workshop in the AE high-rise building, on the 8th floor. These are very fragile, as their bonded wires are exposed. As such, the box should be handled with extra care (and especially not tilted or flipped from the current horizontal position). W6R3C07 can be found in the thesis box itself.

Table 5.3: Assembled thrusters (with or without soldered header pins) that can be found in the SpE cleanroom workshop. Some additional details are included in the table.

Batch	Thruster	Nozzle type	Soldered header pins	Fluidic interface iteration	Notes
1	W6R3C01	No nozzle	Yes	2	Successfully tested during the maximum temperature test. Fully functional.
1	W6R3C02	Aerospike 1	Yes	2	Cracked longitudinally during maximum temperature tests. Most heaters are interrupted, making an electrical flow of current through them impossible.
1	W6R3C07	Long nozzle 1	Yes	2	Nozzle was blocked for maximum pressure tests. The bonded wires are encapsulated in epoxy. Cannot be used for high temperatures - epoxy starts decomposing, heaters lose electrical contact. Not fragile.
2	W6R2C06	Short nozzle 6	No	3	Not used for any tests. Marked with a "6" on its PCB.
2	W6R4C07	Short nozzle 7	No	3	Not used for any tests. Marked with a "7" on its PCB.
2	W6R2C10	Short nozzle 10	No	3	Not used for any tests. Marked with a "10" on its PCB.
2	W6R2C11	Short nozzle 11	No	3	Not used for any tests. Marked with an "11" on its PCB.
2	W6R2C12	Short nozzle 12	No	3	Not used for any tests. Marked with a "12" on its PCB.
2	W6R3C06	No nozzle	No	3	Not used for any tests. No marking on the PCB.

Other hardware manufactured, ordered, or used during this thesis, that can be found in the above-mentioned thesis box, includes:

- Heater cables with banana plugs and header connectors (blue & red) (see Figure 6.21 for reference of the blue one).
- P/T sensor only holder for 2nd iteration inlet fluidic interface, made from white PLA (see Figure 5.11 for reference).
- Thermocouple & P/T sensor holder for 2nd iteration inlet fluidic interface, made from dark blue PLA (see Figure 6.28 for reference).
- Thermocouple & P/T sensor holder for 2nd iteration inlet fluidic interface, made from semi-transparent white polycarbonate (see Figure 5.29 for reference).
- 45° inclined holder, used to measure a thruster's throat and microchannel profiles. made from orange PLA (see Figure 4.22 for reference).

- 2×8 header pin connectors from TME[4], with 2.54 mm pitch. 24 connectors were ordered, of which 20 remain unsoldered.
- 1.78 mm by 1.76 mm NBR70 O-rings for the P/T sensors (see Figure 5.9 for reference).
- 3 or 4 MS5837-30BA P/T sensors, in various states (in original packaging, only with soldered wires, or glued to an interface made by Melaika [54].
- Various MINSTAC components (tubing, safety screens, check-valves, solenoid valves, etc.). Additional MINSTAC components can be found in a plastic bag with zip, labelled "Micropropulsion", in the project boxes rack in the SpE cleanroom workshop. The thesis boxes of Gabriel Alves Teixeira and of Jules Vaes might also contain some MINSTAC components.
- Various bolts and nuts: M1.4×10 stainless steel and M1.4×12 brass bolts ordered from King Microschroeven[5]. Additionally, some M2 bolts, M2 nuts and M1.4 nuts were taken from a drawer in DASML near the DEMO workshop at AE. Normally, only M2 bolts and nuts should be used to connect the P/T holder (as is the case for 3rd iteration fluidic interfaces). However, as a design mistake was done in the 2nd iteration fluidic interfaces (as explained in Subsection 5.4.2), for this iteration of interface, M1.4 bolts and nuts have to be used.
- TCA9548A I2C Multiplexer from Adafruit trough Kiwi Electronics[6]. This is required to be able to read two MS5837-30BA sensors at the same time, for the no-nozzle configuration. However, this multiplexer was not used in this thesis, due to time constraints.
- K-type thermocouples (also in the thesis boxes of Gabriel Alves Teixeira and of Jules Vaes).
- Syringes and needles of different capacities and sizes.

[4] https://www.tme.eu/nl/en/details/77313-818-16lf/pin-headers/amphenol-communications-solutions/
[5] https://www.kingmicroschroeven.nl
[6] https://www.kiwi-electronics.com/en/tca9548a-i2c-multiplexer-2762

6

Preliminary Tests

In this chapter, the preliminary tests that were performed on the VLMs and other components are explained. The chapter begins by deriving the uncertainties expected from the measurements in Section 6.1. The results of the exploratory thermal camera tests are given in Section 6.2. Flow rate sensor and syringe pump calibrations are performed in Section 6.3. The oscillations resulting from the syringe pump are analysed in Section 6.4. The results from the maximum pressure and temperature tests are presented in Section 6.5 and Section 6.6, respectively. The derivation of the temperature coefficient of resistivity (TCR) is performed in Section 6.7.

6.1. Measurement Uncertainties

Several sensors and equipment are required for performing both preliminary tests, as well as the main tests of this thesis. In this section, the uncertainty in measurement is estimated for the used equipment. Unless otherwise mentioned, a $\pm 3\sigma$ (three times the standard deviation) confidence interval is taken, which provides a 99.7% probability that the true value falls in the mentioned interval, assuming a Gaussian distribution of the measurements.

The equipment for which the uncertainties are estimated, as well as the corresponding measured values, are given in the following list:

- TE Connectivity MS5837-30BA01 pressure & temperature sensor: inlet pressure p_{in} and temperature T_{in}
- K-type thermocouple (including reading with the NI-9211 DAQ): heater temperature T_H (or during exploratory testing T_{tc})
- Delta Elekronika SM 7020 power supply for the thruster heaters (including reading with the NI PCI-6229 DAQ): I_{PSU} and V_{PSU}
- FLIR A35SC thermal camera: thermal camera temperatures T_{cam}
- Sensirion SLI-1000 flow meter: water volume rate $\dot{V}_{SLI}$
- Mettler Toledo AG245 Analytical Balance: water mass during calibration m_{H_2O}
- Callipers: different distances and geometries d_{cal}
- Sensirion SHT4x Smart Gadget, using SHT40 humidity and temperature sensor: ambient temperature T_{amb}

For the MS5837-30BA01 sensor, its datasheet [95] shows that a pressure reading accuracy of ±50 mbar is valid between 0 and 45 °C, and of ±100 mbar between −20 and 85 °C. These values were also used by Versteeg [59], and are valid for readings up to 6 bar absolute pressures. For higher absolute pressures up to 20 bar, these uncertainties double. The same datasheet mentions a ±4 K accuracy for temperature.

For the accuracy of K-type thermocouples, a similar uncertainty estimation method as described by Versteeg [59] is used, but modified. The K-type thermocouples themselves have an accuracy of ±2.2 K

or 0.75% (in K), whichever is greater [96]. As these will not be used to measure temperatures below 20 °C, the 0.75% value is leading. On top of this, there is a ±2.5 K uncertainty from using the NI-9211 data acquisition board (DAQ) [97]. On top of these, Vesteeg adds a 5 K uncertainty from the uneven temperature distribution in his thruster. However, a very different version of thruster is studied in this thesis, and it is not assumed that the value read by the thermocouple is the propellant temperature in the acceleration temperature, as the thermocouple will be placed on the outside, only making thermal contact with the heaters. As such, this 5 K uncertainty source is not added. Combining the other two sources and assuming they are independent of each other, the measurement uncertainty for the thermocouple is (in K):

$$3\sigma_{T_{tc}} = \sqrt{(0.0075 \cdot T_{tc})^2 + 2.5^2} \tag{6.1}$$

For the expected temperatures of 20 to 200 °C, the accuracy range is 3.3 to 4.3 K.

The SM 7020 power supply unit (PSU) is used to power the heaters of the VLM. In its datasheet [98], a monitoring output accuracy of ±0.2% for the voltage reading and of ±0.5% for the current reading are given. The output from the PSU monitoring is a voltage in the 0–5 V range, proportional to the PSU voltage (maximum 70 V) or the PSU current (maximum 20 A). Additionally, the absolute full range accuracy (taken as a worst-case scenario) from the NI PCI-6229 DAQ in the ±5 V range is ±1.62 mV according to its datasheet [99]. This transforms to ±22.7 mV for the PSU voltage reading, and ±6.5 mA for the current reading. Combining these uncertainty sources together and assuming they are independent of each other, the measurement uncertainties for the PSU voltage and current are (in V and A, respectively):

$$3\sigma_{V_{PSU}} = \sqrt{(0.002 \cdot V_{PSU})^2 + 0.0227^2} \qquad 3\sigma_{I_{PSU}} = \sqrt{(0.005 \cdot I_{PSU})^2 + 0.0065^2} \tag{6.2}$$

For the full range of the PSU, the accuracies vary between ±22.7 mV and ±142 mV for the voltage, and between ±6.5 mA and ±100 mA. However, for the largest values measured during this thesis (25 V and 0.4 A), the accuracies are ±55 mV and ±6.8 mA respectively.

For the A35SC thermal camera, an accuracy of ±5 K is mentioned in the datasheet [100]. This value is what was used in previous works at TU Delft as well [59, 2].

For the Sensirion SLI-1000 flow meter, the accuracy is taken from its datasheet [101]. This is either 5% of the measured value, or 0.2% of the full scale, whichever is greater. These values are for water at 23 °C. As will be shown, the calibration tests were all within (0.5 ± 0.4)°C of this value. As such, the accuracy error corresponding to 0.9 °C of temperature difference is added according to the datasheet. This leads to a final accuracy of 5.09% of the measured value, or 0.204% of the full scale, whichever is greater. This means that for flow rates below 40 µL/min, the latter is leading, with an accuracy of ±2.04 µL/min. In the other cases, an accuracy of 5.09% is used. During tests, it was made sure that the sensor is placed horizontally; this is such that an additional error of 1% of the full range is not added to the accuracy.

For the Mettler Toledo AG245 Analytical Balance, the datasheet [102] mentions multiple sources of uncertainty: 0.1 mg readability, 0.1 mg repeatability (1σ), ±0.2 mg linearity, ±1.5 ppm/°C temperature drift, and ±0.003 %/year long-term drift. Additionally, a 3 s stabilisation time is mentioned, which coupled with estimated 3.3 µL/min evaporation rate during the tests (as will be shown later) and a water density of 997.42 kg/m^3 at 23.5 °C [91], leads to an estimated error of 0.16 mg. The temperature drift cannot be estimated, as the reference temperature is not mentioned in the datasheet. This is the same for the long-term drift, as the author does not know when the scale was first used. Combining all the mentioned sources (and using a 3σ repeatability value), an uncertainty of 0.41 mg for the mass measurements.

For standard 150 mm callipers, it is mentioned that the reading accuracy is of ±0.02 mm regardless of type [103]. As human errors are harder to estimate, this is the value that will be used to document the uncertainty.

For the syringe pump and flow meter calibration, the density of water is required, which is calculated from an online model based on temperature. The water is assumed to be in thermal equilibrium with

the atmosphere, and as such the ambient atmospheric temperature is used, measured with a Sensirion SHT40 sensor. According to its datasheet [104], it has a ±0.4 K maximum temperature accuracy. This value will be used as temperature uncertainty.

The uncertainties are summarised in Table 6.1.

Table 6.1: Measurement uncertainties of values used in the preliminary tests.

Parameter	Uncertainty (3σ)
p_{in}	±50 mbar (0 °C to 45 °C) or ±100 mbar (−20 °C to 85 °C)
T_{in}	±4 K
T_{tc}	$\pm\sqrt{(0.0075 \cdot T_{tc})^2 + 2.5^2}$
I_{PSU}	$\pm\sqrt{(0.005 \cdot I_{PSU})^2 + 0.0065^2}$
V_{PSU}	$\pm\sqrt{(0.002 \cdot V_{PSU})^2 + 0.0227^2}$
T_{cam}	±5 K
$\dot{V}_{SLI}$	±5.09% or ±2.04 µL/min, whichever is greater
m_{H_2O}	±0.41 mg
d_{cal}	±0.02 mm
T_{amb}	±0.4 K

6.2. Exploratory Thermal Camera Tests

Initially, the intention was to measure the temperature of the heaters and body of the thrusters using the A35SC thermal camera. However, as the thermal camera showed quite inaccurate temperature readings of objects at room temperature, and the surface of the thrusters was very specular reflective, this made measurements challenging. As such, exploratory testing was done to compare reading the temperature using the A35SC thermal camera, compared to a K-type thermocouple.

Two tests were done for this: one where the readings and different surface covers were compared on an aluminium bar, and one on the thruster chip itself. The thermal camera data was captured using the FLIR ResearchIR, while for the thermocouple the NI-9211 DAQ was used together with LabView 2019 software. The two tests are elaborated on in the next subsections.

6.2.1. Temperature Comparison Aluminium Bar

In this test, a K-type thermocouple was taped on an aluminium bar using vacuum tape available in the Space Engineering (SpE) Cleanroom at the Faculty of Aerospace Engineering (AE). Below it, a gap was left to measure the temperature on the aluminium bar directly. Below that, black electrical tape was applied for comparison, given that it has a high coefficient of emissivity. The thermocouple was connected to the NI-9211 DAQ, while the thermal camera was placed in front of the assembly to measure the temperatures. A picture of the test setup can be seen in Figure 6.1 together with a detailed view of the area measured with the thermal camera.

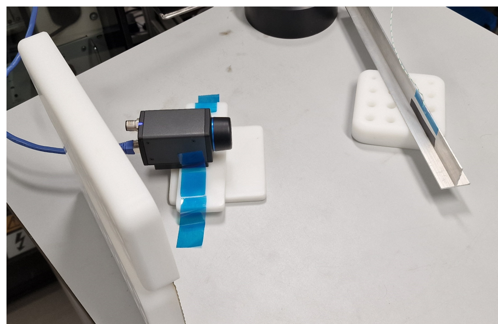

(a) Setup of the test.

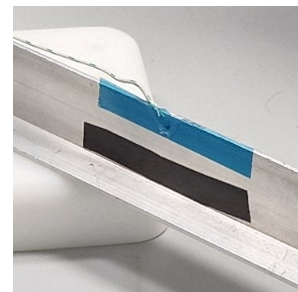

(b) Detailed view of the IR camera measurement area.

Figure 6.1: Aluminium bar temperature test comparison between thermocouple and thermal camera. The thermocouple is between the blue vacuum tape and the aluminium bar.

The shield that can be seen behind the thermal camera was placed such that any movement of the operator would not reflect off the aluminium surface into the thermal camera, affecting the results.

In the thermal camera software, three locations were selected for data collection, each representing the average of a 3×3 pixel area. A picture of their locations can be seen in Figure 6.2. Their evolution through time was recorded, along with that of the thermocouple.

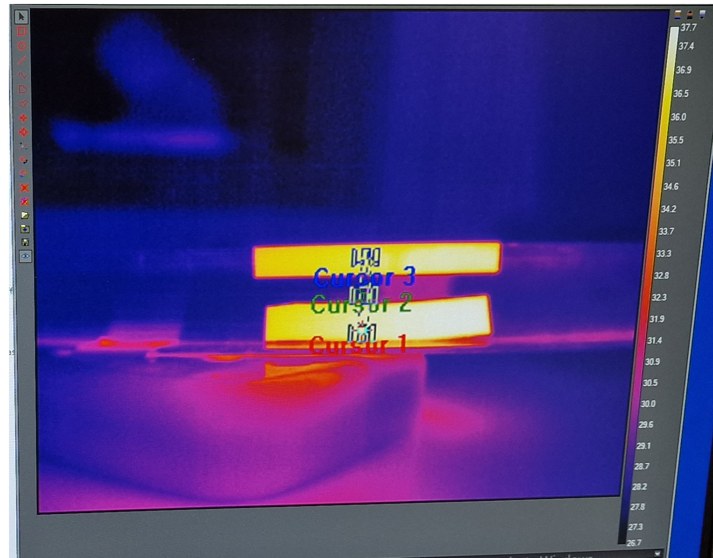

Figure 6.2: Data collection locations from the thermal camera measurement during the aluminium bar temperature comparison test.

The aluminium bar was heated from behind using a heat gun, in order to simulate the heating up from running current through the VLM heaters. The results are plotted in Figure 6.3.

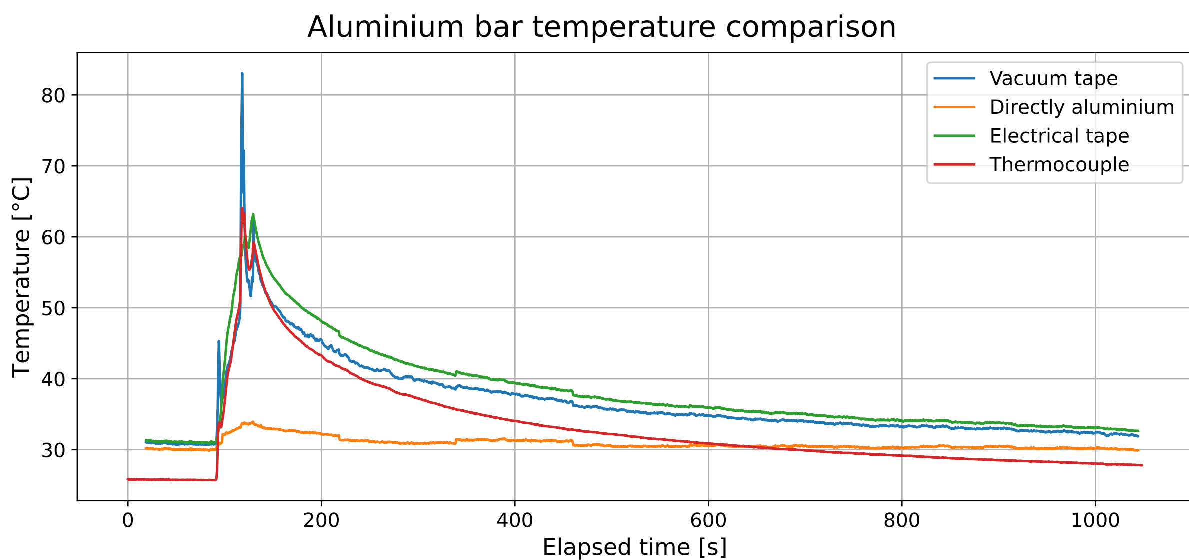

Figure 6.3: Aluminium bar temperature comparison test results after heating up with heat gun. The uncertainties mentioned in Section 6.1 apply.

Measuring the temperature directly on the bare aluminium has no significance to the true temperature. This is because the aluminium bar has a specular reflective finish, which in turn makes the thermal camera read the temperature of the room instead of the bar itself.

The other thermal camera readings and the thermocouple react similarly to the drop in temperature, showing a quasi-exponential drop behaviour. The time constant is similar, in the order of 103–108 s. However, the thermal camera readings have a number of issues:

- The room temperature values (before heating, and the asymptotic trend after heating) are much above expected conditions. Even though the room temperature in the cleanroom can vary, it is temperature controlled, and only temperatures between 23 and 24 °C were measured in other days (with an uncertainty of ±0.4 K). The thermocouple room temperature is below 26 °C, within its uncertainty, as estimated earlier. However, for the thermal camera readings, this room temperature is somewhere between 30–32 °C, outside the expected ±5 K uncertainty range.
- The thermal camera sometimes does some focus adjustments that can cause sudden, small jumps in reading. These can be observed at the 218 s, 339 s, and 460 s timestamps.
- The difference between the thermal camera and thermocouple readings is not constant. While immediately after heating these match (especially for the vacuum tape), as the temperature drops closer to room temperature, this difference increases.

6.2.2. Temperature Comparison VLM Thruster

A similar test was done for the VLM thruster directly. The K-type thermocouple was placed on the surface of the chip on the heater side, where it was taped with vacuum tape. Additionally, thermal paste was applied to improve thermal contact. In hindsight, this was not needed, as the temperature response of the thermocouple seemed to be good even without from the previous test. Furthermore, it is messy to work with, and it ended up clogging the nozzle of the thruster when trying to remove it; as such, it was not used again.

The setup of the test can be seen in Figure 6.4, along with a detailed view of the thruster assembly. The same shield from the previous test was also used here. The thermal camera had two measurement locations this time, as no black electrical tape was used. These were on the bare titanium heaters, as well as on the vacuum tape close to the thermocouple. As before, the average of a 3×3 area was considered for each location. A picture of these locations can be seen in Figure 6.5.

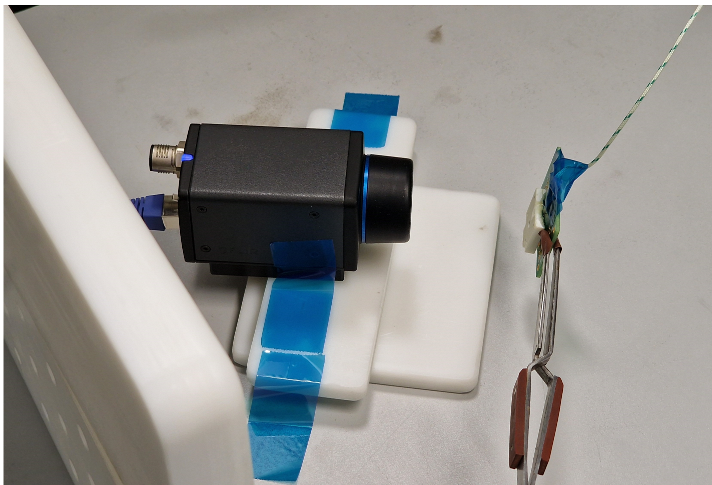

(a) Setup of the test.

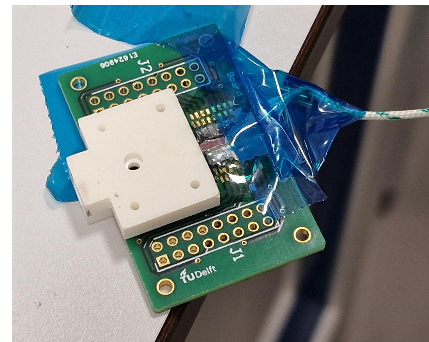

(b) Detailed view of the thruster assembly.

Figure 6.4: VLM thruster assembly temperature test comparison between thermocouple and thermal camera. The thermocouple is between the blue vacuum tape and the heater side of the thruster.

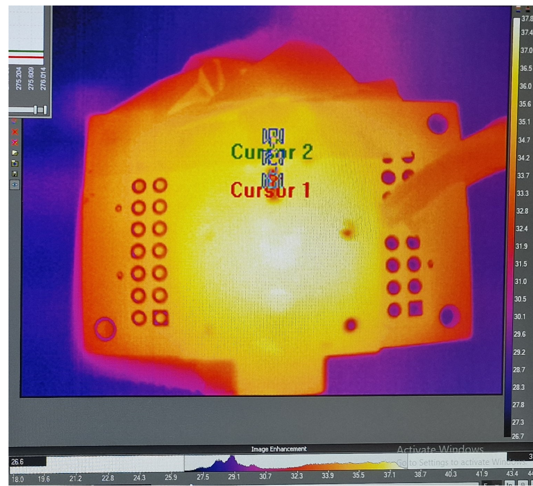

Figure 6.5: Data collection locations from the thermal camera measurement during the VLM thruster assembly temperature comparison test.

The thruster assembly was heated from behind using a heat gun, similar to the previous test. The results are plotted in Figure 6.6.

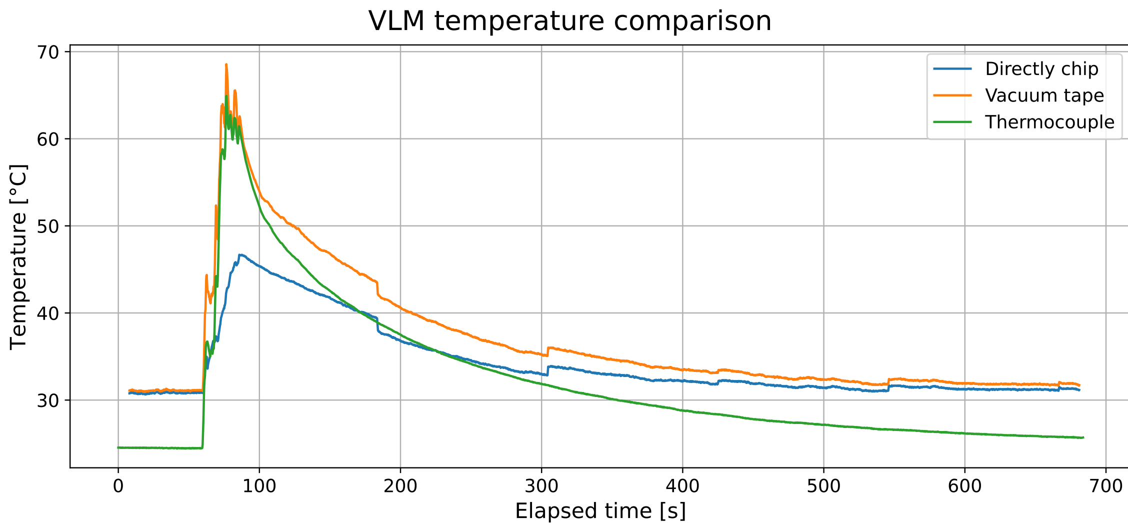

Figure 6.6: VLM assembly temperature comparison test results after heating up with heat gun. The uncertainties mentioned in Section 6.1 apply.

Very similar behaviours as in the previous test are observed. While the thermal camera measurement, done directly on the chip heaters, is more influenced by the true temperature, it is still well below the other readings. This difference, compared to the aluminium bar reading, might stem from the impurities and debris present on the surface of the chip, from the attempt of encapsulating the bonding wires between the thruster and the PCB.

Comparing the vacuum tape thermal camera reading to the thermocouple one, the same characteristics as in the previous temperature comparison test can be observed. These are namely the similar reaction time of the measurement reading, the too large room temperature readings of the camera, the small sudden jumps in the camera measurements, and the not constant difference between the two measurement methods.

For these reasons, together with the fact that the thermocouple has a smaller measurement uncertainty, it is preferred to use it versus the thermal camera. Furthermore, the thermal camera cannot be used in the vacuum chamber. This would require to use the resistance of the heaters to derive their temperature,

which while possible, is expected to be very noisy when using the voltage and current values directly from the power supply.

This high level of noise in the prediction of temperature from resistance was observed both in the work of Silva [2] (noise in the order of $\pm 20 - 40\,\mathrm{K}$) and in the predictions performed in Section 6.7 (noise in the order of $\pm 10 - 15\,\mathrm{K}$). Unless filtering is applied, this temperature reading method is of lower quality than the thermocouple for a future temperature control method. And as mentioned in Section 6.7, a high order filter can introduce significant delay in the measurement. An alternative resistance reading method that is less noisy could be derived, as shortly touched upon in Section 6.6; however, this would increase the complexity of the test set-up.

6.3. Flow Rate Sensor and Syringe Pump Calibrations

The NE-1000 syringe pump is used to dispense the water at a theoretically constant volume rate. Furthermore, the Sensirion SLI-1000 is used to measure the volume rate being dispensed into the system. The pump relies on knowing the internal diameter of the syringe in order to dispense the correct volume rate. Due to measurement uncertainties in determining the correct diameter, a calibration of the device is preferred. The SLI-1000 was not used before, as it was recently bought by Ir. Barry Zandbergen for the MSc thesis of Jules Vaes; as such, this also required a verification of the values being read.

A calibration test was designed for checking both the flow meter as well as the pump at the same time, similar to the one performed by Hutten in his thesis [56]. The test required the following components:

- NE-1000 syringe pump.
- Syringe (in this calibration, a 22 mL syringe was used) including needle fitting MINSTAC tubing.
- Sensirion SLI-1000 flow meter.
- Mettler Toledo AG245 analytical balance.
- MINSTAC 062 tubing of different lengths.
- Adaptors for the SLI-1000 to MINSTAC, borrowed from Jules Vaes.
- MINSTAC 062 check valves. This is required mostly as a female-female adaptor for connecting the tubing to the flow meter, in case the ends of the adaptors are male.
- A water recipient such as a Berzelius beaker (a 150 mL version was used in this test).
- Demineralised water
- Stopwatch

The basis of the test consists in pumping the water from the syringe, through the flow meter and into the beaker that is on the scale. The mass is noted down when the flow is started and stopped, and using the time measured with a stopwatch, the average flow rate is calculated. This is compared both with the flow rate setting used on the pump, as well as with the average flow rate measured by the flow meter. A picture of the test setup can be seen in Figure 6.7.

The stopwatch function on a smartphone was used to measure the time. The average human reaction time is 250 ms [105]. For a conservative estimate, the error in each measurement is assumed to be twice that, at $\pm 0.5\,\mathrm{s}$.

The SLI-1000 is mounted horizontally, to not induce additional reading errors in the sensor. The internal diameter of the syringe of $18.98 \pm 0.02\,\mathrm{mm}$ was measured using calipers and used for the syringe pump. The exit tube was mounted using a wooden skewer. This was required such that the tube would not touch the beaker and affect the measurements. Furthermore, it had to be insured that the exit of the tube was submerged in water. Otherwise, due to surface tension, drops would form at the end instead of being a continuous flow, which would show periodic ripples in the flow meter when the droplet would detach and drop in the beaker. A detailed view of the exit of the tube can be seen in Figure 6.8.

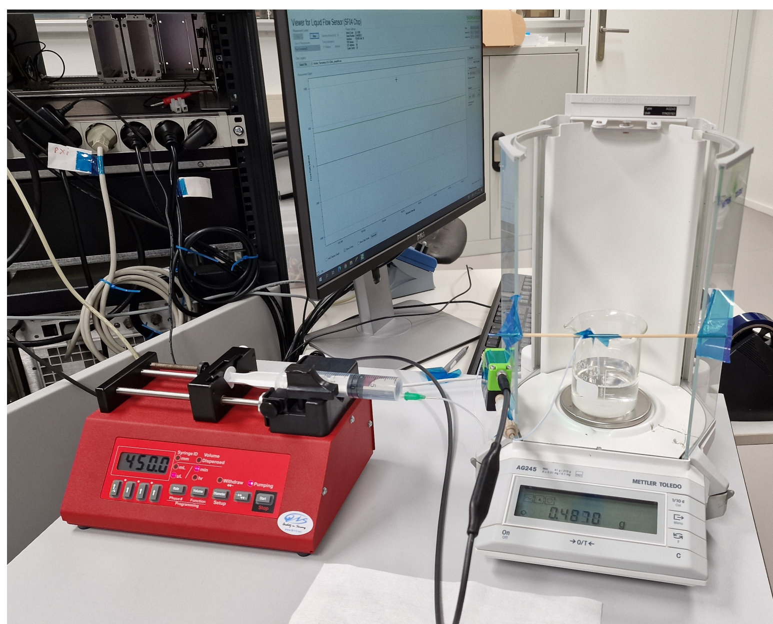

Figure 6.7: Test setup of the flow meter and pump calibration.

Figure 6.8: Detailed view of the exit tube in the beaker. The tube does not touch the sides or the bottom of the beaker, and its exit is fully submerged underwater.

After these measurements, a longer-duration test was also done without the pump functioning, to measure the evaporation rate of the water in the beaker. This way, it can be seen what is the impact on the calculated values, and if correcting them for this effect helps. The results of the normal measurements and of the evaporation test are presented in Table 6.2 and Table 6.3.

Table 6.2: Flow rate calibration measurements, part 1. Where N/A is mentioned, the author forgot to turn on the data acquisition and storage of the SLI software.

Test no.	Set flow rate [µL/min]	Measured by flow meter [µL/min]	Start mass [mg]	End mass [mg]	Start time [s]	End time [s]
1	700	713.46 ± 36.32	−4 ± 0.4	4093 ± 0.4	38.7 ± 0.5	387.3 ± 0.5
2	700	713.41 ± 36.31	−6 ± 0.4	4799 ± 0.4	100.9 ± 0.5	507.8 ± 0.5
3	700	712.97 ± 36.29	−4 ± 0.4	3857 ± 0.4	52.3 ± 0.5	377.5 ± 0.5
4	450	N/A	−1 ± 0.4	4405 ± 0.4	120.1 ± 0.5	700.4 ± 0.5
5	450	454.22 ± 23.12	−1 ± 0.4	2434 ± 0.4	17.5 ± 0.5	338.8 ± 0.5
6	450	452.22 ± 23.02	60 ± 0.4	2636 ± 0.4	34.6 ± 0.5	375.7 ± 0.5
7	450	455.76 ± 23.20	−4 ± 0.4	2637 ± 0.4	66.9 ± 0.5	415.1 ± 0.5
8	150	149.47 ± 7.61	−2 ± 0.4	1034 ± 0.4	29.7 ± 0.5	449.6 ± 0.5
9	150	N/A	−3 ± 0.4	1101 ± 0.4	24.8 ± 0.5	470.9 ± 0.5
10	150	149.91 ± 7.63	1097 ± 0.4	1873 ± 0.4	27.2 ± 0.5	342.5 ± 0.5
11	150	149.59 ± 7.61	1882 ± 0.4	2848 ± 0.4	34.2 ± 0.5	425.6 ± 0.5
12	50	49.34 ± 2.51	2849 ± 0.4	3164 ± 0.4	58.9 ± 0.5	464.7 ± 0.5
13	50	49.46 ± 2.52	3161 ± 0.4	3475 ± 0.4	32.1 ± 0.5	433.5 ± 0.5
14	50	49.69 ± 2.53	3500 ± 0.4	3763 ± 0.4	67.0 ± 0.5	392.6 ± 0.5
15	15	16.72 ± 2.04	3769 ± 0.4	3874 ± 0.4	102.6 ± 0.5	600.3 ± 0.5
16	15	16.15 ± 2.04	3874 ± 0.4	3949 ± 0.4	120.2 ± 0.5	477.7 ± 0.5
17	15	15.92 ± 2.04	3965 ± 0.4	4042 ± 0.4	134.8 ± 0.5	517.8 ± 0.5
Evap	-	-	389 ± 0.4	0.176 ± 0.4	6.1 ± 0.5	3899.0 ± 0.5

Table 6.3: Flow rate calibration measurements, part 2.

Test no.	Set flow rate [µL/min]	Calculated mass flow rate [mg/s]	Ambient temperature [°C]	Calculated volume rate [µL/min]	Corrected volume rate [µL/min]
1	700	11.752 ± 0.024	23.2 ± 0.4	706.95 ± 1.44	710.24 ± 1.44
2	700	11.807 ± 0.021	23.2 ± 0.4	710.25 ± 1.24	713.54 ± 1.24
3	700	11.871 ± 0.026	23.2 ± 0.4	714.09 ± 1.56	717.39 ± 1.56
4	450	7.594 ± 0.009	23.2 ± 0.4	456.79 ± 0.56	460.08 ± 0.56
5	450	7.578 ± 0.017	23.4 ± 0.4	455.82 ± 1.01	459.11 ± 1.01
6	450	7.552 ± 0.016	23.4 ± 0.4	454.29 ± 0.95	457.59 ± 0.95
7	450	7.585 ± 0.015	23.5 ± 0.4	456.23 ± 0.93	459.52 ± 0.93
8	150	2.467 ± 0.004	23.5 ± 0.4	148.41 ± 0.26	151.71 ± 0.26
9	150	2.475 ± 0.004	23.5 ± 0.4	148.86 ± 0.25	152.15 ± 0.25
10	150	2.461 ± 0.006	23.5 ± 0.4	148.05 ± 0.35	151.34 ± 0.35
11	150	2.468 ± 0.005	23.5 ± 0.4	148.47 ± 0.28	151.76 ± 0.28
12	50	0.776 ± 0.002	23.5 ± 0.4	46.70 ± 0.12	49.99 ± 0.12
13	50	0.782 ± 0.002	23.5 ± 0.4	47.05 ± 0.12	50.34 ± 0.12
14	50	0.808 ± 0.002	23.5 ± 0.4	48.59 ± 0.15	51.88 ± 0.15
15	15	0.211 ± 0.001	23.5 ± 0.4	12.69 ± 0.07	15.98 ± 0.07
16	15	0.210 ± 0.002	23.5 ± 0.4	12.62 ± 0.10	15.91 ± 0.10
17	15	0.201 ± 0.002	23.5 ± 0.4	12.09 ± 0.09	15.38 ± 0.09
Evap	-	−0.055 ± −0.00015	23.5 ± 0.4	−3.29 ± −0.009	-

In these tables, the mass flow rate from the Toledo readings $\dot{m}_{bal}$ is calculated as follows:

$$\dot{m}_{bal} = \frac{m_f - m_i}{t_f - t_i} \tag{6.3}$$

where m_i and m_f are the initial and final mass readings, and t_i and t_f are the initial and final stopwatch readings. The balance volume flow rate $\dot{V}_{bal}$ is then calculated by dividing by the average density of water during measurements, which is 997.45 kg/m^3 at 23.35 °C [91]. As during the tests, according to the tables, the ambient temperature could have varied from 22.8 °C to 23.9 °C (including uncertainties), a total uncertainty of ±0.13 kg/m^3 for the water density is introduced.

Lastly, this volume rate is corrected to take into account the average evaporation rate measured at the end of the experiments and reported in the last row of the table. The absolute of this value is added to $\dot{V}_{bal}$ to obtain the corrected volume rate $\dot{V}_{corr}$.

The flow rate measured by the flow meter $\dot{V}_{SLI}$ that is reported in the tables is the average calculated over the period when the pump was at full rate in quasi-steady-state, disregarding the start-up and slow-down periods.

In order to quantify the effect of correcting for evaporation during the calibration tests, the relative error of the SLI-1000 flow rate is plotted in Figure 6.9 for the 15 tests that include it. The accuracy value as reported by the Sensirion datasheet is given, as well as relative error compared to $\dot{V}_{bal}$ and $\dot{V}_{corr}$.

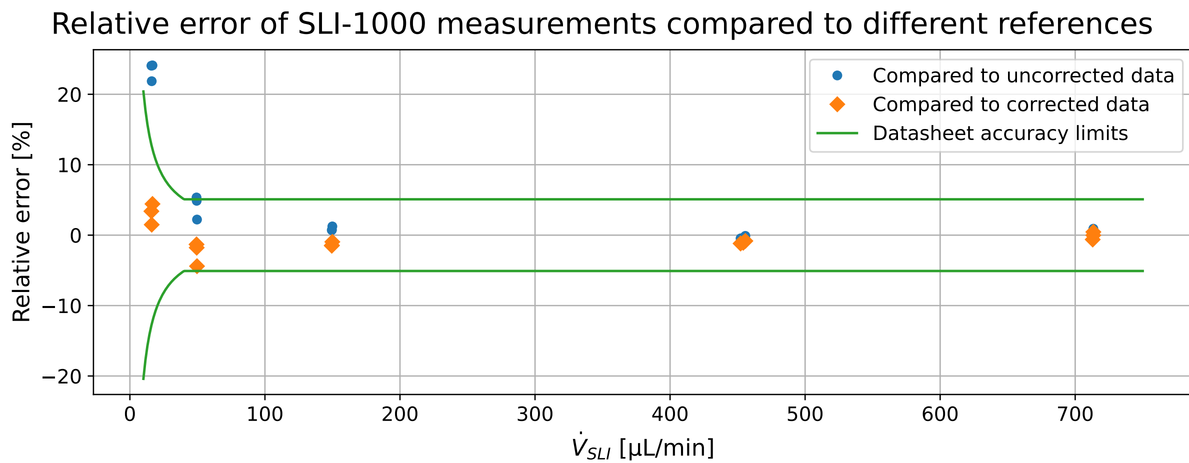

Figure 6.9: Relative error of SLI-1000 measurements compared to uncorrected and corrected flow rate, as measured using the analytical balance.

It can be seen that, on average, the error compared to the corrected data is smaller than for the uncorrected one, especially at low flow rates. It is out of the datasheet range for all 15 µL/min tests and for one of the 50 µL/min test. This shows that, while the evaporation has a limited impact on the calibration results at high flow rates, at flow rates lower than 50 µL/min this becomes significant and has to be considered. From now on, only the evaporation-corrected weigh scale data will be considered.

Another result of this comparison is that the accuracy of the SLI-1000 seems to not only be within the specifications in the datasheet, but actually better. This is especially true for the 15 µL/min tests, where an accuracy of ±4.5% can be observed, much better than the one calculated from the datasheet (around ±12.5%). This shows that the sensor is suitable also for very low flow rate measurement, and switching to the SLI-430 sensor is not required in these conditions.

In order to check the linearity of the SLI sensor compared to the measured values from the weight scale method, they are plotted one versus the other. The least-squares fit is calculated for a first order polynomial, with the intercept set at zero. This is shown in Figure 6.10.

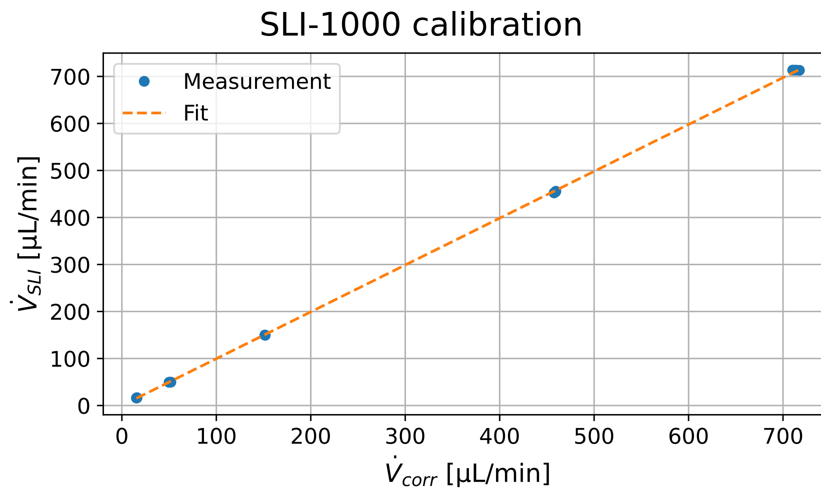

Figure 6.10: Measured SLI-1000 flow rates $\dot{V}_{SLI}$ plotted against evaporation-corrected weigh scale-calculated flow rates $\dot{V}_{corr}$.

An R^2 value of 0.9999 is obtained for the fit, showing a high degree of linearity between the two measurements.

For the syringe pump, a method of predicting the true average flow rate from the value set on the pump is derived, similar to the one performed by Hutten [56]. However, the values including the evaporation rate are also included in the current estimate. The corrected flow rate $\dot{V}_{corr}$ is plotted against the pump set value $\dot{V}_{set}$ in Figure 6.11, and again the least-squares fit is calculated for a first order polynomial, with the intercept set at zero.

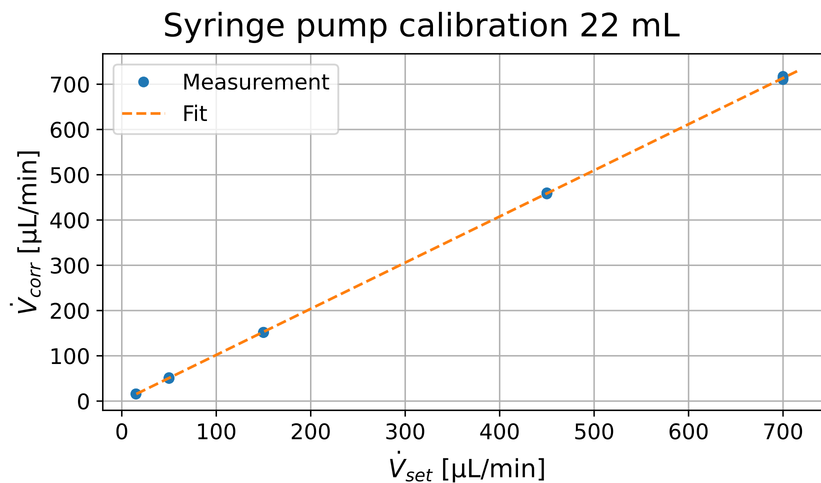

Figure 6.11: Evaporation-corrected weigh scale-calculated flow rates $\dot{V}_{corr}$ plotted against syringe pump-set flow rate values $\dot{V}_{set}$.

An R^2 value of 1.0000 is obtained, showing very high degree of linearity in the data, proving that the pump set value can be used to estimate the real average flow rate. The value of the slope is 1.0195 ± 0.0046 (3σ), which means a 0.45% uncertainty in estimating the slope. From Table 6.3, a maximum measurement relative uncertainty for the corrected volume rate is estimated to be 0.64% for the 15 µL/min average flow rate test. As such, the maximum overall uncertainty for using the pump value (multiplied with the aforementioned slope) to estimate the true average flow rate is 0.78% at 15 µL/min and up, or 0.54% at 50 µL/min and up.

As observed, the uncertainty of estimating the flow rate from the pump setting is lower than the SLI-1000 accuracy mentioned in its datasheet, especially for low flow rates. This is also the case if a maximum SLI uncertainty of 4.5% is assumed for the 15 µL/min tests. As such, for steady-state flow rate estimations, it

is recommended to use the corrected value from the syringe pump. However, this has the disadvantage that if a different syringe than the 22 mL one is used, the calibration has to be done again. Furthermore, it is still recommended to connect the flow meter to the future test setups, as it can capture the transitory start-up and shut-down values, as well the flow rate oscillations in steady state. This behaviour can then be compared to the one observed from the reading of the pressure sensor.

6.4. Syringe Pump Oscillations

As previously also observed by Silva [2], pump-induced oscillations in the flow were observed during operations. Silva observed them in the pressure reading during the operational tests; however, they could also be observed for this thesis in the flow rate readings during the calibration tests. The flow rate reading through time from the SLI-1000 sensor can be observed in Figure 6.12 for the 22 mL syringe, at a set flow rate of 450 µL/min.

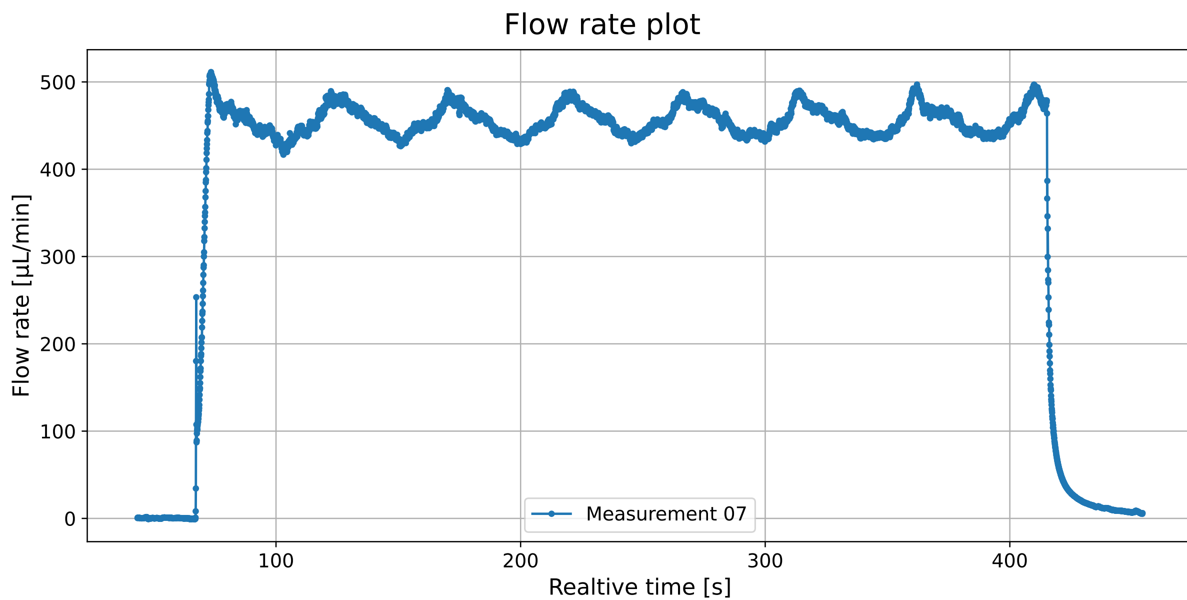

Figure 6.12: Flow rate sensor reading through time for 22 mL calibration test number 7.

Clear periodic oscillations can be seen, with relatively long periods. When studying the microchannel- and thruster-induced oscillations during the operation of the VLM, it is important to be able to differentiate between the oscillations from the pump, and those from the VLM itself. As such, an attempt is made to determine the frequencies at which oscillations appear only due to the test setup (mainly due to the pump). Additionally, trends are derived that are able to predict at which frequencies these oscillations will appear, depending on average flow rate and syringe diameter, such that they can be filtered out from any future instability analysis of the microchannels/thruster.

In order to isolate the frequencies in the signal, only the part that is not affected by start-up and shut-down transients is considered. The average value of the signal is then subtracted from the flow rate reading, to remove the DC component. During data acquisition, it was observed that the SLI software sometimes stores the measurements after a timestep of 1.5 times the usual sample period. For this reason, the data is interpolated to fit with the original sample period of 0.064 s, which corresponds to a sample frequency of 15.625 Hz. Afterwards, a Fast Fourier Transform is applied to the interpolated data, to obtain the frequency-domain components of the signal. An example for the 22 mL syringe at 150 µL/min is given in Figure 6.13.

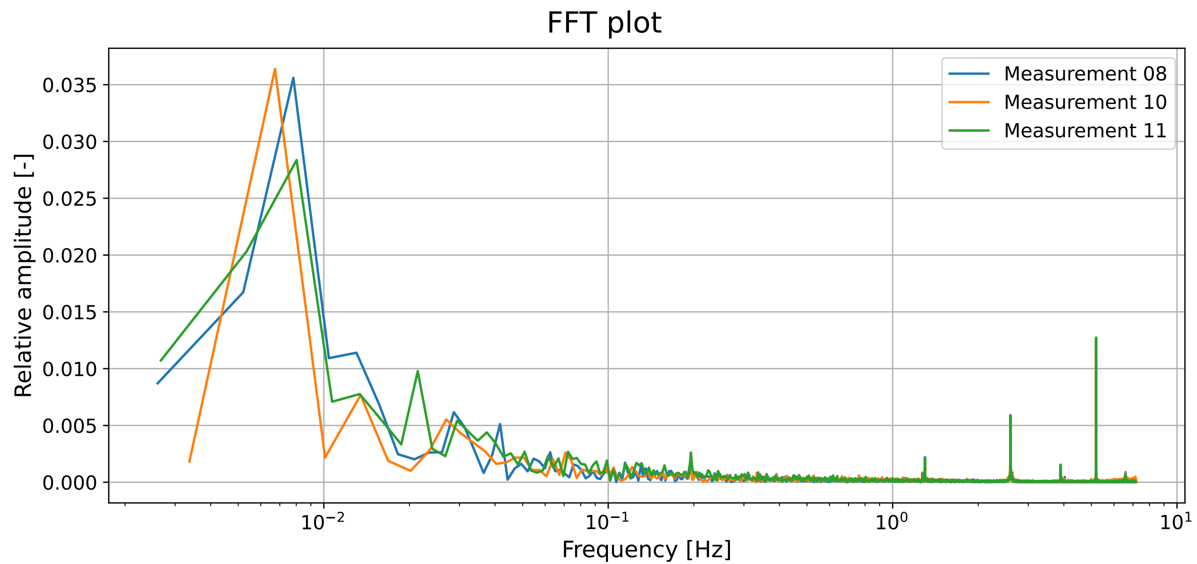

Figure 6.13: Fast Fourier Transform (FFT) plot for the quasi-steady-state component of the flow rate for 22 mL syringe calibration tests at 150 µL/min. The average of the signal was subtracted from the data before performing the FFT. The relative amplitude is calculated as the ratio between the true amplitude of the oscillations and the average of the quasi-steady-state flow rate value. Please note that the x-axis is logarithmic,

The main observed frequencies were extracted manually for each set flow rate and tabulated in Table 6.4. This includes data from the previously-mentioned 22 mL syringe done for the calibration. Additionally, measurements were also processed for a 5 mL syringe, which was initially intended to be used for the tests and was also partially calibrated. However, for this syringe only 6 tests we made for 3 different flow rates. It is to be mentioned that harmonics of the base frequency were not included, besides the case where their amplitude was larger than the base frequency, or the only one visible. This is especially the case for the third base frequency, for which the fourth harmonic has a larger amplitude than the base frequency, or is the only one visible (which is the case for the 15 µL/min measurements for the 22 mL syringe).

Table 6.4: Main oscillation frequencies observed in the flow rate calibration tests. *The value of f_1 at 50 µm/min is at the limit of what the FFT can calculate, and might thus be inaccurate.

$\dot{V}_{set}$ [µL/min]	$\langle \dot{V}_{SLI} \rangle$ [µL/min]	f_1 [Hz]	f_2 [Hz]	f_3 [Hz]	$4 \cdot f_3$ [Hz]	**Additional frequencies [Hz]**
22 mL syringe (18.98 mm internal diameter)						
700	713.3	0.033079	0.909	6.0615	-	-
450	454.1	0.020939	0.5849	3.897	-	6.5692
150	149.7	0.007523	0.19526	1.2995	5.1953	-
50	49.5	0.002944*	-	0.433	1.732	-
15	16.3	-	-	-	0.5295	6.012
5 mL syringe (12.03 mm internal diameter)						
664.3	711.6	0.076471	2.14706	-	-	-
511.0	547.3	0.05886	1.652	-	-	-
61.3	64.4	0.007143	0.19841	1.32141	5.28644	3.73249, 6.3761

In the above table, $\dot{V}_{set}$ is the flow rate set in the syringe pump, $\langle \dot{V}_{SLI} \rangle$ is the average of the SLI-1000 average flow rates through a set of measurements with the same $\dot{V}_{set}$, f_1 through f_3 are the three observed base frequencies that repeated across most conditions, $4 \times f_3$ represents the fourth harmonic of f_3, and the last column shows the frequencies that could not be correlated to either of the base

frequencies, or to their harmonics. The three base frequencies are not harmonics of each other, as they are not integer multiples of the lower one(s).

For the 5 mL syringe, 11.9 mm was used erroneously as syringe diameter in the syringe pump settings, instead of the true value of 12.03 mm from the table. As such, the $\dot{V}_{set}$ was off by a factor of about 1.022. The value of $\dot{V}_{set}$ reported in the table is already corrected for this error.

In literature, only one oscillation frequency due to the syringe pump is reported, and correlated to the natural frequency of the pump-syringe system [106]. This frequency is reported to be:

$$f_p = \frac{4 \cdot \langle \dot{V} \rangle}{\pi \cdot D \cdot s} \tag{6.4}$$

where f_p is the predicted oscillation frequency, D is the diameter of the syringe, and s is the pitch of the screw of the syringe pump, which is turned by the pump's motor. This is equivalent to the ratio between the average flow rate at the numerator, and the product between syringe inner cross-sectional area and pump screw pitch, at the denominator. For the pump used in this thesis, the pitch was measured to be 1.27 mm.

In order to check which of the frequencies mentioned above is the one that is reported in literature, and to see if there is a correlation with the average flow rate and square of syringe diameter also for the other base frequencies, a frequency factor k_f is defined as:

$$k_f = \frac{f \cdot D^2}{\langle \dot{V} \rangle} \tag{6.5}$$

This factor should be independent of which syringe is used and at which flow rate is the test performed. It should only be dependent on the pump and for which base frequency it is calculated. For the pump used in this thesis, and with the predicted oscillation frequency reported in literature, it is calculated to be $k_{f,p} = 4/(\pi s) = 1003\,\mathrm{m^{-1}}$. For the frequencies observed in the experimental tests, the factors are calculated and given in Table 6.5.

Table 6.5: Main oscillation frequency factors k_f observed in the flow rate calibration tests. *The value of the f_1 factor at 50 µm/min is at the limit of what the FFT can calculate, and might thus be inaccurate.

$\dot{V}_{set}$ [µL/min]	$\langle \dot{V}_{SLI} \rangle$ [µL/min]	f_1 **factor** [m^{-1}]	f_2 **factor** [m^{-1}]	f_3 **factor** [m^{-1}]	$4 \cdot f_3$ **factor** [m^{-1}]	**Additional frequencies factors** [m^{-1}]
22 mL syringe (18.98 mm internal diameter)						
700	713.3	1002	27550	183700	-	-
450	454.1	997	27840	185500	-	312700
150	149.7	1087	28200	187700	750300	-
50	49.5	1286*	-	189100	756400	-
15	16.3	-	-	-	703700	7990000
5 mL syringe (12.03 mm internal diameter)						
664.3	711.6	933	26200	-	-	-
511.0	547.3	934	26210	-	-	-
61.3	64.4	964	26770	178300	713300	503600, 860300
	Average	1029	27130	183400		
	3σ	36.4%	9.5%	8.6%		

As it can be seen, the values obtained along each column are close to each other, showing a strong correlation with $\langle \dot{V} \rangle$ and D for all base frequencies and their harmonics. The average for each base frequency is also calculated and reported at the end of the table. For f_3, as there was no distinguishable

frequency reading for the 15 µL/min flow rate for the 22 mL syringe, the value from the $4 \cdot f_3$ divided by 4 is used to calculate the average contribution for that particular flow rate.

The average of the f_1 factor is within 2.6% of the theoretical value calculated from literature, proving that this is the predicted oscillation frequency. The 3σ deviation in its value is quite large at 36.4%. However, this is mostly due to the value for 50 µL/min for the 22 mL syringe, as the frequency was at the limit of what the FFT could calculate given the total length of the signal. Without taking that value into account, a 3σ deviation of 17.5% is obtained and brings the average factor to within 1.7% of the literature value, namely to 986 m^{-1}. The other base frequency factors have better predicted values, at less than 10% 3σ deviation.

In order to prove the accuracy of these factors in predicting the pump-induced oscillation frequencies, the measured and calculated oscillation frequencies are plotted against the average flow rate in Figure 6.14, the top plot. For f_2 and f_3, the previously-derived factors are used to calculate the frequencies; for f_1, the theoretical value from literature is used, due to the relatively large uncertainty in its derived factor value.

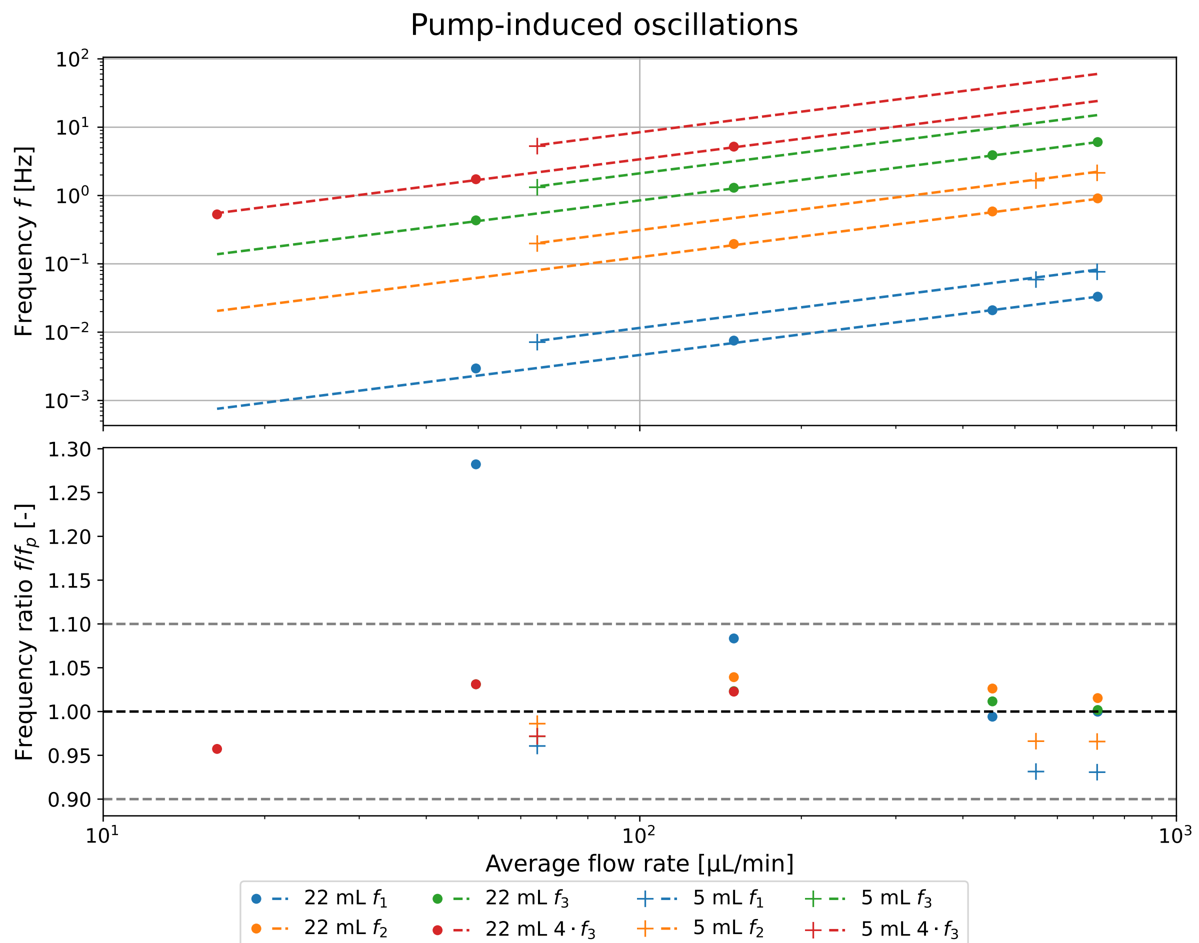

Figure 6.14: Comparison between the measured and predicted main oscillation frequencies at different flow rates. The graph on the bottom shows the ratio between the measured frequency f and the predicted f_p at the same average flow rate. Note that the frequency f in the top graph, as well as the average flow rate in both graphs, are plotted logarithmically.

At first sight, the calculated values follow quite well the measurements. In order to quantify the error, the ratio between the measured and predicted frequency for the available values is plotted versus flow rate in the bottom plot of the same figure. As it can be seen, all measured values fall within ±10% of the calculated ones, except for the f_1 base frequency measurement at 50 µL/min for the 22 mL syringe. However, as previously mentioned, the calculated frequency for this case was very close to the lower calculation limit of the FFT, and thus can be ignored as an outlier.

This proves that the calculated factors and the formula from literature can be used with a high degree of confidence to predict the pump-induced oscillation frequencies. In the context of studying the oscillations induced by the VLM thruster itself, the ones from the pump can be filtered out, aiding in the understanding of flow instabilities in VLMs and microchannels.

6.5. Maximum Pressure Tests

In order to test whether the assembly leaks at higher operational pressures, a maximum pressure test using liquid water was done. This test consisted in only a visual check on liquid water leaks in the system. It is not straightforward to calculate a liquid leakage rate just from pressure data, as liquids are considered incompressible. As such, if the assembly is to be tested also with a gaseous propellant (such as nitrogen), it is recommended to do also a gaseous leakage and maximum pressure test, as well as to derive the gaseous leakage rate.

This test consisted in pressurising the system using the syringe pump up to at least 6 bar relative pressure in normal atmosphere (7 bar absolute pressure) in order to check for any leaks and whether the system survives the theoretical operational pressure value of 6 bar in vacuum (as mentioned in [15]). Due to time constraints, the test setup was kept relatively simple. It is very similar to the one for the pump & flow meter calibration, with the important difference that instead of draining the water in the beaker, it is pushed into the thruster assembly. Furthermore, a MS5837-30BA01 pressure and temperature sensor was used to obtain the pressure in the system. This was held in place using a 3D-printed holder, some screws and nuts. A picture of the sensor being held in place is shown in Figure 5.11.

For this test, it was decided to block the nozzle. This allowed for better visualisation of possible leakages, as no water should flow out of the thruster system at all. In the case the nozzle would be left free, the water exiting the nozzle normally could coalesce on the thruster surface, and make harder the observation of leakages immediately around the thruster.

Another reason to block the nozzle is the fact that liquid water is an incompressible fluid, which means that chocked flow conditions in the throat of the nozzle would not be achieved. Thus, Equation 3.7 could not be used. This would make the estimation of the required mass flow rate much more complex, for a subsonic flow in complex geometry. An alternative would be to heat up the water to vaporisation in the microchannels. However, the electrical connections were not yet tested, which would only happen afterwards. Furthermore, these initially had issues, as explained in Section 6.6.

Initially, it was attempted to use the thruster that was used in the temperature comparison test, as its nozzle was accidentally blocked with thermal paste. A microscope picture of this is shown in Figure 6.15.

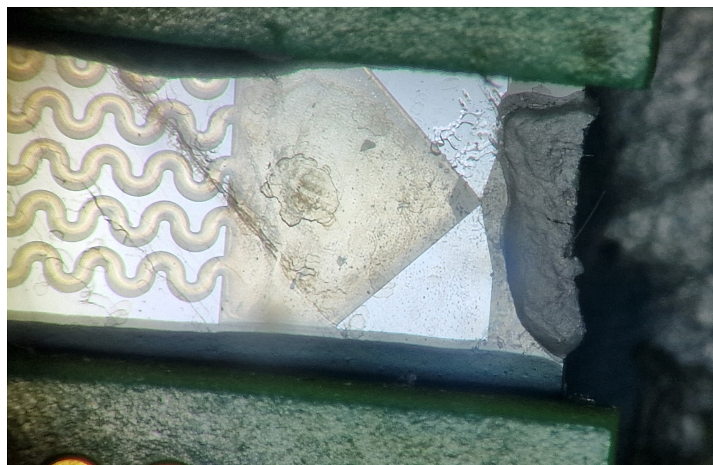

Figure 6.15: Blocked nozzle of the W6R3C07 thruster.

However, when attempting the test, the nozzle partially unclogged at around 3.5 bar absolute pressure. Afterwards, an attempt was made to block it using Pritt poster putty and vacuum tape, but this failed at around 1.8 bar absolute pressure. As such, it was decided that a temporary blockage of the nozzle was

not possible short-term, and a permanent solution was employed. This consisted in using 2-component epoxy adhesive (Pattex Power Epoxy, see Figure 6.16 for reference) on the nozzle and leaving it to harden overnight. This worked well in sealing the nozzle and allowing for pressure-testing the assembly.

Figure 6.16: Pattex Power Epoxy bought from Praxis in Delft.

Initially, the 22 mL syringe was used to perform the maximum pressure test. However, when the absolute pressure reached around 5.2 bar (relative pressure of 4.2 bar), the syringe pump started making periodic hitting noises, indicating that it has reached the maximum force it can give to the syringe plunger. Thus, it is estimated that the pump has a maximum pushing force of around 120 N.

The test was subsequently stopped to not damage the pump. It was decided to retry the test using the 5 mL syringe, as it has a smaller diameter. This way, the pump can provide a larger pressure for the same force (estimated at around 10.5 bar relative pressure). Furthermore, there was no need for a large amount of water for the water pressure test. Additionally, the SLI-1000 flow meter was also connected, to observe whether any water was flowing back into the syringe during the test.

The final test setup can be seen in Figure 6.17. Two check valves were used for both as an interface for the SLI-1000, as well as to try to prevent any flow back into the syringe. The readings from the pressure sensor and the flow meter are shown in Figure 6.18.

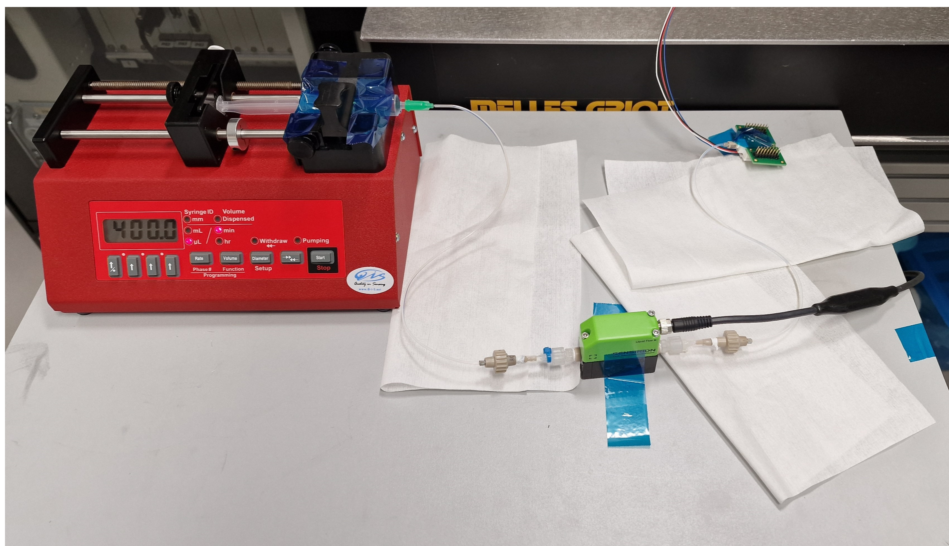

Figure 6.17: Maximum pressure test setup.

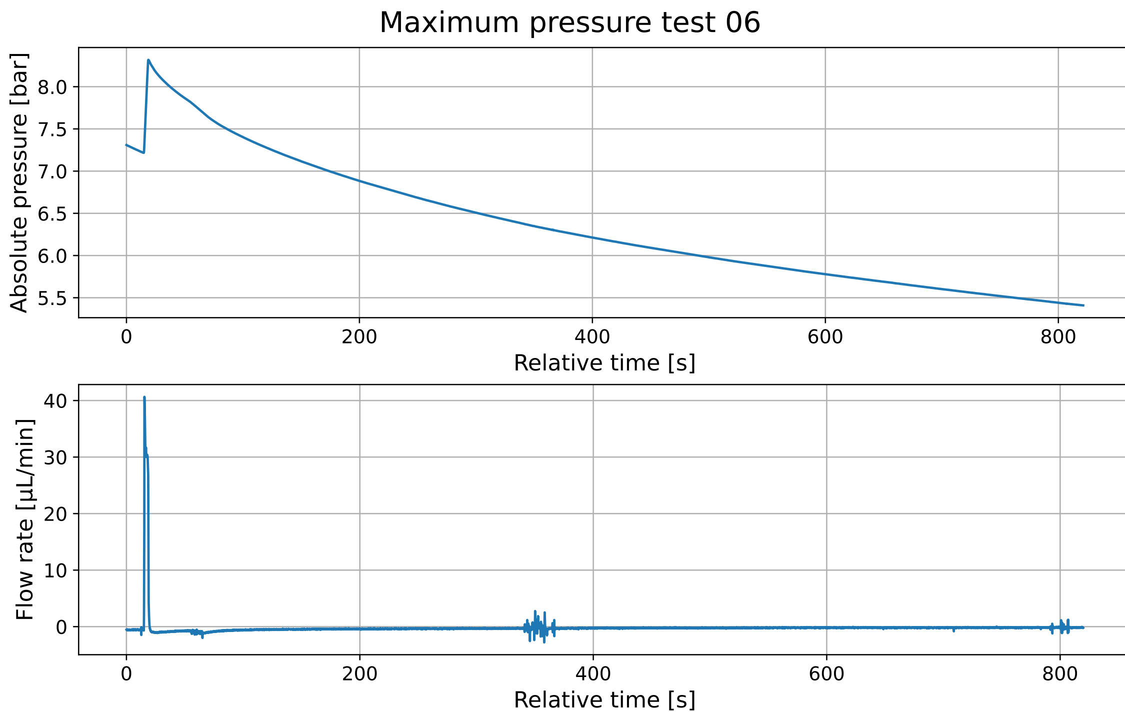

Figure 6.18: Maximum pressure test results.

The maximum absolute pressure that was achieved is above 8 bar (or 7 bar relative pressure), more than the requirement set at the beginning of this section. The pressure after the pump stops operating decreases relatively fast with time. This can be caused either by flow back into the syringe, or by a leak somewhere in the system.

The flow rate reading shows an average flow-back rate of around −1 µL/min. While this is smaller than the accuracy of the sensor, it is larger than the value that was observed that the sensor shows when there is no flow through it and is filled with water, which varies between −0.6 and −0.3 µL/min. As such, while the value reported by the sensor cannot be fully trusted, some flow-back into the syringe is expected, even with the check valves installed.

Regarding leaks, the only one that could be observed was at the syringe nozzle-tube interface, as shown in Figure 6.19. This can be easily corrected with a zip-tie; however, this was not available in the workshop when doing the test.

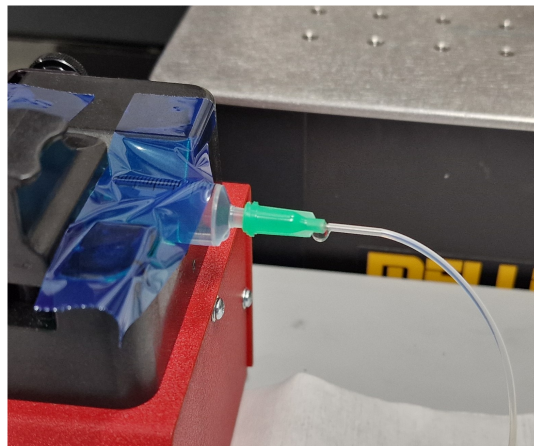

Figure 6.19: Water leak observed during the maximum pressure test. This appeared at the interface between the syringe needle and the MINSTAC tubing.

No other leakage sources were observed in the assembly. The system was checked especially at the tube-safety screen-fluidic interface-PCB-truster interfaces, both visually and with absorbent tissues, and no leak was observed while at these large pressures.

As only a small leak was observed, and very little flow-back into the syringe is expected, it was initially thought that the relatively large drop in pressure can be explained by the incompressibility of water, and the small volume that it is filling. As such, even a little amount of flow back or leakage could cause a significant drop in pressure. However, preliminary order-of-magnitude calculations showed that the expected pressure drop would have to be significantly larger than what was observed during the measurements, ruling out this possibility.

Another hypothesis was elaborated, that the observed flow back and drop in pressure is caused by a small amount of air expanding, which was trapped in the system before pumping the water. Before connecting the fluid system to the thruster assembly, all of its components (MINSTAC tubing and SLI-1000 flow rate meter) were filled with water. However, the thruster assembly itself was still filled with air at atmospheric pressure when the final tubing was connected. As gases are much more compressible than fluids, it is believed that the expansion of air was the driving mechanism behind the pressure drop. It is proven in Subsection 6.5.1 that first-order estimations have the same order of magnitude as the measured values; as such, this is considered to be a suitable explanation for this phenomenon.

During normal operation, however, the flow back that was observed in this test is not a concern, as the pressure will only be high during forward flow. Furthermore, with the zip-tie, no leakage can be expected in the system, especially on the more-critical thruster side. As such, it is concluded that this assembly can survive the required pressure levels. However, when operating above 4 bar relative pressure, the 22 mL syringe cannot be used, as explained earlier in this section. As such, a 5 mL or 10 mL syringe is recommended for higher pressures.

In order to be confident that any produced system is able to survive this pressure level, multiple assemblies would have to be tested. Usually, in engineering applications, a test to bogey method is applied in calculating the numbers of samples required to be confident that a system has a certain reliability during its lifetime [107]. For this, a minimum required reliability of the system R_b and a confidence level C_b (the probability that the reliability is indeed larger or equal to R_b) need to be defined. Once these are defined, the required number of samples to be tested n_{samp} can be calculated as:

$$n_{samp} = \frac{\ln(1 - C_b)}{\ln(R_b)} \tag{6.6}$$

Craggs [107] mentions that common practice in non-critical applications is to target $R_b = 90\%$ and $C_b = 90\%$, which results in a sample size of 22. This assembly is however intended only for testing purposes, and its proven reliability will increase as more experimental studies are done on the thruster at TUD. As such, it can be argued that an initial reliability requirement of minimum 75% (i.e., fewer than 1 or in 4 parts would fail) is satisfactory. This would lead to only 8 samples needing to be tested. However, even with this new initial sample size, it might be more worthwhile to directly test the thruster assembly for both high pressure and high temperature operations at the same time, verifying both REQ-VLM-INT-11 and REQ-VLM-INT-12. Alternatively, the first efficiency tests (for calculating η_h, C_d, etc.) could have the additional role of also verifying the above-mentioned requirements, bypassing the need for specific maximum pressure and temperature tests.

6.5.1. Coarse Estimation of Pressure Loss From Flow-Back

In this subsection, a short back-of-the-envelope analysis is made, in order to check if the small amount of flow-back in the flow meter can explain the large drop in pressure. As many of the variables used in this calculation are not accurately known and are only estimates, the most important findings are regarding the order of magnitude, not on the actual values.

For this analysis, the time period between seconds 24 and 26 (according to Figure 6.18) is considered. In this period, the transients from the sudden shutdown of the syringe pump settle. It will be assumed that the trapped air in the system went only through adiabatic changes throughout the test. While there

is some heat transfer taking place between the trapped mass of air and its surroundings, it is hard to quantify, and would require numerical simulations.

In this two seconds interval, the pressure drops from 8198 mbar to 8160 mbar, for an average pressure loss rate of $\mathrm{d}p/\mathrm{d}t = -19$ mbar/s. The average pressure is thus taken to be $\overline{p} = 8179$ mbar. In this interval, the average reading of the flow meter is of −1.5 µL/min. However, knowing that the bias of the sensor readout at zero flow rate is between −0.6 and −0.3 µL/min, an average bias of −0.45 µL/min is assumed. This leads to an estimated true flow of −1.15 µL/min.

Under adiabatic conditions, the following relation between pressure p and volume V is true:

$$p \cdot V^{\gamma_a} = a = \text{constant} \tag{6.7}$$

Where $\gamma_a = 1.4$ is the isentropic exponent of air, and a is a constant. To calculate the constant a, the initial conditions of the trapped air can be used. It is assumed that only the thruster assembly was filled with air, as was previously mentioned. This results in an initial volume $V_i = 44\,\mathrm{mm}^3$, the internal volume of the assembly (estimated from the CAD model). The initial pressure was of atmospheric air, assumed to be $p_i = 1$ atm. The constant a can be calculated to be $a = p_i \cdot V_i^{\gamma_a} = 5.088 \cdot 10^{-6}\,\mathrm{Pa} \cdot \mathrm{m}^{3 \cdot 1.4}$.

Rearranging Equation 6.7 to obtain the pressure as a function of volume, and differentiating with respect to time t, the following expression is obtained for the pressure change rate:

$$\frac{\mathrm{d}p}{\mathrm{d}t} = -\gamma_a \cdot V^{-\gamma_a - 1} \cdot a \cdot \frac{\mathrm{d}V}{\mathrm{d}t} = -\gamma_a \cdot \left(\frac{a}{p}\right)^{-1-1/\gamma_a} \cdot a \cdot \frac{\mathrm{d}V}{\mathrm{d}t} \tag{6.8}$$

In this equation, the instantaneous volume V was replaced with $(a/p)^{1/\gamma_a}$, which can be straightforwardly derived from Equation 6.7. Using this equation, and the value of $\overline{p}$ as the instantaneous pressure p, the pressure drop rate is estimated to be around −22 mbar/s, close to the −19 mbar that were measured.

This slight difference can be partially explained by the fact that measurements were inexact, with the flow rate particularly so (absolute value less than its measurement uncertainty). Furthermore, the assumption of adiabatic transformation is also not fully respected, as some heat transfer is still expected. The initial volume of trapped air could also be slightly larger or smaller than estimated. As such, only the order of magnitude of the results are relevant for the current comparison. Given that the calculated value and the measured one are in the same order of magnitude, it is considered plausible that most of the pressure drop was caused by the expansion of the trapped air and the slight flow back into the syringe, once the pump was stopped.

6.6. Powering Up and Maximum Temperature Tests

In order to test the correct operation of the heaters, as well as the operational limits of the assembly, powering-up and maximum temperature tests were performed. These required the creation of electrical cable interfaces between the thruster assembly and the power supply in the cleanroom.

Initially, it was considered to connect the heaters in series to the power supply. This had the advantage that all heaters would have the same amount of current flowing through them, and as such only the voltage drop across them would need to be read to calculate the individual resistances of the heaters. However, there were some issues with this approach.

Using an average heater resistance value of 140 Ω, and a maximum value of 20.75 W power required for operation at 4 bar absolute pressure of a thruster with 75 µm wide throat (value estimated from Section 3.5), connecting all heaters in series would result in a supply voltage of almost 153 V. The two power supplied available for powering the heaters each can supply maximum 70 V. While it would be close to connect 4 heaters per PSU and operating at a slightly lower pressure, this is not ideal. Furthermore, another issue is that the NI PCI-6229 data acquisition board used for reading voltage values can only read voltage differences of ±10 V, and only within ±11 V of the analogue input ground [99]. This is below the expected maximum 19.6 V voltage drop across each heater. As such, connecting in series is impractical.

It was decided then to connect the heaters in parallel. For the same operational requirements as mentioned before, the power supply requirements would be of 19.1 V voltage and 1.1 A, well within the capabilities. However, now there appears the issue that in the case that each heater resistance is needed to be measured (for example for determining the temperature along the thruster), the current through each heater would need to be known. As the PCI-6229 can only read voltages, a resistor in series to each heater is needed, across which the voltage could be read, and the current estimated. A diagram of a possible configuration is shown in Figure 6.20.

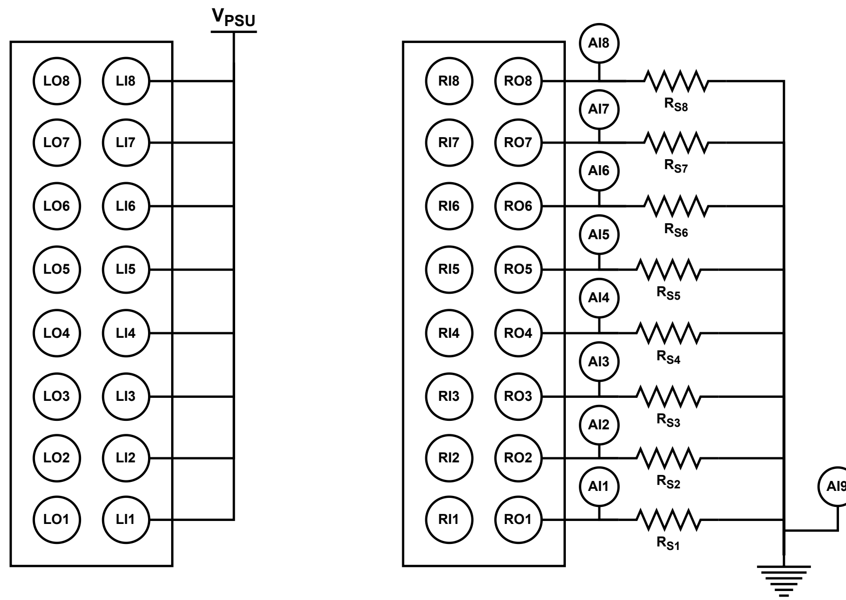

Figure 6.20: Electrical diagram of a possible powering of the VLM heaters in parallel. LO, LI, RI, and RO represent the connections on the PCB, as explained in Subsection 5.6.2. The R_S are the resistances that would be in series with each heater. AI represent the analogue inputs on the PCI-9226. V_{PSU} is the positive voltage connection of the power supply, while the icon on the bottom-right represents its ground connection.

The voltage drop over the resistors would be measured as the difference between AI1 through AI8 and the reference AI9 ground. Assuming that all R_S are known beforehand, dividing these voltages by their resistance values gives the current flowing through each heater. The voltage drop over each heater can be calculated as the difference between V_{PSU} and the readings of AI1 through AI8. A voltage drop through the cable from the positive end of the power supply up to the PCB would have to be estimated beforehand, as the voltage is too large to be measured there.

There are several constraints with this method. The first would be that the R_S resistors would need to have a very small temperature drift to not change resistance too much compared to the room-temperature values. Another would be that they would need to be small enough to not dissipate too much power during operation, which would heat them up. On the other hand, they need to be large enough such that a good reading precision is obtained when converting from voltage to current.

Due to time constraints, it was decided to not research and implement this version of the power setup that would allow reading the resistance of the individual heaters. The heaters were connected in parallel without any R_S resistors and without any analogue inputs for the PCI-9226. Only the voltage and current from the power supply were read. However, interface cables still needed to be created. An example of such cable made by the author is shown in Figure 6.21.

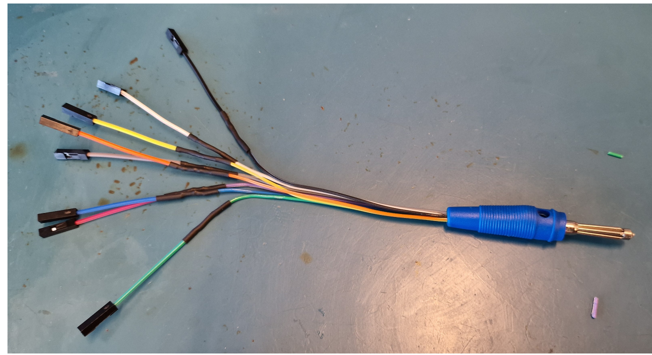

Figure 6.21: Heater connector cable.

This was made by cutting female-female breadboard jumper cables, soldering them to similar coloured cables, and then applying a male banana plug at the other end. Another version with a red banana plug was also created. This cable has the advantage that the female jumper ends can be attached to any of the header pins on the thruster, making particular connections easy to implement. However, it is quite fragile to work with. For the purposes of future exploratory tests, this is suitable. However, once a certain configuration will be fixed, it is recommended to use a 2.54 mm pitch 2×8 female connector instead of the female jumper ends.

In order to connect the cable to the PSU, its male banana plug end was connected to a female-female banana plug adaptor, and then using longer male-male banana plug cables to the power interface in the vacuum oven in the cleanroom. The jumper cable ends were connected to the headers on the VLM PCB. A picture of the initial test setup is shown in Figure 6.22.

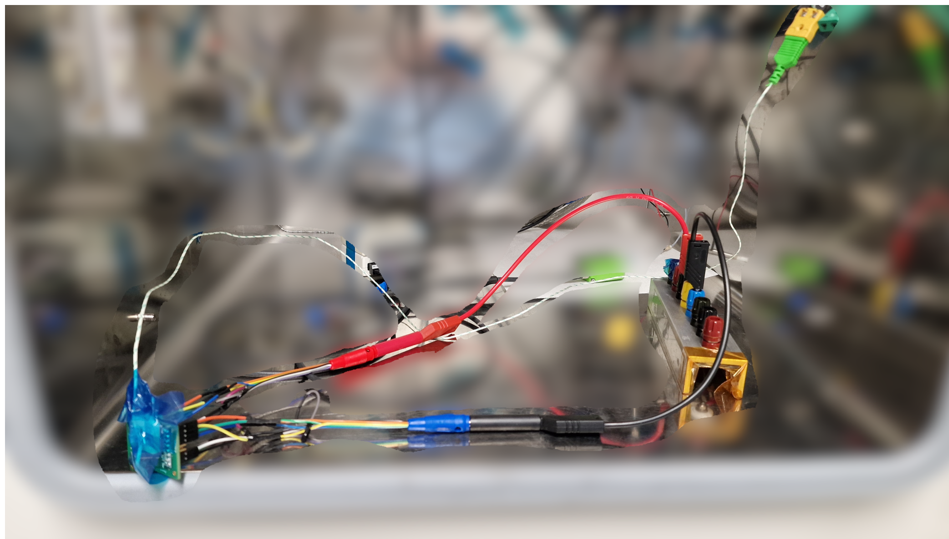

Figure 6.22: Initial test setup for the maximum temperature tests. The parts not relevant to this test were blurred, to focus the attention to the relevant components.

Additionally, the temperature had to be read. As a result of the test done in Section 6.2, a thermocouple was used for this purpose. The first thruster that was tested was the sacrificial W6R3C07, which had its wire bonds encapsulated in the Pattex epoxy adhesive to protect them during handling. As the wire bonds were encapsulated, the thermocouple could be placed on the chip without the risk of breaking the wires, and was thus just taped down, as shown in Figure 6.23.

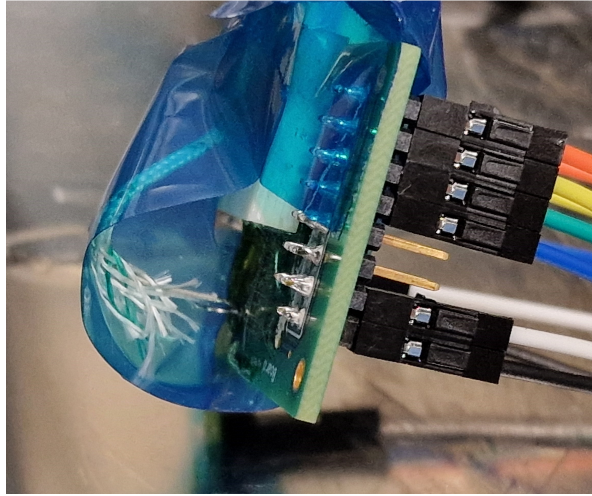

Figure 6.23: Initial thermocouple placement on the thruster assembly. the thermocouple is taped down using vacuum tape.

Initially, the heaters were connected to the Delta Elektronica SM-7020-D PSU operating in current-control mode. However, during the first tests, some heaters disconnected spontaneously from the power supply, which in turn increased the equivalent resistance and led to the PSU overcompensating the voltage supply, reaching saturation at 70 V. As this was clearly not the intended behaviour, it was decided to switch to using the SM-7020 PSU in voltage-control mode for future tests.

During the first test, the thruster managed to reach 180 °C, but a strong pungent smell from the assembly appeared, likely from the overheated epoxy. Some of the heaters no longer made electrical contact afterwards. In a subsequent test, a periodic behaviour was observed between the temperature value and connection status, as presented in Figure 6.24.

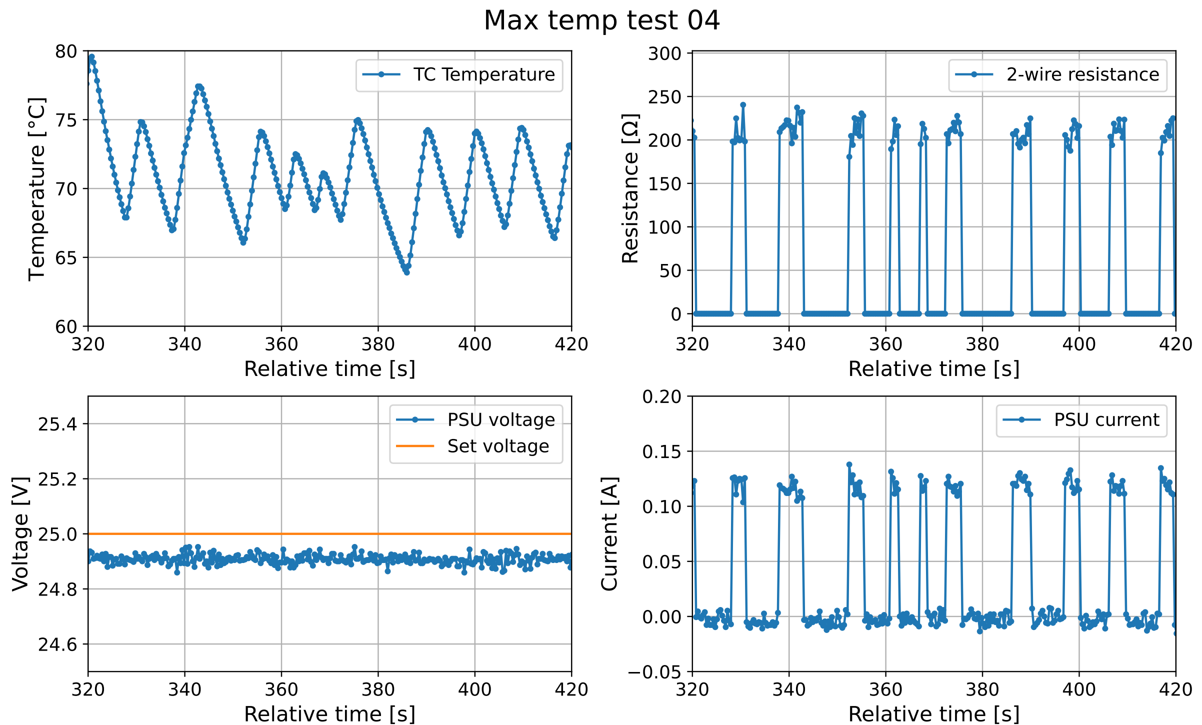

Figure 6.24: Detail of the results of maximum temperature test 4. The PSU voltage and current values were corrected by their 0-value readings of 0.8 V and −14.9 mA. The resistance was calculated as the ratio between PSU voltage and current. The value of the resistance was set to zero when the current reached close-to-zero values, to prevent unrealistically extreme measurements.

In a subsequent test, a Dino-Lite AM4113ZT camera was used to observe the behaviour of the epoxy encapsulation during power application. Panning through the resulting video, a small but discernible thermal expansion can be seen. When discussing these results with Dr. van Zeijl, he mentioned that these small expansions would be enough to break the wire bond connections. As such, the cyclic behaviour previously-observed can be explained as follows:

- The heaters are receiving power and heating up, which leads to the epoxy coating to heat up.
- As the epoxy coating heats up, it expands and breaks the electrical connection.
- The heaters no longer receive power, and cool down alongside the epoxy.
- As the epoxy cools down, it contracts and brings the wires back to the original position, re-establishing electrical connection.
- The cycle repeats, with the heaters receiving power again.

Therefore, it was decided that using the epoxy as wire encapsulant is not suitable, due to its thermal expansion. No other chips had their wires encapsulated. However, as the wires were now exposed and very fragile, a holder had to be designed, that would keep the thermocouple from moving during handling and would prevent it touching the bonded wires. It was decided to use the holder for the pressure and temperature sensor, and expand it with an overhang that could be tightened via some screws. It was made of two parts, as shown in Figure 6.25. It was subsequently 3D printed using 123-3D Dark Blue Jupiter Series PLA. The result can be seen in Figure 6.26, mounted on the thruster assembly and with a thermocouple in place.

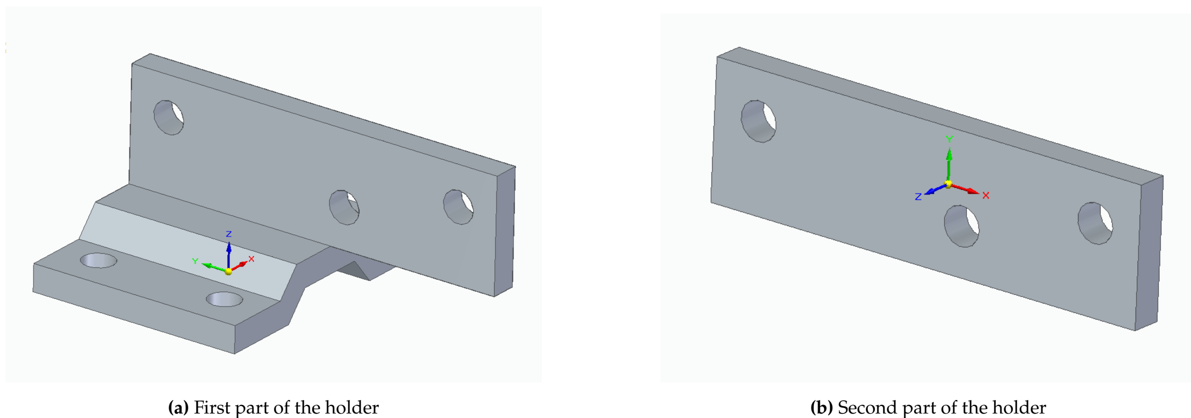

(a) First part of the holder

(b) Second part of the holder

Figure 6.25: New designed MS5837-30BA and thermocouple holder. The first part would be screwed into the inlet fluidic interface of the thruster assembly, and the second part would be screwed on the first part.

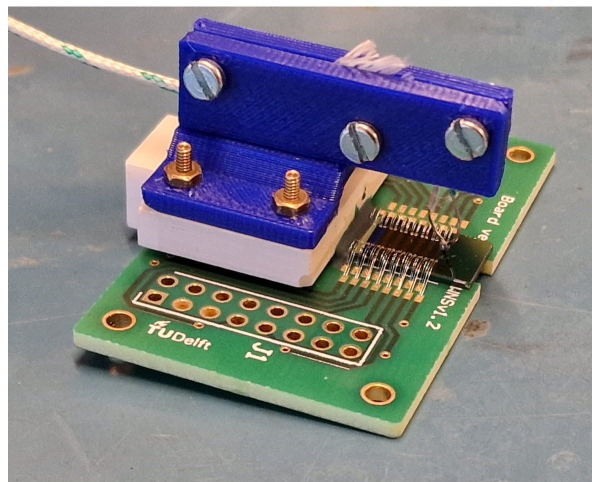

Figure 6.26: Thermocouple holder assembled on top of the W6R3C02 thruster assembly.

A subsequent test was done using thruster W6R3C02 and the thermocouple holder. However, after powering it up and heating it up to around 100 °C, the heaters started disconnecting one by one again. Observing the thruster under the microscope after the test, it was seen that the chip cracked, which disconnected most of the heaters. A picture of the cracks can be seen in Figure 6.27.

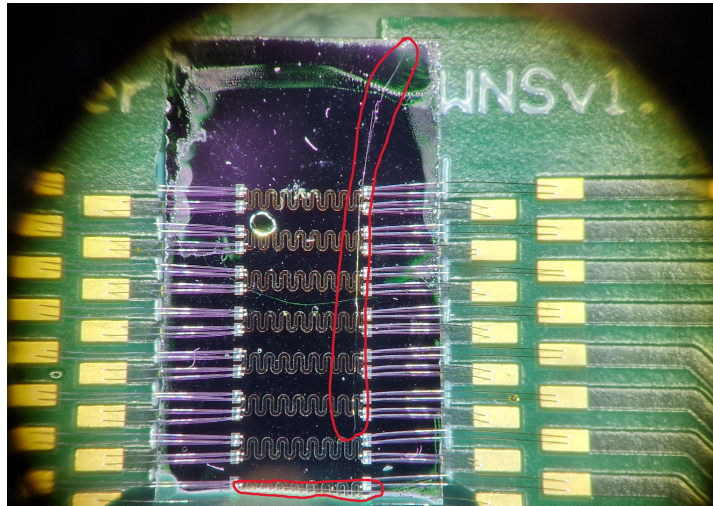

Figure 6.27: W6R3C02 thruster showing cracks on the heater side after temperature test. The cracks are encircled in red.

Two causes were hypothesised for this behaviour: thermal shock and pressure from the thermocouple pressing perpendicular to the chip surface. The thermal shock would be caused by the different expansion rate of silicon, glass, and PCB material at high temperature. Combined with the fact that the chip is constrained to the PCB with adhesive on 3 of its 4 edges, this can lead to cracks. Furthermore, the thermocouple being pressed perpendicular to the chip surface can impose high shear stresses in the silicon, also leading to cracks.

In order to counteract these issues, two changes were made to the testing strategy. Firstly, the chip would be charged slowly, with the voltage increasing by 1 V in steps of approximately 1 min, or how long is needed for the temperature stabilises before further increasing the voltage. This should ensure that the temperature distribution on the assembly is more uniform, minimising the risk of elevated thermal stresses. Secondly, the thermocouple was placed at an angle to the surface normal, and some flexibility was given to it by using less tightening screws (or not screwing them so tight), allowing the thermocouple to move if needed. The slight elastic deformation of the thermocouple was used to ensure thermal contact was still made. A picture of the new placement is shown in Figure 6.28.

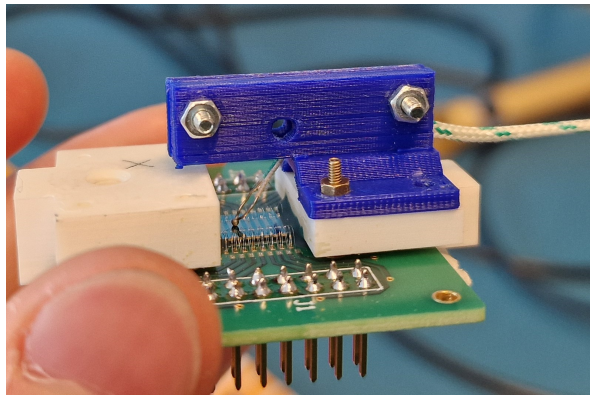

Figure 6.28: Thermocouple holder assembled on top of the W6R3C01 thruster assembly. The thermocouple was placed at an angle, and fewer screws were used.

During the next tests, using these two modifications, the heaters no longer disconnected, and the thruster remained intact. However, it was observed that the temperature reading would not increase past 120 °C even when it was expected to. However, the resistance reading did increase as if the heaters were heating up beyond 120 °C. This was caused by the high temperatures of the system: the screws that hold the thermocouple holder would heat up and also heat up the holder in the immediate vicinity. At around this temperature, the PLA would begin to lose its physical strength and sag, making the thermocouple lose thermal connection. As such, a new holder was 3D printed using Polymaker PolyLite PC (polycarbonate), which has a higher glass transition temperature. A new test was done with the new holder, and the results can be seen in Figure 6.29.

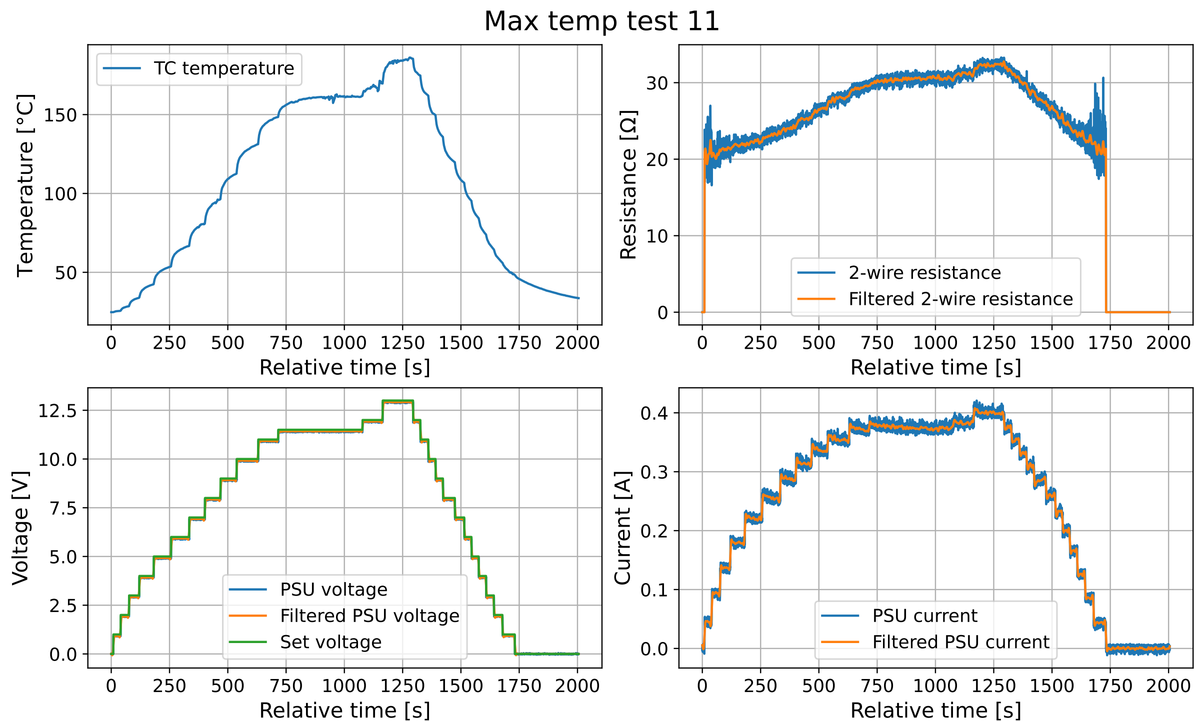

Figure 6.29: Results of maximum temperature test 11. The PSU voltage and current values were corrected by their 0-value readings of 0.8 V and −14.9 mA. The resistance was calculated as the ratio between PSU voltage and current. The value of the resistance was set to zero when the current reached close-to-zero values, to prevent unrealistically extreme measurements. The PSU voltage and current values were also filtered using a low-pass filter.

During this test, no issues were observed, and the thruster heaters reached a temperature of above 180 °C. The resistance also showed the expected behaviour of increasing with temperature. During subsequent investigations of the chip with a microscope and a multimeter, no irregularities were found. As such, this thruster assembly is considered to survive up to at least 180 °C when operated correctly. The maximum operational temperature is likely even higher, but it was not further tested due to time constraints.

A subsequent test that allows the temperature to reach steady state at different voltages is recommended. This way, the required power to reach a certain temperature without propellant can be identified and used to calculate or check the derived heat losses. This test should be performed also in vacuum, to quantify the effect of convective cooling in ambient atmosphere.

Regarding the reliability and confidence that any of the thruster assemblies would survive this temperature as the assembly that was tested, the same discussion and recommendations apply as in the end of Section 6.5 for the maximum pressure test.

6.7. Temperature Coefficient of Resistivity

Using the data from the maximum temperature test 11, the temperature coefficient of resistivity (TCR) of the heaters can also be obtained. In its simplest form, it can be estimated by the slope of the resistance-versus-temperature graph. However, for more accurate results, the resistances of the different connective components need to also be taken into account.

The sources of resistance in the system are the banana cables and connectors from the PSU to the newly made heater connector cables, the heater connector cables themselves, and any resistance in the path of the thruster assembly, such as the header pins, PCB threads, bonding wires. A diagram of the electrical connection and resistances are shown in Figure 6.30.

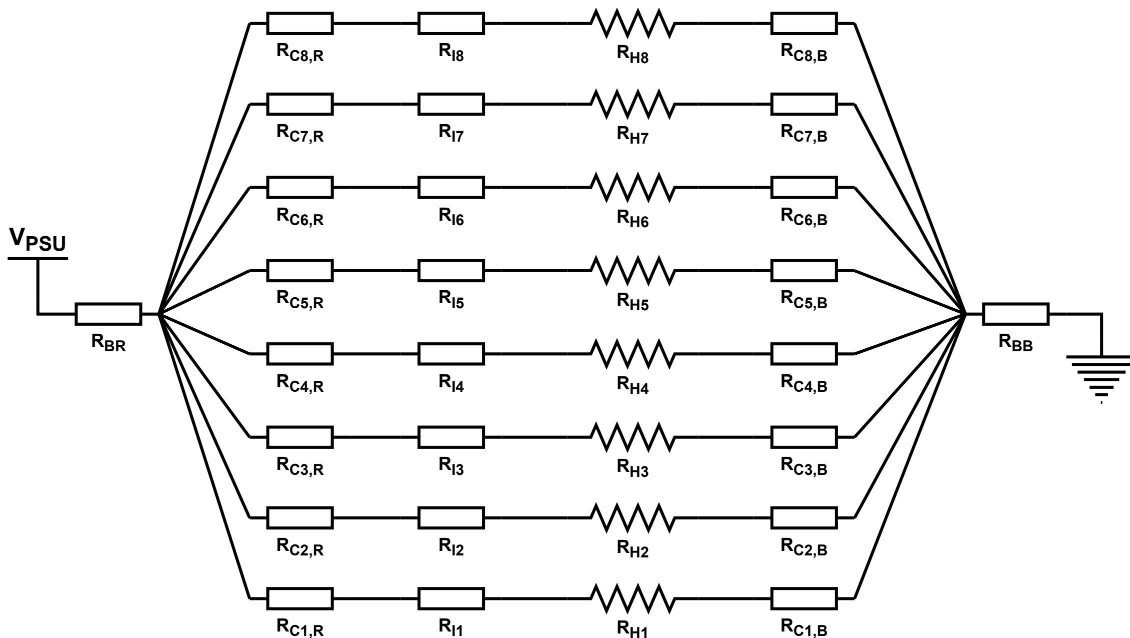

Figure 6.30: Diagram of the resistance sources for powering the VLM. The resistances with index H are those of the heaters on the chip themselves. Those with I are the combination of header pins, PCB, and bonding wires. The ones with C correspond to the new heater connector cables, with R for red and B for black. R_{BR} and R_{BB} are for the banana cable connections to the PSU on the positive and negative side, respectively.

These resistances were measured at room temperature, in an attempt to take into account their effect on reading the heaters' resistances during the maximum temperature test. Most of the measurements were done with the HP 34401A Multimeter. When using the 100 Ω range of the multimeter, while measuring values less than 0.5 Ω, the uncertainty is ±0.004 Ω according to the datasheet [71]. However, for the same reasons as mentioned in Subsection 4.1.2, a value slightly higher than double was assumed for these measurements – namely ±0.01 Ω.

The resistance of the banana cable connections were measured in the SpE cleanroom using a hand-held digital multimeter. As this had a reading resolution of 0.1 Ω, an uncertainty of ±0.05 Ω was assumed for the measurements done with this tool.

When performing 2-wire resistance measurements, first the reading of the resistance of the measuring leads touching was noted. This value was then subtracted from the initial measurements, and the uncertainty calculated accordingly. For the HP 34401A, the leads' resistance measured to be 0.19 ± 0.01 Ω. For the cleanroom hand-held multimeter, this was 0.3 ± 0.05 Ω.

All of the performed resistance measurements at room temperature are reported in Table 6.6, together with some derived values used further in this section. The two-wire values are given after already subtracting the measurement leads' resistances.

Table 6.6: Resistance values (in Ω) of cables and internal connections. The thruster-dependant measurements were done on thruster W6R3C01's assembly.

Heater no. n	**Heater cable colour**	$R_{Cn,B}$ **(4W)**	$R_{Cn,R}$ **(4W)**	$R_{In} + R_{Hn}$ **(2W)**	R_{Hn} **(4W)**	R_{In}	$R_{Cn,R} + R_{Cn,B} + R_{In}$
1	orange	0.16	0.34	145.8	143.0	2.77	3.27
2	yellow	0.18	0.28	146.1	143.1	2.96	3.42
3	green	0.21	0.18	148.5	145.6	2.93	3.32
4	blue	0.20	0.24	148.2	145.4	2.79	3.23
5	purple	0.22	0.19	148.6	145.6	2.95	3.36
6	grey	0.23	0.26	149.6	146.4	3.21	3.70
7	white	0.20	0.37	150.5	146.8	3.66	4.23
8	black	0.18	0.20	152.1	148.8	3.34	3.72
Uncertainty		±0.01	±0.01	±0.05	±0.05	±0.07	±0.07

To calculate the value of $R_{BR} + R_{BB}$ (as only the sum is needed), the resistance of the whole assembly at room temperature was measured to be $20.0 \pm 0.07\,\Omega$. Without the banana cables, the resistance was $18.6 \pm 0.01\,\Omega$. It resulted that $R_{BR} + R_{BB} = 1.4 \pm 0.07\,\Omega$. This value was subtracted from the resistance calculated by the division between PSU voltage and current in all following cases. This "corrected" value is also the one that is plotted in Figure 6.29.

Multiple methods were considered for calculating the temperature coefficient of resistance (TCR) α. However, they all require the resistance versus temperature data. The simplest is to assume that the sum $R_{Cn,R} + R_{Cn,B} + R_{In}$ in series with each VLM heater is negligible compared to the resistance of the heater itself. In this case, a linear relationship between the read resistance and temperature should appear, according to Equation 2.5, which can be rewritten as:

$$R = R_0\,(1 - \alpha T_0) + \alpha R_0 T \tag{6.9}$$

As such, a first order polynomial linear least-squares fit can be performed on the resistance-versus-temperature plot (using the `numpy.polynomial.polynomial.polyfit()` function from the NumPy Python module), and obtain some coefficients c_0 and c_1 satisfying the following equation:

$$R = c_0 + c_1 \cdot T \tag{6.10}$$

Assuming a fixed reference temperature T_0, the TCR can be calculated to be:

$$\alpha = \frac{c_1}{c_0 + c_1 \cdot T_0} \tag{6.11}$$

and $R_0 = c_1/\alpha$. It has to be mentioned that this definition of TCR used everywhere in literature assumes a certain reference temperature T_0. This is not a standard in industry, nor is it always reported in measurements. For this thesis, the value is assumed to be 24.2 °C, the room temperature measured while measuring the resistances of the cables and thruster assembly connections.

The above-mentioned calculation method is the first tried for this set of measurements. However, another method taking into account also the resistances of the connections in the parallel branches of the circuit was attempted. However, as the resistances are not in series with the whole circuit, a non-linear least-squares fit is required, which is achieved using the `scipy.optimize.curve_fit()` function from the SciPy Python module. The following function is defined for the fit:

$$R = \frac{1}{\sum_{n=1}^{8} \frac{1}{R_n + R_{Hn,0}[1+\alpha(T-T_0)]}} \tag{6.12}$$

where R_n is $R_{Cn,R} + R_{Cn,B} + R_{In}$ from Table 6.6 and $R_{Hn,0}$ is the room-temperature heater resistance from Table 6.6 (where it is denoted as R_{Hn}). The only fitting parameter is α, and is thus a direct output of the routine.

A third method that uses the same equation as method 2, but where the values of $R_{H1,0}$ to $R_{H8,0}$ are also left free as fitting parameters, was employed for comparison.

The results of the three models plotted against the measured resistance-versus-temperature data can be seen in Figure 6.31. Furthermore, the values of the calculated TCRs and the fitness quality are given in Table 6.7. It has to be noted that only the measurements between timesteps 50 s and 1650 s were used for these calculations, as they did not include the lower-power readings, which are very noisy.

It has to be noted that the average slope of the measured resistance versus temperature in Figure 6.31 tends to decrease at lower temperatures, indicating a lower apparent α. This is believed to be caused by measurement uncertainties: at lower temperatures, lower voltage and current levels are needed, which in turn mean that the relative uncertainties are higher (according to Table 6.1).

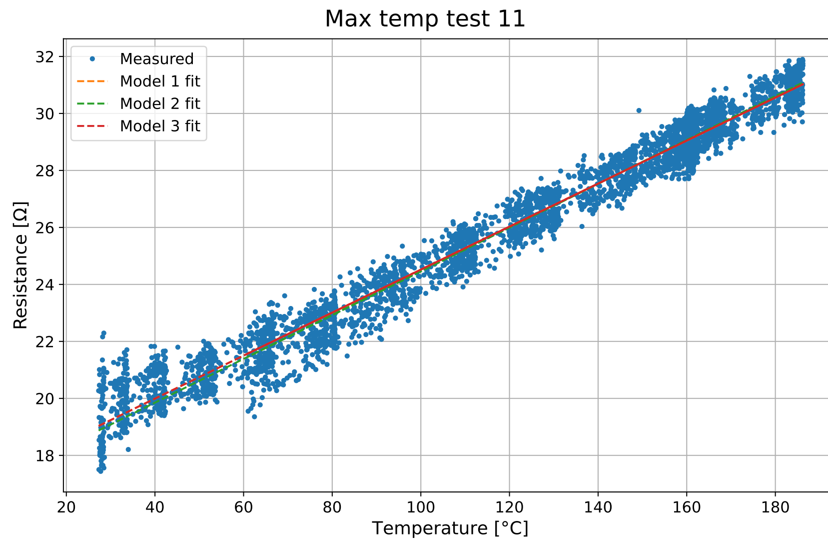

Figure 6.31: Resistance measured during the maximum temperature test 11, plotted versus measured temperature from the thermocouple. The fits of the three mentioned models are included.

Table 6.7: Descriptions and derived quantities of the three resistance models and their fits.

Model no.	Model description	$\alpha_{24.2}$ [K^{-1}]	R^2 value	R_0 prediction [Ω]
1	Linear relation	0.004013	0.9728	18.80
2	Non-linear relation	0.004222	0.9724	18.64
3	Non-linear relation with free heater resistances	0.004109	0.9728	18.80

The three models all fit to the data well, with R^2 values in excess of 0.97. The second model has a slightly lower R^2 value, but the difference is negligible. This model has the advantage that the predicted R_0 value is closer to the measured 18.6 Ω, due to the forcing done by the heater resistance values used in the fitting function.

Model 3, due to its free heater resistances, outputs their values from the fitting process. It was observed that deviations up to 4.9% compared to measured values are present. Furthermore, over-parametrisation is predicted from the very large values on the diagonal of the covariance values (in the order of 10^{13}). As such, this model is considered unreliable and will not be used further.

Between models 1 & 2, the difference in fitting performance is minimal. However, it is considered that

model 2 captures better the expected physics of the electrical system, and also produces a slightly more realistic value for the reference resistance. As such, model 2 is chosen as the model to calculate the final value of the TCR.

In Figure 6.32, the TCR value from model 2 is used to predict the temperature of the thruster from the test setup resistance measurement. Additionally, a filtered value of the resistance is also used for this purpose. The filter is actually applied to the PSU voltage and current readings. A low-pass fourth order Butterworth filter is used, with 0.1 Hz critical frequency, which is generated using the `scipy.signal.butter()` function [108]. The filter is the applied using the `scipy.signal.sosfiltfilt()` function [109], which applies the filter in both forward and backward directions, essentially doubling its order.

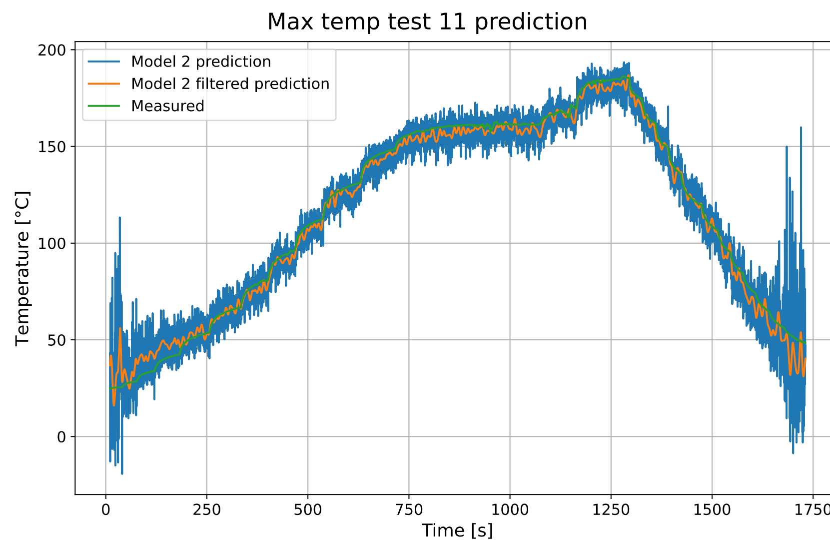

Figure 6.32: Prediction of the heaters' temperature from the measured resistance, alongside the measured temperature.

It can be seen that the model captures well the measured value, especially at higher temperatures and using the filtered data. The worse fit at lower temperatures can be explained by the lower relative accuracy and larger noise of the PSU current measurements at low powers.

However, it has to be noted that a forward-backwards filter was used, which insures no phase delay between the filtered and unfiltered data. However, in a real-time application (for example, while performing the test) this cannot be done, and only forward filters can be used. This induces a phase (and thus time) delay in reading the temperature, which can affect any temperature-control scheme that could be implemented. Furthermore, the current setup only allows the reading of a single equivalent temperature, which assumes a uniform temperature distribution. This assumption has to be verified during operation with propellant.

As such, it is recommended, in the current test setup, to continue using the thermocouple for measuring more accurate and real-time temperatures for future test. In another iteration of the test setup, better resistance measurements techniques could be employed (such as measuring the voltage drop across the heaters themselves, as well as the individual current reading using the method explained in the previous section).

7
Conclusion

The aim of this thesis was to remanufacture and characterise the resulting new generation Micro-Electromechanical System (MEMS) Vaporising Liquid Microthrusters (VLM), as well as to create and validate a testing interface for them. For clarity, the updated research objective is repeated below:

Updated Research Objective

The research objective is to remanufacture and prepare the new generation TU Delft MEMS VLM thruster for future operational validation, heat transfer and instability studies, through experimental testing, by simplifying the manufacturing process, creating a testing interface, and performing measurements and extensive experimental characterisation of the thruster and test set-up.

The research questions that should be answered to achieve this research objective are:

Updated Research Question 1

How can the testing interface of the VLM thruster be designed to survive harsh operational conditions, be easy to operate, and obtain more data?

- URQ1.1: How can the interface of the thruster be designed to provide data about heat transfer in the microchannels?
- URQ1.2: How can the mechanical, electrical and fluidic interfaces be designed for ease of operations and control?
- URQ1.3: What are the operational conditions at which the interface survives?
- URQ1.4: How can instabilities be studied using the new testing interface?

Updated Research Question 2

How does the remanufactured TU Delft VLM thruster compare to its original design?

- URQ2.1: How can the fabrication process be made more efficient?
- URQ2.2: Which problems can be expected during the fabrication process?
- URQ2.3: What are the differences between the measured and design properties of the thruster?

In the following sections, the research questions are answered. The subquestions of the Updated Research Question 1 are answered in Section 7.1, while those of Updated Research Question 2 are answered in Section 7.2. Lastly, the overall conclusions are presented in Section 7.3.

7.1. Testing Interface Conclusions

In this section, the subquestions of the Updated Research Question 1 are answered, regarding the testing interface.

7.1.1. Updated Research Question 1.1

The most important heat transfer mechanism for the propellant flow in the microthruster is the convection heat transfer from the silicon wall to the fluid in the microchannels. Using the newly designed and fabricated testing interface, the heat transfer efficiency can be calculated from the measured power draw from the power supply, and using an estimate of the theoretically required heat to fully vaporise the propellant flow. The full vaporisation of the propellant flow can be checked through the optical access on the microchannel side of the thruster.

Furthermore, using a thermocouple and a heat distribution model through the silicon wall, the wall temperature of the silicon at the exit from the microchannels can be estimated. Using the assumed vaporisation temperature of water at the operational pressure, the coefficient of heat transfer could be calculated. This can be done for different degrees of vaporisation, once the heat transfer efficiency is known.

In order to support these tests, the thruster interface was designed such that the supply pressure reading is available through the pressure & temperature sensor, as well as initial propellant temperature. Furthermore, the local temperature of the heaters / exterior silicon layer can be read using a thermocouple, which can be manually repositioned using its holder. The optical access maintained through the cut-out in the PCB ensures that the user can check whether the flow is fully vaporised or not during operation.

As the heaters can be individually connected to the power supply through the header pins, tests could also be done utilising only a subset of the available heaters, to check its influence on the heat transfer efficiency.

7.1.2. Updated Research Question 1.2

The interface was designed such that testing flexibility is provided. On the electrical side, this is guaranteed by providing individual connections to each of the heater pads, enabling theoretically any power supply configuration required by the user. In the future, this could also be used for temperature control of the thruster, with or without the use of the thermocouple.

On the fluidic side, using the standard MINSTAC connections ensures that the thrusters are ready to be tested in a plug-and-play method, by only requiring the additional 12-micron safety screen. Providing the additional interface option of the no-nozzle inlet+outlet configuration, further testing flexibility is insured – for example, for pressure drop measurements, or for determining the operational conditions for the appearance of instabilities.

Including the outer mounting holes in the PCBs makes for an easy assembly point to any external structures, including a potential adaptor for the thrust pendulum.

7.1.3. Updated Research Question 1.3

As shown through the preliminary tests, one interface + thruster assembly is able to sustain relative pressures of at least 6-7 bar and heater temperatures of at least 180 °C. These values are higher than the design values. They are also higher than what was achieved in previous works for testing a MEMS VLM at the Faculty of Aerospace Engineering at TU Delft, where absolute pressures did not exceed 5.15 bar, and temperatures did not exceed 152 °C. However, the values obtained in this work still have to be checked during a combined operational test of the thruster. Additionally, multiple tests would need to be carried out to increase the confidence that any thruster assembly would survive these conditions.

It has to be noted that the interfaces did not fail at the above-mentioned values, but the tests were nevertheless stopped. As such, it is possible that the assembly could sustain even higher pressures and temperatures. However, this should not be the focus of immediate future tests, but rather the operational tests at conditions similar to tests in the past. This will also significantly increase the confidence that any assembly will survive these conditions.

7.1.4. Updated Research Question 1.4

There are multiple ways through which the instabilities can be studied using the new interface. Some of them are:

- Directly through the optical access cut-out. The oscillation of the liquid-vapour front in the microchannels can signify the presence of instabilities in the flow.
- Through the reading of the pressure sensor. Observing periodic changes in pressure can signify the presence of instabilities in the flow, caused by the microchannels. However, these instabilities could also be caused by the pumping system. The frequencies at which flow rate oscillations (and hence also pressure oscillations) occur due to the syringe pump in the SpE cleanroom were extensively characterised, and can be predicted from the average flow rate and syringe diameter. As such, these oscillations can be filtered out from any future tests in the data processing step, leaving only the oscillations inherent to the microthruster to be studied.
- Through the pressure drop versus mass flow rate curve, at different heat flux levels. This plot can be used to determine the likelihood of the appearance of instabilities like Ledinegg instability, density wave instability, or pressure drop instability. The most important are the density wave oscillations, which can lead to parallel channel instabilities. The no-nozzle interface is designed to make measurement of the pressure drop through the microchannels possible. In combination with a flow meter, the outputs of the power supply, and previously-calculated heat transfer efficiency, this plot can be created, and the conditions for the appearance of these instabilities studied.
- Through the reading of power, temperature, and heater resistance during operation. Observing oscillatory behaviour in these values can prove the existence (or lack thereof) of electro-thermal instabilities.

7.2. Microthruster Manufacturing Conclusions

In this section, the subquestions of the Updated Research Question 2 are answered, regarding the manufacturing and characterisation of the VLM.

7.2.1. Updated Research Question 2.1

The fabrication process was made more efficient by reducing the number of process steps from 45 to 39. This also eliminates some steps that encountered issues in the past, such as unanticipated oxide deposition on the heater side from the fluidic side, and adhesion issues with protective photoresist.

The proposed changes required tuning of some parameters, especially as a soft mask from photoresist was used instead of a hard mask from silicon oxide. The selectivity, etching rate, and surface properties were evaluated, and deemed to be acceptable, thus validating the proposed process changes.

Eliminating the need for dicing separately the silicon and glass layers of the VLM wafer also simplified the production process, allowing faster and more consistent fabrication with a higher yield.

7.2.2. Updated Research Question 2.2

A summary of the problems encountered during manufacturing of the thruster chips, and how to mitigate them, is included below.

- Contamination was observed during processing, on the photoresist layer, but also in the thruster after etching. The operator must ensure that they bring no foreign material in the cleanroom without approval. Furthermore, the staff must ensure that all equipment is clean and properly maintained prior to any use.
- An artefact was observed for one nozzle design on all wafers, signifying that there is residue on the photolithography mask. As such, this mask could be cleaned; although this has the risk of introducing even more contaminants. Additionally, the defect could be accepted, or this nozzle design not used in the future.
- Errors due to wafer handling by the author were observed during a development step. Paying attention at all times during the fabrication process is of paramount importance, as well as only concentrating on one task at a time.

- Surface quality degradation and unpredictable etching performance can appear, caused by restarting the Deep Reactive Ion Etching (DRIE) process. As such, it is highly advised to perform the DRIE process in one go.

7.2.3. Updated Research Question 2.3

Horizontal surface-level dimensions deviation varies from -12.6% up to 13.2% for different features. However, the mentioned maximum deviations correspond to the throat dimensions of the two different types of nozzles. This would have a corresponding effect on the expected thrust, given that it is proportional to the throat area. Comparing the average convergent-divergent throat width (which takes into account also the profile of the throat), a maximum deviation of 22.8% is observed. This can significantly affect the expected thrust.

The effect of the surface horizontal dimensions is however not of great concern, as these can still be measured even after the thrusters are fully fabricated, through the glass layer. On the other hand, this is not the case for the average throat width, which requires also the depth of the throat, and the slope angle of the taper. For the former, the recommendations in the following paragraphs apply. For the latter, while some initial measurements were already performed, more are recommended, to increase the confidence in these values.

Comparing directly the true etching depth to the design 150 μm value is not as straightforward, as different etching steps were attempted for different wafers. The etching process encountered observable variations, with differences in etching rates of up to 8% between wafers that had no or multiple DRIE process restarts. As such, the measured or estimated values for the final production wafer (W6) are used to answer the current research subquestion.

A tendency of higher etch rates for thrusters near the edge of the wafer was observed, also called the bull's eye effect. For the final production wafer 6, this effect generated (estimated) relative variations between maximum and minimum depths of 7.6% for microchannel, 4.5 to 12.0% for CD nozzle throats, and 8.6 to 11.3% for AS nozzle throats. Furthermore, (estimated) relative deviations from the ideal 150 μm depth on wafer 6 were between −1.2% and −8.2% for the microchannels, and between +3.5% and −16.5% for the nozzle throats. These latter deviations are a result of both incorrect etch rate prediction, and aspect ratio-dependent etching effects, the latter of which can only be measured experimentally. These variations and deviations are considered significant for further experimental studies, and need to be predicted or suppressed.

Regarding the deviation from incorrect etch rate, this can be easily minimised by manufacturing thrusters in the future with a single DRIE step, which would also be beneficial for the surface quality. On the other side, the effect of aspect ratio-dependent etching is hard to quantify non-experimentally. As such, at least one measurement of the depth of each type of nozzle would be needed on a particular wafer. However, if multiple wafers go through identical process steps, the measurements from one wafer can be used on the others as well, for this specific effect.

In contrast to the incorrect etch rate, the variation from the bull's eye effect is harder to counteract. It would require either to discard the thrusters close to the edge of the wafer, or to perform the etching in two steps, using an intermediate protector layer at the edge of the wafer. These would either result in waste, or increased complexity of the process. For this reason, it was attempted to predict the bull's eye effect on the etch depth, by fitting the data to some polynomials.

Results show that microchannel depth and throat depths for throats at least 50 μm wide can be predicted well, and do not require measurements to obtain their values. The general trend of the increase in depth of 25 μm CD nozzle throats with distance from the centre of the wafer can also be predicted well, although individual values will vary more from the prediction than for wider throats. For 25 μm aerospike nozzles, the polynomial fit fails to predict the expected depth; as such, measurements will always be required for this type of nozzle for accurate values.

Regarding the heaters, it was shown that attempting to predict the ideal resistance values is not straightforward, with significant deviations between design, expected, and measured quantities. As such, it is not considered important to compare the measured values with the ideal ones, but rather to just perform the resistance measurements. These can be done easily once the thrusters are assembled

with the newly-designed interfaces.

7.3. Overall Conclusions

The updated research objective of remanufacturing and preparing the VLM for future testing is considered to be successful. The thrusters have been fabricated and measured. Testing interfaces were created for them. Preliminary tests were performed to ensure the correct functioning of the interfaces and thrusters, and the findings were included in the current work. As such, future master students can pick up the work from where it was left at, and focus on performing tests at the Faculty of Aerospace Engineering.

The original research objective of performing these tests in the current work, as well as to create a temperature control method, were not achieved. These proved to be too ambitious goals. Furthermore, the initial state of the thrusters was much less evolved fabrication-wise, which lead to the complete remanufacturing of them, further shifting focus from testing to fabrication.

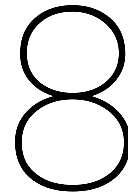

8 Recommendations

In this chapter, the recommendations for improvements and future work are presented.

- The immediate next step would be to attempt to calculate the heat transfer efficiency of the supplied electrical power to the propellant flow. Ideally, this would be done when the flow is just fully vaporised; i.e., when the power input is minimum such that through the optical cutout, it is observed that the flow that reaches the end of the microchannels is fully vaporised. This way, it is ensured that full vaporisation was achieved, but that the vapour was not heated further than the boiling point of water at that particular operational pressure. This is required as the thruster does not have a method of directly measuring the true propellant temperature in its interior. In this way, the approximate propellant temperature at the exit from the microchannels is known. This heat transfer efficiency could be tested both inside and outside the vacuum oven, in order to observe the significance of heat loss to the environment through convection to the air.
- Once the heat transfer efficiency is known, the thrust tests can be done. Alternatively, these two tests can be combined, in the case that a microscope camera could be sacrificed to be used in the vacuum oven. The thrust test can be done using a pendulum test bench already available at the faculty, usually used for measuring thrust levels of less than 5 mN. The pendulum utilises a variable-turn coil to measure the current induced from a magnet moving through it, together with a distance sensor. Alternatively, these can be used in a force-compensation mode, which applies a current to the coil to keep the pendulum at a certain fixed position during thrusting. Details of how this method works are given in the thesis of Hutten [56]. For measuring the flow rate, the SLI sensor can be used, or the steady-state value estimated from the syringe pump settings. Once both the thrust and mass flow rate are known, the thrust efficiency and coefficient of discharge can also be estimated, using the measured or estimated geometry values from this thesis.
- Another important test to be done is for the estimation of the convection heat transfer coefficient (HTC), from the heated silicon walls to the propellant in the microchannels. Knowing the heat transfer efficiency from previous tests, the degree of vaporisation could be varied at the exit of the microchannels. The propellant temperature is thus fixed at the boiling point of water at that specific pressure. The heater temperature would be measured using a thermocouple, and the temperature of the silicon wall at the propellant side would be estimated from a conduction model. Once all these parameters are known, the HTC can be calculated. A more detailed explanation of the process is given in [110].
- With the obtained HTC results, better multiphase flow numerical simulations can be developed based on the work of Bianchi [37], and use these new values for validation in flow regimes not available in literature, but more relevant for the TU Delft MEMS VLM. The results can also be compared with the models found in literature, such as the ones presented in Subsection 2.4.2.
- Another interesting area of research would be the pressure loss through the microchannels, and correlating it with already existing models for larger microchannels, as presented in Subsection 2.4.2. This can be done using the no-nozzle thruster interface developed during this thesis. Furthermore,

using these values, a more accurate pressure at the entrance to the nozzle could be estimated, allowing for a more accurate calculation of the ideal mass flow rate and thrust, and thus also of their efficiency factors. Additionally, once the heater efficiency is known from previous tests, this new pressure loss data can be used to determine the likelihood of the appearance of instabilities like Ledinegg instability, density wave instability, or pressure drop instability, as briefly explained in Subsection 2.2.1. The most important would be the density wave oscillations, which can lead to parallel channel instabilities.

- For the reliable operation of the thrusters, a temperature control method needs to be developed. In the current form, the way of controlling the temperature is indirectly by increasing or decreasing the supply voltage to the heaters. However, this is a trial-and-error method, which distracts the operator from other tasks to be performed during the test. Furthermore, as the heaters heat up, their resistance increases. This means that the supplied power also changes, requiring further adjustments. Another argument for the usefulness of a temperature control method would be to prevent the appearance of electro-thermal instabilities, as observed in the work of [12].
- A more robust method for reading the resistance of individual heaters would be useful for determining the local temperature, without the need for multiple thermocouples. Performing it with the current setup would be possible, requiring some additional resistor and voltage measurement points. However, ideally, a more elegant solution would need to be found. Options include adding external analogue-to-digital converters that can support the voltage drop over the heaters, external current readers etc. Alternatively, a new PCB could be designed that incorporates these sensors, and provides a simple data reading interface for future operators. Additionally, a power-controlling scheme could also be included in such PCBs for the individual control of temperature in the heaters, significantly increasing the operational flexibility of the thrusters. However, this is considered to be a very time-consuming endeavour.
- On the thruster manufacturing side, it is highly recommended to etch future wafers in only one go, due to the disadvantages of having to stop and restart the DRIE process. However, there are already wafers that were etched and await assembly, such that this would not be a priority until another batch of wafers needs to be designed.
- Further measurements of the throat and microchannel profiles should be performed on the thrusters of wafer 15. This is to observe if there is a variation in the profile geometry (specifically taper slope angle) between the thrusters, especially between different nozzle geometries (not only affected by throat width). This would also decrease the uncertainty in the estimation of these angles, which currently can reach as much as 33.3%.
- For the thrust measurements, Hutten [56] observed in his work that the magnetic field generated by the power cables for the heaters affect the operation of the variable-turn coil, and thus also of the thrust measurements. This was however done for a different thruster architecture (non-MEMS), and external heaters that require more power than the current heaters. However, the expected thrust levels for the current MEMS VLM thruster are lower, and thus could be significantly influenced by the magnetic field. It is recommended to test this effect, to determine if it is something that has to be corrected for in future measurements or not.
- In the work of Hutten [56], but also of another student (Jules Vaes) doing his master thesis at the same time as the author, it was observed that when using water dispensed by the syringe pump, bubbles can form in the propellant line. This can happen when the pump is in ambient atmosphere outside the vacuum over, while the rest of the test setup with the pendulum is in vacuum. It has to be observed if such an effect appears also for the current test setup and if yes, find mitigation actions. Options include to deaerate the water before use, or to see if the syringe pump can be used from inside the vacuum oven.

References

[1] E. Kulu. 'Nanosatellite Launch Forecasts 2022 - Track Record and Latest Prediction'. In: *36th Annual Small Satellite Conference (SmallSat 2022)*. Logan, Utah, 2022. URL: https://digitalcommons.usu.edu/smallsat/2022/all2022/7/ (visited on 20/02/2024).

[2] M. de Athayde Costa e Silva. 'MEMS Micropropulsion Design, Modeling and Control of Vaporizing Liquid Microthrusters'. PhD thesis. Delft University of Technology, 2018. DOI: 10.4233/uuid:57f725e1-b3f3-455c-83ce-9156b2123c88. URL: https://doi.org/10.4233/uuid:57f725e1-b3f3-455c-83ce-9156b2123c88.

[3] D. Fontanarosa et al. 'MEMS Vaporazing Liquid Microthruster: A Comprehensive Review'. In: *Applied Sciences 2021, Vol. 11, Page 8954* 11.19 (Sept. 2021), p. 8954. ISSN: 2076-3417. DOI: 10.3390/APP11198954. URL: https://www.mdpi.com/2076-3417/11/19/8954/htm%20https://www.mdpi.com/2076-3417/11/19/8954 (visited on 09/04/2024).

[4] J. Mueller et al. 'Design, Analysis and Fabrication of a Vaporizing Liquid Micro-Thruster'. In: (1997). DOI: 10.2514/6.1997-3054. URL: http://arc.aiaa.org (visited on 09/04/2024).

[5] D. K. Maurya, S. Das and S. K. Lahiri. 'Silicon MEMS vaporizing liquid microthruster with internal microheater'. In: *Journal of Micromechanics and Microengineering* 15.5 (Mar. 2005), p. 966. ISSN: 0960-1317. DOI: 10.1088/0960-1317/15/5/010. URL: https://iopscience.iop.org/article/10.1088/0960-1317/15/5/010/meta (visited on 09/04/2024).

[6] P. Kundu, T. K. Bhattacharyya and S. Das. 'Design, fabrication and performance evaluation of a vaporizing liquid microthruster'. In: *Journal of Micromechanics and Microengineering* 22.2 (Jan. 2012). ISSN: 0960-1317. DOI: 10.1088/0960-1317/22/2/025016. URL: https://iopscience.iop.org/article/10.1088/0960-1317/22/2/025016/meta (visited on 09/04/2024).

[7] J. W. Cen and J. L. Xu. 'Performance evaluation and flow visualization of a MEMS based vaporizing liquid micro-thruster'. In: *Acta Astronautica* 67.3-4 (Aug. 2010), pp. 468–482. ISSN: 00945765. DOI: 10.1016/j.actaastro.2010.04.009.

[8] K. Karthikeyan et al. 'Low temperature co-fired ceramic vaporizing liquid microthruster for microspacecraft applications'. In: *Applied Energy* 97 (Sept. 2012), pp. 577–583. ISSN: 0306-2619. DOI: 10.1016/J.APENERGY.2011.11.078.

[9] K. H. Cheah and K. S. Low. 'Fabrication and performance evaluation of a high temperature co-fired ceramic vaporizing liquid microthruster'. In: *Journal of Micromechanics and Microengineering* 25 (Dec. 2014). ISSN: 0960-1317. DOI: 10.1088/0960-1317/25/1/015013. URL: https://iopscience.iop.org/article/10.1088/0960-1317/25/1/015013/meta (visited on 09/04/2024).

[10] B. Liu et al. 'A new vaporizing liquid microthruster with planar induction heating'. In: *Sensors and Actuators A: Physical* 308 (June 2020). ISSN: 0924-4247. DOI: 10.1016/J.SNA.2020.112010.

[11] P. W. Kwan, X. Huang and X. Zhang. 'Design and testing of a microelectromechanical-system-based high heat flux vaporizing liquid microthruster'. In: *Acta Astronautica* 170 (May 2020), pp. 719–734. ISSN: 0094-5765. DOI: 10.1016/J.ACTAASTRO.2020.01.017.

[12] D. Fontanarosa et al. 'Flow regime characterization of a silicon-based vaporizing liquid microthruster'. In: *Acta Astronautica* 193 (Apr. 2022), pp. 691–703. ISSN: 00945765. DOI: 10.1016/j.actaastro.2021.07.050.

[13] D. Fontanarosa et al. 'Towards an optimized heat transfer process in vaporizing liquid microthrusters using pulsed heating control'. In: *Acta Astronautica* (Feb. 2024). ISSN: 00945765. DOI: 10.1016/j.actaastro.2024.02.041. URL: https://linkinghub.elsevier.com/retrieve/pii/S0094576524001139.

[14] X. Wang et al. 'Additively manufactured vaporizing liquid microthruster with micro pin fins for enhanced heat transfer'. In: *Acta Astronautica* 199 (Oct. 2022), pp. 58–70. ISSN: 00945765. DOI: 10.1016/j.actaastro.2022.07.001.

[15] S. I. Singh. 'Design, Fabrication and Characterization of Microresistojet Thrusters'. Delft University of Technology, Nov. 2023.

[16] C. E. Brennen. *Fundamentals of multiphase flow*. Cambridge University Press, 2005, p. 345. ISBN: 0521848040.

[17] S. G. Kandlikar. 'Heat transfer mechanisms during flow boiling in microchannels'. In: *Journal of Heat Transfer* 126.1 (Feb. 2004), pp. 8–16. ISSN: 00221481. DOI: 10.1115/1.1643090.

[18] G. Spernovasilis. 'Design and fabrication of smart vaporizing liquid microthruster for Cubesat applications'. Delft University of Technology, 2023.

[19] T. Zhang et al. 'Ledinegg instability in microchannels'. In: *International Journal of Heat and Mass Transfer* 52.25-26 (2009), pp. 5661–5674. ISSN: 00179310. DOI: 10.1016/j.ijheatmasstransfer.2009.09.008.

[20] S. K. Saha and G. P. Celata. *Instability in Flow Boiling in Microchannels*. 1st ed. Springer Cham, Sept. 2015. ISBN: 978-3-319-23431-1. DOI: https://doi.org/10.1007/978-3-319-23431-1. URL: https://link.springer.com/book/10.1007/978-3-319-23431-1 (visited on 10/03/2024).

[21] J. A. Boure, A. E. Bergles and L. S. Tong. 'Review of two-phase flow instability'. In: *Nuclear Engineering and Design* 25.2 (July 1973), pp. 165–192. ISSN: 0029-5493. DOI: 10.1016/0029-5493(73)90043-5.

[22] M. Ozawa et al. 'Flow Instabilities in Boiling Channels : Part 2 Geysering'. In: *Bulletin of JSME* 22.170 (1979), pp. 1119–1126. ISSN: 0021-3764. DOI: 10.1299/JSME1958.22.1119.

[23] T. A. Kingston, J. A. Weibel and S. V. Garimella. 'Ledinegg instability-induced temperature excursion between thermally isolated, heated parallel microchannels'. In: *International Journal of Heat and Mass Transfer* 132 (Apr. 2019), pp. 550–556. ISSN: 0017-9310. DOI: 10.1016/J.IJHEATMASSTRANSFER.2018.12.017. URL: https://www.sciencedirect.com/science/article/pii/S0017931018337086 (visited on 30/10/2024).

[24] C. Huh, J. Kim and M. H. Kim. 'Flow pattern transition instability during flow boiling in a single microchannel'. In: *International Journal of Heat and Mass Transfer* 50.5-6 (Mar. 2007), pp. 1049–1060. ISSN: 0017-9310. DOI: 10.1016/J.IJHEATMASSTRANSFER.2006.07.027. URL: https://www.sciencedirect.com/science/article/pii/S001793100600473X (visited on 30/10/2024).

[25] S. Kakac and B. Bon. 'A Review of two-phase flow dynamic instabilities in tube boiling systems'. In: *International Journal of Heat and Mass Transfer* 51.3-4 (Feb. 2008), pp. 399–433. ISSN: 0017-9310. DOI: 10.1016/J.IJHEATMASSTRANSFER.2007.09.026. URL: https://www.sciencedirect.com/science/article/pii/S0017931007005959 (visited on 30/10/2024).

[26] M. M. Padki et al. 'Bifurcation analysis of pressure-drop oscillations and the Ledinegg instability'. In: *International Journal of Heat and Mass Transfer* 35.2 (Feb. 1992), pp. 525–532. ISSN: 0017-9310. DOI: 10.1016/0017-9310(92)90287-3. URL: https://www.sciencedirect.com/science/article/pii/0017931092902873 (visited on 30/10/2024).

[27] B. Wang et al. 'Dynamic instabilities of flow boiling in micro-channels: A review'. In: *Applied Thermal Engineering* 214 (Sept. 2022), p. 118773. ISSN: 1359-4311. DOI: 10.1016/J.APPLTHERMALENG.2022.118773. URL: https://www.sciencedirect.com/science/article/pii/S1359431122007141 (visited on 30/10/2024).

[28] W. Qu and I. Mudawar. 'Measurement and prediction of pressure drop in two-phase micro-channel heat sinks'. In: *International Journal of Heat and Mass Transfer* 46.15 (July 2003), pp. 2737–2753. ISSN: 0017-9310. DOI: 10.1016/S0017-9310(03)00044-9.

[29] H. Y. Wu and P. Cheng. 'Boiling instability in parallel silicon microchannels at different heat flux'. In: *International Journal of Heat and Mass Transfer* 47.17-18 (Aug. 2004), pp. 3631–3641. ISSN: 0017-9310. DOI: 10.1016/J.IJHEATMASSTRANSFER.2004.04.012.

[30] G. Wang, P. Cheng and H. Wu. 'Unstable and stable flow boiling in parallel microchannels and in a single microchannel'. In: *International Journal of Heat and Mass Transfer* 50.21-22 (Oct. 2007), pp. 4297–4310. ISSN: 0017-9310. DOI: 10.1016/J.IJHEATMASSTRANSFER.2007.01.033.

[31] D. Bogojevic et al. 'Two-phase flow instabilities in a silicon microchannels heat sink'. In: *International Journal of Heat and Fluid Flow* 30.5 (Oct. 2009), pp. 854–867. ISSN: 0142-727X. DOI: 10.1016/J.IJHEATFLUIDFLOW.2009.03.013.

[32] K. Balasubramanian et al. 'Experimental investigation of flow boiling heat transfer and instabilities in straight microchannels'. In: *International Journal of Heat and Mass Transfer* 66 (Nov. 2013), pp. 655–671. ISSN: 0017-9310. DOI: 10.1016/J.IJHEATMASSTRANSFER.2013.07.050.

[33] G. Wang, P. Cheng and A. E. Bergles. 'Effects of inlet/outlet configurations on flow boiling instability in parallel microchannels'. In: *International Journal of Heat and Mass Transfer* 51.9-10 (May 2008), pp. 2267–2281. ISSN: 0017-9310. DOI: 10.1016/J.IJHEATMASSTRANSFER.2007.08.027.

[34] Y. Liu, D. F. Fletcher and B. S. Haynes. 'On the importance of upstream compressibility in microchannel boiling heat transfer'. In: *International Journal of Heat and Mass Transfer* 58.1-2 (Mar. 2013), pp. 503–512. ISSN: 0017-9310. DOI: 10.1016/J.IJHEATMASSTRANSFER.2012.11.068.

[35] W. Wan et al. 'Experimental study and optimization of pin fin shapes in flow boiling of micro pin fin heat sinks'. In: *Applied Thermal Engineering* 114 (Mar. 2017), pp. 436–449. ISSN: 1359-4311. DOI: 10.1016/J.APPLTHERMALENG.2016.11.182.

[36] P. Cui and Z. Liu. 'Enhanced flow boiling of HFE-7100 in picosecond laser fabricated copper microchannel heat sink'. In: *International Journal of Heat and Mass Transfer* 175 (Aug. 2021), p. 121387. ISSN: 0017-9310. DOI: 10.1016/J.IJHEATMASSTRANSFER.2021.121387.

[37] F. M. Bianchi. 'Numerical analysis of microchannel flow in vaporizing resistojet thrusters'. Delft University of Technology, Mar. 2023. URL: http://repository.tudelft.nl/..

[38] J. R. Thome and A. Cioncolini. 'Flow Boiling in Microchannels'. In: *Advances in Heat Transfer* 49 (Jan. 2017), pp. 157–224. ISSN: 0065-2717. DOI: 10.1016/BS.AIHT.2017.06.001.

[39] S. M. Kim and I. Mudawar. 'Review of databases and predictive methods for heat transfer in condensing and boiling mini/micro-channel flows'. In: *International Journal of Heat and Mass Transfer* 77 (Oct. 2014), pp. 627–652. ISSN: 0017-9310. DOI: 10.1016/J.IJHEATMASSTRANSFER.2014.05.036.

[40] C. B. Tibiriçá et al. 'A complete set of simple and optimized correlations for microchannel flow boiling and two-phase flow applications'. In: *Applied Thermal Engineering* 126 (Nov. 2017), pp. 774–795. ISSN: 13594311. DOI: 10.1016/j.applthermaleng.2017.07.161.

[41] B. T. C. Zandbergen. *Thermal Rocket Propulsion - Course AE4S01*. Delft, Sept. 2022.

[42] I. Langella et al. *Combustion for Propulsion and Power Technologies Lecture 5: Laminar and turbulent transport processes*. Deft, 2023.

[43] M. G. De Giorgi and D. Fontanarosa. 'A novel quasi-one-dimensional model for performance estimation of a Vaporizing Liquid Microthruster'. In: *Aerospace Science and Technology* 84 (Jan. 2019), pp. 1020–1034. ISSN: 12709638. DOI: 10.1016/j.ast.2018.11.039.

[44] Z. Tang et al. 'New empirical flow-regime-based model of water boiling in rectangular microchannels'. In: *Applied Thermal Engineering* 234 (Nov. 2023). ISSN: 13594311. DOI: 10.1016/j.applthermaleng.2023.121251.

[45] X. Ma et al. 'Saturated/subcooled flow boiling heat transfer inside micro/mini-channels: A new prediction correlation and experiment evaluation'. In: *International Journal of Heat and Mass Transfer* 210 (Aug. 2023). ISSN: 00179310. DOI: 10.1016/j.ijheatmasstransfer.2023.124184.

[46] A. Parameswaran. 'Modelling of MEMS Micro-resistojet Thrusters: An Analytical Study'. Delft: Delft University of Technology, Dec. 2023. URL: http://resolver.tudelft.nl/uuid:b0ae1de8-52c3-4965-b544-cd6008b6749e (visited on 08/04/2024).

[47] G. J. A. Theodoulou. 'VLM optimization: Increasing efficiency through heating chamber optimization'. Delft: Delft University of Technology, Jan. 2022. URL: http://resolver.tudelft.nl/uuid:ed4c5594-322a-4467-999c-ef290adcff69 (visited on 08/04/2024).

[48] J. N. Weinmiller. 'Multiphase flow in micro-thrusters using lattice Boltzmann modeling'. Delft: Delft University of Technology, Jan. 2021. URL: https://resolver.tudelft.nl/uuid:1ae02b2d-fa0b-485c-a8b4-cb08afd0ff3e (visited on 25/03/2024).

[49] S. Succi, M. Sbragaglia and S. Ubertini. 'Lattice Boltzmann Method'. In: *Scholarpedia* 5.5 (2010), p. 9507. ISSN: 1941-6016. DOI: 10.4249/SCHOLARPEDIA.9507.

[50] A. Cervone. *Micro-Propulsion AE4S07 – Course Reader*. Delft, the Netherlands, June 2022.

[51] P. J. Linstrom and W. G. Mallard, eds. *NIST Chemistry WebBook, NIST Standard Reference Database Number 69*. Gaithersburg MD, 20899. DOI: https://doi.org/10.18434/T4D303. URL: https://webbook.nist.gov/chemistry/ (visited on 19/08/2024).

[52] G. P. Smith et al. *NASA Polynomials from GRI-Mech 3.0*. URL: http://combustion.berkeley.edu/gri-mech/data/nasa_plnm.html (visited on 19/08/2024).

[53] D. Koutsoyiannis. 'Clausius–Clapeyron equation and saturation vapour pressure: simple theory reconciled with practice'. In: *European Journal of Physics* 33.2 (Jan. 2012), p. 295. ISSN: 0143-0807. DOI: 10.1088/0143-0807/33/2/295. URL: https://iopscience.iop.org/article/10.1088/0143-0807/33/2/295%20https://iopscience.iop.org/article/10.1088/0143-0807/33/2/295/meta (visited on 21/08/2024).

[54] A. Melaika. 'Design and Verification of Delfi-PQ Satellite Propulsion Subsystem'. Delft: Delft University of Technology, July 2019. URL: http://repository.tudelft.nl/..

[55] Y. A. Çengel, J. M. Cimbala and R. H. Turner. 'Appendix 1 Property Tables and Charts (SI Units)'. In: *Fundamentals of Thermal-Fluid Sciences*. Fifth Edition. McGraw-Hill Education, 2017, pp. 978–979.

[56] R. Hutten. 'Vaporizing Liquid Micro-resistojet experimentation'. Delft: Delft University of Technology, Feb. 2021. URL: http://repository.tudelft.nl/..

[57] International Organization for Standardization. *ISO 9300:2005 - Measurement of gas flow by means of critical flow Venturi nozzles*. 2005. URL: https://www.iso.org/standard/34272.html (visited on 20/08/2024).

[58] F. M. White. *Viscous Fluid Flow*. 3rd Edition. Boston: McGraw-Hill, 2006.

[59] H. S. E. Versteeg. 'Novel fabrication method for a hot gas supersonic micro-thruster'. Delft: Delft University of Technology, May 2020. URL: http://resolver.tudelft.nl/uuid:ac2482ad-0f8e-4569-8bd4-fd11bd6327bd (visited on 20/08/2024).

[60] Confocal NL. *What is Confocal laser scanning and how does it work?* 2024. URL: https://www.confocal.nl/resources/what-is-confocal-laser-scanning-and-how-does-it-work/ (visited on 03/11/2024).

[61] R. Danzl, F. Helmli and S. Scherer. 'Focus Variation - A New Technology for High Resolution Optical 3D Surface Metrology'. In: *The 10th International Conference of the Slovenian Society for Non-Destructive Testing*. Ljubljana, Slovenia, Sept. 2009, pp. 484–491. URL: https://www.ndt.net/?id=8113.

[62] JEOL Ltd. *Scanning Electron Microscope A To Z*. Tech. rep. URL: https://www.jeol.com/applications/pdf/sm/sem_atoz_all.pdf (visited on 03/11/2024).

[63] Lurie Nanofabrication Facility. *Stylus profilometry - LNF Wiki*. Mar. 2020. URL: https://lnf-wiki.eecs.umich.edu/wiki/Stylus_profilometry (visited on 03/11/2024).

[64] Filmetrics. *Comparison of Spectroscopic Ellipsometry and Spectral Reflectance: Thickness Measurement Guide*. 2024. URL: https://www.filmetrics.com/ellipsometry (visited on 03/11/2024).

[65] S. Bell. *A Beginner's Guide to Uncertainty of Measurement*. Tech. rep. Teddington, United Kingdom: national Physical Laboratory, Mar. 2001. URL: https://www.esscolab.com/uploads/files/measurement-guide.pdf (visited on 15/10/2024).

[66] Veeco Instruments Inc. *Dektak 8 Advanced Development Profiler Manual*. Tech. rep. Tucson, Arizona, Dec. 2004. URL: https://www.yumpu.com/en/document/read/16730205/dektak-8-advanced-development-profiler-manual (visited on 15/10/2024).

[67] UCLA Nanolab. *Veeco Dektak 8 Profilometer*. 2024. URL: https://nanolab.ucla.edu/project/dentak8-profilometer/ (visited on 15/10/2024).

[68] Keyence International Belgium. *VK-X1000 Controller Datasheet*. Oct. 2024. URL: https://www.keyence.eu/products/microscope/laser-microscope/vk-x100_x200/models/vk-x1000/ (visited on 15/10/2024).

[69] Keyence International Belgium. *VK-X250K Controller Datasheet*. Oct. 2024. URL: https://www.keyence.eu/products/microscope/laser-microscope/vk-x100_x200/models/vk-x250k/ (visited on 15/10/2024).

[70] ThetaMetrisis. *FR-Scanner*. 2019. URL: https://thetametrisis.com/fr-scanner (visited on 15/10/2024).

[71] Keysight Technologies. *34401A Digital Multimeter Datasheet*. July 2022. URL: https://www.keysight.com/us/en/assets/7018-06774/data-sheets-archived/5968-0162.pdf (visited on 10/10/2024).

[72] C .Hierold. *Microsystems I Lecture 5 - Film Deposition I*. Zurich, Switzerland, Oct. 2021.

[73] C. Roman, M. Haluska and C. Hierold. *Microsystems I Tutorial 7: Dry etching*. Zurich, Switzerland, Nov. 2021.

[74] C. Hierold. *Microsystems I Lecture 9 - Dry Etch*. Zurich, Switzerland, Nov. 2021.

[75] A. G. Nagy. 'Radial Etch Rate Nonuniformity in Reactive Ion Etching'. In: *Journal of The Electrochemical Society* 131.8 (Aug. 1984), pp. 1871–1875. ISSN: 0013-4651. DOI: 10.1149/1.2115981/XML. URL: https://iopscience.iop.org/article/10.1149/1.2115981 (visited on 15/10/2024).

[76] Matplotlib. *Matplotlib 3.9.2 documentation - matplotlib.pyplot.boxplot*. 2024. URL: https://matplotlib.org/stable/api/_as_gen/matplotlib.pyplot.boxplot.html (visited on 15/10/2024).

[77] D. Nečas and P. Klapetek. *Characterisation of surface roughness*. Brno, Czech Republic, June 2012. URL: http://gwyddion.net/presentations/talk-roughness-David-Necas-2012.pdf (visited on 15/10/2024).

[78] Evident. *Surface Roughness Measurement—Evaluating Parameters*. 2024. URL: https://www.olympus-ims.com/en/metrology/surface-roughness-measurement-portal/evaluating-parameters/ (visited on 15/10/2024).

[79] Keyence America. *Sku (Kurtosis) - Area Roughness Parameters - Introduction To Roughness*. 2024. URL: https://www.keyence.com/ss/products/microscope/roughness/surface/sku-kurtosis.jsp (visited on 15/10/2024).

[80] Evident. *Surface Roughness Measurement—Parameters Areal Method*. 2024. URL: https://www.olympus-ims.com/en/metrology/surface-roughness-measurement-portal/parameters/#!cms%5Bfocus%5D=cmsContent14709 (visited on 15/10/2024).

[81] MatWeb. *Titanium Material Property Data*. 2024. URL: https://www.matweb.com/search/DataSheet.aspx?MatGUID=66a15d609a3f4c829cb6ad08f0dafc01&ckck=1 (visited on 15/10/2024).

[82] N. Arshi et al. 'Thickness effect on properties of titanium film deposited by d.c. magnetron sputtering and electron beam evaporation techniques'. In: *Bull. Mater. Sci* 36.5 (Oct. 2013), pp. 807–812. DOI: https://doi.org/10.1007/s12034-013-0552-2. URL: https://www.ias.ac.in/article/fulltext/boms/036/05/0807-0812 (visited on 15/10/2024).

[83] N. Muslim et al. 'Influence of sputtering power on properties of titanium thin films deposited by rf magnetron sputtering'. In: *ARPN Journal of Engineering and Applied Sciences* 10.16 (Sept. 2015), pp. 7184–7189. ISSN: 1819-6608. URL: https://www.researchgate.net/publication/285219938_Influence_of_sputtering_power_on_properties_of_titanium_thin_films_deposited_by_rf_magnetron_sputtering (visited on 15/10/2024).

[84] M. E. Day et al. 'Correlation of electrical resistivity and grain size in sputtered titanium films'. In: *Thin Solid Films* 254.1-2 (Jan. 1995), pp. 285–290. ISSN: 0040-6090. DOI: 10.1016/0040-6090(94)06259-N. URL: https://www-sciencedirect-com.tudelft.idm.oclc.org/science/article/pii/004060909406259N (visited on 15/10/2024).

[85] R. A. Makhan. 'Performance of the MEMS Vaporizing Liquid Microthruster using cold nitrogen gas as propellant'. Delft University of Technology, Dec. 2018.

[86] Asiga. *Asiga Max 2*. 2024. URL: https://www.asiga.com/max-2/ (visited on 17/10/2024).

[87] Forward AM. *Ultracur3D RG 3280 Extended TDS*. 2024. URL: https://move.forward-am.com/hubfs/LFS%20Documentation/Rigid%20Line/RG%203280/Extended%20TDS_Ultracur3D_%20RG%203280.pdf?hsLang=en (visited on 17/10/2024).

[88] TE Connectivity. *MS5837 Series O-ring Mount Application Note*. Aug. 2016. URL: https://www.te.com/commerce/DocumentDelivery/DDEController?Action=showdoc&DocId=Specification+Or+Standard%7FApplication_Note_MS5837_O-Ring_mount%7FA%7Fpdf%7FEnglish%7FENG_SS_Application_Note_MS5837_O-Ring_mount_A.pdf%7FCAT-BLPS0017 (visited on 17/10/2024).

[89] The Lee Company. *Electro-Fluidic Systems Handbook*. Oct. 2019. URL: https://www.theleeco.com/uploads/2021/04/EFS-9th-Edition-Oct-2019.pdf (visited on 17/10/2024).

[90] Machining Doctor. *Thread Dimensions #6-40 UNF*. 2024. URL: https://www.machiningdoctor.com/threadinfo/?tid=13 (visited on 17/10/2024).

[91] The Engineering ToolBox. *Water - Density, Specific Weight and Thermal Expansion Coefficients*. 2003. URL: https://www.engineeringtoolbox.com/water-density-specific-weight-d_595.html (visited on 10/10/2024).

[92] NASA Goddard Space Flight Center. *Outgassing Description*. 2017. URL: https://outgassing.nasa.gov/Description (visited on 17/10/2024).

[93] Henkel. *LOCTITE ABLESTIK 84-3 Technical Data Sheet*. Tech. rep. Sept. 2013. URL: https://datasheets.tdx.henkel.com/LOCTITE-ABLESTIK-84-3-en_GL.pdf (visited on 17/10/2024).

[94] N. A. Walter and J. J. Scialdone. *Outgassing Data for Selecting Spacecraft Materials*. Tech. rep. Greenbelt, Maryland: Goddard Space Flight Center, 2017. URL: https://outgassing.nasa.gov/outgassing-data-table (visited on 17/10/2024).

[95] TE Connectivity. *MS5837-30BA Datasheet*. Tech. rep. Oct. 2023. URL: https://www.te.com/commerce/DocumentDelivery/DDEController?Action=showdoc&DocId=Data+Sheet%7FMS5837-30BA%7FC5%7Fpdf%7FEnglish%7FENG_DS_MS5837-30BA_C5.pdf (visited on 10/10/2024).

[96] AKCP. *What is a K type Thermocouple?* Nov. 2020. URL: https://www.akcp.com/blog/what-is-a-k-type-thermocouple/ (visited on 10/10/2024).

[97] National Instruments. *NI-9211 and sbRIO-9211 Specifications*. May 2024. URL: https://www.ni.com/docs/en-US/bundle/ni-9211-specs/page/specs.html (visited on 10/10/2024).

[98] Delta Elektronika BV. *SM 700-series Datasheet*. Tech. rep. Jan. 2011. URL: https://www.delta-elektronika.nl/sites/default/files/upload/MANUAL_SM700.pdf (visited on 10/10/2024).

[99] National Instruments. *PCI/PXI/USB-6229 Specifications*. Aug. 2023. URL: https://www.ni.com/docs/en-US/bundle/pci-pxi-usb-6229-specs/page/specs.html (visited on 10/10/2024).

[100] Teledyne FLIR. *FLIR A35sc Test Kit Benchtop Thermal Camera*. 2024. URL: https://www.flir.eu/products/a35sc-test-kit/?vertical=rd+science&segment=solutions (visited on 10/10/2024).

[101] Sensirion. *SLI Liquid Flow Meter Series Datasheet*. Tech. rep. Jan. 2020. URL: https://sensirion.com/media/documents/9D0BBC1B/616588DA/Sensirion_Liquid_Flow_Meters_SLI_Datasheet.pdf (visited on 10/10/2024).

[102] Mettler-Toledo. *Operating instructions - METTLER TOLEDO AG balances*. 2004. URL: https://www.mt.com/us/en/home/library/operating-instructions/laboratory-weighing/AG.html (visited on 10/10/2024).

[103] Reid Supply. *Dial vs Digital vs Vernier Calipers: Pros and Cons of Each*. 2024. URL: https://www.reidsupply.com/en-us/industry-news/dial-vs-digital-vs-vernier-calipers (visited on 10/10/2024).

[104] Sensirion. *SHT4x Datasheet*. Tech. rep. Apr. 2024. URL: https://sensirion.com/media/documents/33FD6951/662A593A/HT_DS_Datasheet_SHT4x.pdf (visited on 10/10/2024).

[105] PubNub. *How Fast is Human Reaction Time? Human Perception & Tech*. Mar. 2024. URL: https://www.pubnub.com/blog/how-fast-is-realtime-human-perception-and-technology/ (visited on 10/10/2024).

[106] W. Zeng et al. 'Characterization of syringe-pump-driven induced pressure fluctuations in elastic microchannels'. In: *Lab on a Chip* 15.4 (Feb. 2015), pp. 1110–1115. ISSN: 1473-0189. DOI: 10.1039/C4LC01347F. URL: https://pubs.rsc.org/en/content/articlehtml/2015/lc/c4lc01347f%20https://pubs.rsc.org/en/content/articlelanding/2015/lc/c4lc01347f (visited on 10/10/2024).

[107] D. Craggs. *Test To Bogy Sample Sizes*. 2018. URL: https://accendoreliability.com/test-to-bogy-sample-sizes/ (visited on 08/11/2024).

[108] SciPy. *SciPy v1.14.1 Manual - scipy.signal.butter*. 2024. URL: https://docs.scipy.org/doc/scipy/reference/generated/scipy.signal.butter.html (visited on 10/10/2024).

[109] SciPy. *SciPy v1.14.1 Manual - scipy.signal.sosfiltfilt*. 2024. URL: https://docs.scipy.org/doc/scipy/reference/generated/scipy.signal.sosfiltfilt.html (visited on 10/10/2024).

[110] L. Yin and L. Jia. 'Confined bubble growth and heat transfer characteristics during flow boiling in microchannel'. In: *International Journal of Heat and Mass Transfer* 98 (July 2016), pp. 114–123. ISSN: 00179310. DOI: 10.1016/j.ijheatmasstransfer.2016.02.063.

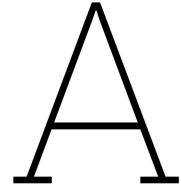

Chemical Species Properties

In this appendix, the properties of the chemical species that were used in the analytical model are presented.

Table A.1: NASA Polynomial coefficients and temperature validity ranges for gaseous water [52]

T_{min} [K]	200.0	1000.0
T_{max} [K]	1000.0	3500.0
a_1	3.03399249	4.19864056
a_2	$2.17691804 \cdot 10^{-3}$	$-2.03643410 \cdot 10^{-3}$
a_3	$-1.64072518 \cdot 10^{-7}$	$6.52040211 \cdot 10^{-6}$
a_4	$-9.70419870 \cdot 10^{-11}$	$-5.48797062 \cdot 10^{-9}$
a_5	$1.68200992 \cdot 10^{-14}$	$1.77197817 \cdot 10^{-12}$
a_6	$-3.00042971 \cdot 10^{4}$	$-3.02937267 \cdot 10^{4}$
a_7	4.96677010	−8.49032208

Table A.2: NIST coefficients and temperature validity ranges for liquid water [51]

T_{min}	298.0
T_{max}	500.0
a_1	−203.6060
a_2	1523.290
a_3	−3196.413
a_4	2474.455
a_5	3.855326
a_6	−256.5478
a_7	−488.7163
a_8	−285.8304

Table A.3: NIST coefficients and temperature validity ranges for gaseous nitrogen [51]

T_{min}	100.0	500.0	2000.0
T_{max}	500.0	2000.0	6000.0
a_1	28.98641	19.50583	35.51872
a_2	1.853978	19.88705	1.128728
a_3	−9.647459	−8.598535	−0.196103
a_4	16.63537	1.369784	0.014662
a_5	0.000117	0.527601	−4.55376
a_6	−8.671914	−4.935202	−18.97091
a_7	226.4168	212.39	224.981
a_8	0.0	0.0	0.0

Table A.4: Other properties of the species used as propellant in the analytical model (water and nitrogen). (g) represents gaseous state for water, while (l) is liquid state. Source for molar mass and enthalpy of formation: [51] and for viscosity properties: [58]

Species	**H_2O**	**N_2**
μ_0 [Pa · s]	$1.12 \cdot 10^{-5}$ (g)	$1.66 \cdot 10^{-5}$
$T_{0,\mu}$ [K]	350 (g)	273
S_μ [K]	1064 (g)	107
M_W [g/mol]	18.0146	28.014
$\overline{H}_f^0$ [kJ/mol]	-285.83 (l)	0

B

New Wafer Layouts

In this appendix, the new wafer layouts used for the fabrication of the new generation MEMS VLMs are given. The layouts are presented as screenshots from the original Excel document `Wafer Configurations Andrei v3.xlsx`, which can be found in the Micropropulsion server. These are in the sheets `Wafer_1 (3)` through `Wafer_5 (3)`, corresponding to images W01A through W05A in the wafer stepper. A tally of the used nozzles/configurations is summarised in the sheet `Nozzles(3)`.

Almost all thrusters have a 3-cell inlet section and a 6-cell serpentine channels section. Exceptions to this rule are a few thrusters that have no microchannels, such as R1C04 and R1C09 in Figure B.1. These instead have also channel element cells, such as the inlet.

The nozzle can be 1 cell high (for the Short Nozzles), 2 cells high (for Long Nozzles), or 3 cells high (for the Aerospike Nozzles). These are either placed immediately after the microchannels when the space above the microchannels fits exactly that amount of cells that make up the nozzle (such as all thrusters on rows 2 and 5 in Figure B.1), or have a channel element cell before the nozzle to make up the difference (such as R4C04 to R4C11 in Figure B.1). When a design without nozzle is used, the space is replaced with channel element cells, which is the case for R3C01, R3C06, and R3C12 in Figure B.1.

The following images were used for the manufactured wafers:

- Wafer 1: image W01A
- Wafer 2: image W02A
- Wafer 3: image W03A
- Wafer 4: image W04A
- Wafer 5: image W05A
- Wafer 6: image W01A
- Wafer 7: image W03A
- Wafer 15: image W01A

The wafer image layouts are given in the following figures, from image W01A to W05A.

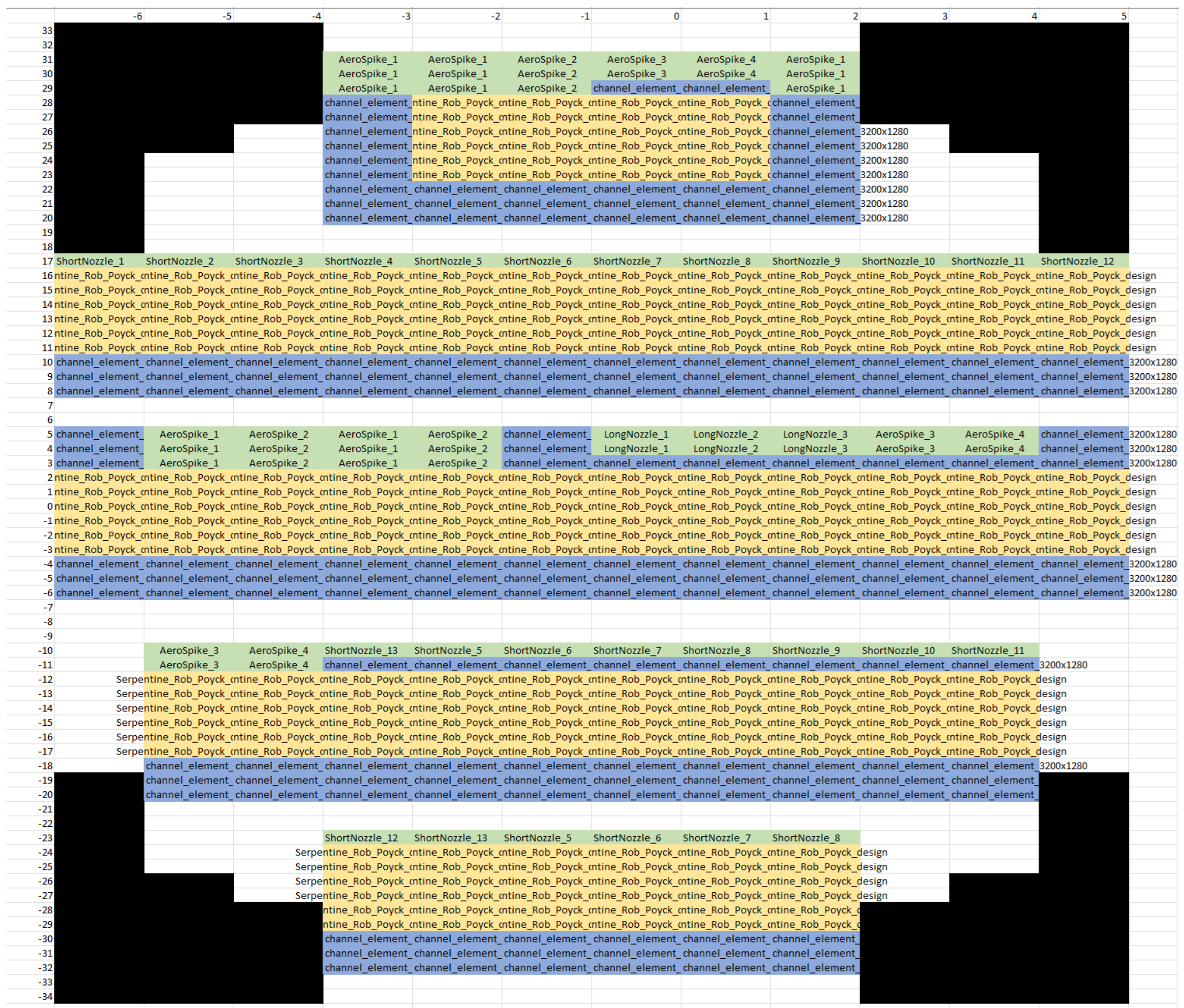

Figure B.1: W01A wafer layout, with configurations rearranged for this thesis. Rearranged from the original design in [15].

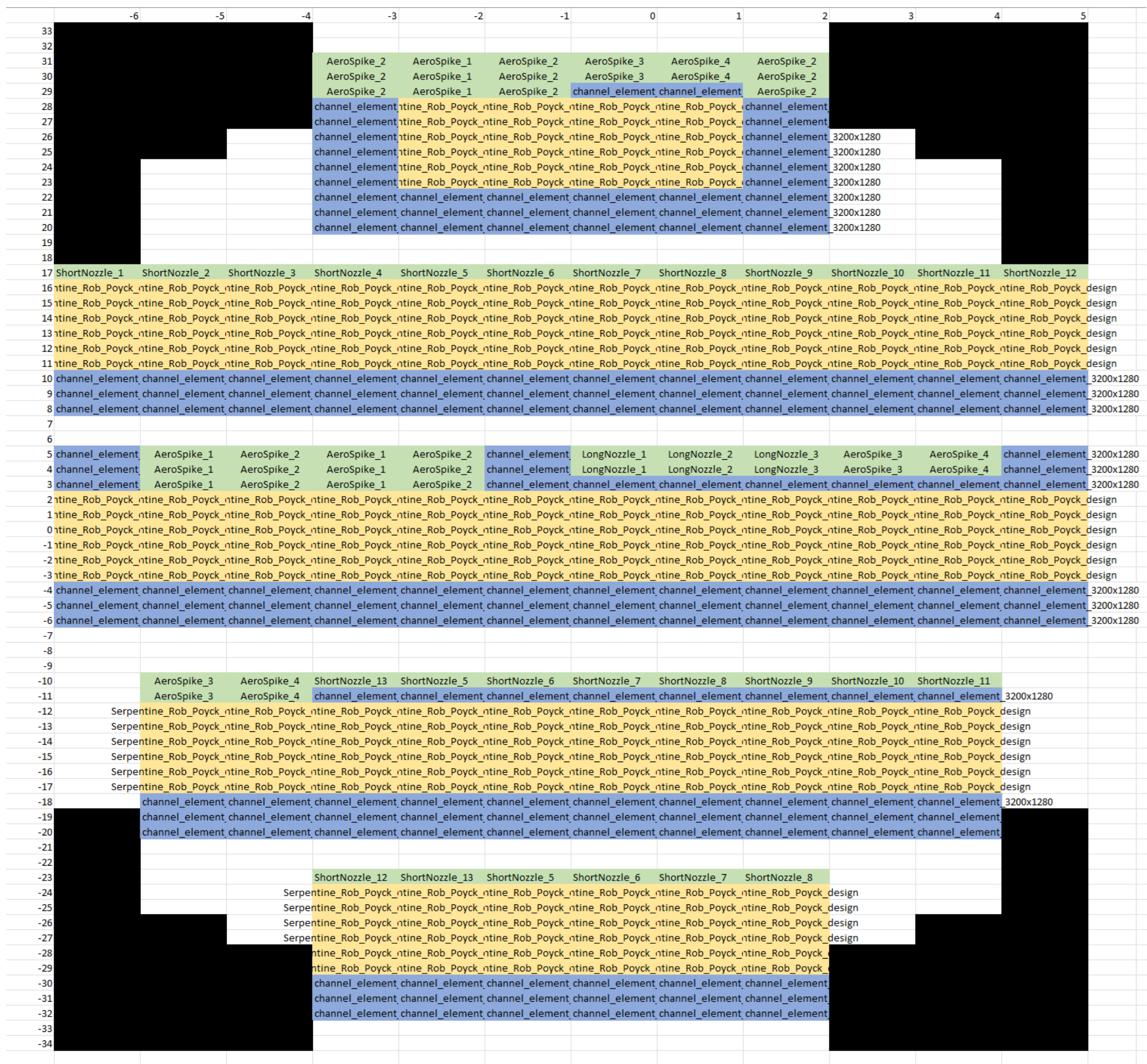

Figure B.2: W02A wafer layout, with configurations rearranged for this thesis. Rearranged from the original design in [15].

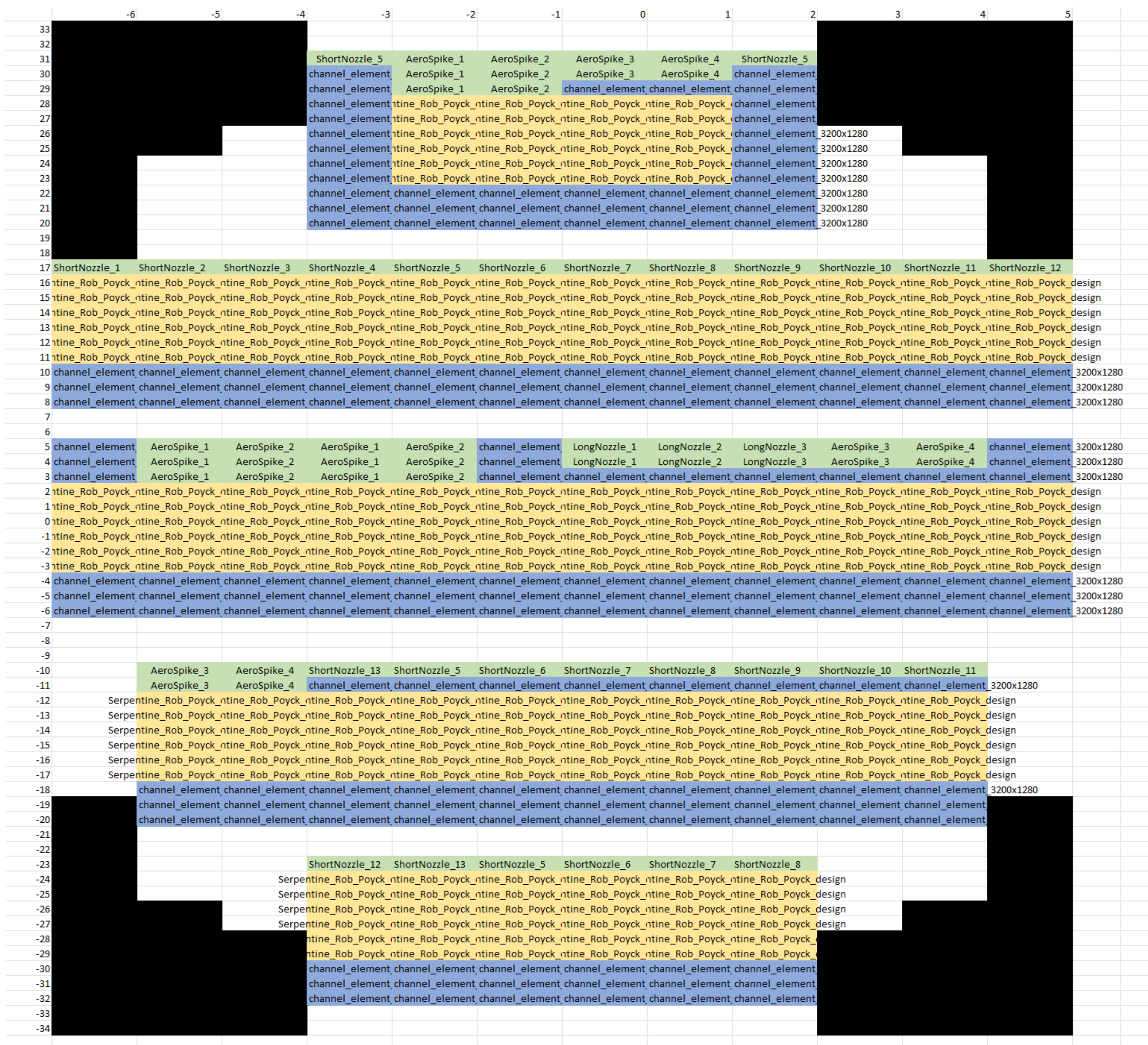

Figure B.3: W03A wafer layout, with configurations rearranged for this thesis. Rearranged from the original design in [15].

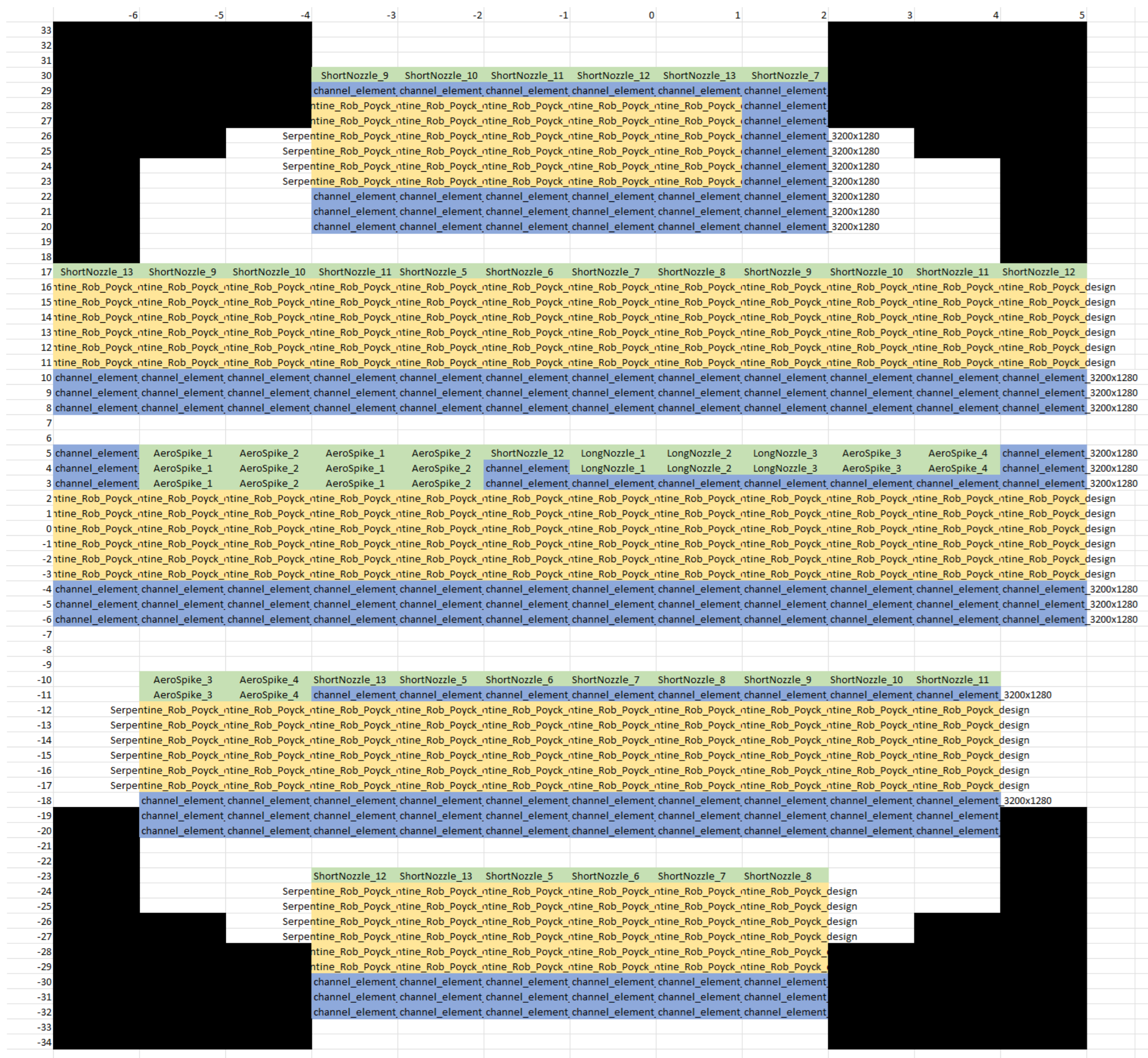

Figure B.4: W04A wafer layout, with configurations rearranged for this thesis. Rearranged from the original design in [15].

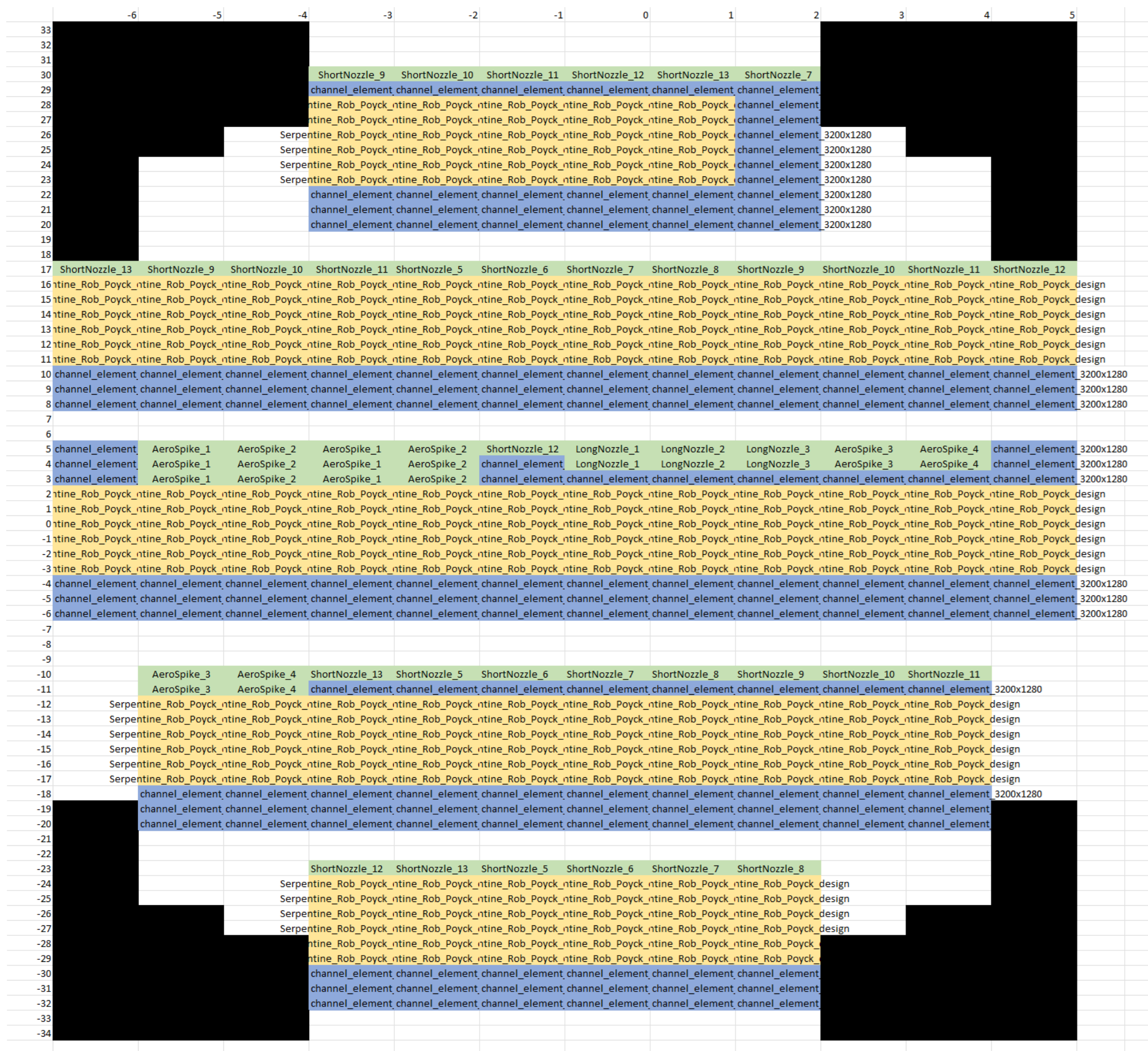

Figure B.5: W05A wafer layout, with configurations rearranged for this thesis. Rearranged from the original design in [15].

C

EKL Manufacturing Flowchart

In this chapter, the MEMS manufacturing flowchart is included for future reference. This is a modified and updated version of the flowchart of Singh [15].

Else Kooi Laboratory

TU Delft

VLM Wafer Manufacturing

FLOWCHART

VERSION 2

2024

BATCH INFORMATION			
NAME OF OWNER :	Andrei Pârvulescu	MASK SET :	MICROT
NAME OF MENTOR :	Henk van Zeijl	MASK BOX :	MICROT2
RUN NUMBER :	1	DIE SIZE :	Custom (7 mm X 1.28 mm)
WAFER AMOUNT :	7	START DATE :	16/05/2024
SUBJECT TO PCC :		PCC APPROVED :	

DELFT UNIVERSITY OF TECHNOLOGY ELSE KOOI LABORATORY

Adress	:	Feldmannweg 17, 2628 CT Delft, The Netherlands
P.O. Box	:	5053, 2600 GB Delft, The Netherlands
Phone	:	+31 - (0)15 - 2783868
Fax	:	+31 - (0)15 - 2622163
Website	:	www.tudelft.nl/ewi/onderzoek/faciliteiten/else-kooi-lab

© Copyright EKL - Delft University of Technology

STARTING MATERIAL

Use **DOUBLE SIDED** polished **LOW RESISTIVITY (LRES)** wafers, with the following specifications:

Type:	NA
Orientation:	<100>
Resistivity:	1-5 Ω·cm
Thickness:	300 ± 10 µm
Diameter:	100 mm

Additionally, use Borofloat® borosilicate **double-sided glass wafers** with the following specifications:

Thickness:	525 µm
Diameter:	100 mm

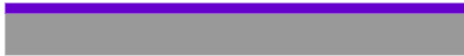

- SiO_2 deposition on front side **(steps 10 – 11)**

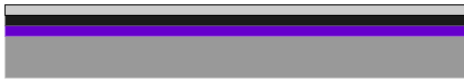

- Metal stack (Al + Ti) deposition **(steps 12 – 15)**

- Photoresist for Al pads **(steps 16 – 19)**

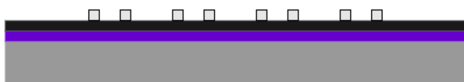

- Etching Al pads and stripping PR **(steps 20 – 22)**

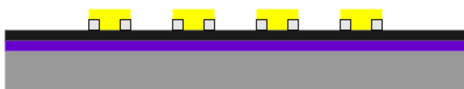

- Photoresist for Ti heaters **(steps 23 – 26)**

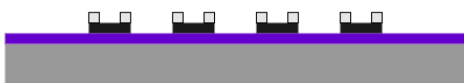

- Etching Ti heaters and stripping PR **(steps 27 – 29)**

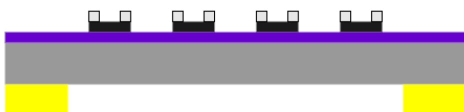

- Photoresist backside for Si etch **(steps 30 – 33)**

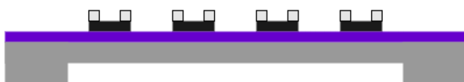

- DRI etching in Si and stripping PR **(steps 34 – 36)**

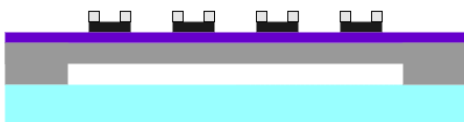

- Glass wafer bonding **(steps 37 – 38)**

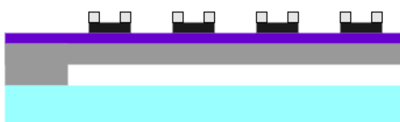

- Dicing **(step 39)**

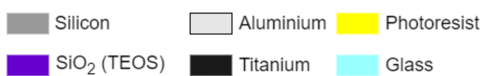

•

Zero layer (alignment markers)

1. CLEANING: HNO_3 99% and 69.5%

Clean 10 minutes in fuming nitric acid at ambient temperature. This will dissolve organic materials. Use wet bench "HNO_3 99% (Si)" and the carrier with the white dot.
Rinse Rinse in the Quick Dump Rinser with the standard program until the resistivity is 5 MΩ.
Clean 10 minutes in concentrated nitric acid at 110 °C. This will dissolve metal particles. Use wet bench "HNO_3 69,5% 110C (Si)" and the carrier with the white dot.
Rinse Rinse in the Quick Dump Rinser with the standard program until the resistivity is 5 MΩ.
Dry Use the "Avenger Ultra-Pure 6" rinser/dryer with the standard program, and the white carrier with a red dot.

2. COATING

Use the coater station of the EVG120 system to coat the wafers with photoresist. The process consists of:

- A treatment with HMDS (hexamethyldisilazane) vapor, with nitrogen as a carrier gas, to improve resist adhesion.
- Spin coating of Shipley SPR3012 positive resist, dispensed by a pump.
- A soft bake (a.k.a. pre-bake) at 95 °C for 90 seconds.
- An automatic Edge Bead Removal (EBR) with a solvent.

Always check the relative humidity (48 ± 2 %) in the room before coating, and follow the instructions for this equipment.

Default use program "**1 - Co - 3012 - zero layer**", which has a larger Edge Bead Removal (EBR) than standard, or use program "**1 - Co - 3012 - 1.4 - noEBR**" when the EBR option is out of order.

3. ALIGNMENT AND EXPOSURE

Processing will be performed on the ASML PAS5500/80 automatic wafer stepper. Follow the operating instructions from the manual when using this machine.

Expose **mask COMURK** with job **Litho\epi0.0**. Use the correct exposure energy (check the energy table). This results in stepper alignment markers and verniers for wafers which will not get an Epitaxy (EPI) layer.

4. DEVELOPING

Use the developer station of the EVG120 system to develop the wafers. The process consists of:

- A post-exposure bake at 115 °C for 90 seconds, to prevent ***standing waves*** on the sidewalls of the resist structures.
- Developing with Shipley MF322 with a single puddle process.
- A hard bake (a.k.a. post-bake) at 100 °C for 90 seconds. Always follow the instructions for this equipment.

Use program "**1 - Dev - SP**".

5. INSPECTION

Visually inspect the wafers through a microscope:

- Check if the correct mask is exposed.
- Check if there are no resist residues; these are NOT allowed.
- Check the linewidth of the structures.
- Check the overlay of the exposed pattern (if the mask was aligned to a previous pattern on the wafer).

6. WAFER NUMBERING

Use the glass pen in the lithography room to mark the wafers with the **BATCH** and **WAFER** number.
Write the numbers in the photoresist, just above the waferflat. Always do this after exposure and development! It is **NOT** allowed to use a metal pen or a scriber (pen with a diamond tip) for this purpose.

7. PLASMA ETCHING: Alignment markers (URK's) into Silicon

Use the Trikon Ωmega 201 plasma etcher.

•

Follow the operating instructions from the manual when using this machine.
It is **not** allowed to change the process conditions and times from the etch recipe!

Use sequence **URK_NPD** (with a platen temperature of **20 °C**) to etch 120 nm deep ASM URK's into the Si. The sequence consists of two etch recipes: URK_BRK (to etch native SiO_2) and URK_BULK (to etch Si).

Process conditions from chamber recipe URK_BRK:						
Step	Gasses & flows	Pressure	Platen RF	ICP RF	Platen temp.	Etch time
1. Breakthrough	CF_4/O_2 = 40/20 sccm	5 mTorr	60 W	500 W	20 °C	0'15"

Process conditions from chamber recipe URK_BULK:						
Step	Gasses & flows	Pressure	Platen RF	ICP RF	Platen temp.	Etch time
1. Bulk etch	Cl_2/HBr = 80/40 sccm	60 mTorr	20 W	500 W	20 °C	0'40"

8. LAYER STRIPPING: Photoresist

Strip resist Use the PVA TePla GIGAbatch 360 system to remove the photoresist in an oxygen plasma.
Follow the instructions specified for the Tepla stripper.
Use **program 1**: 1000 watts power and automatic endpoint detection + 2 min. overetching

9. CLEANING: HNO_3 99% and 69.5%

Clean 10 minutes in fuming nitric acid at ambient temperature. This will dissolve organic materials. Use wet bench "HNO_3 99% (Si)" and the carrier with the white dot.
Rinse Rinse in the Quick Dump Rinser with the standard program until the resistivity is 5 MΩ.
Clean 10 minutes in concentrated nitric acid at 110 °C. This will dissolve metal particles. Use wet bench "HNO_3 69,5% 110C (Si)" and the carrier with the white dot.
Rinse Rinse in the Quick Dump Rinser with the standard program until the resistivity is 5 MΩ.
Dry Use the "Avenger Ultra-Pure 6" rinser/dryer with the standard program, and the white carrier with a red dot.

Oxide layer deposition only on the front side

10. PECVD DEPOSITION: 500 nm Silicon oxide (TEOS) on the front side of the wafer

Use the Novellus Concept One PECVD reactor.
Follow the operating instructions from the manual when using this machine.
It is **not** allowed to change the process conditions and time from the deposition recipe!

Use recipe **".xxxnmteos"** to deposit a 500 nm thick layer.

Process conditions from recipe .xxxnmteos:					
Gasses & flows	Pressure	HF power	LF power	Temperature	Time
O_2/TEOS = 5/1.8 mL/min	2.2 Torr	500 W	500 W	350 °C	**17 sec**

Note: ▪ The layer thickness depends on the station deposition time (SDT), which can be calculated from the average deposition rate during recent recipe usage. This can be found in the logbook of the system.
▪ An extra test wafer can be deposited for measurements and etch tests.

Usage note: Make sure to turn on the additional power supply in the maintenance zone when depositing TEOS!

•

11. MEASUREMENT: Oxide thickness

Use the Woollam Ellipsometer system for layer thickness measurements on 1 wafer from each process. Alternatively, use the FR-Scanner Reflectometer. Follow the operating instructions from the manual when using the equipment.

Expected layer thickness: 500 nm   Actual deposit Sampuran: 456 nm   Actual deposit Andrei: 471 nm

Metal layer stack

Front-Side of Wafer

12. CLEANING: HNO_3 99% and 69.5%

Clean 10 minutes in fuming nitric acid at ambient temperature. This will dissolve organic materials. Use wet bench "HNO_3 99% (Si)" and the carrier with the white dot.

Rinse Rinse in the Quick Dump Rinser with the standard program until the resistivity is 5 MΩ.

Clean 10 minutes in concentrated nitric acid at 110 °C. This will dissolve metal particles. Use wet bench "HNO_3 69,5% 110C (Si)" and the carrier with the white dot.

Rinse Rinse in the Quick Dump Rinser with the standard program until the resistivity is 5 MΩ.

Dry Use the "Avenger Ultra-Pure 6" rinser/dryer with the standard program, and the white carrier with a red dot.

13. METALLIZATION: 500 nm Ti

Use the TRIKON SIGMA 204 sputter coater for the deposition of a Titanium metal layer on the wafers. The target must exist of 100% Ti, and deposition must be done at 350 °C with an Ar flow of 100 sccm. Follow the operating instructions from the manual when using this machine.

Use recipe **Ti 500nm @ 350C** to obtain a 500 nm thick layer.

14. METALLIZATION: 200 nm Al (with 1%Si)

Use the TRIKON SIGMA 204 sputter coater for the deposition of an aluminium metal layer on the wafers. The target must exist of 99% Al and 1% Si, and deposition must be done at 350 °C with an Ar flow of 100 sccm. Follow the operating instructions from the manual when using this machine.

Use recipe **AlSi 200nm @ 50C** or **@ 350C** to obtain a 200 nm thick layer.

Visual inspection: the metal layer must look shiny.

ALTERNATIVE FOR STEPS 13 & 14: If it exists, use recipe "Henk_2Pass_Ti_AlSi", which will deposit 500 nm Ti + 200 nm AlSi. **Do check that the recipe contains the correct steps before use!**

15. CLEANING: HNO_3 99% metal

Clean 10 minutes in fuming nitric acid at ambient temperature. This will dissolve organic materials.

Use wet bench "HNO_3 99% (**metal)**" and the carrier with a red and white dot.

Rinse Rinse in the Quick Dump Rinser with the standard program until the resistivity is 5 MΩ.

Dry Use the "Avenger Ultra-Pure 6" rinser/dryer with the standard program, and the white carrier with a black dot.

Aluminium Bonding Pads
Front Side of Wafer

16. COATING

Use the coater station of the EVG120 system to coat the wafers with photoresist. The process consists of:

- A treatment with HMDS (hexamethyldisilazane) vapor, with nitrogen as a carrier gas, to improve resist adhesion.
- Spin coating of AZ Nlof2020 negative resist, dispensed by a pump.
- A soft bake (a.k.a. pre-bake) at 95 °C for 90 seconds.

Always check the relative humidity (48 ± 2 %) in the room before coating, and follow the instructions for this equipment.

Use program "**1 - Co - Nlof - 1.5um--noEBR**".

17. ALIGNMENT AND EXPOSURE

Processing will be performed on the ASML PAS5500/80 automatic wafer stepper. Follow the operating instructions from the manual when using this machine.

Expose **mask MICROT2** (box 502) with job **Job special/2023_Jobs/3ME_MiTh/VLM_device (Layer ID ALU_PADS)**. Use the correct exposure energy (150).

18. DEVELOPING

Use the developer station of the EVG120 system to develop the wafers. The process consists of:

- A post-exposure bake at 115 °C for 90 seconds, to prevent ***standing waves*** on the sidewalls of the resist structures.
- Developing with Shipley MF322 with a single puddle process.
- A hard bake (a.k.a. post-bake) at 100 °C for 90 seconds. Always follow the instructions for this equipment.

Use program "**x-Henk_DEVNLOF1.5um_PB_HB**".

19. INSPECTION

Visually inspect the wafers through a microscope:

- Check if the correct mask is exposed.
- Check if there are no resist residues; these are NOT allowed.
- Check the linewidth of the structures.

20. ALUMINIUM ETCHING

Moisten — Rinse for 1 minute in wet bench "H_2O/Triton X-100 tbv Al. Ets". Use the carrier with the yellow dot.
The bath contains 1 ml Triton X-100 per 5000 ml deionized water.

Etching — Use wet bench "Al. ets 35°C", and the carrier with the yellow dot.
1 liter buffered aluminium etch fluid contains:
770 ml concentrated phosphorus acid (H_3PO_4 85%), 19 ml concentrated nitric acid (HNO_3 65%),
140 ml concentrated acetic acid (CH_3COOH 100%) and 71 ml deionized water.

Etch time — 2 min 15 s (overetch as if 300 nm Al was deposited). Nominal etch time is 170 nm/min

QDR — Rinse in the Quick Dump Rinser with the standard program until the resistivity is 5 MΩ.

Drying — Use the "Avenger Ultra-Pure 6" rinser/dryer with the standard program, and the white carrier with a black dot.

21. LAYER STRIPPING: Photoresist

Strip resist — Use the PVA TePla GIGAbatch 360 system to remove the photoresist in an oxygen plasma.
Follow the instructions specified for the Tepla stripper.
Use **program 4**: 1000 watts power for 15 minutes

•

22. CLEANING: HNO_3 99% metal (optional)

Clean	10 minutes in fuming nitric acid at ambient temperature. This will dissolve organic materials. Use wet bench "HNO_3 99% (**metal)**" and the carrier with a red and white dot.
Rinse	Rinse in the Quick Dump Rinser with the standard program until the resistivity is 5 MΩ.
Dry	Use the "Avenger Ultra-Pure 6" rinser/dryer with the standard program, and the white carrier with a black dot.
Note	**Do not perform a "HNO_3 69,5% 110C (Si)" cleaning step, as that will remove the metal layer!**

Titanium Heating Elements

23. COATING

Use the coater station of the EVG120 system to coat the wafers with photoresist. The process consists of:
- A treatment with HMDS (hexamethyldisilazane) vapor, with nitrogen as a carrier gas, to improve resist adhesion.
- Spin coating of AZ Nlof2020 negative resist, dispensed by a pump.
- A soft bake (a.k.a. pre-bake) at 95 °C for 90 seconds.

Always check the relative humidity (48 ± 2 %) in the room before coating, and follow the instructions for this equipment.

Use program "**1 - Co - Nlof - 1.5um—noEBR**".

24. ALIGNMENT AND EXPOSURE Ti Layer

Processing will be performed on the ASML PAS5500/80 automatic wafer stepper. Follow the operating instructions from the manual when using this machine.

Expose **mask MICROT2** (box 502) with job **Job special/2023_Jobs/3ME_MiTh/VLM_device (Layer ID HEATER)**. Use the correct exposure energy (150).

25. DEVELOPING

Use the developer station of the EVG120 system to develop the wafers. The process consists of:
- A post-exposure bake at 115 °C for 90 seconds, to prevent ***standing waves*** on the sidewalls of the resist structures.
- Developing with Shipley MF322 with a single puddle process.
- A hard bake (a.k.a. post-bake) at 100 °C for 90 seconds. Always follow the instructions for this equipment.

Use program "**x-Henk_DEVNLOF1.5um_PB_HB**".

26. INSPECTION

Visually inspect the wafers through a microscope:
- Check if the correct mask is exposed.
- Check if there are no resist residues; these are NOT allowed.
- Check the linewidth of the structures.

27. Titanium REMOVAL

Use the Trikon Ωmega 201 plasma etcher. Follow the operating instructions from the manual when using this machine. It is **not** allowed to change the process conditions and times from the etch recipe!

Use sequence Ti_500nm (with a platen temperature of **25 °C**) to etch 500 nm deep into the Ti layer.

Process conditions from chamber recipe Ti_500nm**:**						
Step	Gasses & flows	Pressure	Platen RF	ICP RF	Platen temp.	Etch time
1. breakthrough	Cl / HBr = 30 / 40 sccm	5 mTorr	50 W	500 W	25 °C	15 s
2. bulk etch	Cl / HBr = 30 / 40 sccm	5 mTorr	40 W	500 W	25 °C	1 m 05s
3. overetch	Cl / HBr = 15 / 30 sccm	5 mTorr	40 W	500 W	25 °C	20 s

Note: if after etching, Ti is not fully removed (e.g. there are shiny silvery spots near the edge), further etch using sequence Ti_100nm. Check that the etch time is correct before proceeding!

•

28. LAYER STRIPPING: Photoresist

Strip resist Use the PVA TePla GIGAbatch 360 system to remove the photoresist in an oxygen plasma.
Follow the instructions specified for the Tepla stripper.
Use **program 4**: 1000 watts power for 15 minutes

29. CLEANING: HNO_3 99% metal

Clean	10 minutes in fuming nitric acid at ambient temperature. This will dissolve organic materials. Use wet bench "HNO_3 99% (**metal)**" and the carrier with a red and white dot.
Rinse	Rinse in the Quick Dump Rinser with the standard program until the resistivity is 5 MΩ.
Dry	Use the "Avenger Ultra-Pure 6" rinser/dryer with the standard program, and the white carrier with a black dot.
Note	**Do not perform a "HNO_3 69,5% 110C (Si)" cleaning step, as that will remove the metal layer!**

Silicon etching of inlet, microchannels and nozzle

Back Side of Wafer

30. COATING

Use the coater station of the EVG120 system to coat the wafers with photoresist. The process consists of:

- A treatment with HMDS (hexamethyldisilazane) vapor, with nitrogen as a carrier gas, to improve resist adhesion.
- Spin coating of AZ ECl3027 positive resist, dispensed by a pump.
- A soft bake (a.k.a. pre-bake) at 95 °C for 90 seconds.

Always check the relative humidity (48 ± 2 %) in the room before coating, and follow the instructions for this equipment.

Use program **"1-Co-3027-4,0µm-noEBR"**

31. ALIGNMENT AND EXPOSURE

Processing will be performed on the ASML PAS5500/80 automatic wafer stepper. Follow the operating instructions from the manual when using this machine.

Expose **mask MICROT2** (box 502). The job depends on the preferred distribution of thruster configurations on the wafer. There are 5 options currently implemented on the 2024 version of the VLM. These are:

- Wafer 1A: job **Job special/2024_Jobs/AE_MiTh/W01A (Layer ID W01A)**
- Wafer 2A: job **Job special/2024_Jobs/AE_MiTh/W02A (Layer ID W02A)**
- Wafer 3A: job **Job special/2024_Jobs/AE_MiTh/W03A (Layer ID W03A)**
- Wafer 4A: job **Job special/2024_Jobs/AE_MiTh/W04A (Layer ID W04A)**
- Wafer 5A: job **Job special/2024_Jobs/AE_MiTh/W05A (Layer ID W05A)**

Other configurations from the 2023 version of the VLM can be used. The jobs for these can be found in the folder **Job special/2023_Jobs/3ME_MiTh/**, and are **W06 (Layer ID W06)** through **W10 (Layer ID W10)**. Check Excel file with configurations to choose the preferred one (contact Dr. Henk van Zeijl, Dr. Angelo Cervone, or check the Micropropulsion drive of the Space Engineering department of the Faculty of Aerospace Engineering – contact person Vidhya Pallichadath). If this cannot be found, contact previous student that has worked on this (Andrei Pârvulescu).

Use the following settings for exposure: **exposure energy 450 J/cm^2; focus offset –1 µm**.

32. DEVELOPING

Use the developer station of the EVG120 system to develop the wafers. The process consists of:

- A post-exposure bake at 115 °C for 90 seconds, to prevent ***standing waves*** on the sidewalls of the resist structures.
- Developing with Shipley MF322 with a single puddle process.
- A hard bake (a.k.a. post-bake) at 100 °C for 90 seconds. Always follow the instructions for this equipment.

Use program "**1–Dev–DP1**".

•

33. INSPECTION

Visually inspect the wafers through a microscope:
- Check if the correct mask is exposed.
- Check if there are no resist residues; these are NOT allowed.
- Check the linewidth of the structures.

34. PLASMA ETCHING: Silicon Channels
Use the Rapier Omega i2L DRIE etcher.
Use wafer recipe **0EKL_FlatBottom_xxx** (with a platen temperature of **-10 °C**) to etch 150 μm depth into the Si.

Parameter	Units	d1	E1	E2
Time	s	3	3	8
Primary Power	W	2200	2200	2200
Secondary Power	W	-	-	-
Platten Power	W	15	100	30
Coil Current	A	10	10	10
Pressure	torr	60	60	60
He Pressure	torr	5	5	5
SF_6	sccm	1	450	450
C4F8	sccm	350	1	1
O_2	sccm	0	0	0
Ar	sccm	0	0	0

Parameter		Value
Etching Rate, Si	μm/cycle	2.41*
	μm/m	10.5*
Selectivity – Si/SiO2		300*
Sidewall angle (°)		90.5*
Undercut (nm)		0
Sidewall		380 nm scallops
Wafer Uniformity (%)		1*
Ramping		No
Temperature (°C)		-10

* See the next paragraph for information regarding latest findings.

The information mentioned in the table above comes from the recipe itself. However, the last time it was used, different etch rates were observed when etching the same total number of cycles in different steps (62+10 versus 62+7+3). 70 – 71 cycles are probably ideal for etching 150 μm, but for more exact values, further experiments are needed. Check the MSc thesis of Andrei Pârvulescu (TU Delft repository) for details on the different effects on the etch depth. Consider also the bull's eye effect, where at the edges of the wafer the etch rate is higher.

The following data represents the latest finding of the VLM 2024 batch:
- Etching rate, Si: 2.13 μm/cycle (average for larger open structures, such as the inlet and microchannels)
- Selectivity – Si/3027(PR): 168 ± 14
- Sidewall angle: 93.0º ± 0.4° (for larger open structures, such as the microchannels entrance walls. For the nozzle throats, angles can be larger / smaller. Check MSc thesis of Andrei Pârvulescu)
- Uniformity Index: 4.2% (defined as $\frac{R_{max}-R_{min}}{2 \cdot R_{avg}}$, where R is the etch rate of the microchannels)

For conditioning recipe use **0Clean_-10C**. The recipes might be under the cassette recipe **HENK**.

35. INSPECTION (partially optional) – optionally and/or after photoresist stripping (step 36)
Inspect the wafers through the Keyence VK-X250:
- Check the depth of the etch (alternatively using the Dektak Surface Profiler)
- Check the surface finish
- Check the dimensions of the features (microchannels, nozzles etc.)

•

36. LAYER STRIPPING: Photoresist

Strip resist Use the PVA TePla GIGAbatch 360 system to remove the photoresist in an oxygen plasma.
Follow the instructions specified for the Tepla stripper.
Use **program 4**: 1000 watts power for 15 minutes

Add borosilicate glass wafers (double-sided and 525 µm thick)

37. CLEANING: HNO_3 99% metal (both Si and glass wafers)

Clean — 10 minutes in fuming nitric acid at ambient temperature. This will dissolve organic materials. Use wet bench "HNO_3 99% (**metal)**" and the carrier with a red and white dot.

Rinse — Rinse in the Quick Dump Rinser with the standard program until the resistivity is 5 MΩ.

Dry — Use the "Avenger Ultra-Pure 6" rinser/dryer with the standard program, and the white carrier with a black dot.

Note — **Do not perform a "HNO_3 69,5% 110C (Si)" cleaning step, as that will remove the metal layer!**

38. ANODIC WAFER BONDING

Use the AML wafer bonder, follow the tool specific procedures for anodic bonding.
Anodic bonding will be performed with graphite sheets added to the wafer stack. Two graphite sheet sizes are available, 100 mm diameter and approximately 90 mm diameter. Note that the smallest sheet should be placed on the glass.

- Load a graphite sheet on the cathode.
- Load the silicon wafer on the sheet **with the channels facing up**.
- Load the glass wafer (Borofloat glass).
- Load the graphite sheet on the glass.

Wafer bonding conditions:

- Vacuum
- Compression force = 4 kN
- Temperature = 400 ºC
- Bond voltage = 800 V
- Current ≤ 10 mA
- Total charge > 3 C

39. WAFER DICING

Leave the cleanroom to go dicing in the MEMS Lab.
The stack consists of 300 µm thick Si and 525 µm thick borosilicate glass. Dicing is performed through the whole stack at once.

The dicing order is (also check diagram on next page):

1. Dice horizontally along the nozzle outlet edge (without any dicing markers), variable pitch
2. Dice horizontally along the inlet edge (without any dicing markers), variable pitch
3. Dice vertically midway between the thrusters (1.9 mm from the side edge of the inlet), with a pitch of 7 mm

FURTHER STEPS: For further steps (glueing inlet & PCB, wire bonding, soldering header pins), please check the information in the MSc thesis of Andrei Pârvulescu.

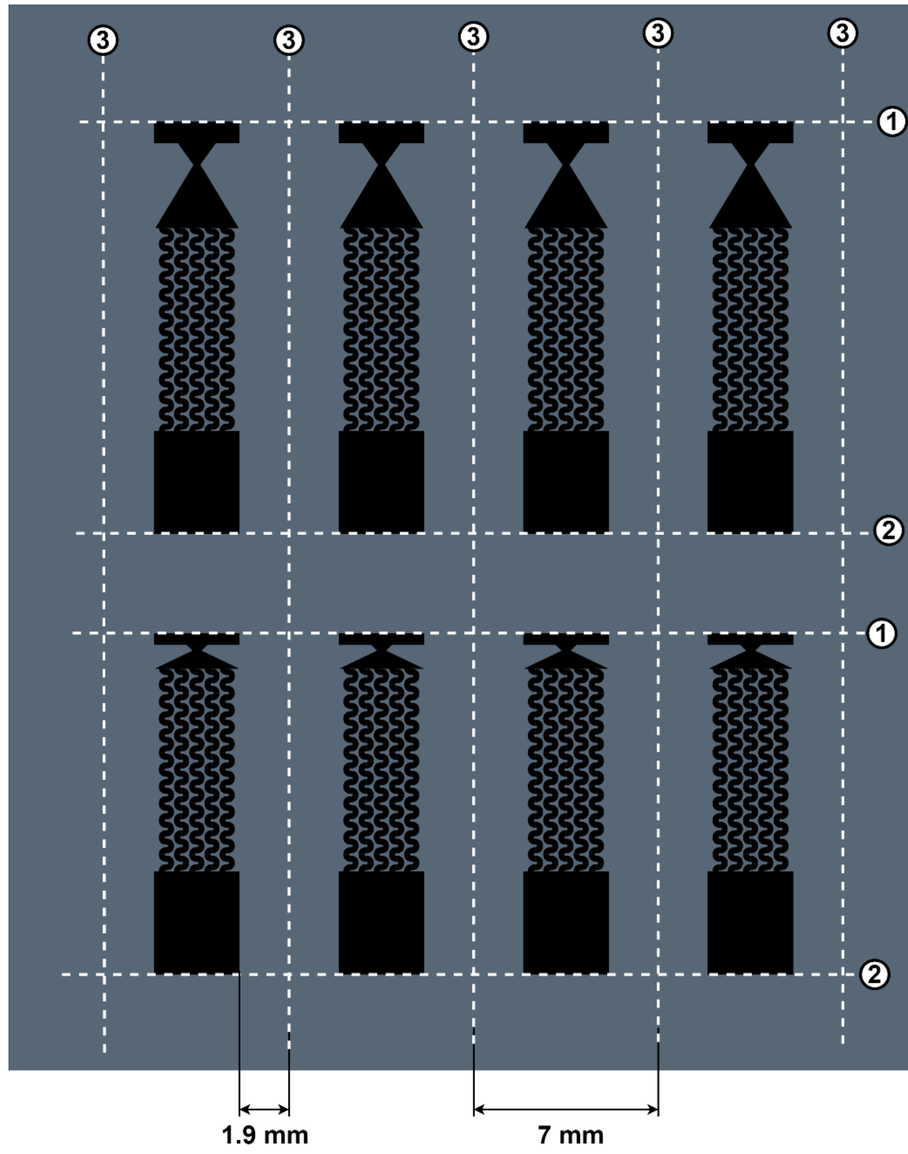

Figure 1. Dicing diagram

D
Thruster Dimensional Measurements

In this chapter, the measured values of depth and horizontal dimensions for the thrusters on wafer 3 and wafer 6 are included.

The measured depths of the wafer 3 thruster microchannels are given in Table D.1, and the depths of the nozzle throats in Table D.2. For wafer 6, these depths were mostly estimated using the calculated W6/W3 ratio in Subsection 4.5.3. For the microchannels, these are included in Table D.3, and for the nozzle throats in Table D.4.

The horizontal dimensions are given only for the thrusters on wafer 6. The microchannel widths are shown in Table D.5, the top surface nozzle throat widths in Table D.6, the convergent angle of the nozzles in Table D.7, the divergent angle of the nozzles in Table D.8, and the nozzle exit widths in Table D.9. Furthermore, the calculated average throat widths for the CD nozzles are included in Table D.10. These were calculated with the following formula:

$$w_{t,av} = w_t + d_t \cdot \tan\beta \tag{D.1}$$

Where $w_{t,av}$ is the average width of the throat of a thruster, w_t is its measured surface throat width, d_t is the measured or estimated throat depth, and β is the etching taper slope angle, as calculated in Subsection 4.5.1.

Table D.1: Microchannel depth measurements on wafer 3 using VK-X250. Values are in µm. N/A means that the thruster location is outside the wafer, while dashes signify that no measurements were done for that thruster.

	C1	C2	C3	C4	C5	C6	C7	C8	C9	C10	C11	C12
R1	N/A	N/A	N/A	-	-	149.9 ± 1.7	-	-	-	N/A	N/A	N/A
R2	159.8 ± 1.8	153.2 ± 1.7	150.4 ± 1.7	149.2 ± 1.7	147.0 ± 1.7	147.0 ± 1.7	147.1 ± 1.7	147.4 ± 1.7	148.5 ± 1.7	150.4 ± 1.7	153.1 ± 1.7	159.4 ± 1.8
R3	-	-	-	-	-	147.1 ± 1.7	-	-	-	-	-	-
R4	N/A	-	-	-	-	149.8 ± 1.7	-	-	-	-	-	N/A
R5	N/A	N/A	N/A	-	-	156.7 ± 1.8	-	-	-	N/A	N/A	N/A

Table D.2: Nozzle throat depth measurements on wafer 3 using VK-X250. Values are in µm. N/A means that the thruster location is outside the wafer, while NN signifies a thruster with no nozzle.

	C1	C2	C3	C4	C5	C6	C7	C8	C9	C10	C11	C12
R1	N/A	N/A	N/A	160.8 ± 1.8	145.6 ± 1.7	156.4 ± 1.8	132.6 ± 1.5	155.6 ± 1.8	161.5 ± 1.8	N/A	N/A	N/A
R2	163.5 ± 1.8	162.9 ± 1.8	158.6 ± 1.8	152.9 ± 1.7	152.4 ± 1.7	145.3 ± 1.7	147.2 ± 1.7	152.2 ± 1.7	153.6 ± 1.7	158.0 ± 1.8	163.4 ± 1.8	166.1 ± 1.9
R3	NN	138.1 ± 1.6	146.7 ± 1.7	135.9 ± 1.6	144.1 ± 1.6	NN	148.0 ± 1.7	148.0 ± 1.7	149.5 ± 1.7	130.9 ± 1.5	148.1 ± 1.7	NN
R4	N/A	136.0 ± 1.6	149.6 ± 1.7	146.3 ± 1.7	151.4 ± 1.7	145.1 ± 1.7	146.6 ± 1.7	151.1 ± 1.7	151.3 ± 1.7	153.7 ± 1.7	158.6 ± 1.8	N/A
R5	N/A	N/A	N/A	158.3 ± 1.8	149.7 ± 1.7	156.3 ± 1.8	148.5 ± 1.7	151.6 ± 1.7	159.3 ± 1.8	N/A	N/A	N/A

Table D.3: Microchannel depths on wafer 6. Values are in µm. N/A means that the thruster location is outside the wafer, while dashes signify that no measurements were done for that thruster. BD means that the thruster was broken during dicing. For thrusters R2C07 to R2C12, the values are measured, whereas for the rest they are estimated based on the W6/W3 ratio.

	C1	C2	C3	C4	C5	C6	C7	C8	C9	C10	C11	C12
R1	N/A	N/A	N/A	-	-	140.4 ± 1.6	-	-	-	N/A	N/A	N/A
R2	BD	143.5 ± 1.6	140.9 ± 1.6	139.8 ± 1.6	137.7 ± 1.6	137.7 ± 1.6	138.3 ± 1.6	138.4 ± 1.6	139.5 ± 1.6	141.0 ± 1.6	143.2 ± 1.6	148.2 ± 1.7
R3	-	-	-	-	-	137.8 ± 1.6	-	-	-	-	-	
R4	N/A	-	-	-	-	140.3 ± 1.6	-	-	-	-	-	N/A
R5	N/A	N/A	N/A	-	-	146.8 ± 1.7	-	-	-	N/A	N/A	N/A

Table D.4: Nozzle throat depth measurements on wafer 6. Values are in µm. N/A means that the thruster location is outside the wafer, while NN signifies a thruster with no nozzle. Dashes signify no estimations for that thruster, while BD means that the thruster was broken during dicing. For thrusters R2C07 to R2C12, the values are measured, whereas for the rest they are estimated based on the W6/W3 ratio.

	C1	**C2**	**C3**	**C4**	**C5**	**C6**	**C7**	**C8**	**C9**	**C10**	**C11**	**C12**
R1	N/A	N/A	N/A	-	139.3 ± 1.6	147.9 ± 1.7	126.9 ± 1.5	147.1 ± 1.7	-	N/A	N/A	N/A
R2	BD	154.0 ± 1.7	149.9 ± 1.7	144.6 ± 1.6	142.8 ± 1.6	139.0 ± 1.6	140.9 ± 1.6	143.6 ± 1.6	145.3 ± 1.7	149.5 ± 1.7	152.7 ± 1.7	155.3 ± 1.8
R3	NN	132.1 ± 1.5	138.7 ± 1.6	130.0 ± 1.5	136.2 ± 1.6	NN	138.7 ± 1.6	138.7 ± 1.6	140.1 ± 1.6	125.2 ± 1.5	140.0 ± 1.6	NN
R4	N/A	130.1 ± 1.5	141.4 ± 1.6	140.0 ± 1.6	141.8 ± 1.6	138.8 ± 1.6	140.2 ± 1.6	141.6 ± 1.6	143.0 ± 1.6	145.3 ± 1.7	148.6 ± 1.7	N/A
R5	N/A	N/A	N/A	148.3 ± 1.7	143.2 ± 1.6	146.4 ± 1.7	142.1 ± 1.6	145.0 ± 1.7	149.3 ± 1.7	N/A	N/A	N/A

Table D.5: Microchannel widths measured on wafer 6, using VK-X1000. Values are in µm. N/A means that the thruster location is outside the wafer, while dashes signify that no measurements were done for that thruster. BD means that the thruster was broken during dicing. For all measurements, the uncertainty is ±1.8 µm.

	C1	**C2**	**C3**	**C4**	**C5**	**C6**	**C7**	**C8**	**C9**	**C10**	**C11**	**C12**
R1	N/A	N/A	N/A	-	-	-	218.8	-	-	N/A	N/A	N/A
R2	BD	218.5	219.7	219.4	218.5	219.1	218.5	219.1	219.4	218.5	219.8	219.8
R3	219.1	218.8	-	-	-	-	219.8	-	-	-	-	-
R4	N/A	-	-	-	-	-	218.8	-	-	-	-	N/A
R5	N/A	N/A	N/A	-	-	-	220.1	-	-	N/A	N/A	N/A

Table D.6: Surface throat widths measured on wafer 6, using VK-X1000. Values are in µm. N/A means that the thruster location is outside the wafer. BD means that the thruster was broken during dicing, while NN signifies that the thruster does not have a nozzle. For all measurements, the uncertainty is ±1.8 µm.

	C1	**C2**	**C3**	**C4**	**C5**	**C6**	**C7**	**C8**	**C9**	**C10**	**C11**	**C12**
R1	N/A	N/A	N/A	26.8	28.3	53.9	27.6	53.8	27.9	N/A	N/A	N/A
R2	BD	48.7	53.1	47.4	73.0	21.9	22.5	75.5	49.3	48.7	76.8	73.7
R3	NN	27.4	53.2	27.7	56.0	NN	73.7	76.2	73.7	27.4	52.9	NN
R4	N/A	28.2	52.6	22.5	75.5	22.5	22.5	78.0	49.3	49.3	77.4	N/A
R5	N/A	N/A	N/A	74.3	23.1	79.3	23.1	23.1	79.3	N/A	N/A	N/A

Table D.7: Nozzle convergent (full) angles measured on wafer 6, using VK-X1000. Values are in degrees. N/A means that the thruster location is outside the wafer, while AS signifies that the nozzle is of the aerospike type. BD means that the thruster was broken during dicing, while NN signifies that the thruster does not have a nozzle.

	C1	**C2**	**C3**	**C4**	**C5**	**C6**	**C7**	**C8**	**C9**	**C10**	**C11**	**C12**
R1	N/A	N/A	N/A	AS	AS	AS	AS	AS	AS	N/A	N/A	N/A
R2	BD	120.0	149.4	120.0	150.5	150.0	150.0	150.1	140.1	140.2	149.8	150.9
R3	NN	AS	AS	AS	AS	NN	90.6	89.6	90.1	AS	AS	NN
R4	N/A	AS	AS	149.9	150.5	149.9	149.7	149.8	139.8	139.9	149.5	N/A
R5	N/A	N/A	N/A	149.4	149.6	149.8	150.3	150.1	149.9	N/A	N/A	N/A

Table D.8: Nozzle divergent (full) angles measured on wafer 6, using VK-X1000. Values are in degrees. N/A means that the thruster location is outside the wafer, while AS signifies that the nozzle is of the aerospike type. BD means that the thruster was broken during dicing, while NN signifies that the thruster does not have a nozzle.

	C1	**C2**	**C3**	**C4**	**C5**	**C6**	**C7**	**C8**	**C9**	**C10**	**C11**	**C12**
R1	N/A	N/A	N/A	AS	AS	AS	AS	AS	AS	N/A	N/A	N/A
R2	BD	149.9	149.5	110.3	150.3	60.5	89.8	150.4	120.7	120.1	150.2	89.8
R3	NN	AS	AS	AS	AS	NN	149.3	149.3	150.0	AS	AS	NN
R4	N/A	AS	AS	59.9	150.1	59.7	90.1	150.0	120.3	119.8	149.9	N/A
R5	N/A	N/A	N/A	90.2	59.9	149.9	59.4	90.1	150.4	N/A	N/A	N/A

Table D.9: Nozzle exit widths measured on wafer 6, using VK-X1000. Values are in µm. N/A means that the thruster location is outside the wafer, while AS signifies that the nozzle is of the aerospike type. BD means that the thruster was broken during dicing, while NN signifies that the thruster does not have a nozzle.

	C1	**C2**	**C3**	**C4**	**C5**	**C6**	**C7**	**C8**	**C9**	**C10**	**C11**	**C12**
R1	N/A	N/A	N/A	AS	AS	AS	AS	AS	AS	N/A	N/A	N/A
R2	BD	327.7 ± 1.8	513.2 ± 1.8	256.6 ± 1.8	931.4 ± 3.4	931.4 ± 3.4	511.3 ± 1.8	491.9 ± 1.8	700.4 ± 1.8	997.8 ± 3.4	1499.4 ± 6.7	385.2 ± 1.8
R3	NN	AS	AS	AS	AS	NN	1497.0 ± 6.7	933.8 ± 3.4	1118.6 ± 3.4	AS	AS	NN
R4	N/A	AS	AS	736.9 ± 3.4	930.2 ± 3.4	971.2 ± 3.4	514.4 ± 1.8	491.9 ± 1.8	701.1 ± 1.8	1001.4 ± 3.4	1494.6 ± 6.7	N/A
R5	N/A	N/A	N/A	385.2 ± 1.8	738.1 ± 3.4	932.6 ± 3.4	977.3 ± 3.4	513.8 ± 1.8	492.6 ± 1.8	N/A	N/A	N/A

Table D.10: Average throat widths calculated for the CD nozzles on wafer 6. Values are in µm. N/A means that the thruster location is outside the wafer, while AS signifies that the nozzle is of the aerospike type. BD means that the thruster was broken during dicing, while NN signifies that the thruster does not have a nozzle.

	C1	**C2**	**C3**	**C4**	**C5**	**C6**	**C7**	**C8**	**C9**	**C10**	**C11**	**C12**
R1	N/A	N/A	N/A	AS	AS	AS	AS	AS	AS	N/A	N/A	N/A
R2	BD	57.0	61.2	55.3	85.3	26.3	27.0	87.8	57.2	56.8	89.9	87.0
R3	NN	AS	AS	AS	AS	NN	85.6	88.0	85.7	AS	AS	NN
R4	N/A	AS	AS	27.0	87.7	27.0	27.0	90.2	57.1	57.2	90.1	N/A
R5	N/A	N/A	N/A	87.0	27.7	91.8	27.7	27.8	92.1	N/A	N/A	N/A

E

Technical Drawings of the Fluidic Interfaces

The technical drawings of the 3rd iteration with-nozzle inlet, no-nozzle inlet, and no-nozzle outlet fluidic interfaces, are included in this appendix, in this order.

REVISION HISTORY			
REV	DESCRIPTION	DATE	APPROVED

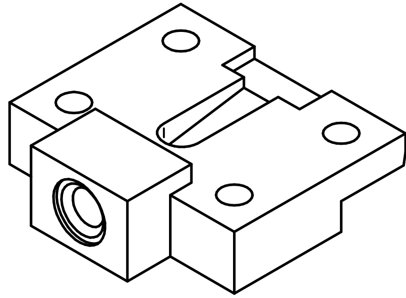

Isometric View

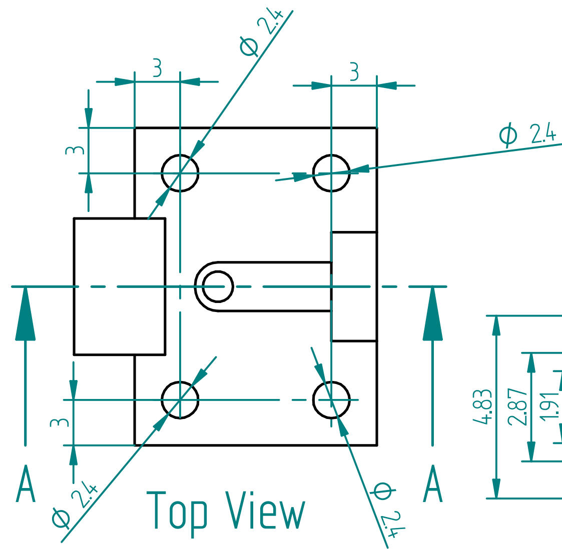

Top View

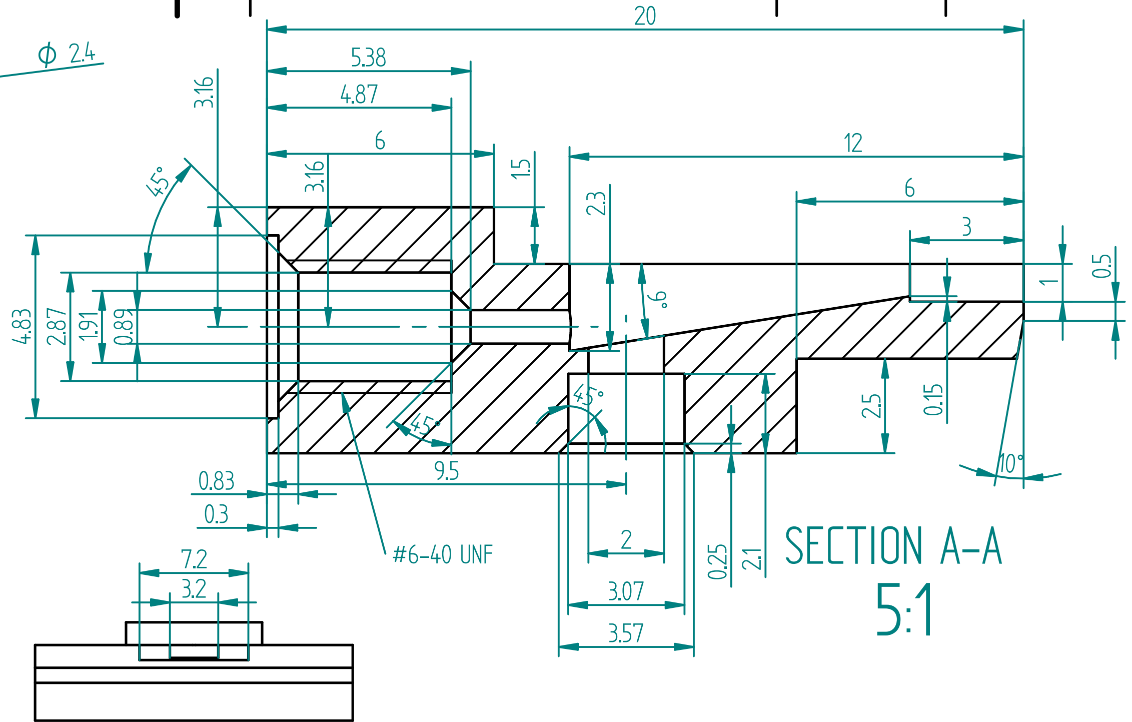

SECTION A-A
5:1

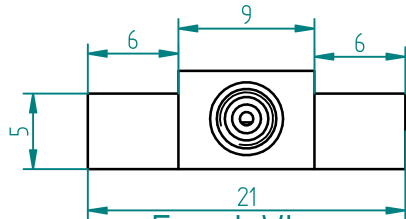

Front View

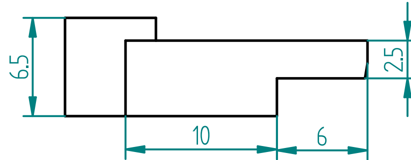

Side View

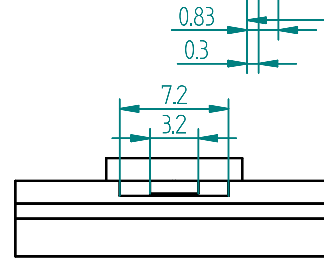

Back View

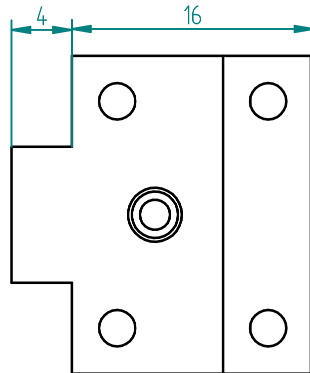

Bottom View

SOLID EDGE ACADEMIC COPY

DRAWN BY	Andrei Pârvulescu
DATE	04/11/2024

UNLESS OTHERWISE SPECIFIED
DIMENSIONS ARE IN MILLIMETERS
THIRD ANGLE PROJECTION

Solid Edge

TITLE
Inlet Fluid Interface With Nozzle

SIZE	DWG NO	REV
A4	VLM-AP24-IFIWN-V3	1

FILE NAME: Inlet_bottom_v3.0_withNozzle.dft

SCALE: 2:1	WEIGHT:	SHEET 1 OF 1

REVISION HISTORY			
REV	DESCRIPTION	DATE	APPROVED

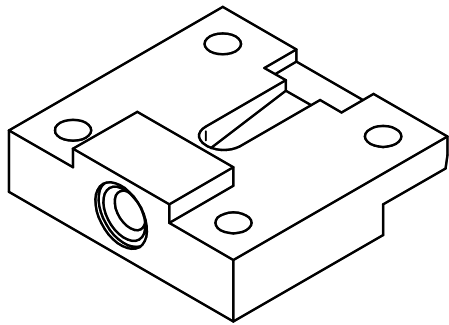

Isometric View

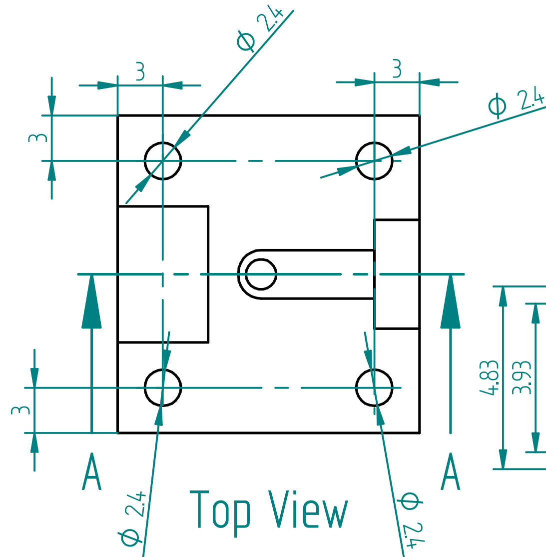

Top View

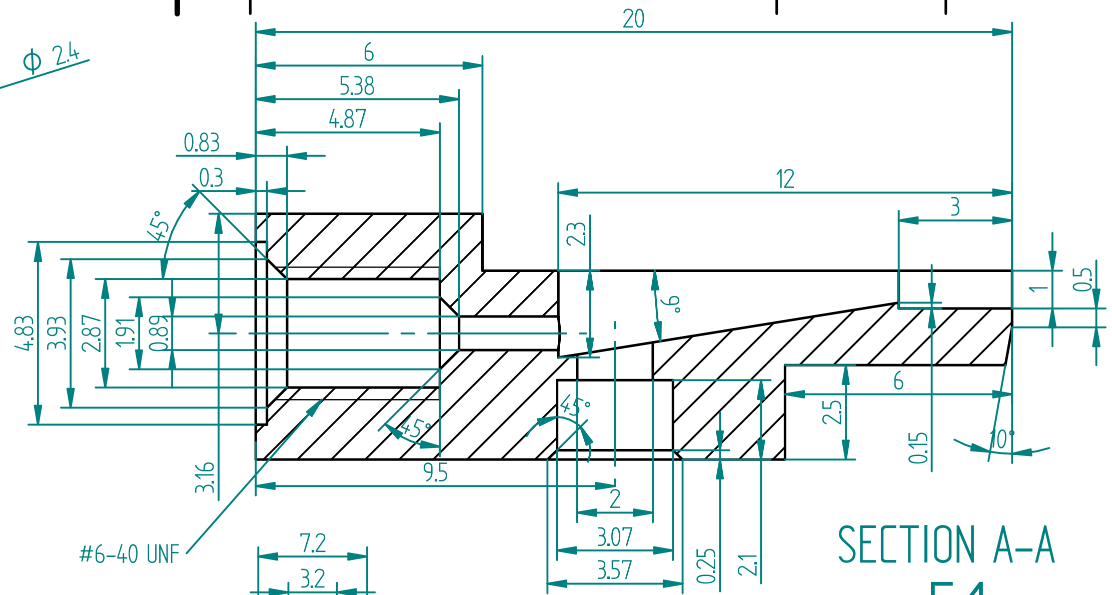

SECTION A-A
5:1

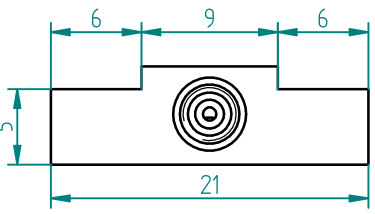

Front View

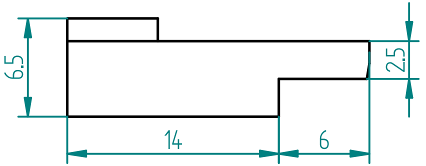

Side View

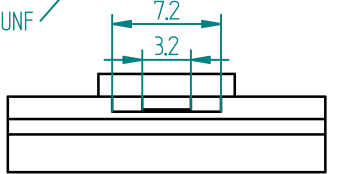

Back View

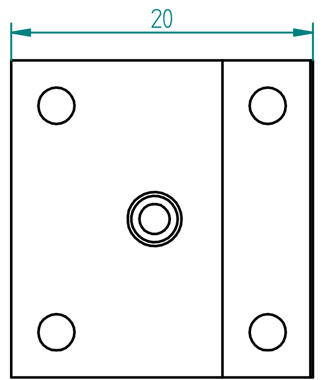

Bottom View

SOLID EDGE ACADEMIC COPY

DRAWN BY	Andrei Pârvulescu
DATE	04/11/2024

UNLESS OTHERWISE SPECIFIED
DIMENSIONS ARE IN MILLIMETERS
THIRD ANGLE PROJECTION

Solid Edge

TITLE
Inlet Fluid Interface No Nozzle

SIZE	DWG NO	REV
A4	VLM-AP24-IFINN-V3	1

FILE NAME: Inlet_bottom_v3.0_noNozzle.dft

SCALE: 2:1	WEIGHT:	SHEET 1 OF 1

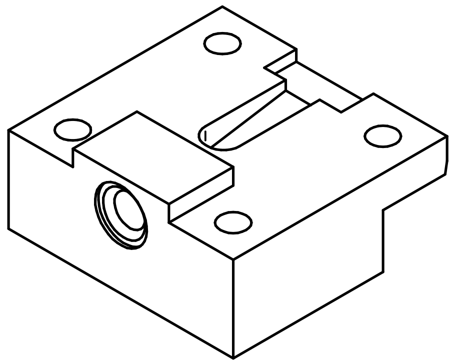

Isometric View

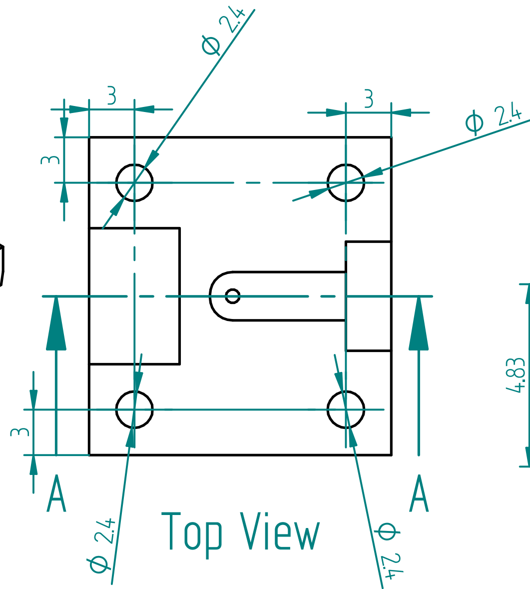

Top View

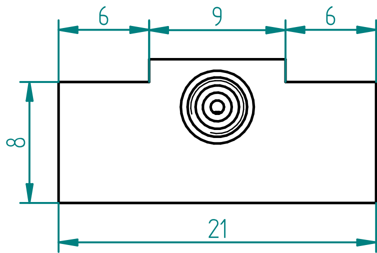

Front View

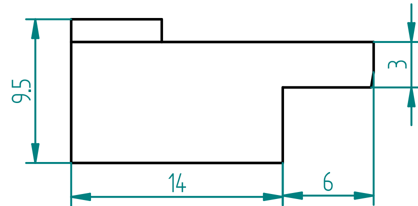

Side View

7.2
3.2

Back View

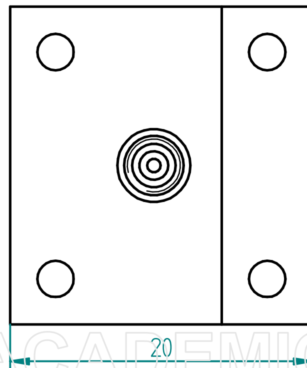

Bottom View

SOLID EDGE ACADEMIC COPY

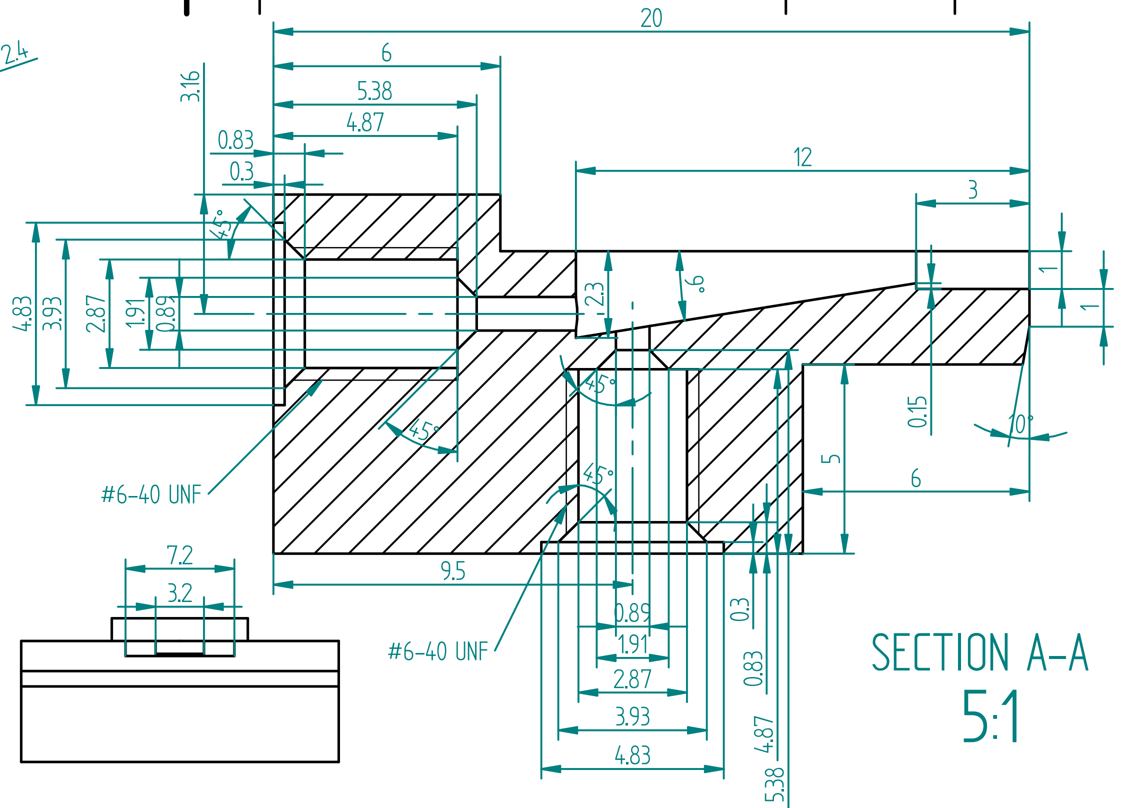

SECTION A-A
5:1

REVISION HISTORY

REV	DESCRIPTION	DATE	APPROVED

DRAWN BY	Andrei Pârvulescu
DATE	04/11/2024

UNLESS OTHERWISE SPECIFIED
DIMENSIONS ARE IN MILLIMETERS
THIRD ANGLE PROJECTION

Solid Edge

TITLE
Outlet Fluid Interface No Nozzle

SIZE	DWG NO	REV
A4	VLM-AP24-OFINN-V3	1

FILE NAME: Outlet_bottom_v3.0_noNozzle.dft

SCALE: 2:1 | WEIGHT: | SHEET 1 OF 1